



저작자표시-비영리-변경금지 2.0 대한민국

이용자는 아래의 조건을 따르는 경우에 한하여 자유롭게

- 이 저작물을 복제, 배포, 전송, 전시, 공연 및 방송할 수 있습니다.

다음과 같은 조건을 따라야 합니다:



저작자표시. 귀하는 원저작자를 표시하여야 합니다.



비영리. 귀하는 이 저작물을 영리 목적으로 이용할 수 없습니다.



변경금지. 귀하는 이 저작물을 개작, 변형 또는 가공할 수 없습니다.

- 귀하는, 이 저작물의 재이용이나 배포의 경우, 이 저작물에 적용된 이용허락조건을 명확하게 나타내어야 합니다.
- 저작권자로부터 별도의 허가를 받으면 이러한 조건들은 적용되지 않습니다.

저작권법에 따른 이용자의 권리는 위의 내용에 의하여 영향을 받지 않습니다.

이것은 [이용허락규약\(Legal Code\)](#)을 이해하기 쉽게 요약한 것입니다.

[Disclaimer](#)

이학박사학위논문

논-도핑 유기발광 소자용 형광 물질의 합
성과 색 가변 유기 발광 소자의 개발

**Development of Fluorescent Materials for
Non-doped Organic Light-emitting Diodes
and Color Tunable Devices**

2018 년 2 월

서울대학교 대학원

화학부 유기화학 전공

정 성 진

논-도핑 유기발광 소자용 형광 물질의 합성과 색 가변
유기 발광 소자의 개발

**Development of Fluorescent Materials for Non-doped Organic
Light-emitting Diodes and Color-tunable Devices**

지도교수 홍종인

이 논문을 이학박사학위 논문으로 제출함.

2017년 12월

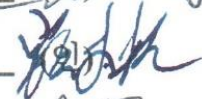
서울대학교 대학원 화학부
유기화학전공
정성진

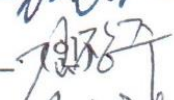
정성진의 이학박사 학위논문을 인준함.

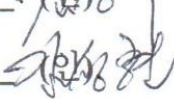
2017년 12월

위원장 이성훈 (인) 

부위원장 홍종인 (인) 

위원 최태림 

위원 김장주 

위원 김성현 

Abstract

Development of Fluorescent Materials for Non-doped Organic Light-emitting Diodes and Color-tunable Devices

Seongjin Jeong

Major in Organic Chemistry

Department of Chemistry

Graduate School

Seoul National University

Organic light-emitting diodes (OLEDs) have been attracting great attention as next-generation displays due to advantages such as self-emitting, high brightness, high contrast ratio, fast response and ultra-thin thickness. The materials used for the emitting layer (EML) are the key part of the OLEDs and demand high color purity,

high quantum efficiency and easy reproducibility of production. Among them, since it is particularly difficult to obtain high color purity and quantum efficiency for blue luminescent materials, research on them is further required than other primary colors. In this study, the development of fluorescent materials for the blue emission and the delayed fluorescence (DF) is discussed, and followed by the structure of color-tunable OLEDs (CTOLEDs) fabrication. The blue fluorescent materials exhibit better color purity and quantum efficiency than conventional blue materials, and the delayed fluorescent materials show higher quantum efficiency in a non-doped condition without a host material in the EML than those of doped condition. The CTOLED using an exciton blocking layer (EBL) is applied to the development of ultra-thin carbon nanotube (CNT)-based electrocardiogram (ECG) monitors and shows sensitive color change according to heart rate.

Part I summarizes basic theories for the understanding of the overall photophysical phenomena involved in the OLEDs. Understanding the mechanism of absorption and emission processes is necessary to analyze the principle of electroluminescence, its quantum efficiency and lifetime in an actual device. Also, this understanding is helpful to devise novel blue fluorescent materials and delayed fluorescent materials for use in OLEDs.

Part II is a study on the development of the highly efficient blue fluorescent emitters without a host material in the EML. It has been known to be difficult to develop blue fluorescent materials with the standard blue color coordinates corresponding to CIE (0.15, 0.07) and high quantum efficiency, because of the inherent high band-gap energy characteristic and the imbalanced charge transporting properties. In this study, donor-chromophore-acceptor type blue fluorescent materials are developed where hole transport and/or electron transport functional

groups are twisted with respect to the plane of the chromophore. These materials show high charge balance and prevent the bathochromic shift of emission in the solid state. In the first section, four bipolar luminescent molecules (3PAA, IQAA, 3QAA, and PTAA) with anisole-anthracene (AA) cores attached to the electron withdrawing group such as pyridine, isoquinoline, quinoline and phenanthroline, respectively, are designed and synthesized for use as non-doped blue fluorescent materials. Because of highly twisted molecular structure, each molecule shows deep-blue to sky-blue emission in solution state. The emission of the quinoline-attached 3QAA is shifted to the longer wavelength region (bathochromic shift) compared to those of 3PAA and IQAA, whereas phenanthroline-attached PTAA emitted relatively longer wavelength region than that of 3QAA. These results come from the difference in the conjugation length and position of the electron accepting group. In the second section, blue fluorescent emitters named T1B and T2B are synthesized by direct coupling of triphenylamine with good hole mobility and benzimidazole with good electron mobility, for use as deep-blue emitters for efficient non-doped fluorescent OLEDs, where the correlation between the device performance and the molecular packing density is investigated. Fluorescent OLEDs using sterically bulky T2B as an emitter without a host material show deep-blue emissions and higher external quantum efficiency (EQE) than that of T1B owing to more efficient inhibition of exciton quenching. In the third section, three blue fluorescent materials, named QT, XT, and ZT, are developed by combining triphenylamine for good hole mobility, quinoline, quinoxaline and quinazoline for good electron mobility, respectively. Non-doped OLEDs based on QT, XT, and ZT generate saturated blue to sky-blue EL emission. Among them, OLEDs fabricated using QT exhibit the highest efficiency and color coordinates close to the standard blue color, and is also used as a host material for XT and ZT. In the fourth section, a new indenophenanthrene core structure is

developed to induce a deep blue emission by hybridizing a phenanthrene moiety with fluorene. TIP and DIP are synthesized by coupling triphenylamine and diphenylamine with good hole mobility to the indenophenanthrene core, respectively. DIP-based non-doped OLED devices exhibit higher efficiency compared to TIP-based devices, as they have well-matched hole and electron density at the same driving voltage.

Part III is a study on the development of high-efficiency materials that produce delayed fluorescence without a host material. Thermally activated delayed fluorescent (TADF) molecules tend to aggregate easily, through π - π interactions arising from their innate hydrophobicity and rigid-planar structures. This phenomenon leads to aggregation-caused quenching (ACQ) and exciton concentration quenching in the solid state, which is the fatal weakness in OLEDs using solid-state emission. To overcome this problem, two materials named AmT and AmmT are designed. These two emitters are composed of electron donor (acridine) and acceptor (triphenyltriazine) moieties, which are connected at the meta positions so that intra- and intermolecular charge transfer (CT) states can be induced through exciplex-like interactions between the same emitters. These materials also show DF characteristic. AmT-and AmmT-based non-doped OLEDs devices exhibit higher external quantum efficiencies than those of doped devices, due to not only the formation of excitons by intramolecular interaction, but also by intermolecular interaction.

In part IV, a method for manufacturing wearable ECG monitors is developed using a CNT based ultra-thin electronic device and a CTOLEDs based display. A p-type metal-oxide semiconductor (p-MOS) inverter with four CNT transistors leads to successful acquisition of the ECG signals by allowing high amplification. In the

CTOLEDs, an ultrathin EBL of bis[2-(diphenylphosphino)phenyl]ether oxide (DPEPO) is used to manipulate the balance of charges between two adjacent emission layers; blue EML by bis[2-(4,6-difluorophenyl)pyridinato-C₂,N](picolato) iridium(III) (FIrpic) and red EML by bis(2-phenylquinolyl-N,C(2'))-iridium(acetylacetonate) (pq2Ir(acac)), which thereby produces different colors with respect to applied voltages. These ultrathin fabricated devices support superior wearability yielding the conformal integration for the on-skin sensor, with high resilience verified through repetitive bending/folding fatigue tests. The wearable CTOLEDs integrated with CNT electronics are used to display human ECG changes in real-time using tunable colors.

Keywords: Fluorescent organic light emitting device, Bipolar, Blue fluorescent material, Delayed fluorescent material, Intermolecular interaction, Carbon nanotube, Color tunable organic light emitting device, Wearable sensor

Student Number: 2011-30103

Contents

Abstract	ii
Part I. Basics of OLEDs	1
1. Introduction	2
2. Absorption of UV-Vis Light	8
3. Characteristics of Fluorescent Emission	15
4. Intra- and Intermolecular Photophysical process	28
Part II. Development of Non-doped Blue Fluorescent Materials for OLEDs	43
Background	44
1. Blue fluorescent materials	44
2. Doped blue fluorescent materials	47
3. Non-doped blue fluorescent materials	48
Section 1. Blue Fluorescent Emitters for Non-doped Organic Light- emitting Diodes Based on an Anisole-Anthracene Core with Various Electron Withdrawing Pyridine Derivatives	66
1. Introduction	67
2. Materials and methods	68
3. Results and Discussions	74
4. Conclusion	82

Section 2. Efficient deep-blue emitters based on triphenylamine-linked benzimidazole derivatives for non-doped fluorescent organic light-emitting diodes.....	83
1. Introduction	84
2. Materials and methods	85
3. Results and Discussion.....	91
4. Conclusion.....	102
Section 3 Development of multifunctional materials for OLEDs using triphenylamine-quinoline, quinoxaline and quinazoline hybrid compounds for deep blue fluorescent emitters and host materials	104
1. Introduction	105
2. Materials and general methods.....	106
3. Results and discussion.....	110
4. Conclusion.....	122
Section 4 Extremely deep-blue fluorescent emitters with CIE_y ≤ 0.04 for non-doped organic light-emitting diodes based on an indenophenanthrene core	123
1. Introduction	124
2. Materials and general methods.....	125
3. Results and discussion.....	133
4. Conclusion.....	144

Part III. Development of Non-doped Thermally Activated Delayed Fluorescent Materials for OLEDs	147
Background	148
1. Delayed fluorescent from singlet exciton	148
2. About TADF	156
3. Development of TADF emitters.....	164
Section 1. Highly Efficient Non-doped Thermally Activated Delayed Fluorescent Organic Light-emitting Diodes Using Intra- and Intermolecular Exciplex System by a meta-linked Acridine- Triazine Conjugate.....	181
1. Introduction	182
2. Materials and general methods.....	185
3. Results and discussion.....	192
4. Conclusion.....	205
5. Supplementary data.....	207
Part IV. Flexible and Stretchable Bio-Electronic Devices Integrated with Color Tunable Organic Light-emitting Diodes	215
Background	216
1. Flexble and stretchable bio-electronic devices	216

2. Color-tunable devices.....229

Section 1 Wearable Electrocardiogram Monitor Using Carbon

**Nanotube Electronics and Color-Tunable Organic Light-Emitting
Diodes237**

1. Introduction237
2. Results and Discussion.....239
3. Conclusion.....254
4. Supporting information254

References and Notes261

국문초록 i

감사의 글Error! Bookmark not defined.

Part I. Basics of OLEDs

1. Introduction

1.1. The rise of OLED displays (By J.-F. Tremblay)

Long the focus of research at academic and corporate labs worldwide, organic light-emitting diode (OLED) displays are starting to trickle into the market. Although they currently represent only a small slice of the total pie and are so far mostly used in mobile phones, OLEDs are poised to rapidly gain market share in the coming years. This growth will open up billions of dollars of market opportunity for chemical companies that supply materials to the electronics industry. But at the same time, such firms are keen to hold on to the business they have with makers of displays based on incumbent liquid-crystal display, or LCD, technology.

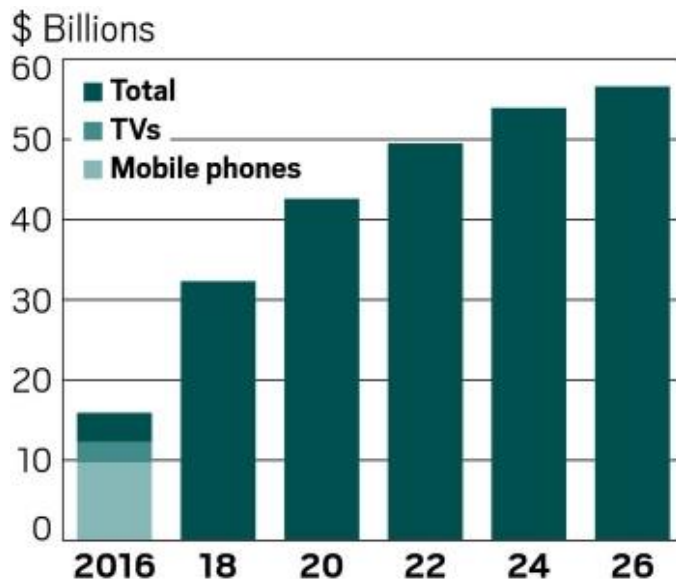


Figure 1.1. **Bright future** of the OLED display market.

Note: Mobile phone and TV data available only for 2016. Source: IDTechEx.

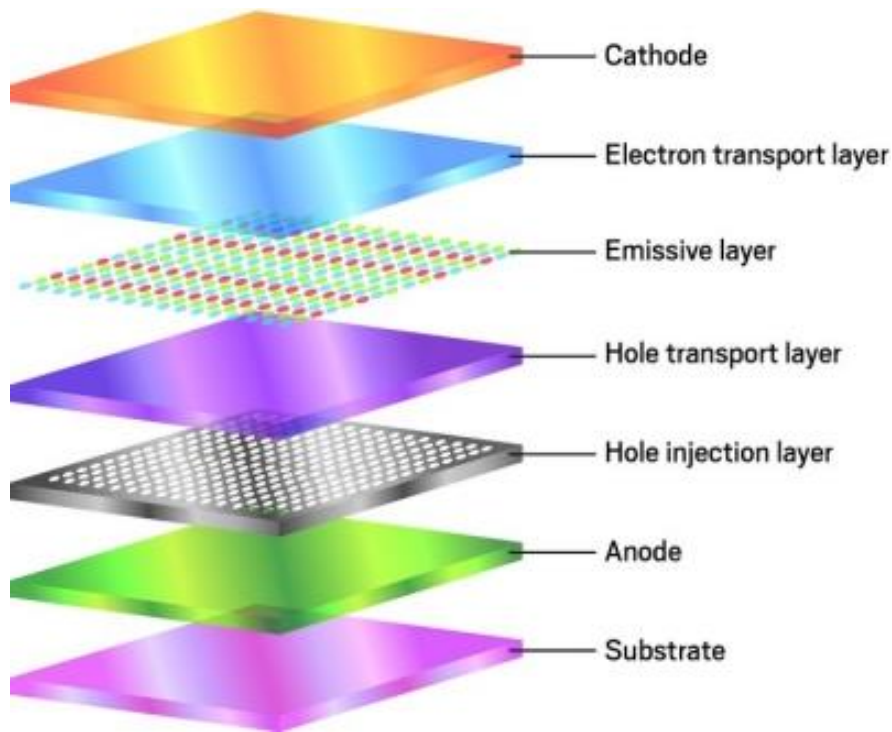


Figure 1.2. **How OLEDs work.** Source: Universal Display

An OLED can be manufactured using a variety of substrates, including glass, plastic, and metal. It consists of several layers of organic materials sandwiched between two electrodes. When a voltage is applied across the OLED, a current of electrons flows from the cathode to the anode, adding electrons to the emissive layer and taking them away or creating electron holes—at the anode. At the boundary between these layers, electrons find holes, fall in, and give up a photon of light. The color of the light depends on the type of organic molecule in the emissive layer. The most advanced OLEDs use electron and hole injection and transport layers to modulate electron movement.

“OLED displays can be lighter, they can be flexible, and they allow designers more leeway with the shape of their devices,” says Guillaume Chansin, senior technology analyst at IDTechEx. Theoretically, he adds, OLEDs can be far more energy-efficient than the LCDs found in most TVs today. And because they are now manufactured on a plastic substrate instead of a glass one, “OLED displays can make phone screens shatterproof, or even foldable.” The promise of OLEDs has generated much interest among researchers for decades. In an LCD, images are generated by a backlight—a light-emitting diode nowadays—that sends light through liquid crystals, polarizers, color filters, and several image-enhancing filters. The color black in an LCD is created not by turning off the backlight but by electro-orienting the liquid crystals to affect the angle at which the passing light hits the polarizers. OLED displays are much simpler and thus can be far thinner than LCDs. Instead of a backlight, OLEDs feature pixels that individually emit the red, green, and blue lights required to form an image. OLEDs consist of organic molecules positioned between two electrodes. As current flows from the cathode to the anode, electrons and electron holes in the molecules combine, emitting flashes of light. In an OLED display, black is created by leaving the corresponding pixels off rather than by blocking a backlight. OLED advocates claim that the resulting “true black” is one reason OLEDs can display sharper images. And energy is saved, because the parts of an OLED display that are dark don’t consume electricity.

Although the basic concept behind OLEDs is elegant and simple, turning it into practice has been another matter entirely. The color blue is a perennial headache because the molecules that create it don’t last as long as their red and green counterparts. The bonds in the blue molecules tend to break down, partly because they are fluorescent rather than phosphorescent and require more electricity to

operate. In addition, the charge carriers in blue OLEDs recombine through the absorption of ultraviolet light. Moreover, from a performance point of view, the energy efficiency of blue OLEDs is also lower than for other colors.

The cost of making OLED displays is another issue. The core compounds at the heart of OLED displays are often made with expensive substances such as iridium, a rare metal that sells for nearly \$19 per gram. What's more, the standard technique for depositing organic materials on an OLED substrate is a vacuum evaporation process in which a mask is laid over a substrate, molecules are deposited, the mask is taken off, and the mask is cleaned in a vacuum chamber. Industry insiders estimate that the process "wastes" between 70 and 90% of the expensive materials coated on the mask.

In recent years, commitments to OLED production have multiplied. LG Display announced a massive \$9 billion investment in an OLED TV plant scheduled to open in 2018. Numerous reports say Apple is going to source billions of dollars' worth of OLED displays from Samsung for use in future iPhone models. Meanwhile, Applied Materials, a supplier of precision manufacturing equipment, disclosed that demand for tools to make OLEDs is sharply strengthening in 2016.

Red and green light are now created with phosphorescent organic compounds that have greater quantum efficiency than the fluorescent compounds traditionally used in OLEDs. More research still has to be done on phosphorescent blue, DuFour says, but "we are hoping for a breakthrough soon." Ink-jet printing for OLED displays is steadily advancing, confirms Christopher Savoie, chief executive officer of Kyulux, a developer of OLED display materials based in Fukuoka, Japan. The question, he says, is whether materials developers will succeed in designing inks that can last long enough for use in a television. "The high energy that blue materials are

put through, it creates oxidation, causes all sorts of reactions, breaks bonds,” he says. So far, he says, phosphorescent blue materials aren’t commercially available because their metallo-organic bonds are relatively weak and achieving long lifetimes is difficult. Kyulux has developed fluorescent blue materials that it claims perform almost as well as phosphorescent ones. Significantly, Savoie explains, the materials that Kyulux offers don’t contain expensive metals such as iridium. Using materials that do not contain rare metals reduces the cost of making displays, even with the deposition process, Savoie says.



Figure 1.3. Examples of emitter molecules that can be used in OLED displays. Credit: Kateeva

In response to this need, thermally activated delayed fluorescence (TADF) is the most promising exciton harvesting mechanism used in OLED devices. Since the first reported OLED based on an organic TADF emitter in 2011 tremendous attention in recent years has been devoted to improving their performance (Figure 1.4). One important advantage of TADF emitters is that they can be purely organic, thus avoiding the problems associated with the use of heavy-metal-based organometallic complexes.

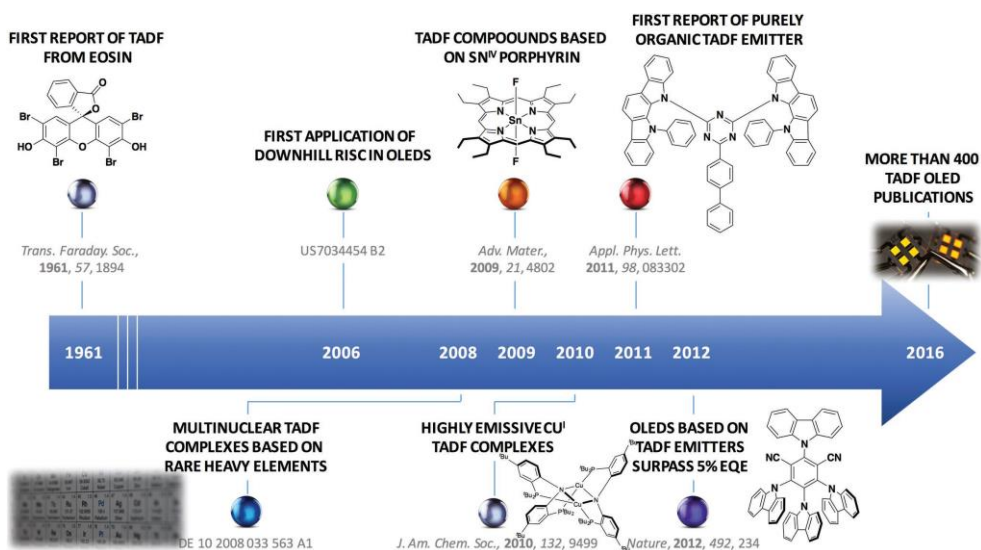


Figure 1.4. Timeline of developments of TADF-based OLEDs. Reproduced with permission. Copyright 2017, Wiley-VCH.¹

With OLED technology becoming standard in mobile phones but making only hesitant progress in TVs, the display industry is currently at a crossroads, says Uno, the IHS analyst. “It all really depends on the adoption rate by companies like Apple,” he says. But OLED displays provide such significant advantages over LCDs in terms of weight, thinness, robustness, and flexibility that change will happen fast once key hurdles are overcome, Uno adds. “If manufacturers can develop a process that achieves high yields,” he says, “I am certain the whole display industry will shift to OLEDs.”

2. Absorption of UV-Vis Light

2.1. Type of electronic transition in aromatic molecules

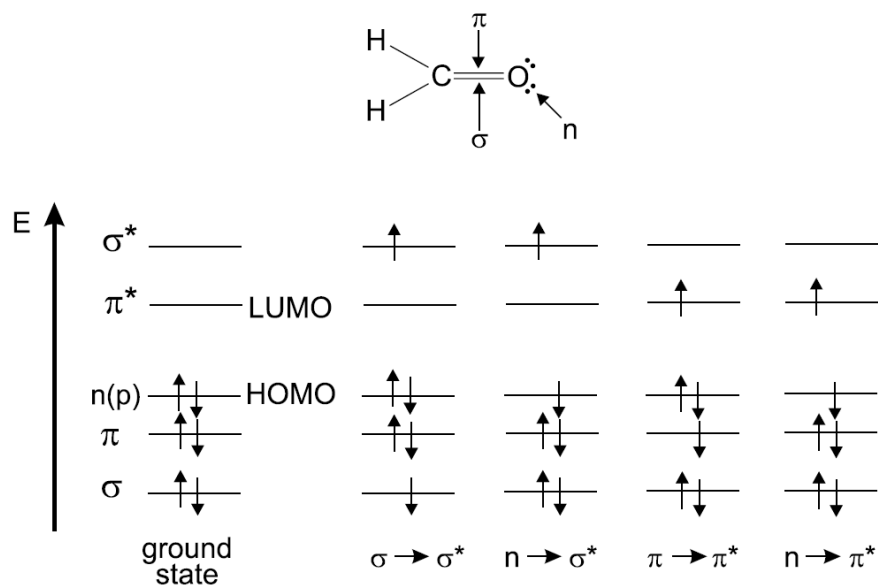


Figure 1.5. Example of Energy levels of molecular orbitals (HOMO: Highest Occupied Molecular Orbitals; LUMO: Lowest Unoccupied Molecular Orbitals) and possible electronic transitions. Copyright 2001, Wiley-VCH.²

Figure 1.5 exhibits energy levels of molecular orbitals. An electronic transition consists of the promotion of an electron from an orbital of a molecule in the ground state to an unoccupied orbital by absorption of a photon. This molecule is said to be in an excited state. A σ orbital can be formed either from two s atomic orbitals, or from one s and one p atomic orbital, or from two p atomic orbitals having a collinear axis of symmetry. The bond formed in this way is called a σ bond. A π

orbital is formed from two p atomic orbitals overlapping laterally. The resulting bond is called a π bond. Absorption of a photon of appropriate energy can promote one of the π electrons to an antibonding orbital denoted by π^* . The transition is then called π - π^* . A molecule may also possess non-bonding electrons located on heteroatoms such as oxygen or nitrogen. The corresponding molecular orbitals are called n orbitals. Promotion of a non-bonding electron to an antibonding orbital is possible and the associated transition is denoted by n- π^* . The energy of these electronic transitions is generally in the following order:

$$n-\pi^* < \pi-\pi^* < n-\sigma^* < \sigma-\pi^* < \sigma-\sigma^*$$

The n- π^* transition deserves further attention: upon excitation, an electron is removed from the oxygen atom and goes into the π^* orbital localized half on the carbon atom and half on the oxygen atom. The n- π^* excited state thus has a charge transfer character, as shown by an increase in the dipole moment of about 2D with respect to the ground state dipole moment of C=O (3D). In absorption and fluorescence spectroscopy, two important types of orbitals are considered: the Highest Occupied Molecular Orbitals (HOMO) and the Lowest Unoccupied Molecular Orbitals (LUMO). Both of these refer to the ground state of the molecule.

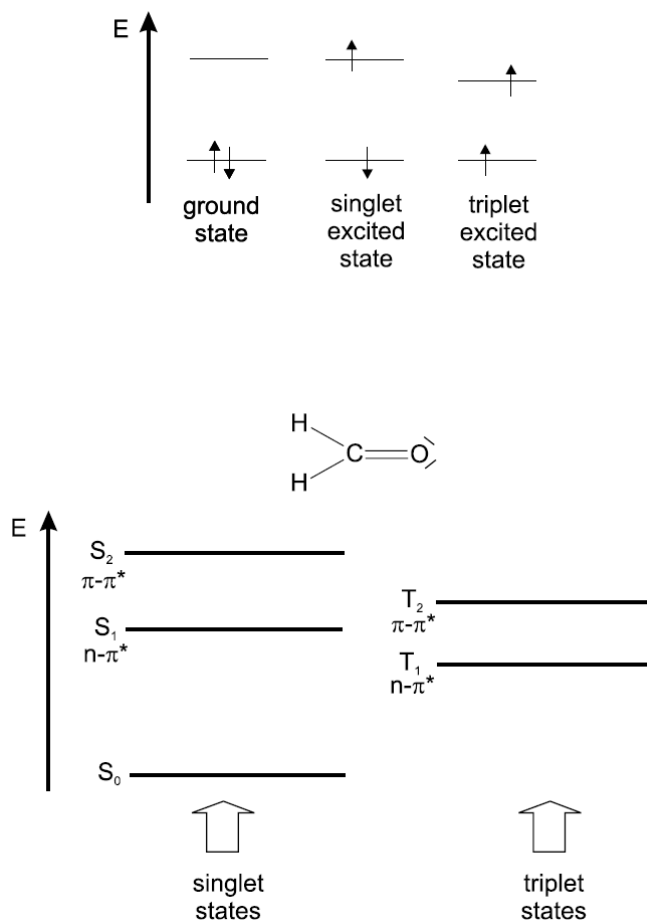


Figure 1.6. Distinction between singlet and triplet states, using formaldehyde as an example. Copyright 2001, Wiley-VCH.²

Figure 1.6 depicts the classification of excited states. When one of the two electrons of opposite spins (belonging to a molecular orbital of a molecule in the ground state) is promoted to a molecular orbital of higher energy, its spin is in principle unchanged so that the total spin quantum number ($S = \sum S_i$, with $S_i = +\frac{1}{2}$ or $-\frac{1}{2}$) remains equal to zero. Because the multiplicities of both the ground and

excited states ($M = 2S + 1$) is equal to 1, both are called *singlet state* (usually denoted S_0 for the ground state, and S_1 ; S_2 ; ...for the excited states). The corresponding transition is called a singlet-singlet transition. When a molecule in a singlet excited state may undergo conversion into a state where the promoted electron has changed its spin; because there are then two electrons with parallel spins, the total spin quantum number is 1 and the multiplicity is 3. Such a state is called a *triplet state* because it corresponds to three states of equal energy. According to Hund's Rule, the triplet state has a lower energy than that of the singlet state of the same configuration. However, in aromatic molecules, there is no overlap between the σ and π orbitals, the π electron system can be considered as independent of the σ bonds. It is worth remembering that the greater the extent of the π electron system, the lower the energy of the low-lying π - π^* transition, and consequently, the larger the wavelength of the corresponding absorption band.

Experimentally, the efficiency of light absorption at a wavelength λ by an absorbing medium is characterized by the *absorbance* $A(\lambda)$ or the *transmittance* $T(\lambda)$, defined as Beer-Lambert Law. (Equation 1.1)

$$A(\lambda) = \log \frac{I_{\lambda}^0}{I_{\lambda}} = -\log T(\lambda) = \varepsilon(\lambda)lc \text{ (Eq. 1.1)}$$

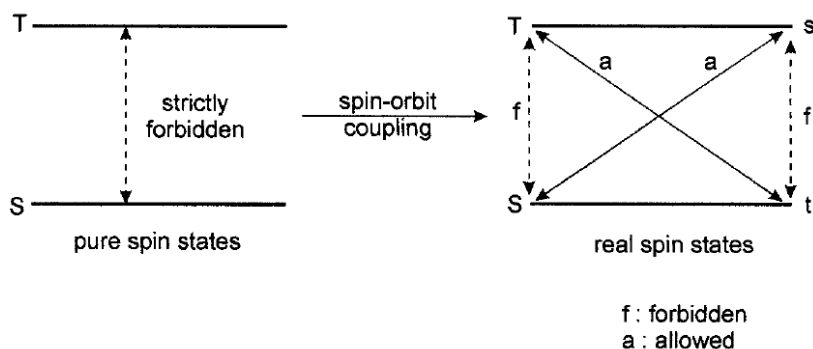
where I_{λ}^0 and I_{λ} are the light intensities of the beams entering and leaving the absorbing medium, respectively. And $\varepsilon(\lambda)$ is the *molar absorption coefficient* ($L \text{ mol}^{-1} \text{ cm}^{-1}$), c is the concentration (mol L^{-1}) of absorbing species and l is the absorption path length (cm). The molar absorption coefficient, $\varepsilon(\lambda)$, expresses the ability of a molecule to absorb light in a given solvent. In the classical theory, molecular absorption of light can be described by considering the molecule as an

oscillating dipole, which allows us to introduce a quantity called the *oscillator strength*, which is directly related to the integral of the absorption band as follows:

$$f = 2303 \frac{mc_0^2}{N_A \pi e^2 n} \int \varepsilon(\bar{\nu}) d\bar{\nu} = \frac{4.32 \times 10^{-9}}{n} \int \varepsilon(\bar{\nu}) d\bar{\nu} \text{ (Eq. 1.2)}$$

where m and e are the mass and the charge of an electron, respectively, c_0 is the speed of light, n is the index of refraction, and $\bar{\nu}$ is the wavenumber (cm^{-1}). f is a dimensionless quantity and values of f are normalized so that its maximum value is 1.

2.2. Selection rule



Scheme 1.1. Spin-orbit coupling. Copyright 2001, Wiley-VCH.²

Transitions between states of different multiplicities are forbidden, i.e. singlet–singlet and triplet–triplet transitions are allowed, but singlet–triplet and triplet–singlet transitions are forbidden. However, there is always a weak interaction between the wavefunctions of different multiplicities via spin–orbit coupling. As a result, a wavefunction for a singlet (or triplet) state always contains a small fraction

of a triplet (or singlet) wavefunction $\Psi = \alpha^1\Psi + \beta^3\Psi$; this leads to a small but non-negligible value of the intensity integral during a transition between a singlet state and a triplet state or vice versa (see Scheme 1.1). In spite of their very small molar absorption coefficients, such transitions can be effectively observed.

Intersystem crossing (ISC): Crossing from the first singlet excited state S_1 to the first triplet state T_1 is possible thanks to spin-orbit coupling. The efficiency of this coupling varies with the fourth power of the atomic number, which explains why ISC is favored by the presence of a heavy atom.

2.3. The Franck-Condon principle

According to the Born-Oppenheimer approximation, the motions of electrons are much more rapid than those of the nuclei (i.e. the molecular vibrations). Promotion of an electron to an antibonding molecular orbital upon excitation takes about 10^{-15} s, which is very quick compared to the characteristic time for molecular vibrations (10^{-10} ~ 10^{-12} s). This observation is the basis of the *Franck-Condon principle* (Figure 1.7): an electronic transition is most likely to occur without changes in the positions of the nuclei in the molecular entity and its environment. The width of a band in the absorption spectrum of a chromophore located in a particular microenvironment is a result of two effects: homogeneous and inhomogeneous broadening. Homogeneous broadening is due to the existence of a continuous set of vibrational sublevels in each electronic state. Inhomogeneous broadening results from the fluctuations of the structure of the solvation shell surrounding the chromophore.

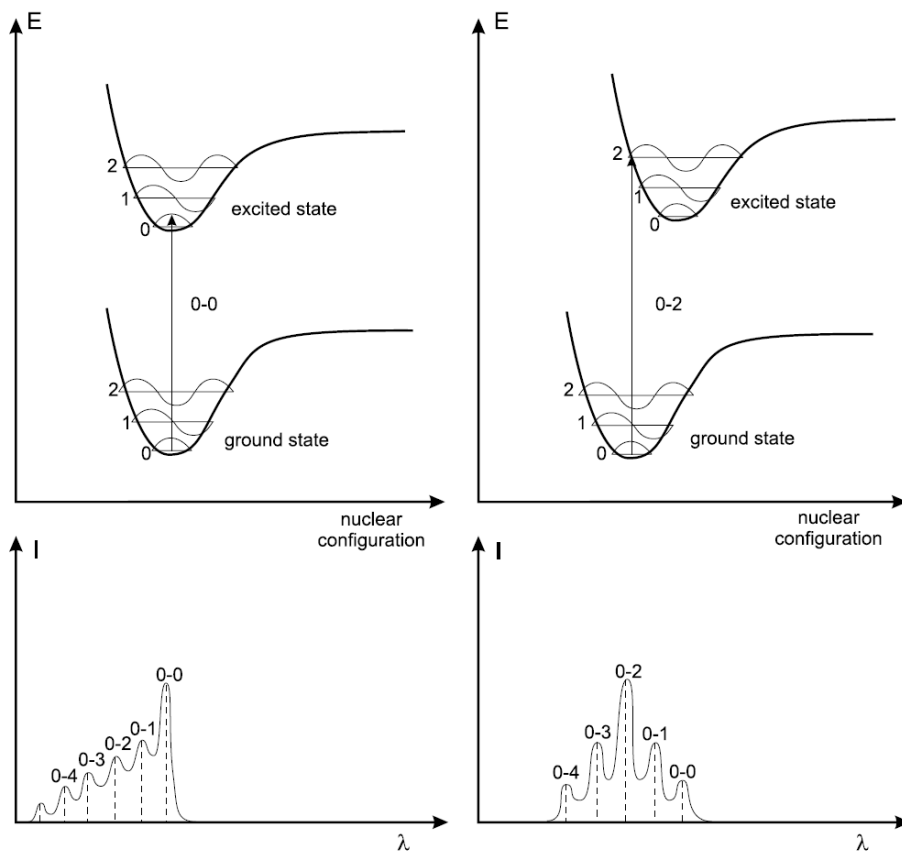


Figure 1.7. Top: Potential energy diagrams with vertical transitions (Franck-Condon principle). Bottom: shape of the absorption bands; the vertical broken lines represent the absorption lines that are observed for a vapor, whereas broadening of the spectra is expected in solution (solid line). Copyright 2001, Wiley-VCH.²

3. Characteristics of Fluorescent Emission

3.1. Radiative and non-radiative transitions between electronic states

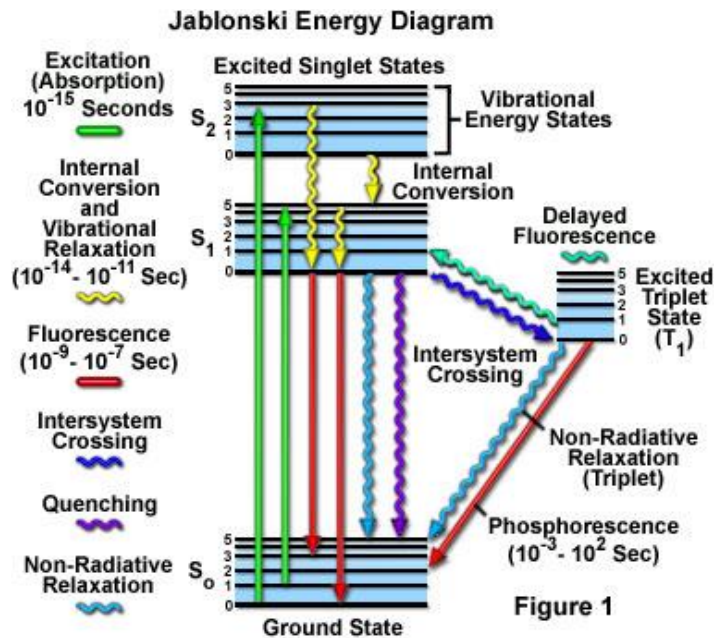


Figure 1.8. Perrin-Jablonski diagram and illustration of the relative position of absorption, fluorescence and phosphorescence spectra. Source: <https://micro.magnet.fsu.edu/optics/timeline/people/jablonski.html>

The singlet electronic states are denoted S_0 (fundamental electronic state), S_n and the triplet states, T_n . Vibrational levels are associated with each electronic state. It is noted that absorption is very fast ($\approx 10^{-15}$ s) with respect to all other processes because of there is no concomitant displacement of the nuclei according to the

Franck-Condon principle. Absorption of a photon can bring a molecule to one of the vibrational levels of from S_0 to above S_1 .

Internal conversion (IC) is a non-radiative transition between two electronic states of the same spin multiplicity. When a molecule is excited to an energy level higher than the lowest vibrational level of the first electronic state, vibrational relaxation (and IC if the singlet excited state is higher than S_1) leads the excited molecule towards the zero vibrational level of the S_1 singlet state with a time-scale of $10^{-13}\sim 10^{-11}$ s. From S_1 , IC to S_0 is possible but is less efficient than conversion from S_2 to S_1 , because of the much larger energy gap between S_1 and S_0 . Therefore, IC from S_1 to S_0 can compete with emission of photons (fluorescence) and ISC to the triplet state from which emission of photons (phosphorescence) can possibly be observed.

3.2. Fluorescence

Emission of photons accompanying the $S_1\rightarrow S_0$ relaxation is called fluorescence. The 0-0 transition is usually the same for absorption and fluorescence. However, the fluorescence spectrum is located at higher wavelengths (lower energy) than the absorption spectrum because of the energy loss in the excited state due to vibrational relaxation (Figure 1.8). In most cases, the absorption spectrum partly overlaps the fluorescence spectrum, i.e. a fraction of light is emitted at shorter wavelengths than the absorbed light. In general, the differences between the vibrational levels are similar in the ground and excited states, so that the fluorescence spectrum often resembles the first absorption band. The gap between the maximum of the first absorption band and the maximum of fluorescence is called the *Stokes*

shift (Figure 1.9). This important parameter can provide information on the excited states. For instance, when the dipole moment of a fluorescent molecule is higher in the excited state than in the ground state, the *Stokes shift* increases with solvent polarity. From a practical point of view, the detection of a fluorescent species is of course easier when the *Stokes shift* is larger.

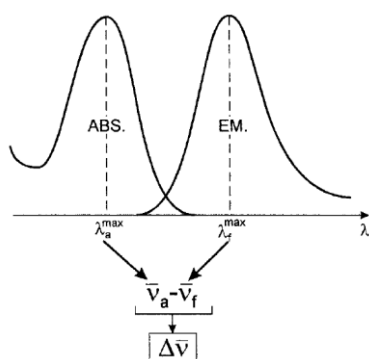


Figure 1.9. Definition of the Stokes shift. Copyright 2001, Wiley-VCH.²

It should be noted that emission of a photon is as fast as absorption of a photon. However, excited molecules stay in the S_1 state for a certain time before emitting a photon or undergoing other de-excitation processes (IC, ISC). Thus, after excitation of a population of molecules by a very short pulse of light, the fluorescence intensity decreases exponentially with a characteristic time, reflecting the average lifetime of the molecules in the S_1 excited state. The emission of fluorescence photons described is a spontaneous process.

3.3. Solvatochromic Shift

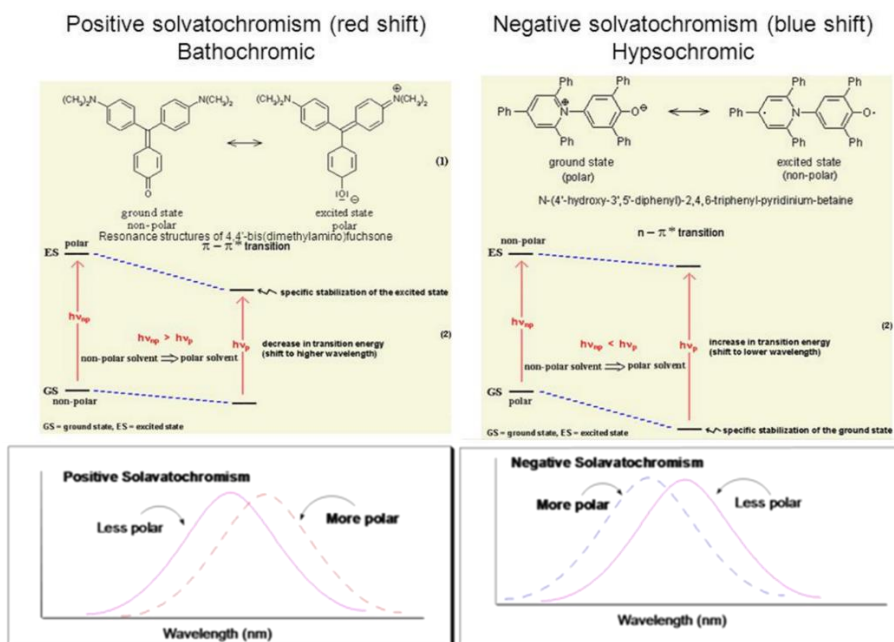


Figure 1.10. Examples of positive and negative solvatochromic shifts. Source: http://www.chemie.uni-regensburg.de/Organische_Chemie/diaktik/Keusch/D-pos_sol-e.htm.

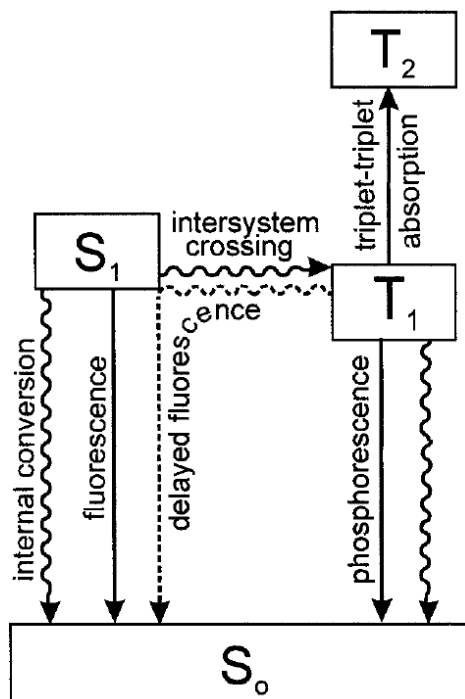
Broadening of the absorption and fluorescence bands results from fluctuations in the structure of the solvation shell around a solute. Moreover, shifts in absorption and emission bands can be induced by a change in solvent nature or composition. This phenomenon is called *solvatochromic shifts*, which is experimental evidence of changes in solvation energy (Figure 1.10). In other words, when a solute is surrounded by solvent molecules, its ground state and its excited state are more or less stabilized by solute-solvent interactions, depending on the chemical nature of both solute and solvent molecules. Solute-solvent interactions are commonly described in terms of Van der Waals interactions and possible specific interactions

like hydrogen bonding. In solution, the solute-solvent interactions result not only from the permanent dipole moments of solute or solvent molecules, but also from their polarizabilities.

To describe solvatochromic shifts, an additional energy term relative to the solute should be considered. This term is related to the transition dipole moment that results from the migration of electric charges during an electronic transition.

The term 'polarity' is used to express the complex interplay of all types of solute-solvent interactions, i.e. nonspecific dielectric solute-solvent interactions and possible specific interactions such as hydrogen bonding. Therefore, polarity cannot be characterized by a single parameter, although the 'polarity' of a solvent (or a microenvironment) is often associated with the static dielectric constant ϵ (macroscopic quantity) or the dipole moment μ of the solvent molecules (microscopic quantity).

3.4. Intersystem crossing and subsequent processes



Scheme 1.2. De-excitation process from S_1 . (Fluorescence, phosphorescence, delayed fluorescence). Copyright 2001, Wiley-VCH.²

A third possible de-excitation process from S_1 is ISC toward the T_1 triplet state followed by other processes, according to Scheme 1.2. ISC is a non-radiative transition between two isoenergetic vibrational levels belonging to electronic states of different multiplicities. An excited molecule in the 0 vibrational level of the S_1 state can move to the isoenergetic vibrational level of the T_n triplet state; then vibrational relaxation brings it into the lowest vibrational level of T_1 . ISC may be fast enough (10^{-7} – 10^{-9} s) to compete with other pathways of de-excitation from S_1 (fluorescence and IC $S_1 \rightarrow S_0$). Crossing between states of different multiplicity is in principle forbidden, but spin-orbit coupling (i.e. coupling between the orbital

magnetic moment and the spin magnetic moment) can be large enough to make it possible. The probability of ISC depends on the singlet and triplet states involved. Because of the presence of heavy atoms increases spin-orbit coupling, favors efficient ISC.

3.5. Phosphorescence versus non-radiative de-excitation

In solution at room temperature, non-radiative de-excitation from the triplet state T_1 , is predominant over radiative de-excitation called phosphorescence. The transition $T_1 \rightarrow S_0$ is forbidden (but it can be observed because of spin-orbit coupling), and the radiative rate constant is thus very low. During such a slow process, the numerous collisions with solvent molecules favor ISC and vibrational relaxation in S_0 . On the contrary, at low temperatures and/or in a rigid medium, phosphorescence can be observed. The lifetime of the triplet state may, under these conditions, be long enough to observe phosphorescence on a time-scale up to seconds, even minutes or more. The phosphorescence spectrum is located at wavelengths higher than the fluorescence spectrum (Figure 1.8) because the energy of the lowest vibrational level of the triplet state T_1 is lower than that of the singlet state S_1 .

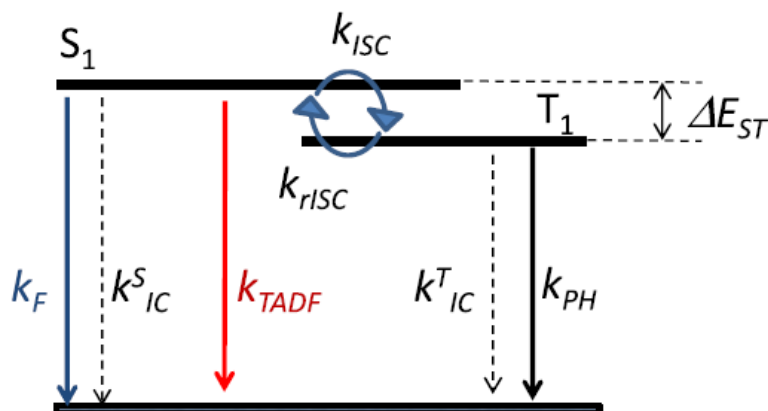
3.6. Delayed fluorescence

Thermally activated delayed fluorescence (TADF) Reverse intersystem crossing $T_1 \rightarrow S_1$ can occur when the energy difference between S_1 and T_1 is small and when the lifetime of T_1 is long enough. This results in emission with the same spectral distribution as normal fluorescence but with a much longer decay time constant because the molecules stay in the triplet state before emitting from S_1 . This

fluorescence emission is thermally activated, consequently, its efficiency increases with increasing temperature. It is also called delayed fluorescence of E-type because it was observed for the first time with eosin. It hardly occur in aromatic hydrocarbons because of the relatively large difference in energy between S_1 and T_1 .

Triplet–triplet annihilation In concentrated solutions, a collision between two molecules in the T_1 state can provide enough energy to allow one of them to return to the S_1 state. Such a triplet–triplet annihilation thus leads to a delayed fluorescence emission (also called delayed fluorescence of P-type because it was observed for the first time with pyrene). The decay time constant of the delayed fluorescence process is half the lifetime of the triplet state in dilute solution, and the intensity has a characteristic quadratic dependence with excitation light intensity.

3.7. Lifetimes



Scheme 1.3. The rate constants for the various at excited state. Reproduced with permission. Copyright 2017, IOP publishing group.³

The rate constants for the various processes will be denoted as follows at scheme 1.3. Where k_F is the rate constant for radiative deactivation $S_1 \rightarrow S_0$ with emission of fluorescence, k_{IC}^S is the rate constant for IC $S_1 \rightarrow S_0$, and k_{isc} is the rate constant for ISC. Regarding the two latter non-radiative pathways of de-excitation from S_1 , it is convenient to introduce the overall non-radiative rate constant k_{nr}^S such that $k_{nr}^S = k_{IC}^S + k_{isc}$. For deactivation from T_1 , k_{PH} is rate constant for radiative deactivation $T_1 \rightarrow S_0$ with emission of phosphorescence and k_{IC}^T : rate constant for non-radiative deactivation (reverse intersystem crossing) $T_1 \rightarrow S_0$.

TADF relies on a small singlet–triplet energy gap (ΔE_{ST}) defined as the gap between the T_1 and S_1 . When ΔE_{ST} is sufficiently small taken usually as <0.1 eV, thermal upconversion from the T_1 to the S_1 by reverse intersystem-crossing (RISC) becomes possible.⁴ For the TADF, k_{RISC} is the rate constant of RISC and the k_{TADF} is the rate constant of the delayed fluorescence for additional singlet exciton after RISC process.

where τ_S and τ_T lifetime of excited state S_1 and T_1 , are given by

$$\tau_S = \frac{1}{k_F + k_{nr}^S} \text{ (Eq. 1.3)}$$

$$\tau_T = \frac{1}{k_{PH} + k_{nr}^T} \text{ (Eq. 1.4)}$$

delayed fluorescence lifetime, τ_d has been found to decrease with either an increasing of k_{ISC} or of k_{RISC} . In particular τ_d can be expressed mathematically as

$$\frac{1}{\tau_d} = k_{nr}^T + \left(1 - \frac{k_{ISC}}{k_F + k_{nr}^S + k_{ISC}}\right) k_{RISC} \text{ (Eq. 1.5)}$$

For organic molecules, the lifetime of the singlet state ranges from tens of picoseconds to hundreds of nanoseconds, whereas the triplet lifetime is much longer (microseconds to seconds). However, such a difference cannot be used to make a

distinction between fluorescence and phosphorescence because some inorganic compounds (for instance, uranyl ion) or organometallic compounds may have a long lifetime. Monitoring of phosphorescence or delayed fluorescence enables us to study much slower phenomena.

3.8. Quantum Yields

The fluorescence quantum yield Φ_F is the fraction of excited molecules that return to the ground state S_0 with emission of fluorescence photons. In other words, the fluorescence quantum yield is the ratio of the number of emitted photons to the number of absorbed photons. Φ_F can be expressed mathematically as

$$\Phi_F = \frac{k_F}{k_F + k_{nr}^S + k_{ISC}} = k_F \tau_S \quad (\text{Eq. 1.6})$$

The quantum yields of intersystem crossing (Φ_{ISC}) and phosphorescence (Φ_{PH}) are given by

$$\Phi_{ISC} = \frac{k_{ISC}}{k_F + k_{nr}^S + k_{ISC}} = k_{ISC} \tau_S \quad (\text{Eq. 1.7})$$

$$\Phi_{PH} = \frac{k_{PH}}{k_{PH} + k_{nr}^T} \Phi_{ISC} \quad (\text{Eq. 1.8})$$

Using the radiative lifetime, as previously defined, the fluorescence and delayed fluorescence quantum yield can also be written as

$$\Phi_F = \frac{\tau_S}{\tau_r} \quad (\text{Eq. 1.9})$$

τ_r is radiative lifetime from S_1 to S_0 .

For TADF materials, quantum efficiency of prompt (Φ_{PF}) and delayed fluorescent component (Φ_{DF}) via RISC process should be considered separately.

$$\Phi_{PF} = \Phi_F = \frac{k_F}{k_F + k_{nr}^S + k_{ISC}} = k_F \tau_S \quad (\text{Eq. 1.10})$$

$$\Phi_{DF} = \sum_{k=1}^{\infty} (\Phi_{ISC} \Phi_{RISC})^k \Phi_{PF} = \frac{\Phi_{ISC} \Phi_{RISC}}{1 - \Phi_{ISC} \Phi_{RISC}} \Phi_{PF} \quad (\text{Eq. 1.11})$$

where Φ_{ISC} and Φ_{RISC} are the intersystem crossing efficiency and reverse intersystem crossing efficiency, respectively, which can be expressed by the follow equations

$$\Phi_{ISC} = \frac{k_{ISC}}{k_F + k_{nr}^S + k_{ISC}} = \frac{k_{ISC}}{k_{PF}} \quad (\text{Eq. 1.12})$$

$$\Phi_{RISC} = \frac{k_{RISC}}{k_{RISC} + k_{nr}^T} \quad (\text{Eq. 1.13})$$

Experimentally, the fluorescence efficiency of PF (Φ_{PF}) and DF (Φ_{DF}) are distinguished from the total photoluminescence quantum yields (PLQY) by comparing the integrated intensity of their components in the transient photoluminescence spectra, according to their different luminescent lifetime.⁵

3.9. Calculation of measured lifetime

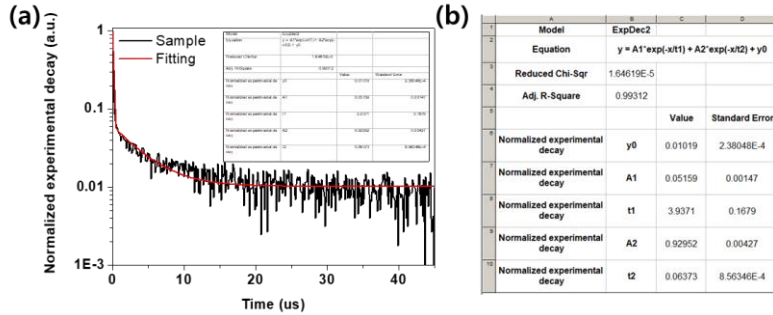


Figure 1.11. (a) Radiative decay lifetime graph based on experimental results and (b) calculated lifetimes and their ratios (t_n : lifetime, A_n : Amplitude).

Determination of the lifetimes requires the fitting of a multi-exponential decay expression to each experimental curve. Some fitting parameters are shared among these curves, so a global fitting routine is required. “Origin” program is used for its advanced non-linear fitting capabilities (Figure 1.11).

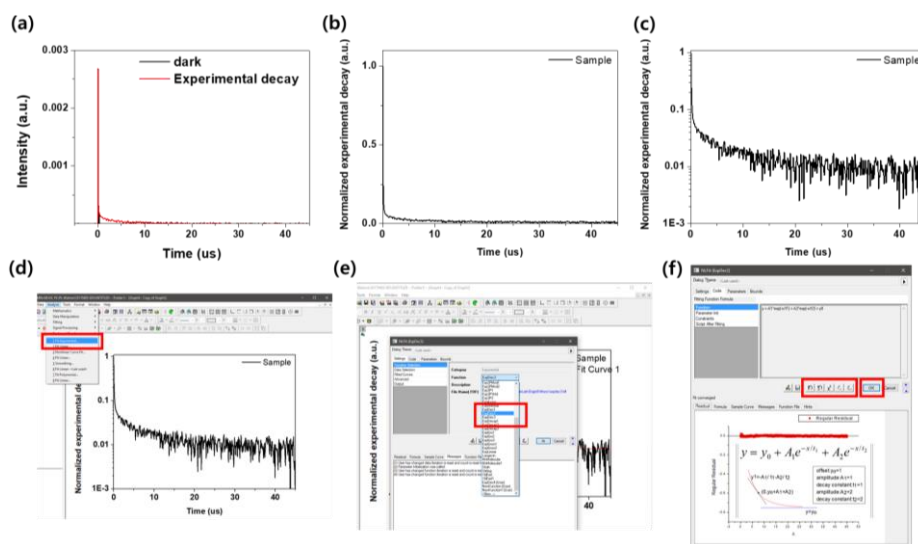


Figure 1.12. Process of luminescence lifetime measurement by fitting through experimental results. (a) transform from experimental results to the graph (dark data correction), (b) normalization of obtained graph, (c) convert from the normalized graph to log style, (d) non-linear fit or fit exponential of at the analysis term, (e) select single, double or triple exponential and (f) fitting.

When luminescence shows two or more lifetimes, their respective lifetimes and portions calculate as follows (Figure 1.12),

first, click on the data file from the experiment, open it in the **Origin** program, fit the dark state and get a normalized graph. In the Project Explorer window, select the Built-In Function folder. Next, with graph active, go to the **Analysis** → **Fitting** → **Nonlinear Curve Fit** menu item and select the **fit exponential** or **NLFit** dialog box and select single, double or triple exponential decay. Lastly, fit the **residual parameter** close to zero. The summary of the calculated fit curve is automatically converted to a new table file (Figure 1.11(b)).

4. Intra- and Intermolecular Photophysical process

4.1. Intramolecular Charge Transfer

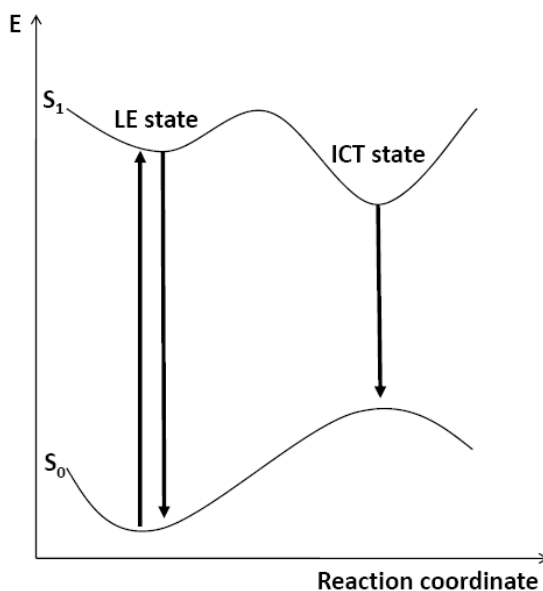


Figure 1.13. The ground and excited state potential energy surface for the D-A molecular system which is showing red-shifted emission from the intramolecular charge transfer (ICT) state with a small barrier (ΔE) between LE and ICT state. The environmental effect of solvent polarity stabilized the ICT state. Copyright 2001, Wiley-VCH.²

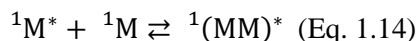
Molecules that exhibit intramolecular electron transfer are large conjugate organic π -systems with acceptor (A) and donor (D) subunits linked by a formally single bond. The photoexcitation of D-A molecules is followed by an electron transfer from D to A. Much experimental evidence has been accumulated in favor of photoinduced electron transfer as a key process in the photophysics of a large number

and variety of DA compounds. These molecules can be classified into different families with respect to the angular orientation of the D and A moieties. Intrinsic factors, controlling the electron transfer in excited states, seem to be determined by the reaction medium. The most important issues related to the photophysics of such compounds are the electronic structure and the conformation of excited charge transfer states. Information on their photophysical properties can be obtained from the analysis of the charge transfer absorption and emission phenomena.

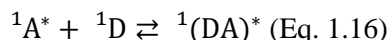
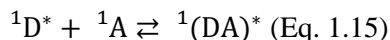
Excitation of a D-A system induces the motion of an electron from one orbital to another. If the initial and final orbital is separated in space, the electronic transition is accompanied by an almost instantaneous change in the dipole moment of the D-A system in the same molecule. When an electron-donating group (e.g. $-\text{NH}_2$, $-\text{N}(\text{CH}_3)_2$, $-\text{CH}_3\text{O}$) is conjugated to an electron-withdrawing group (e.g. $>\text{C}=\text{O}$, $-\text{C}\equiv\text{N}$), the dipole moment can be increased substantially. Consequently, the Franck-Condon (FC) state ($\pi\pi^*$) reached by electronic excitation is not in equilibrium with the surrounding solvent molecules. Solvent molecules rotate during the lifetime of the excited state until the solvation shell is in thermodynamic equilibrium with the molecule. A relaxed *intramolecular charge transfer* state is then reached (Figure 1.13). Such a solvent relaxation explains the increase in the red-shift of the fluorescence spectrum as the polarity of the solvent increases. The system which shows two fluorescence bands in solutions is a very good model for study of experimental and theoretical calculations to understand structures and reactivities of the electronically excited molecules.

4.2. Formation of Excimers and Exciplexes

Excimers are dimers in the excited state (the term excimer results from the contraction of ‘**excited dimer**’). They are formed by collision between an excited molecule and an identical unexcited molecule



The symbolic representation (MM)* shows that the excitation energy is delocalized over the two moieties. *Exciplexes* are excited-state complexes (the term exciplex comes from ‘**excited complex**’). They are formed by collision of an excited molecule (electron donor or acceptor) with an unlike unexcited molecule.



The formation of excimers and exciplexes are diffusion-controlled processes. The photophysical effects are thus detected at relatively high concentrations of the species so that a sufficient number of collisions can occur during the excited-state lifetime. Temperature and viscosity are of course important parameters.

[Excimer]

Many aromatic hydrocarbons such as naphthalene or pyrene can form excimers. The fluorescence band corresponding to an excimer is located at wavelengths higher than that of the monomer and does not show vibronic bands (Figure 1.14).

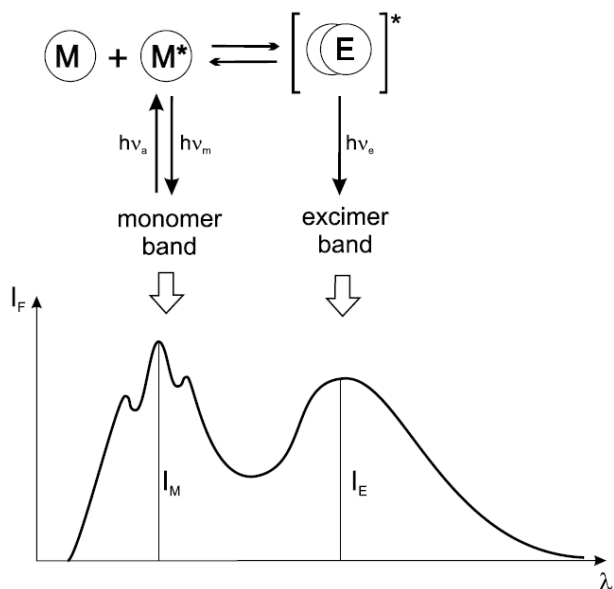
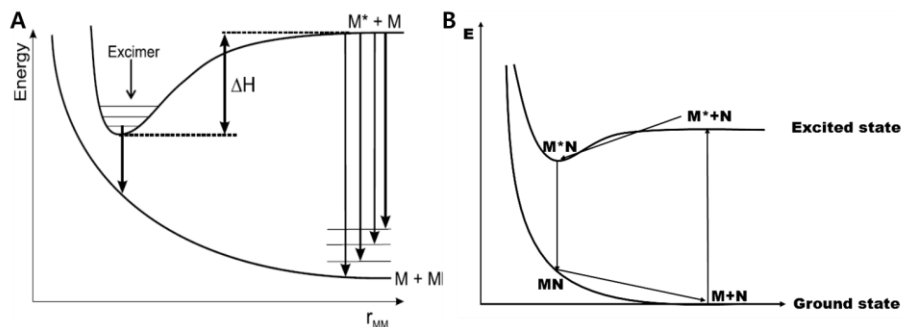


Figure 1.14. Excimer formation, with the corresponding monomer and excimer bands. Copyright 2001, Wiley-VCH.²

These features can be explained on the basis of energy surfaces as shown in Scheme 1.4a. The lower monotonous curve represents the repulsive energy between the two molecules in the ground state. The upper curve, which is relative to two molecules (one of them being in the ground state), exhibits a minimum corresponding to the formation of an excimer in which the two aromatic rings are facing at a distance of about 3~4 Å. In contrast to the monomer band, the excimer band is structureless because the lowest state is dissociative and can thus be considered as a continuum.



Scheme 1.4. Energy level diagram of a) excimer and b) exciplex formation.
 Copyright 2001, Wiley-VCH.²

[Exciplex]

Interactions between electronically excited species M^* and ground-state molecules N lead to charge transfer interactions and excitation exchange interactions, and hence to the formation of stabilized complexes M^*N . Exciplexes have a large binding energy between molecules ($5\sim 20 \text{ kcal mol}^{-1}$), and exhibit partial charge character on each molecule.

Scheme 1.4b shows a potential energy diagram of exciplex formation and emission. Here, monomer M^* is located far from monomer N , and the transition energy is the same as for monomer M^* . Monomer M^* is then located close to monomer N , and the binding energy between M^* and N increases due to charge transfer interactions, resulting in a U-shaped potential (upper surface). The ground state energy increases as the distance between the molecules decreases due to the lack of substantial attractions between M and N (lower surface). Thus, there are a few MN ground state complexes and no associated optical absorption due to instabilities of the ground state complexes. Exciplex emission occurs vertically,

according to the Franck–Condon principle, from the excited state minimum to the repulsive ground state. Thus, ground state MN complexes dissociate rapidly following emission, resulting in a short lifetime. For this reason, exciplex emission is red-shifted with a long decay lifetime, and is featureless because of the short lifetime and indefinite vibrational character of the ground state.

4.3. Energy transfer

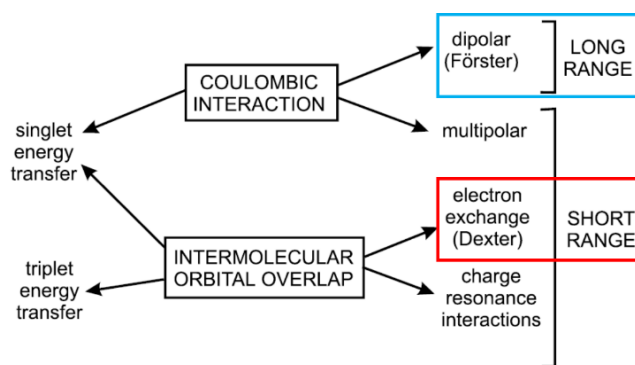


Figure 1.15. Types of interactions involved in non-radiative transfer mechanisms.

The interactions due to intermolecular orbital overlap, which include electron exchange and charge resonance interactions, are of course only short range (Figure 1.15). Non-radiative transfer of excitation energy requires some interaction between a donor molecule and an acceptor molecule, and it can occur if the emission spectrum of the donor overlaps the absorption spectrum of the acceptor, so that several vibronic transitions in the donor have practically the same energy as the corresponding transitions in the acceptor. Such transitions are coupled are resonance

(Figure 1.16). It is classified that either excitation energy transfer or electronic energy transfer (EET) or resonance energy transfer (RET).

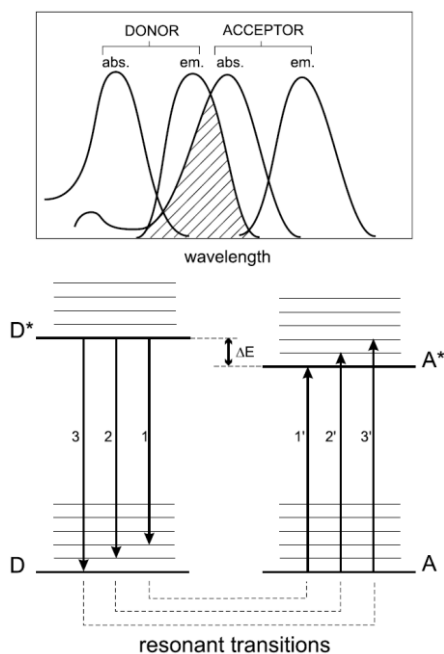


Figure 1.16. Energy level scheme of donor and acceptor molecules showing the coupled transitions in the case where vibrational relaxation is faster than energy transfer (very weak coupling) and illustration of the integral overlap between the emission spectrum of the donor and the absorption of the acceptor. Copyright 2001, Wiley-VCH.²

Energy transfer can result from different interaction mechanisms. The interactions may be Coulombic and/or due to intermolecular orbital overlap. The Coulombic interactions consist of long-range dipole-dipole interactions (Förster's

mechanism) and short-range multi-polar interactions. The interactions due to intermolecular orbital overlap, which include electron exchange (Dexter's mechanism) and charge resonance interactions, are of course only short range (Figure 1.15). It should be noted that for singlet-singlet energy transfer (${}^1D^* + {}^1A \rightarrow {}^1D + {}^1A^*$), all types of interactions are involved, whereas triplet-triplet energy transfer (${}^3D^* + {}^1A \rightarrow {}^1D + {}^3A^*$) is due only to orbital overlap.

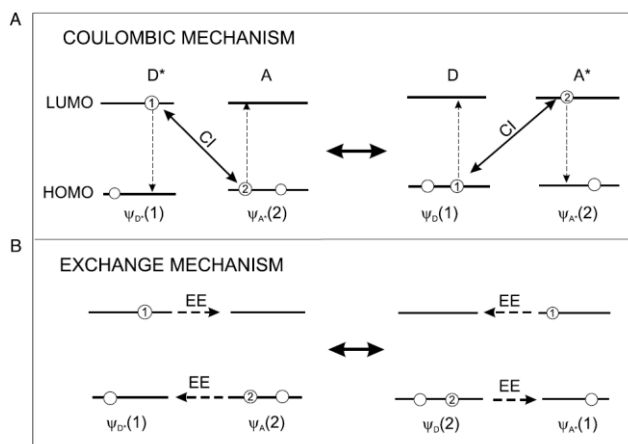


Figure 1.17. Schematic representation of the (A) Coulombic and (B) exchange mechanisms of excitation energy transfer (CI: Coulombic interaction, EE: electron exchange). Copyright 2001, Wiley-VCH.²

The Coulombic term corresponds to the energy transfer process in which the initially excited electron on the donor D returns to the ground state orbital on D, while simultaneously an electron on the acceptor A is promoted to the excited state (Figure 1.17A). The exchange term (which has a quantum-mechanical origin)

corresponds to an energy transfer process associated with an exchange of two electrons between D and A (Figure 1.17B).

For allowed transitions on D and A the Coulombic interaction is predominant, even at short distances. For forbidden transitions on D and A (e.g. in the case of transfer between triplet states $^3D^* + ^1A \rightarrow ^1D + ^3A^*$, in which the transitions $T_1 \rightarrow S_0$ in D^* and $S_0 \rightarrow T_1$ in A are forbidden), the Coulombic interaction is negligible and the exchange mechanism is found, but is operative only at short distances ($< 10 \text{ \AA}$) because it requires overlap of the molecular orbitals. In contrast, the Coulombic mechanism can still be effective at large distances (up to $80\sim 100 \text{ \AA}$).

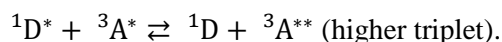
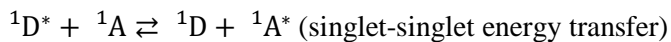
4.4. Dipole-dipole mechanism (Förster resonance energy transfer)

Förster derived the following expression for the transfer rate constant from classical considerations as well as on quantum-mechanical grounds,

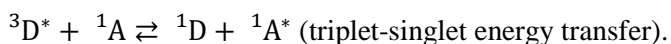
$$R_0^6 = \frac{9000(\ln 10)\kappa^2\phi_D^0}{128\pi^5N_A n^4} \int_0^\infty I_D(\lambda) \varepsilon_A(\lambda)\lambda^4 d\lambda \quad (\text{Eq. 1.17})$$

where κ^2 is the orientational factor, ϕ_D^0 is the fluorescence quantum yield of the donor in the absence of transfer, n is the average refractive index of the medium in the wavelength range where spectral overlap is significant, $I_D(\lambda)$ is the fluorescence spectrum of the donor normalized so that $\int_0^\infty I_D(\lambda) d\lambda = 1$, and $\varepsilon_A(\lambda)$ is the molar absorption coefficient of the acceptor. Equation 1.17 shows that R_0 , and consequently the transfer rate, is independent of the donor oscillator strength but depends on the acceptor oscillator strength and on the spectral overlap. Therefore, provided that the acceptor transition is allowed (spin conservation) and its absorption

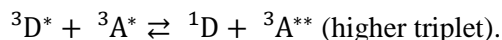
spectrum overlaps the donor fluorescence spectrum, the following types of energy transfer are possible:



This type of transfer requires overlap of the fluorescence spectrum of D and the T-T absorption spectrum of A



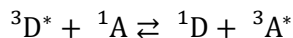
This type of transfer leads to phosphorescence quenching of the donor.



This type of transfer requires overlap of the phosphorescence spectrum of D* and the T-T absorption spectrum of A.

4.5. Exchange mechanism (Dexter energy transfer)

Because the energy rate does not imply the transition moments in the exchange mechanism, triplet-triplet energy transfer is possible:



It is worth mentioning that triplet-triplet energy transfer can be used to populate the triplet state of molecules in which ISC is unlikely. When D and A are identical ${}^3D^* + {}^1D \rightleftharpoons {}^1D + {}^3D^*$, triplet-triplet annihilation (TTA) leads to a delayed fluorescence, called P-type delayed fluorescence because it was first observed with pyrene. Part of the energy resulting from annihilation allows one of the two partners to return to the singlet state from which fluorescence is emitted, but with a delay

after staying in the triplet state. In crystals or polymers, the annihilation process often takes place in the vicinity of defects or impurities that act as energy traps.

4.6. Aggregation induced emission (AIE)

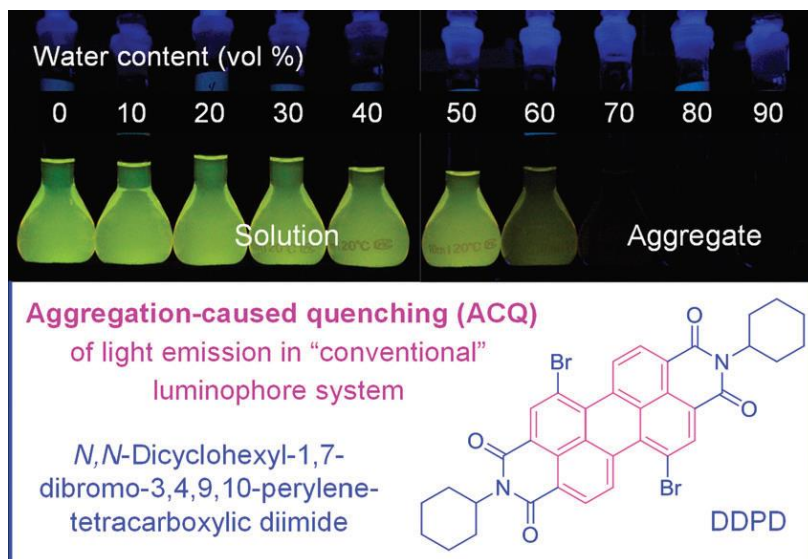
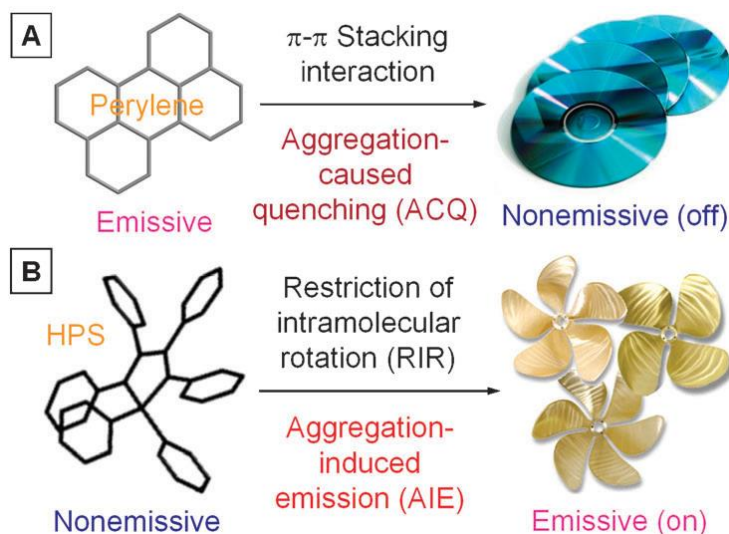


Figure 1.18. Fluorescence photographs of solutions/suspensions of DDPD (10 mM) in THF/water mixtures with different water contents.

Luminescence is often weakened or quenched at high concentrations, a phenomenon widely known as “concentration quenching”. A main cause for the quenching process is mechanistically associated with the “formation of aggregates”,⁶ which is probably why the concentration quenching effect has frequently been referred to as “aggregation-caused quenching” (ACQ).



Scheme 1.5. (a) Planar luminophoric molecules such as perylene tend to aggregate as discs pile up, due to the strong π - π stacking interactions between the aromatic rings, which commonly turns “off” light emission. (b) Non-planar luminogenic molecules such as hexaphenylsilole (HPS) behave oppositely, with their light emissions turned “on” by aggregate formation, due to the restriction of the intramolecular rotation (RIR) of the multiple phenyl rotors against the silole stator in the aggregate state.

An example of the ACQ effect is shown in Figure 1.18. The dilute solution (10 mM) of N,N-dicyclohexyl-1,7-dibromo-3,4,9,10-perylenetetra-carboxylic diimide (DDPD) in THF is highly luminescent. Its emission is weakened when water is added into THF, because the immiscibility of DDPD with water increases the local luminophore concentration and causes DDPD molecules to aggregate. When the water content is increased to > 60 vol%, the solvating power of the THF/water mixture becomes so poor that most of the DDPD molecules become aggregated. As

a result of the aggregate formation, the light emission of DDPD is completely quenched. The DDPD molecule contains a disc-like perylene core. In the DDPD aggregates, the perylene rings may experience strong π - π stacking interactions. This prompts the formation of such detrimental species as excimers, thus leading to the observed ACQ effect (Scheme 1.5).

The ACQ effect is “common to most aromatic hydrocarbons and their derivatives”.⁶ A structural reason for the ubiquity of the ACQ effect is because conventional luminophores are typically comprised of planar aromatic rings (e.g., perylene). Since organic luminescence is mainly dictated by electronic conjugation, a popular structural design strategy has been to increase the extent of π -conjugation by melding more aromatic rings together. The resulting bigger plates can indeed luminesce more efficiently in the solutions but concurrently their ACQ effects become severer because the chances for such large luminophores to form excimers or exciplexes are also increased.

In 2001, Tang et al. discovered an uncommon luminogen system, in which aggregation worked constructively, rather than destructively as in the conventional systems.⁷⁻⁸ They found that a series of silole derivatives were non-emissive in dilute solutions but became highly luminescent when their molecules were aggregated in concentrated solutions or cast into solid films. Since the light emission was induced by aggregate formation, the process is called "aggregation-induced emission" (AIE).⁷

Hexaphenylsilole (HPS) is among the first silole derivatives, from which the AIE phenomenon was unearthed. Structural scrutinization reveals that unlike conventional luminophores such as the disc-like planar perylene, HPS is a propellershaped non-planar molecule (Scheme 1.5). In a dilute solution, six phenyl rotors in an HPS molecule undergo dynamic intramolecular rotations against its

silacyclopentadiene or silole stator, which non-radiatively annihilates its excited state and renders its molecule non-luminescent. In the aggregate states, the HPS molecules cannot pack through a π - π stacking process due to its propeller shape, while the intramolecular rotations of its aryl rotors are greatly restricted owing to the physical constraint. This restriction of intramolecular rotations (RIR) blocks the non-radiative pathway and opens up the radiative channel. As a result, the HPS molecules become emissive in the aggregate state.⁹

According to proposed mechanism, the RIR process is responsible for the AIE effect. At the molecular level, Covalent bonds used to internally set off the RIR process for fasten the aryl rotors. In response to both the external and internal controls, the luminogens become emissive, thus offering experimental evidence to support AIE's mechanistic hypothesis.⁹ Guided by the mechanistic understanding, Tang group has synthesized different kinds of luminogenic molecules with a structural feature of one conjugated stator carrying multiple aromatic peripheral rotors, such as polyarylated ethenes, butadienes, pyrans, fulvenes and arylenes.¹⁰⁻¹⁴ All the luminogens show AIE activity, with emission colour covering the entire visible region and luminescence efficiency reaching unity.

Part II. Development of Non-doped Blue Fluorescent Materials for OLEDs

Background

1. Blue fluorescent materials

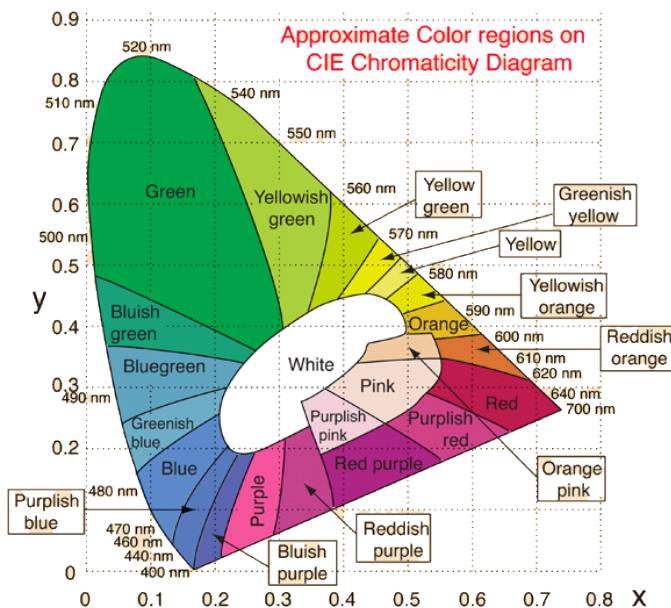


Figure 2.1 CIE 1976 chromaticity diagram. Source: <http://hyperphysics.phy-astr.gsu.edu/hbase/vision/die.html>.

Extensive research has been carried out to promote OLEDs into commercial applications as flat-panel displays and solid-state lighting resources.¹⁵⁻¹⁶ A full-color display requires red, green, and blue emission of relatively equal stability, efficiency, and color purity. In full-color OLEDs, the blue emitter can not only effectively reduce power consumption of the devices but also be utilized to generate light of other colors by energy cascade to lower energy fluorescent or phosphorescent dopants. However, the performance of a blue emitting device is often inferior to that of green and red devices for the intrinsic wide band gap of the blue emitting material.

The development of high efficiency blue OLEDs, in particular deep-blue OLEDs, is a pressing concern to realize commercial applications in display and solid-state lighting.

Given that electro-phosphorescence based on phosphors approaches a 100% internal quantum efficiency in theory by harvesting both singlet and triplet excitons, a great deal of effort has been devoted to develop efficient phosphors that can emit colors covering the whole visible region. Green, yellow and red phosphorescent OLEDs (PhOLEDs) have achieved at very high efficiency with admirable device lifetime during the past decades; however, the design of efficient blue phosphors still remains a formidable challenge as discussed in recent review.¹⁷ On the one hand, it is very difficult to realize efficient deep blue phosphorescent emission, which is defined as having a Commission Internationale de L'Eclairage (CIE) y coordinate value < 0.15 along with an $(x + y)$ value < 0.30 (Figure 2.1), due to the net result of an increasing energy gap and a reduction in the corresponding emission quantum yield. On the other hand, stability and longevity of the blue phosphorescent devices to date falls short of the requirement for applications.

Recently, a new concept to fabricate white OLEDs by combining blue fluorescent emitters with green, red and/or orange phosphorescent emitters has been promoted by Leo et al.¹⁸ This approach allows the harvesting of both the fluorescence from the host of blue emitters and the complementary phosphorescence from the triplet dopants simultaneously to generate white emission. In this context, highly efficient blue fluorescent materials have been considered as a promising alternative to promote the commercialization of OLEDs. But the performance of blue emitting devices is often retarded by the intrinsic wide band gap of blue emitting materials, which makes it hard to inject charges into emitters. Solving this problem is a

materials related issue. Significant efforts have been made to design versatile blue fluorescent materials aiming at further improving device efficiency, chromaticity and lifetime. The output is very prosperous.

To obtain high efficiency, electroluminescent devices normally require sophisticated configurations with several functional organic layers sandwiched between the anode and cathode to facilitate charge injection and transportation as well as effective exciton confinement. In this regard, tedious and complicated device fabrication processes are far too cost-effective to compete with other contemporary flat-display technologies. In order to simplify the device structure, many multifunctional materials possessing luminescent and charge injection/transporting characteristics have been developed. The utilization of simple devices with high efficiency can help reduce the overall cost.

There are two kinds of blue fluorescent OLEDs: (i) one is fabricated by doping blue fluorescent dyes in host matrix to suppress the fluorescence quenching. This doping system may intrinsically suffer from the limitation of efficiency and stability, aggregation of dopants and potential phase separation; (ii) the other is achieved by using non-doped blue fluorescent emitters, which has been demonstrated to be an efficient strategy to get rid of phase separation and concentration quenching; but, there is still the problem of charge injection and transportation arising from the intrinsic wide band gap of blue emitting materials. This chapter will firstly introduce some typical blue fluorescent dopants in brief. Then, some non-doped blue fluorescent emitters are discussed, which are mainly pure hydrocarbon materials with reduced intermolecular interactions in the solid state. Finally, blue fluorescent emitting materials endowed with hole-, electron-, or bipolar-transporting properties will be discussed comprehensively.

2. Doped blue fluorescent materials

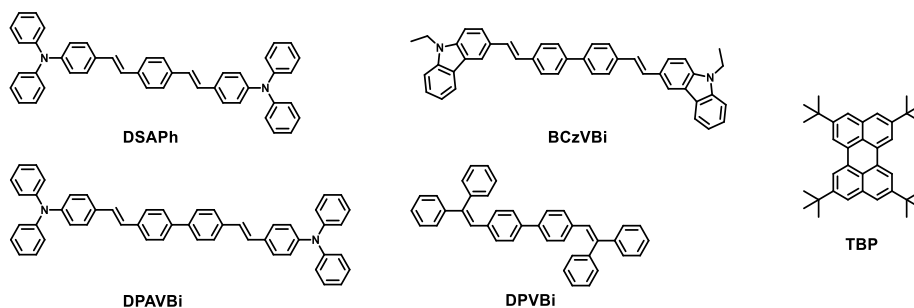


Figure 2.2. Some typical blue fluorescent dopant materials

Figure 2.2 displays the chemical structures of the commonly used blue fluorescent dopants. These blue fluorescent materials need to be doped into a wide band-gap host material to reduce concentration quenching in the emission layer (EML). During operation, the singlet excitons formed in the host under electrical excitation can be transferred to the dopant via Förster energy transfer. Förster energy transfer is a Coulombic interaction between the host exciton and the dopant, which is a fast ($\sim 10^{-12}$ s) and long-range process (up to 10 nm). Efficient Förster energy transfer requires that the emission spectrum of a host to overlap significantly with the absorption spectrum of a dopant (Figure 2.3). Besides, the doping concentrations required for optimal device performance are usually lower than 3%, which means sophisticated control during device fabrication and may cause performance variation.

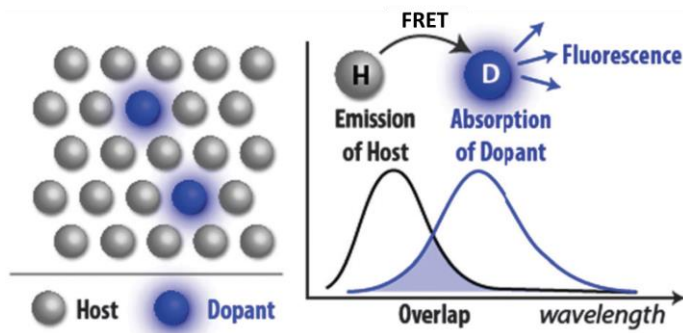


Figure 2.3. Schematic representation of host–dopant approach for the realization of blue fluorescent OLEDs; FRET = Förster resonance energy transfer.

Simultaneously, the use of a wide band-gap host usually hinders the charge injection and causes a high driving voltage. To address this issue, most of the host–dopant devices tend to have multilayer configurations with hole- and electron-injection/ transporting layers to facilitate charge transfer into the EML. Kido et al. optimized the charge balance of blue fluorescent OLEDs with two hole-transporting layers and five electron transporting layers to achieve a high external quantum efficiency of 8.2%.¹⁹ The performance is encouraging, while the device fabrication is rather tedious.

3. Non-doped blue fluorescent materials

Although the host-dopant system can produce high efficiency, the intrinsic phase separation could deteriorate the performance severely during operation. Besides, it requires the additional design of suitable hosts which further complicate

the evaluation of blue emitters. The use of non-doped emitters would be more pragmatic for their application.

Tremendous efforts have been made to investigate various kinds of blue fluorescent emitters, such as anthracene, fluorene, di(styryl)arylene, and pyrene derivatives to improve their electroluminescence (EL) properties. For instance, 9,10-diphenylanthracene (**DPA**), promoted by Adachi et al., is often quoted as a reference during the measurements of PLQY for its near unity fluorescence quantum efficiency in dilute solution.²⁰ However, its fluorescence in the solid state can be easily quenched due to aggregation.

Intrigued by the good PL properties of anthracene in solution, much effort has been devoted to developing anthracene derivatives as deep-blue emitters with reduced luminescent quenching in films. At the start, the modification strategy was to attach aryl groups to the 9,10-position of anthracene to reduce the intermolecular interactions. In addition, alkyl units such as methyl and tert-butyl were introduced to the 2,3,6,7-position to further suppress the troublesome crystallization. The well-known blue materials of 9,10-di(2-naphthyl)anthracene (**ADN**) and 2-methyl-9,10-di(2-naphthyl)-anthracene (**MADN**) were developed in succession by Tang and Chen et al.²¹⁻²² These compounds exhibited improved thermal and morphological properties but failed to qualify for self-host emitters. When applied as non-doped emitters, the EL spectra were broad and featureless due to the close packing in thin film.

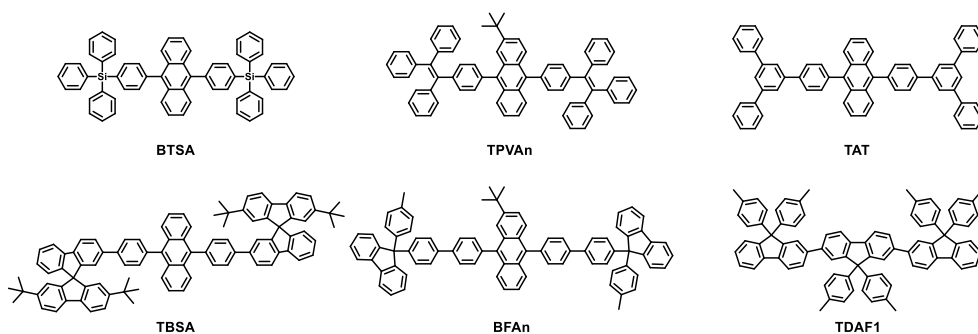


Figure 2.4. Reported non-doped blue fluorescent materials.

To pursue non-planar molecular structures in anthracene derivatives, the introduction of more rigid and bulky substituents such as tetraphenylsilane seems to be a rational strategy. Kwon et al. reported a blue fluorescent material of **BTSA** composed of anthracene as the core and triphenylsilylphenyl as a side unit (Figure 2.4).²³ **BTSA** showed a high glass transition temperature (T_g) of 168 °C, higher than those of **DPAVBi** (64 °C) and **MADN** (120 °C). Theoretical calculations revealed that the tetrahedral molecular skeleton twisted towards the anthracene backbone with an angle of 80°. The resulting non-coplanar structure was supposed to inhibit the intermolecular interactions. Besides, **BTSA** maintained the photophysical properties of the anthracene core due to the disrupted π -conjugation. Density functional theory (DFT) calculations indicated that the electron densities of the HOMO (highest occupied molecular orbital) and LUMO (lowest unoccupied molecular orbital) were mainly located on the anthracene unit. A device based on **BTSA** as an emitter achieved a current efficiency of 1.3 cd A⁻¹ with CIE coordinates of (0.148, 0.09).

The incorporation of tetraphenylsilane into anthracene derivatives could easily suppress intermolecular interactions in the solid state to obtain non-doped blue

emitters. However, the devices fabricated from these materials usually turn on at voltages as high as 6~7 V, and thus result in low power efficiency. It was caused by the hampered charge injection due to the large band gap (> 2.90 eV) and the disturbed charge transport because of the breakdown of the π system.

An alternative approach for non-doped blue anthracene emitters is to conjugate aryl groups to the 9,10-position of the anthracene unit. Using tetraphenylethylene as the substituent, Shu et al. observed a higher film-state PLQY of 0.89 (relative to DPA) for **TPVAn** than the value of 0.06 measured in dilute solution.²⁴ This phenomenon was attributed to the restricted intramolecular rotation of the phenyl peripheries in the solid state. In dilute solution, the twisting of the double bond of the 4-(1,2,2-triphenylvinyl)phenyl group might facilitate an approach between the excited and ground states of **TPVAn** and cause efficient internal conversion (IC), which was insufficient in the solid state due to the inhibition from the rigid environment. Meanwhile, the non-planarity of this molecular structure effectively diminished the degree of intermolecular π - π stacking and reduced the fluorescence quenching. The **TPVAn**-based non-doped devices displayed high performance: a maximum current efficiency of 5.3 cd A^{-1} and a maximum power efficiency of 2.8 lm W^{-1} as well as deep-blue emission with CIE coordinates of (0.14, 0.12). In addition, a white OLEDs with a maximum current efficiency of 13.1 cd A^{-1} was fabricated using **TPVAn** as a host for an orange fluorophore.

Simple 1,3,5-triphenylbenzene could also be attached to the 9,10-positions of anthracene to generate the non-doped deep-blue emitter **TAT**. Park et al. demonstrated a maximum external quantum efficiency of 7.18% with CIE coordinates of (0.156, 0.088) at 10 mA cm^{-2} by using **TAT** as emitter.²⁵ It seems that the integration of geometrically bulky aryl groups to emission centers could easily

form blue emitters with reduced close packing and consequent high fluorescent quantum yield in films. With this in mind, more pure hydrocarbon groups with steric hindrance were selected and incorporated into the anthracene core to obtain non-doped blue emitters.

Bulky spirobifluorene as a building block has been widely used in optoelectronic materials due to its steric hindrance effect. Kwon et al. reported that linking the t-butylated spirobifluorene moieties to the 9,10-position of anthracene could obtain a deep-blue emitter **TBSA**.²⁶ It was anticipated that the introduction of a spiro center into a defined low molecular structure could allow the formation of a thermally stable amorphous film. Owing to the non-coplanar structure, **TBSA** showed good thermal stability with a high thermal-decomposition temperature (T_d , corresponding to a 5% weight loss) of 420 °C and a high T_g of 207 °C. A non-doped multilayer device based on **TBSA** exhibited a current efficiency of 3.0 cd A⁻¹ and power efficiency of 1.2 lm W⁻¹ at a brightness of 300 cd m⁻². Since the nonplanar molecular structure prevented the close packing in films, the EL spectrum of **TBSA** was identical with that of PL with CIE coordinates of (0.15, 0.11).

Replacing the periphery spirofluorene moieties with fluorene units, Shu et al. designed a deep-blue emitter **BFA**n.²⁷ The presence of the sterically congested fluorene groups imparted **BFA**n with a high T_d of 510 °C and a T_g of 227 °C. As biphenyl groups were used as linkages, the calculated PLQY (Φ) was as high as 0.93 (using $\Phi = 0.90$ of DPA in cyclohexane as a calibration standard). Meanwhile, the mitigation of the close packing in the solid state had not yet been clarified. A device featuring **BFA**n as a neat emitter exhibited a good external quantum efficiency of 5.1% and current efficiency of 5.6 cd A⁻¹ with CIE coordinates of (0.15, 0.12).

Besides anthracene, fluorene derivatives have also been widely investigated as blue emitters due to their high PLQYs and good thermal stabilities. However, the long-wavelength emissions observed in fluorene-based devices, possibly due to the photo- or electro-oxidized cleavage of C9-substituted alkyl pendant group(s), result in poor color purity and have inhibited their application. To solve this problem, Wong et al. designed the ter(9,9-diarylfluorene) **TDAF1**,²⁸ in which the C9-aryl substituents provide hindrance on interchromophore packing. **TDAF1** exhibited a high film-state PLQY of 0.90 and a high T_g up to 204 °C. The corresponding device achieved a high external quantum efficiency of 5.3% with CIE coordinates of (0.158, 0.041).

3.1. Non-doped multifunctional blue fluorescent materials

It is mentioned above that the EL performances of blue materials often suffer from the retarded charge injection and transportation in the emission layer. High efficiencies of blue OLEDs are usually obtained through optimizing the charge balance in multilayer devices. In terms of the materials, an emission layer featured with improved charge injection and transport characteristics could effectively elevate the device performances as discussed in our recent review.²⁹ Therefore, except for good thermal stabilities and the capability to suppress close-packing in the solid state, desirable blue emitters had better possess good charge carrier transport ability to provide more balance in hole and electron fluxes in simple device structure. In this context, hole and/or electron transport units have been incorporated into the blue parent to design multifunctional blue emitters.

3.2. P-type non-doped blue fluorescent emitting materials

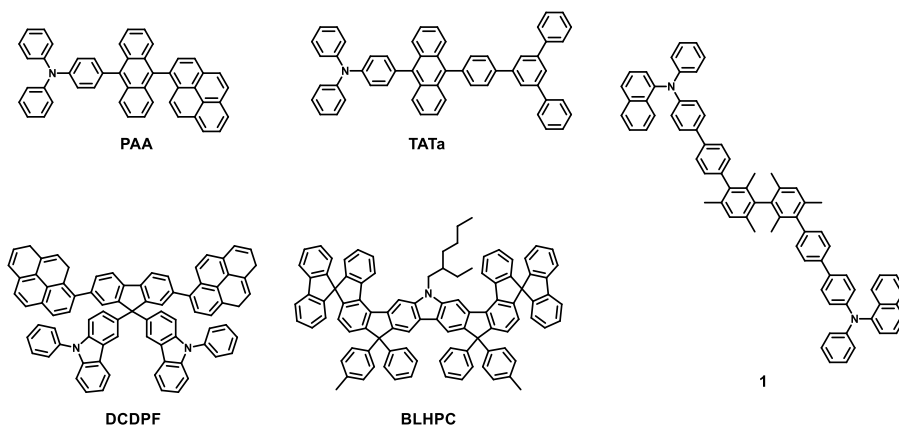


Figure 2.5. P-type non-doped blue fluorescent materials.

The triarylamine group is well-known for its good hole-transporting ability via the radical cation species with high stability. They have been incorporated into molecules to improve hole-injection and -transporting properties, and to increase bulky volumes and thermal stability.

Intrigued by the luminescent properties of anthracene and charge-transporting abilities of triarylamine, Tao et al. reported the anthracene derivative **PAA** end-capped with triphenylamine for efficient hole transportation (Figure 2.5).³⁰ The PAA-based non-doped device exhibited efficient blue emission with a maximum current efficiency up to 7.9 cd A^{-1} . Furthermore, given the facile hole-injection from the anode to the emission layer due to the well-matched HOMO level, the power efficiency was as high as 6.8 lm W^{-1} . But the emission color was greenish-blue with CIE coordinates of (0.15, 0.30).

In order to improve the color purity, Park et al. attached triphenylamine and 1,3,5-triphenylbenzene to the 9,10-position of anthracene to form the asymmetric compound **TATa**.³¹ The corresponding non-doped device realized a maximum efficiency of 6.07 cd A⁻¹ with CIE coordinates of (0.149, 0.177). Compared with symmetrical 1,3,5-triphenylbenzene substituted **TAT**, the PL emission of **TATa** is red-shifted to the sky-blue region, which might be caused by intramolecular charge transfer from the strong electron-donor triphenylamine to the anthracene core. According to these results, it would be rational to use a meta- and/or ortho-linkage instead of the paralinkage between the donor and anthracene core with phenyl ring as spacer, which could relieve the intramolecular charge transfer and then reduce the bathochromic shift.

Inspired by the application of tetraarylimesityls for aminebased hole-transporting materials, Moorthy et al. reported the diarylaminobiphenyl-functionalized bimesityl **1** with diarylaminosubstituted biphenyls linked to a unique 3-dimensional bimesitylene core, which were found to exhibit bright blue emission in the solid state.³² It could simultaneously function as a hole-transporting and emissive material as demonstrated by simple non-doped bilayer devices with external quantum efficiency up to 4.23% and CIE coordinates of (0.15, 0.09). The carbazole-fluorene hybrids have been explored as host materials for phosphorescent OLEDs, but the reports using the hybrids as deep-blue emitters are still rare. Tao et al. designed and prepared a p-type blue emitter, 9,9-bis-(3-(9-phenyl-carbazoyl))-2,7-dipyrenylfluorene (**DCDPF**).³³ A device using **DCDPF** as the non-doped emitter exhibited pure-blue emission with a peak at 458 nm and CIE coordinates of (0.15, 0.15). The maximum efficiency of the device was 4.4 cd A⁻¹ (3.1 lm W⁻¹). It proves

that the introduction of carbazole units at the 9-position of fluorene is an effective way to avoid molecular aggregation and the associated red shift in emission.

Since the spiro-linkage could suppress the photo/thermal oxidation of the 9-position of the fluorene unit to the undesired ketonic defect, Jiang et al. reported a carbazole-cored ladder-type molecule **BLHPC**.³⁴ The carbazole moiety improve the hole injection and transportation of ladder-type materials, and the spiro-configuration effectively impede the intermolecular π - π interactions and consequently lead to the amorphous morphology of a ladder-type molecule. The almost 100% fluorescence quantum yield of **BLHPC** in CH_2Cl_2 solution indicated that non-radiative decay pathways were completely suppressed by restricting bond rotation in such confined and rigid backbones. Noticeably, **BLHPC** revealed a very stable emission upon heat treatment. Though the emission color was located in the sky-blue region, a maximum current efficiency of 1.46 cd A^{-1} was achieved with a simple device configuration.

3.3. N-type non-doped blue fluorescent emitters

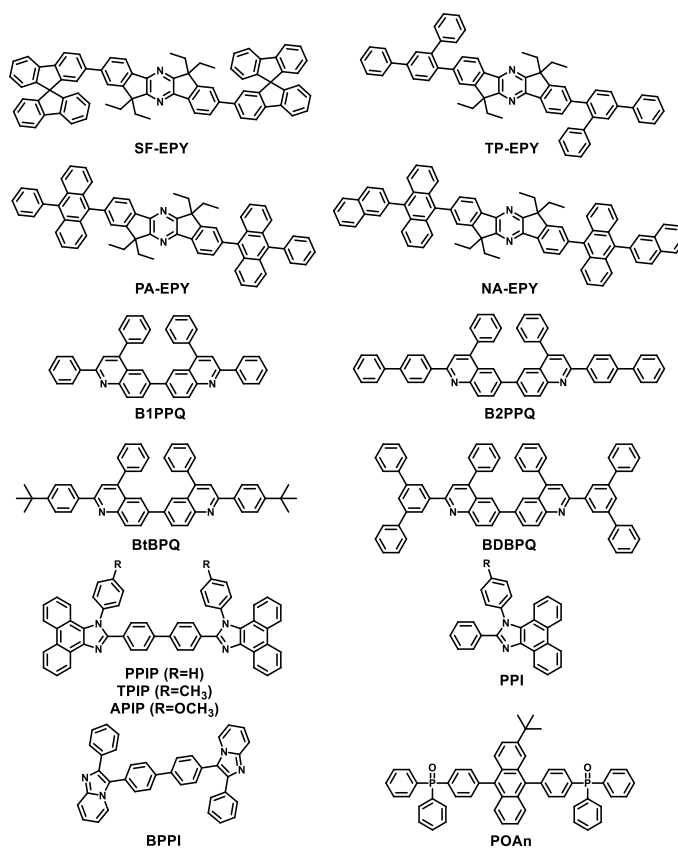


Figure 2.6. N-type non-doped blue fluorescent materials

As mentioned above, most of the developed blue materials exhibit large energy gaps and low electron affinities (EAs), leading to inefficient electron injection into the blue emitters. Poor electron injection can be compensated by using an additional electron-transporting/hole-blocking layer as well as a low work-function cathode, such as Ca or Li. However, these approaches suffer from complicated fabrication processes or the poor environmental stability of the active metals. Therefore, it is desirable to design blue-emitting materials with high EA values, facilitating electron-injection and -transport.

Park et al. developed deep blue emitting materials with indenopyrazine as an electron-accepting group to facilitate electron-injection and -transport (Figure 2.6).³⁵ Though the films of indenopyrazine suffered from fluorescence quenching due to the π - π stacking, the problem was overcome by the substitution of alkyl groups at the 6 and 12 position of the indenopyrazine ring and of various aromatic side groups at the 2 and 8 position. Consequently, a non-doped device based on **TP-EPY** was found to exhibit a maximum external quantum efficiency of 4.6% and color purity of (0.154, 0.078) as well as a narrow emission band with 47 nm of full width at half maximum (FWHM).

Like pyrazine, other electron-withdrawing groups such as quinoline, imidazole, 1,3,4-oxadiazole and phosphine oxide etc. have been utilized to design novel n-type blue emitters. Jenekhe et al. reported several highly emissive n-type conjugated oligoquinolines.³⁶ The compounds emitted blue fluorescence in solution with high quantum yields (73~94%). The oligoquinolines had reversible electrochemical reduction, and high EAs (2.68~2.81 eV). Devices based on **B2PPQ** as the blue emitter gave the best performance with a high brightness (19,740 cd m⁻² at 8.0 V), high efficiency (7.12 cd A⁻¹) and external quantum efficiency of 6.56% at 1175 cd m⁻² with CIE coordinates (0.15, 0.16).

Liu et al. designed a series of n-type imidazole derivatives as deep-blue emitters.³⁷ Non-doped devices based on **PIIP** gave pure-blue light with CIE coordinates of (0.15, 0.14). The **PIIP**-based device can reach not only a high external quantum efficiency of 6.31% but also a high power efficiency of 7.30 lm W⁻¹. Furthermore, the power efficiency remains as high as 4.94 lm W⁻¹ at a practical brightness of 200 cd m⁻². When using **TIIP** or **APIP** as the emissive layer, the devices also exhibited high external quantum efficiencies of more than 5%. The

superiority of phenanthroimidazole attracted considerable attention. Ma et al. developed two blue-emitting compounds based on phenanthro[9,10-d]imidazole group.³⁸ The double-layered device based on **BPPI** (identical to that of **PIIP** reported by Liu et al.) achieved a higher luminance and a lower turn-on voltage than the multi-layered device with an independent electron injection layer. The results suggest that the phenanthroimidazole unit is an excellent building block for tuning the carrier injection properties as well as blue emission. For the first time, Zhang et al. introduced an indolizine group to construct a blue emitter (**BPPI-2**) for OLEDs.³⁹ The indolizine derivative **BPPI-2** exhibited a high quantum yield and sufficient high triplet energy to act as a red or yellow-orange phosphorescent host. The non-doped blue device displayed an external quantum efficiency of 3.16% with CIE coordinates of (0.15, 0.07).

Until recent years, phosphine oxide derivatives have been the subject of electron-transport materials for optoelectronic devices. Shu et al. designed a very efficient n-type deep-blue emitter **POAn**, which comprised of electron-deficient triphenylphosphine oxide and a 2-tert-butylanthracene core.⁴⁰ The aryl substituents at the 9- and 10-positions of the anthracene have highly twisted configurations, with torsion angles of 89.1° with respect to the plane of the central anthracene unit. In addition to serving as an n-type blue light-emitting material, **POAn** also facilitates electron injection from the Al cathode to itself. The simple bilayer device using **POAn** as emitter and electron-transporting materials exhibited a maximum external quantum efficiency of 4.3% with CIE coordinates of (0.15, 0.07). For a device without an electron-transport layer or alkali fluoride, the device based on **POAn** displayed the best performance of such deep-blue OLEDs.

3.4. Bipolar non-doped blue fluorescent materials

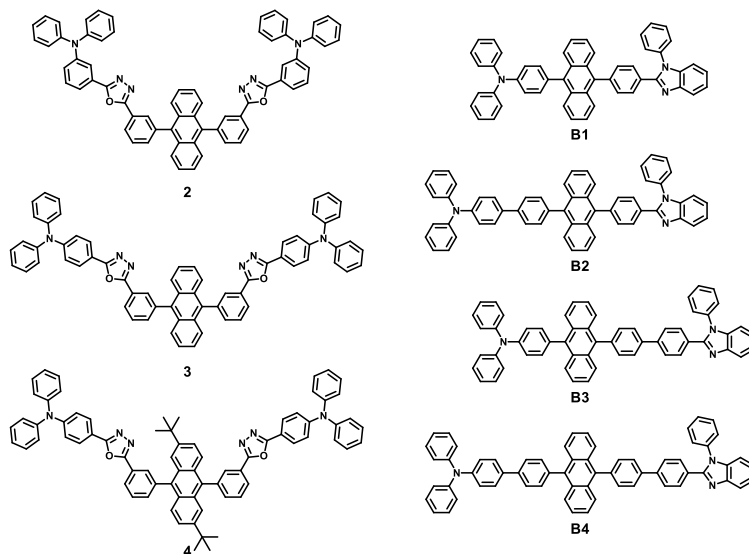


Figure 2.7. Biphenyl anthracene based bipolar materials

After the bipolar material was reported by incorporating triphenylamine and oxadiazole unit initially by Chen et al.,⁴¹ a bipolar phosphor emitter including both an anode and an electron transition region effectively stabilized exciton formation and balanced hole and electron charge in the light emitting layer has been found.

In order to integrate three active components (hole-transporting, electron-transporting, and light-emitting moieties) into a single molecule, Zhu et al. designed blue fluorescent emitters with hole- (triphenylamine and carbazole) and electron-transporting (oxadiazole) moieties appended to the 9,10-position of the anthracene core through meta-linkage (Figure 2.7).⁴² A simple bilayer device using compound **4** as the hole-transporting and emitting-layer exhibited a maximum power efficiency of 2.0 lm W^{-1} and CIE (x, y) of (0.16, 0.10). The well-matched energy level between

anode and compound **4** as well as the intrinsic good charge transport abilities resulted in very low driving voltage (2.7 V). DFT calculations revealed that the electron density distribution of the HOMO and LUMO orbitals of **4** were localized predominantly on the anthracene chromophore, which implied that chemical modification did not alter the photophysical properties of anthracene core.

Tian et al. reported another series of bipolar blue emitters by introducing the hole-transporting triphenylamine and electron-transporting benzimidazole moieties into the 9,10-position of anthracene through para-linkage (Figure 2.7).⁴³ A single layer device based on **B4** exhibited a current efficiency of 3.33 cd A⁻¹ with CIE coordinates of (0.16, 0.16) and a maximum brightness of 8472 cd m⁻² at 8.7 V.

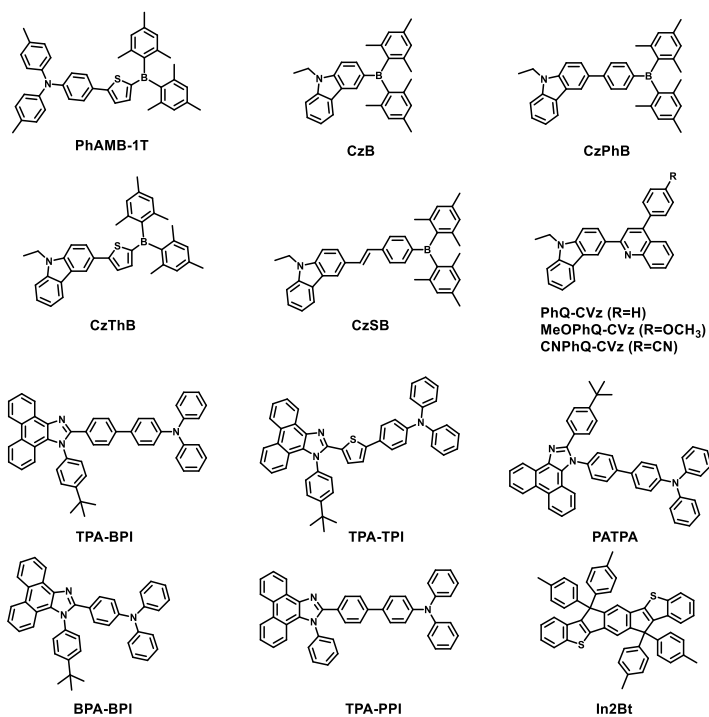


Figure 2.8. Bipolar-type non-doped blue fluorescent materials

Dimesitylboryl moieties with nonplanar molecular structures have been exploited as building blocks for electron-transporting materials. Shirota et al. presented an amorphous emitting material of **PhAMB-1T** by incorporating the triphenylamine and dimesitylboryl moieties.⁴⁴ A device based on **PhAMB-1T** achieved a power efficiency of 1.1 lm W⁻¹ and an external quantum efficiency of 0.8% at the luminance of 300 cd m⁻² with blue-green emission. To improve the color purity, Kuo et al. designed a series of arylborane-containing carbazole bipolar blue fluorophores by a different bridge.⁴⁵ A device based on **CzPhB** achieved a maximum external quantum efficiency of 4.3% with CIE coordinates (0.15, 0.09). Kang et al. designed phenylquinoline-carbazole derivatives as bipolar deep-blue fluorescent emitters.⁴⁶ The energy levels could be easily adjusted by the introduction of different electron-donating and electron-withdrawing groups onto carbazolylphenylquinoline. A non-doped deep-blue device using **PhQ-CVz** as the emitter acquired a maximum external quantum efficiency of 2.45% with CIE coordinates of (0.156, 0.093).

Utilizing the donor- π -acceptor approach, Tong et al. designed several deep-blue phenanthroimidazole derivatives.⁴⁷ The photophysical properties and EL performances could be tuned by linking the spacer and topology between the electron-donating triphenylamine and electron-accepting phenanthroimidazole. A non-doped device based on **TPA-BPI** showed turn-on voltages as low as 2.8 V, high efficiency (2.63 cd A⁻¹, 2.53 lm W⁻¹, 3.08%), with small efficiency roll-off at high current densities, and stable deep-blue emissions with CIEy < 0.10.

Ma et al. demonstrated that the intercrossed-excited-state existed in a twisting donor-acceptor molecule, **TPA-PPI**, through a combined photophysical and DFT investigation.⁴⁸ A non-doped device with **TPA-PPI** as the emitter reached a maximum current efficiency of 5.0 cd A⁻¹, and a maximum external quantum

efficiency of 5.0%, corresponding to an internal quantum efficiency of >25%, breaking through the limit of efficiency for fluorescence-based EL devices. The effective utilization of the excitation energy arising from the intercrossed excited-state (local exciton and charge transfer) is thought to contribute to the improved efficiency. This new insight provides us with an effective strategy to construct highly efficient deep-blue emitters.

Different to the linear linking methodology, Hung et al. utilized an “intramolecular annulations” concept to design blue emitter **In2Bt**.⁴⁹ The rigid and coplanar distyryl-p-phenylene backbone was flattened by two different bridging atoms of carbon and sulfur. The compound exhibited high T_g (192 °C) and bipolar charge transport properties with similar hole and electron mobilities in the range of $10^{-4}\sim 10^{-5}$ cm² V⁻¹ s⁻¹. A non-doped device with **In2Bt** as the emitter gave a maximum current efficiency of 0.86 cd A⁻¹, a maximum power efficiency of 0.76 lm W⁻¹ with CIE coordinates of (0.16, 0.08).

Designing of bipolar blue emitters with high triplet energy is especially very difficult. Since an extended π -conjugation and strong charge-transfer character in the bipolar skeleton would significantly reduce the triplet energy, many groups have been devoted to solving the dilemma.

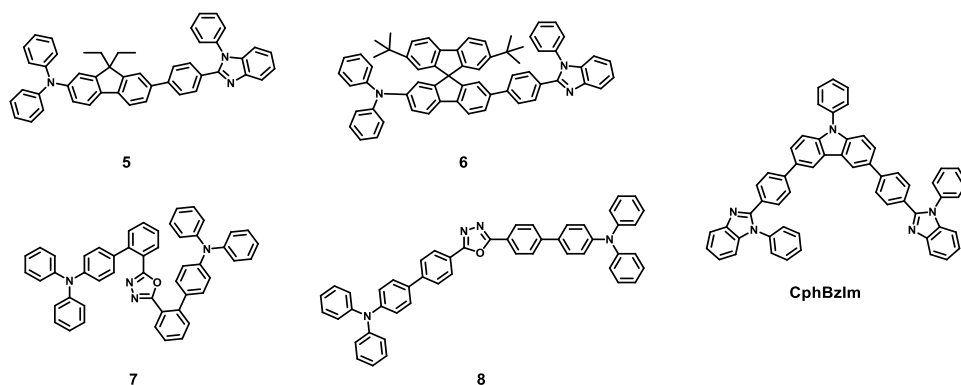


Figure 2.9. Bipolar-type non-doped blue fluorescent materials with high triplet energy.

Wu et al. reported a convenient synthesis of highly emissive compounds containing benzimidazole and arylamine units.⁵⁰ The triplet energies of **5** and **6** were measured to be 2.2 and 2.3 eV, which might render them able to act as appropriate hosts for orange/red phosphorescent complexes. The deep-blue EL performances of **5** and **6** in non-doped single-layer devices were comparable with those of multilayer devices due to the effective bipolar carrier transport.

Through the ortho-linkage of electron-donating triphenylamine units and the electron-accepting oxadiazole units, Tao et al. developed a simple strategy for designing bipolar fluorescent molecules.⁵¹ The twisted molecule of **7** showed a blue-shifted emission, less intramolecular charge-transfer, and a higher triplet energy level compared to its para-structured analogue **8**. The triplet energies of **7** and **8** were determined to be 2.46 and 2.35 eV, respectively. Non-doped blue light-emitting devices based on the two materials achieved a maximum current efficiency of 3.1 cd A⁻¹. By utilizing the dual roles of **7** and **8** as both efficient blue emitters and hosts for

red phosphorescence, white OLEDs were successfully fabricated with a maximum current efficiency of 7.9 cd A^{-1} with CIE value of (0.39, 0.31). The results demonstrated a simple single-doped way to realize two-color based WOLEDs by use of the dual roles of the bipolar blue fluorescent emitters.

Wong et al. reported a bipolar material **CPhBzIm** with two electron-accepting N-phenylbenzimidazole units linked to the C3 and C6 positions of an electron-donating carbazole unit.⁵² The non-coplanar conformation of **CPhBzIm** provided a steric bulk, resulting in stable amorphous thin films and a pronounced solid state PLQY of 69%. The compound **CPhBzIm** also exhibited a high triplet energy of 2.48 eV, and bipolar charge transport ability. A non-doped deep-blue device achieved an external quantum efficiency of 3% with CIE coordinates of (0.16, 0.05).

Section 1. Blue Fluorescent Emitters for Non-doped Organic Light-emitting Diodes Based on an Anisole-Anthracene Core with Various Electron Withdrawing Pyridine Derivatives

Abstract

Four blue luminescent materials with anisole-anthracene core attached to electron withdrawing group as pyridine, quinoline and phenanthroline were designed and synthesized for use as non-doped blue fluorescent emitting materials. Among them, a non-doped device using 3-(10-(4-methoxyphenyl)anthracen-9-yl)quinoline as the emitting material exhibited a maximum EQE of 1.45% with CIE color coordinates of (0.15, 0.10). These results indicate that aryl substituents attached at the C9- and/or C10 positions of anthracene core are highly twisted by the steric hindrance and as a result of can easily emit blue fluorescence.

Keywords: Anthracene, non-doped system, fluorescent organic light-emitting diodes, blue emitter.

1. Introduction

Organic electroluminescent devices have attracted much scientific and commercial interest because of their potential applications in full-color displays and large-area, flexible, light-weight light sources⁵³ ever since Tang and VanSlyke introduced an efficient organic light emitting diodes (OLEDs).⁵⁴ Full-color displays require red, green, and blue emissions of relatively equal stability, efficiency, and color purity. Although significant improvements in OLEDs performance have been achieved over the past decades, further improvement are still required.

In the early days, the fluorescent emitting layer (EML) of the OLEDs device was constructed by introducing a host-dopant system (doping system).^{19, 55-56} By controlling intermolecular interactions through the doping system, high-efficiency luminescence characteristics were obtained through preventing concentration quenching and color purity control. Although doping systems can produce high efficiency, inherent phase separation could seriously decline performance during operation.⁵⁴ In addition, a scrupulous design of the appropriate host is required depending on the energy gap and charge balance of the dopant material. A non-doped system has the advantage of a simple device structure that employs only a single emitting material without using a complicated host-dopant codeposition process.⁵⁷⁻⁶¹ Relatively little attention has been paid to the synthesis of deep-blue emitters because EQEs > 2% and CIE_y < 0.10 in the deep-blue non-doped system are difficult to obtain simultaneously. Therefore, it is still challenging to design deep-blue emitters for reliable device performance.

Anthracene derivatives have been extensively studied and developed as light emitting materials in OLEDs due to their attractive photoluminescence (PL) and electroluminescence (EL) properties.⁶²⁻⁷⁰ Anthracene derivatives have been widely

used as building blocks for conjugated small molecules, polymers, oligomers, and dendrimers with good optoelectronic properties.⁷¹⁻⁷³ Anthracene derivatives comprise of multifunctional properties like light emitting layer^{23, 42}, hole transport layer⁷⁴⁻⁷⁵, electron transport layer,⁷⁶⁻⁷⁷ or dopant.⁷⁸ As an EML, fluorescent spectra color of anthracene derivatives can be easily tuned from blue to green by importing different groups at the C9- and C10 positions. For example, pyridine derivatives of anthracenes used electron transport and host materials to minimize operational voltages and consequently show much better device performance.⁶⁰ When a comparison is made with non-doped device structures such as carbazole, purine and fluorene, anthracene based derivatives exhibited higher electroluminescent performances.⁷⁹⁻⁸²

In this study, we report on the synthesis and characterization of anisole-anthracene (AA) derivatives for bipolar blue non-doped emitting materials for OLEDs. Four AA derivatives attached with strong electron withdrawing groups like pyridine, quinoline and phenanthroline at the opposite position C10 of the anisole-containing anthracene showed deep blue emissions. Among them, a non-doped OLED device using 3-(10-(4-methoxyphenyl)anthracen-9-yl)quinoline (**3QAA**) as an emitting material without a host shows a maximum EQE of 1.45% with CIE color coordinates of (0.15, 0.10)

2. Materials and methods

2.1. Materials

All solvents and materials were used as received from commercial suppliers without further purification. Synthetic routes to anisole-anthracene derivatives are

outlined in scheme 1. All product was purified by temperature gradient vacuum sublimation.

2.2. Synthetic procedure

9-(4-methoxyphenyl)anthracene (2). 9-bromoanthracene (2.64 g, 11.89 mmol), (4-methoxyphenyl)boronic acid (4.45 g, 23.78 mmol), 2 mol L⁻¹ potassium carbonate (in H₂O, 60 mL) and tetrakis(triphenylphosphine)palladium (0.69 g, 0.59 mmol) in toluene (60 mL) and ethanol (5 mL) were heated to reflux in a nitrogen atmosphere for 24 h. After the reaction mixture was concentrated in vacuo, the resulting mixture was extracted with dichloromethane. The organic layer was washed with water and brine and dried using anhydrous sodium sulfate. The filtrate was concentrated in vacuo to give a crude mixture, which was purified by column chromatography (SiO₂, hexane) afford the 9-(4-methoxyphenyl)anthracene (2.7 g, 80.0%) as white solid. ¹H NMR (400 MHz, CDCl₃): δ (ppm) 8.48 (s, 1H), 8.04 (d, *J* = 8.24 Hz, 2H), 7.72 (d, *J* = 8.68 Hz, 2H), 7.48-7.44 (dd, *J* = 2.4, 2.4 Hz, 2H), 7.37-7.35 (m, 4H), 7.12 (d, *J* = 8.68 Hz, 2H), 3.95 (s, 3H).

9-bromo-10-(4-methoxyphenyl)anthracene (3). 9-(4-methoxyphenyl)anthracene (5.00 g, 17.58 mmol) and N-bromosuccinimide (3.75 g, 21.10 mmol) were sealed in a round bottom flask and dried under reduced pressure. Add 200 mL of chloroform and stir with heating for 2 hours. The reaction is terminated by TLC and the solvent is removed. Then, recrystallize using acetone and methanol solvent. The recrystallized solvent was filtered to obtain 4.66 g (73.0%) of 9-bromo-10-(4-methoxyphenyl)anthracene. ¹H NMR (400 MHz, CDCl₃): δ (ppm) 8.61 (d, *J* = 9.16 Hz, 2H), 7.71 (d, *J* = 8.68, 2H), 7.61~7.57 (dd, *J* = 7.76, 7.86 Hz, 2H), 7.40~7.36 (dd, *J* = 9.16, 8.68 Hz, 2H), 7.32 (d, *J* = 8.68, 2H), 7.12 (d, *J* = 8.72, 2H), 3.95 (s,

3H). ¹³C-NMR (300 MHz, CDCl₃): δ (ppm) 160.0, 137.5, 132.1, 131.2, 130.2, 130.1, 127.7, 127.4, 126.8, 125.3, 122.4, 113.8, 55.4.

3-(10-(4-methoxyphenyl)anthracen-9-yl)pyridine (3PAA). 9-bromo-10-(4-methoxyphenyl)-anthracene (2.00 g, 5.51 mmol), pyridin-3-yl boronic acid (0.75 g, 6.06 mmol), 2 M potassium carbonate (in H₂O, 10 mL), tetrakis(triphenylphosphine)palladium (0.64 g, 0.55 mmol) in toluene (100 mL) and ethanol (10 mL) were heated to reflux in a nitrogen atmosphere for 24 h. After the reaction mixture was concentrated in vacuo, the resulting mixture was extracted with dichloromethane. The organic layer was washed with water and brine and dried using anhydrous sodium sulfate. The filtrate was concentrated in vacuo to give a crude mixture, which was purified by column chromatography (SiO₂, hexane:ethyl acetate = 9:1) afford the 3-(10-(4-methoxyphenyl)anthracen-9-yl)pyridine (1.29 g, 65.0%) as yellow solid. ¹H NMR (400 MHz, CDCl₃): δ (ppm) 8.27 (d, *J* = 7.6 Hz, 1H), 7.88 (d, *J* = 7.5 Hz, 1H), 7.80 (d, *J* = 6.2 Hz, 2H), 7.67 (d, *J* = 7.8 Hz, 1H), 7.60 (d, *J* = 10 Hz, 1H), 7.49~7.36 (m, 7H), 7.29, 7.18 (d, *J* = 9 Hz, 2H), 6.77 (d, *J* = 8.7 Hz, 1H). ¹³C-NMR (100 MHz, CDCl₃): δ (ppm) 159.2, 148.3, 139.4, 138.4, 138.1, 134.0, 132.3, 130.7, 130.2, 129.8, 128.3, 127.3, 126.8, 126.1, 125.7, 125.1, 123.6, 55.4.

4-(10-(4-methoxyphenyl)anthracen-9-yl)isoquinoline (IQAA). 9-bromo-10-(4-methoxyphenyl)-anthracene (2.00 g, 5.51 mmol), isoquinolin-4-yl boronic acid (1.01 g, 6.06 mmol), 2 M potassium carbonate (in H₂O, 10 mL), tetrakis(triphenylphosphine)palladium (0.64 g, 0.55 mmol) in toluene (100 mL) and ethanol (10 mL) were heated to reflux in a nitrogen atmosphere for 24 h. After the reaction mixture was concentrated in vacuo, the resulting mixture was extracted with dichloromethane. The organic layer was washed with water and brine and dried using anhydrous sodium sulfate. The filtrate was concentrated in vacuo to give a crude

mixture, which was purified by column chromatography (SiO₂, hexane:ethyl acetate = 9:1) afford the 3-(10-(4-methoxyphenyl)anthracen-9-yl)pyridine (1.62 g, 65.0%) as yellow solid. ¹H NMR (400 MHz, CDCl₃): δ (ppm) 8.40 (d, *J* = 7.5 Hz, 1H), 8.27 (d, *J* = 7.5 Hz, 1H), 8.18 (d, *J* = 8.0 Hz, 1H), 8.00 (d, *J* = 8 Hz, 2H), 7.52~7.35 (m, 10H), 6.88 (d, *J* = 7.8 Hz, 1H), 6.77 (d, *J* = 8.7 Hz, 1H), 6.58 (d, *J* = 4 Hz, 1H).

3-(10-(4-methoxyphenyl)anthracen-9-yl)quinoline (3QAA). 9-bromo-10-(4-methoxyphenyl)-anthracene (2.00 g, 5.51 mmol), quinolin-3-yl boronic acid (1.05 g, 6.06 mmol), 2 M potassium carbonate (in H₂O, 10 mL), tetrakis(triphenylphosphine)palladium (0.64 g, 0.55 mmol) in toluene (100 mL) and ethanol (10 mL) were heated to reflux in a nitrogen atmosphere for 24 h. After the reaction mixture was concentrated in vacuo, the resulting mixture was extracted with dichloromethane. The organic layer was washed with water and brine and dried using anhydrous sodium sulfate. The filtrate was concentrated in vacuo to give a crude mixture, which was purified by column chromatography (SiO₂, hexane:ethyl acetate = 9:1) afford the 3-(10-(4-methoxyphenyl)anthracen-9-yl)quinoline (1.7 g, 75.0%) as yellow solid. ¹H NMR (400 MHz, CDCl₃): δ (ppm) 9.02 (s, 1H), 8.31 (m, 2H), 7.93 (d, *J* = 8 Hz, 1H), 7.85 (t, *J* = 7.2 Hz, 1H), 7.80~7.77 (m, 2H), 7.69~7.62 (m, 3H), 7.42~7.22 (m, 6H), 7.15 (d, *J* = 8.4 Hz, 2H), 3.96 (s, 3H). ¹³C-NMR (100 MHz, CDCl₃): δ (ppm) 160.9, 152.8, 138.3, 138.2, 132.3, 132.2, 130.7, 130.4, 130.2, 129.9, 129.3, 128.9, 128.0, 127.9, 127.4, 127.3, 126.2, 125.7, 125.1, 121.8, 114.0, 113.9, 55.4.

2-(10-(4-methoxyphenyl)anthracen-9-yl)-1,10-phenanthroline (PTAA). A 1.6 M solution of n-butyllithium in hexane (6.90 mL, 11.02 mmol) was slowly added to a solution of 9-bromo-10-(4-methoxyphenyl)anthracene (2.00 g, 5.51 mmol) in 100 mL of diethyl ether at 0 °C. The solution was allowed to stir for 60 min at 0 °C.

A suspension of 1,10-phenanthroline (0.66 g, 3.67 mmol) in 50 mL of toluene was added. The solution first became yellow and then turned dark violet. The mixture was stirred for 48 h at room temperature. After the addition of water (50 mL) the layers were separated and the aqueous layer was extracted three times with dichloromethane (3×10 mL). The combined organic extracts were stirred with 20 g of activated MnO_2 for 2 h. The mixture was dried with magnesium sulfate and filtered. After evaporation of the filtrate the resulting solid was separated by column chromatography (SiO_2 , dichloromethane) afford the 2-(10-(4-methoxyphenyl)anthracen-9-yl)-1,10-phenanthroline (1.40 g, 55.0%) as yellow solid. ^1H -NMR (400 MHz, CDCl_3): δ (ppm) 9.09 (d, $J = 3.6$ Hz, 1H), 8.42 (d, $J = 8$ Hz, 1H), 8.26 (d, $J = 8$ Hz, 1H), 7.26 (t, $J = 8$ Hz, 2H), 7.73 (d, $J = 8.6$ Hz, 2H), 7.50 (m, 1H), 7.46 (m, 2H), 7.40 (d, $J = 8.4$ Hz, 2H), 7.29~7.19 (m, 6H), 7.14 (dd, $J = 8.4$ Hz, 2.8 Hz, 1H), 3.97 (s, 3H). ^{13}C -NMR (100 MHz, CDCl_3): δ (ppm) 159.06, 139.26, 138.0, 136.1, 132.5, 132.2, 131.0, 130.2, 130.0, 128.9, 128.0, 127.5, 127.1, 126.6, 126.5, 126.5, 126.2, 125.3, 124.9, 123.9, 123.0, 122.5, 113.9.

2.3. General methods

^1H - and ^{13}C -NMR spectra were recorded using an Agilent 400 MHz Varian spectrometer in CDCl_3 . ^1H -NMR chemical shifts in CDCl_3 were referenced to CHCl_3 (7.27 ppm). ^{13}C -NMR chemical shifts in CDCl_3 were reported relative to CHCl_3 (77.23 ppm). UV-visible spectra were recorded on a Beckman DU650 spectrophotometer. Fluorescence spectra were recorded on a Jasco FP-6500 spectrophotometer. Fluorescent quantum yields in the solid films were recorded on an Otsuka electronics QE-2000 spectrophotometer. Mass spectra were obtained using matrix-assisted laser desorption-ionization time-of-flight mass spectrometry

(MALDI-TOF-MS) from Bruker. High-resolution masses were measured by either fast atom bombardment (FAB) or electron ionization (EI) using a JEOL HP 5890. Analytical thin-layer chromatography was performed using Kieselgel 60F-254 plates from Merck. Column chromatography was carried out on Merck silica gel 60 (70~230 mesh). Decomposition temperatures (T_d) and glass transition temperatures (T_g) were obtained by thermogravimetric analysis (TGA, Q-5000-IR) and differential scanning calorimetry (DSC, DSC-Q-1000), respectively. The TGA and DSC analyses were performed at a heating rate of $10\text{ }^\circ\text{C min}^{-1}$ under a nitrogen atmosphere. The T_g was determined from the third heating scan. The electrochemical properties of AA derivatives were studied using cyclic voltammetry (CV) in CH_2Cl_2 solutions (1.00 mM) with 0.1 M tetra-*n*-butylammonium hexafluorophosphate (TBAPF_6) as the supporting electrolyte. A glassy carbon electrode was employed as the working electrode and referenced to a Ag reference electrode. All potential values were calibrated against the ferrocene/ferrocenium (Fc/Fc^+) redox couple. The onset potential was determined from the intersection of two tangents drawn at the rising and background current of the cyclic voltammogram.

2.4. Theoretical calculations

The optimized geometries and frontier molecular orbital energy levels for DIP and TIP were obtained using density functional theory (DFT) calculations with Gaussian '09. The geometries were optimized using the Becke 3-parameter Lee-Yang-Parr (B3LYP) functional with the 6-31G(d)-level atomic basis set.

2.5. Device fabrication & characterization

N,N'-Di(1-naphthyl)-*N,N'*-diphenyl-(1,1'-biphenyl)-4,4'-diamine (NPB), 4,4',4''-tris(*N*-carbazolyl)triphenylamine (TCTA), and 1,3,5-tris(*N*-phenylbenzimidazol-2-yl)benzene (TPBI) were purchased from commercial sources and used without purification. The fabrication of OLEDs was conducted by the high-vacuum (2×10^{-6} Torr) thermal evaporation of the organic materials onto indium tin oxide (ITO)-coated glass (sheet resistance: 15 Ω /square; Applied Film Corp.). Glass substrates with patterned ITO electrodes were washed with isopropyl alcohol and then cleaned by O₂ plasma treatment. The OLED devices were fabricated with a configuration of ITO/NPB/TCTA/3QAA/TPBI/LiF/Al. NPB and TCTA (hole transporting layers), TPBI (electron transporting layer), LiF (electron injection layer), and Al electrodes were deposited sequentially on the substrate. The emission properties were determined using a PR-650 SpectraScan SpectraColorimeter as a source meter. The current-voltage characteristics were measured using a programmable electrometer equipped with current and voltage sources (Keithley 2400).

3. Results and Discussions

3.1. Theoretical calculations

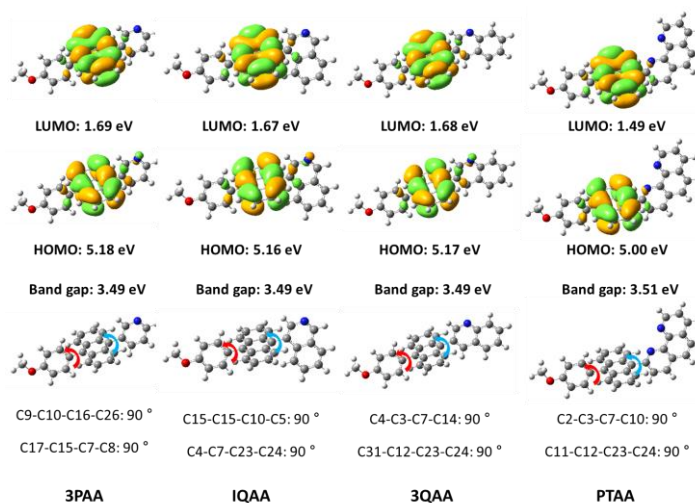


Figure 1. Optimized geometries and calculated molecular orbital density maps obtained from DFT calculations of Anisole-anthracene derivatives performed at the B3LYP/6-31G(d) level of theory.

Optimized geometries and frontier molecular orbital energy levels for **AA** derivatives were obtained from DFT calculations at the B3LYP/6-31G(d) level using Gaussian '09. As shown in Figure 1, the electron donating anisole moiety is highly distorted from the anthracene due to the closed hydrogen-hydrogen interaction between anisole and anthracene. The calculated results show that the dihedral angle connecting the anisole and anthracene is twisted about 90°. The acceptor moieties of pyridine, quinoline and phenantholine are also distorted about 90° with anthracene due to the hydrogen-hydrogen interaction. The introduction of the twisted structure of the anisole and accepting moieties inhibited the aggregation of **AA** derivatives in neat film. The highest occupied molecule orbitals (HOMOs) and lowest unoccupied molecule orbitals (LUMOs) of **AA** derivatives are localized on the anthracene moiety.

The DFT-calculated HOMO and LUMO energies are similar except **PTAA**, which are destabilized HOMO and LUMO energy levels due to the phenanthroline acceptor moiety.

3.2. Synthesis

The synthetic routes to **AA** derivatives are illustrated in Figure 2. The synthesis of 9-bromo-10-(4-methoxyphenyl) anthracene (**3**) was started from (4-methoxyphenyl)boronic acid with 9-bromoanthracene. Next, bromine attached pyridine, quinoline and isoquinoline reacted with compound **3** using the Suzuki cross coupling reaction, while phenanthrene moiety attached to compound **3** using anionic reaction with n-butyllithium and MnO₂. Furthermore, synthesized molecules were characterized by ¹H-NMR and ¹³C-NMR. These four blue emitting materials were purified further by train sublimation under reduced pressure (<10⁻⁴ Torr).

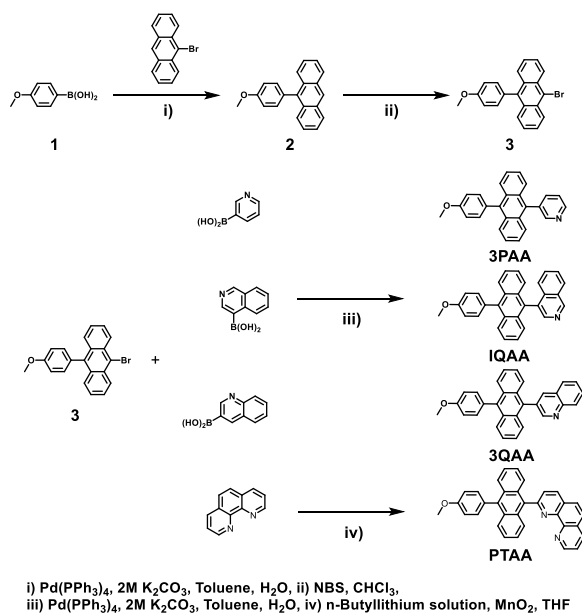


Figure 2. Synthetic routes of AA derivatives.

3.3. Photophysical properties

Table 1. UV and PL properties of **AA** derivatives in dichloromethane (10^{-5} M).

	1PAA	IQAA	PTAA	3QAA
UV (nm)	259, 356, 374, 395	258, 356, 375, 395	259, 358, 375, 395	259, 358, 376, 397
PL λ_{\max} (nm)	423	422	472	438

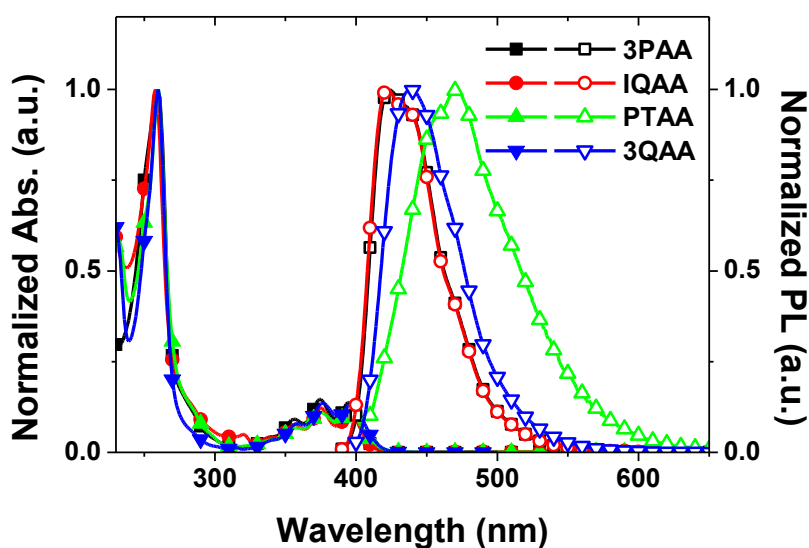


Figure 3. Photophysical properties of anisole-anthracene derivatives in dichloromethane (10^{-5} M).

Photophysical properties of four **AA** derivatives are summarized in Table 1. Figure 3 shows the normalized UV-vis absorbance and PL spectra of **AA** derivatives in dichloromethane solution. In solution, four **AA** derivatives exhibited similar absorbance characteristics as the isolated anthracene units. All absorption spectra has three major bands, with similar absorption peaks in the range of 259 to 397 nm.

These characteristic electronic patterns can be attributed to $n-\pi^*$ and $\pi-\pi^*$ transitions. Absorption bands at 330 ~ 400 nm come from $\pi-\pi^*$ transitions of the substituted aryl groups on the anthracene core⁸³ where the PL emission spectra of these anthracene derivatives were sufficiently overlapped with UV-Vis absorption. Upon excitation approximately at 375 nm, the PL spectra of **AA** derivatives in dichloromethane solution were found to exhibit deep blue to sky blue emission with the peak maxima at 423 to 472 nm. Compared to maximum emission peak of compound **3PAA** (423 nm) or **IPAA** (423 nm), **PTAA** (472 nm) showed red-shifted emission due to stronger electron withdrawing phenanthroline group containing one more nitrogen than pyridine and quinoline groups. Among them, **3QAA** has a suitable PL emission at approximately 438 nm for blue OLEDs. Therefore, electrochemical, thermal and device characteristics of **3QAA** were studied.

3.4. Electrochemical properties of **3QAA**

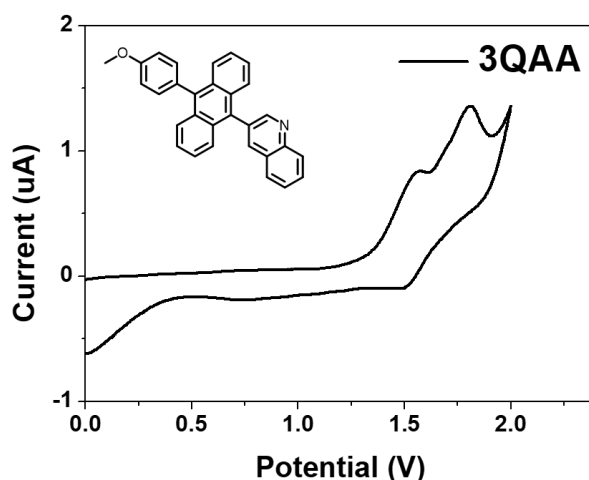


Figure 4. Electrochemical properties of **3QAA**.

To investigate the electrochemical properties of **3QAA**, cyclic voltammetry (CV) measurement was carried out. Consequently, the result was used to determine the HOMO energy level of the compound. The HOMO energy level was calculated from the onset of the oxidation potentials with respect to the energy level of ferrocene. As shown in Figure 4, **3QAA** exhibited irreversible oxidation in dichloromethane at room temperature. Because oxidation potential (E_{ox}) of **3QAA** was estimated to be 1.57 V, HOMO energy of **3QAA** was calculated to be 5.77 eV. The energy band gap (E_{gap}) of **3QAA** was obtained from absorption onset to be 3.01 eV. The LUMO energy level was estimated to be 2.76 eV using the following equation $E_{gap} = (E_{HOMO} + E_{LUMO})$. 3.01 eV of energy gap and appropriate HOMO and LUMO show that **3QAA** is suitable for blue OLEDs used as an emitting layer.

3.5. Thermal properties of **3QAA**

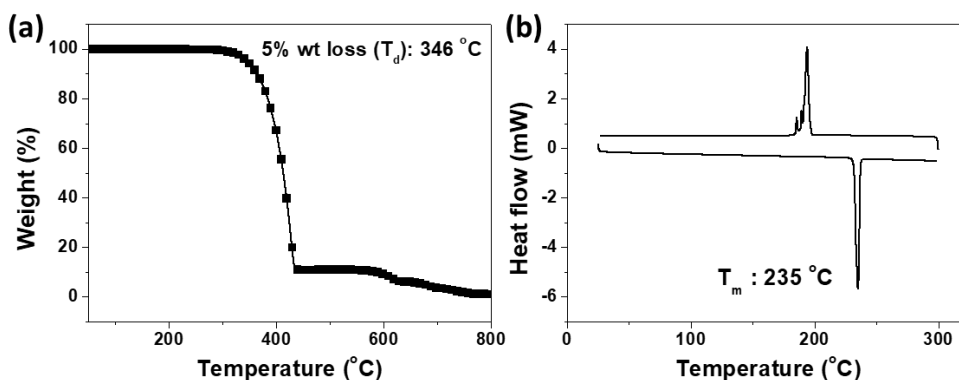


Figure 5. (a) TGA and (b) DSC graphs of **3QAA**.

The thermal properties of **3QAA** were investigated using TGA and DSC (Figure 5). **3QAA** exhibits high thermal stability at a decomposition temperature (T_d ,

corresponding to 5% weight loss) of 346 °C and no T_g , which means that **3QAA** has amorphous characteristic. Because a practical OLED device further requires excellent heat-resistance and durability, it means that the homogeneous, isotropic and easily processable characteristics of amorphous material are useful for an OLED device.

3.6. Electroluminescence properties

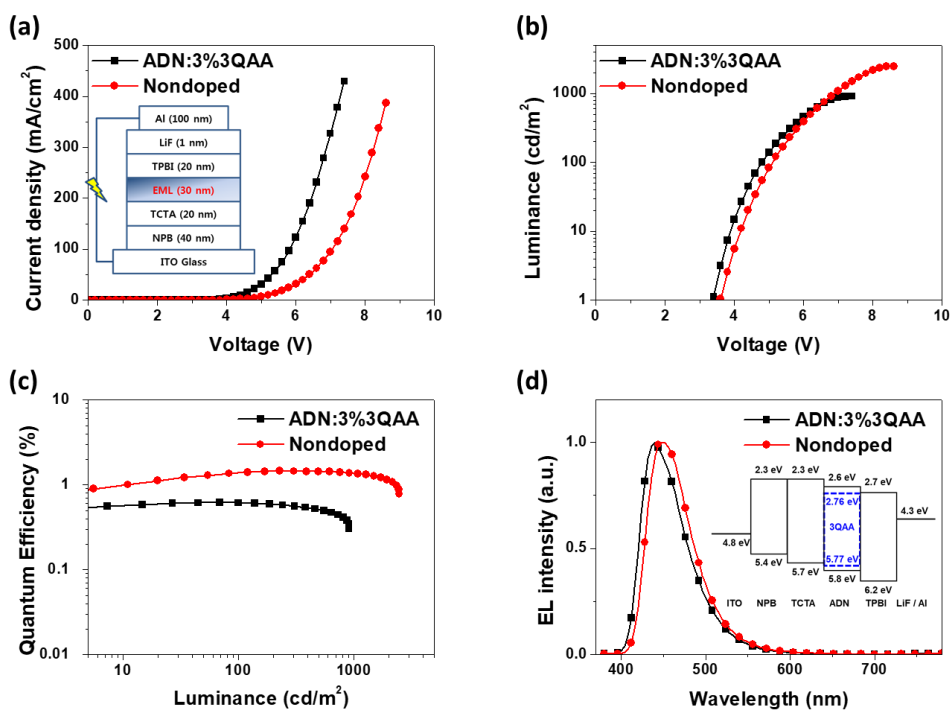


Figure 6. EL performances of **3QAA** based doped and non-doped blue OLEDs.

Table 2. Electroluminescent characteristics of **3QAA** based OLEDs

Doping concentration	V_{on}^a (V)	EQE_{max} (%)	$C.E._{max}^b$ (cd/A)	$P.E._{max}^c$ (lm/W)	EL_{max} (nm)	CIE^d (x,y)
ADN:3wt% 3QAA	3.3	0.62	0.46	0.35	440	(0.15, 0.09)
100% 3QAA	3.5	1.45	1.26	0.75	448	(0.15, 0.10)

^a Turn-on voltage at 1 cd/m², ^b current efficiency, ^c power efficiency, ^d at maximum EQE.

OLED devices were fabricated using **3QAA** as a non-doped deep-blue fluorescent emitter in the emitting layer (EML). The device configuration was ITO/NPB (40 nm)/TCTA (20 nm)/**3QAA** or ADN:3wt% **3QAA** (30 nm)/TPBI (15 nm)/LiF (1 nm)/Al (100 nm). Figure 6a shows the current density-voltage characteristics of the OLED devices containing doped and non-doped condition of **3QAA** used as the EML. In addition, the performances of the OLEDs are summarized in Table 1. Both of the devices had low turn-on voltages (at a luminance of 1 cd/m²) at 3.3 and 3.5 V, respectively, possibly originating from the small injection barriers in the devices. The current density of the doped EML based device was higher than that of the non-doped EML based device at the same voltage. Meanwhile, the luminance values of the non-doped EML based device was higher than that of the doped EML based device at the same current density, as shown in Figure 6b. The quantum efficiency-current density of two devices is plotted in Figure 6c. The non-doped EML based device shows a better maximum EQE of 1.45% compared to that of 0.62 % of the doped EML based device. Figure 6d shows the normalized EL spectra of the doped and non-doped EML based devices with maximum peak wavelengths at 440 and 448 nm, respectively. EL emission of the non-doped EML based device originates from the singlet exciton of **3QAA** without

any other emission from the adjacent layers whereas the **ADN** doped EML based device expected that originates from the **ADN** used as the host material.⁸⁴ The CIE coordinates of the **ADN** doped and non-doped EML based devices are (0.15, 0.09) and (0.15, 0.10), respectively. The low efficiency of the **ADN** doped EML based device show that the **ADN** is an inefficient host material for **3QAA**. Therefore, the generated exciton of host **ADN** does not transfer to the dopant **3QAA**.

4. Conclusion

Bipolar luminescent molecules with anisole-anthracene cores attached to electron withdrawing group like pyridine, quinoline and phenanthroline were designed and synthesized for use as non-doped blue fluorescent emitting materials. Because of the highly twisted molecular structure, each molecule shows deep-blue to sky-blue emissions in solution. A non-doped device using **3QAA** as the emitting material exhibited a maximum EQE of 1.45% with CIE color coordinates of (0.15, 0.10). These results indicate that aryl substituents at the C9- and/or C10 positions of anthracene core have a limited conjugation effect; therefore, using an anthracene core is an easy way to make blue EL emission.

Section 2. Efficient deep-blue emitters based on triphenylamine-linked benzimidazole derivatives for non-doped fluorescent organic light-emitting diodes

Abstract

Two triphenylamine-substituted benzimidazole derivatives were synthesized for use as efficient deep-blue emitters in non-doped fluorescent organic light-emitting diodes (FLOLEDs). The molecular design of 4',4''-(1*H*-benzo[d]imidazole-1,2-diyl)*bis*(*N,N*-diphenylbiphenyl-4-amine) (**T2B**) to limit the molecular packing density enabled **T2B**-based devices to suppress the exciton quenching by a bulky three-dimensional structure. Non-doped FLOLEDs fabricated using **T2B** as a blue emitter exhibited an external quantum efficiency of 4.67% with color coordinates of (0.15, 0.08).

Keywords: Deep-blue emitter, fluorescent organic light-emitting diodes, non-doped system, packing density

1. Introduction

Deep-blue fluorescent organic light-emitting diodes (FLOLEDs) possessing high efficiency and pure Commission Internationale de l'Eclairage (CIE) chromaticity coordinates are a prerequisite for full-color displays and lighting devices. There have been many studies on improving the device performance by optimally designing the emitters using doped or non-doped systems.^{30, 85-86} Nonetheless, owing to the intrinsic wide bandgap nature of deep-blue emitters, only a few examples of high-performance deep-blue FLOLEDs have been reported, in contrast to red and green fluorescent devices.⁸⁷⁻⁹⁰

Doping of emitters into host materials in the emitting layer (EML) was mainly involved for the development of high-efficiency deep-blue FLOLEDs. Chen et al. reported an external quantum efficiency (EQE) of 2.3% with CIE coordinates of (0.15, 0.11) based on mono(styryl)amine-based deep-blue dopants in FLOLEDs.⁹¹ FLOLED devices fabricated using a 9-anthracene-spirobenzofluorene derivative as the host and a diphenylamine-substituted spirobenzofluorene derivative as the dopant showed an EQE of 5.4% with CIE coordinates of (0.13, 0.15).⁹² Deep-blue FLOLEDs based on spirocyclic aromatic hydrocarbon derivatives and purine derivatives exhibited CIE coordinates of (0.16, 0.08) with 1.1 cd/A and CIE coordinates of (0.15, 0.06) with an EQE of 3.1%, respectively.^{81, 93}

A non-doped system has an advantage of a simple device structure that employs only a single emitting material without using a complicated host-dopant codeposition process.⁵⁷⁻⁶¹ However, in this type of system, excimers are usually induced by intermolecular interactions between emitters, or excitons are readily quenched, resulting in a red-shift of the CIE coordinates and/or low quantum efficiency because the emitters tend to be closely packed in the EML.⁹⁴ Relatively

little attention has been paid to the synthesis of deep-blue emitters because EQEs >2% and CIE_y <0.10 in the deep-blue non-doped system are difficult to obtain simultaneously. Therefore, it is still challenging to design deep-blue emitters for reliable device performance.

In this study, we synthesized deep-blue fluorescent-emitting materials, *N,N*-diphenyl-4'-(1-phenyl-1H-benzo[d]imidazol-2-yl)biphenyl-4-amine) (**T1B**) and 4',4''-(1H-benzo[d]imidazole-1,2-diyl)*bis*(*N,N*-diphenylbiphenyl-4-amine) (**T2B**), for the development of highly efficient, non-doped FLOLEDs with deep-blue CIE coordinates, where the correlation between the device performance and the molecular packing density was investigated. FLOLEDs using sterically bulky **T2B** as an emitter without a dopant showed deep-blue emissions with a CIE_y of 0.08 and an EQE of 4.67% at 100 cd/m², which is better than the values obtained from **T1B** owing to more efficient inhibition of exciton quenching.

2. Materials and methods

2.1. Materials.

N-phenyl-*o*-phenylenediamine, 1-fluoro-2-nitrobenzene, 4-bromobenzaldehyde, 4-(diphenylamino)phenylboronic acid, *tetrakis*(triphenylphosphine) palladium, and sodium carbonate were purchased from Aldrich and used without purification.

2.2. Synthetic procedure.

2-(4-Bromophenyl)-1-phenyl-1H-benz[d]imidazole (B1). Acetic acid (20 mL) was added to a flask containing *N*-phenyl-*o*-phenylenediamine (1.50 g, 8.14 mmol) and 4-bromobenzaldehyde (1.66 g, 8.96 mmol). After the mixture was refluxed for 12 h, distilled water was added and the organic layer was extracted with dichloromethane. The organic layer was washed with sodium bicarbonate and brine and dried using anhydrous sodium sulfate. The filtrate was concentrated in vacuo to give a crude mixture, which was then subjected to column chromatography on silica gel using ethyl acetate and hexane (v/v 1:20) as the eluent. Analytically pure 2-(4-bromophenyl)-1-phenyl-1H-benz[d]imidazole was isolated as a white solid (1.39 g, 49%). ¹H NMR (400 MHz, CDCl₃) δ 7.87 (d, *J*=8.4 Hz, 1H), 7.53~7.42 (m, 7 H), 7.35~7.21 (m, 5H). ¹³C NMR (CDCl₃, 100 MHz) δ 151.21, 142.90, 137.25, 136.75, 131.55, 130.84, 130.01, 128.90, 128.77, 127.37, 124.04, 123.58, 123.15, 119.90, 110.48. MALDI-TOF MS: calcd for C₁₉H₁₃BrN₂ 348.03, found 349.20.

***N*-(4-bromophenyl)-*N'*-2-nitroaniline.** A mixture of 1-fluoro-2-nitrobenzene (5.00 g, 35.436 mmol), 4-bromoaniline (12.19 g, 70.87 mmol), and potassium fluoride (2.57 g, 44.30 mmol) was heated at 170–180 °C for 72 h. The resulting mixture was extracted with dichloromethane, and the organic layer was washed with water and brine and dried using anhydrous sodium sulfate. The filtrate was concentrated in vacuo and was then subjected to column chromatography on silica gel using dichloromethane as the eluent. The resulting red solid was recrystallized from methanol to afford *N*-(4-bromophenyl)-*N'*-(2-nitrophenyl)amine as orange needles (3.10 g, 30%). ¹H NMR (400 MHz, CDCl₃) δ 9.37 (s, 1H), 8.19 (d, *J* = 8.6 Hz, 1H), 7.51 (d, *J* = 8.6 Hz, 2H), 7.37 (t, *J* = 7.8 Hz, 1H), 7.24~7.14 (m, 3H), 6.80 (t, *J* = 7.4 Hz, 1H). ¹³C NMR (CDCl₃, 100 MHz) δ 142.36, 137.93, 135.73,

133.50, 132.80, 126.74, 125.70, 118.40, 118.04, 115.94. MALDI-TOF MS: calcd for $C_{12}H_9BrN_2O_2$ 291.98, found 290.37.

***N*-(4-bromophenyl)-1,2-phenylenediamine.** A suspension of *N*-(4-bromophenyl)-*N'*-(2-nitrophenyl)amine (2.00 g, 6.85 mmol) and stannous chloride dihydrate (7.73 g, 34.25 mmol) in ethanol was refluxed for 24 h. The reaction mixture was concentrated in vacuo and neutralized with aqueous sodium bicarbonate solution. The resulting solution was extracted with ethyl acetate, dried using anhydrous sodium sulfate, and concentrated in vacuo to afford the crude product. The product was isolated by column chromatography on silica gel using ethyl acetate and hexane (v/v 1:3) as the eluent (1.78 g, 99%). 1H NMR (400 MHz, $CDCl_3$) δ 7.26 (d, $J = 11.4$ Hz, 2H), 7.08~7.01 (m, 2H), 6.80~6.73 (m, 2H), 6.58 (d, $J = 8.2$ Hz, 2H), 5.16 (s, 1H), 3.71 (s, 2H). ^{13}C NMR ($CDCl_3$, 100 MHz) δ 144.53, 142.12, 132.04, 127.70, 126.28, 125.26, 119.17, 116.62, 116.22, 110.95. MALDI-TOF MS: calcd for $C_{12}H_{11}BrN_2$ 262.01, found 262.32.

1,2-bis(4-bromophenyl)-1H-benzo[d]imidazole (B2). Acetic acid (20 mL) was added to a flask containing *N*-(4-bromophenyl)-1,2-phenylenediamine (1.0 g, 5.43 mmol) and 4-bromobenzaldehyde (1.21 g, 6.51 mmol). After the mixture was refluxed for 12 h, distilled water was added and the organic layer was extracted with dichloromethane. The organic layer was washed with aqueous sodium bicarbonate solution and brine and dried using anhydrous sodium sulfate. The filtrate was concentrated in vacuo to give a crude mixture, which was then subjected to column chromatography on silica gel using ethyl acetate and hexane (v/v 1:6) as the eluent to afford analytically pure 1,2-bis(4-bromophenyl)-1H-benzo[d]imidazole (1.11 g, 47%). 1H NMR (400 MHz, $CDCl_3$) δ 7.86 (d, $J = 7.8$ Hz, 1H), 7.63 (d, $J = 7.9$ Hz, 2H), 7.43 (dd, $J = 8, 12$ Hz, 4H), 7.34 (t, $J = 7$ Hz, 1H), 7.32~7.16 (m, 4H). ^{13}C NMR

(CDCl₃, 100 MHz) δ 151.09, 142.95, 136.91, 135.78, 133.29, 131.74, 130.83, 128.87, 128.57, 124.29, 123.82, 123.40, 122.65, 120.08, 110.22. MALDI-TOF MS: calcd for C₁₉H₁₂Br₂N₂ 425.94, found 427.23.

N,N-diphenyl-4'-(1-phenyl-1H-benzo[d]imidazol-2-yl)biphenyl-4-amine

(T1B). A mixture of compound B1 (0.70 g, 2.00 mmol), 4-(diphenylamino)phenylboronic acid (0.70 g, 2.40 mmol), *tetrakis*(triphenylphosphine)palladium (0.12 g, 0.10 mmol), and aqueous sodium carbonate (2 M, 10 mL) in tetrahydrofuran (40 mL) and methanol (10 mL) was heated to reflux in a nitrogen atmosphere for 24 h. After the reaction mixture was concentrated in vacuo, the resulting mixture was extracted with dichloromethane. The organic layer was washed with water and brine and dried using anhydrous sodium sulfate. The filtrate was concentrated in vacuo to give a crude mixture, which was then subjected to column chromatography on silica gel using dichloromethane and hexane (v/v 1:1) as the eluent to afford analytically pure *N,N*-diphenyl-4'-(1-phenyl-1H-benzo[d]imidazol-2-yl)biphenyl-4-amine as a yellow solid (0.78 g, 76%). ¹H NMR (400 MHz, CDCl₃) δ 7.88 (d, *J* = 8 Hz, 1H), 7.61 (d, *J* = 8.4 Hz, 2H), 7.52 (d, *J* = 8 Hz, 4H), 7.45 (d, *J* = 8.8 Hz, 2H), 7.35 (d, *J* = 7.8 Hz, 2H), 7.27~7.23 (m, 8H), 7.10 (dd, *J* = 8.8, 2 Hz, 6H), 7.02 (t, *J* = 7.2 Hz, 2H). ¹³C NMR (CDCl₃, 100 MHz) δ 152.18, 147.65, 147.51, 141.39, 137.29, 137.09, 133.66, 129.89, 129.79, 129.28, 128.57, 127.62, 127.47, 127.24, 124.53, 123.62, 123.28, 123.09, 122.98, 119.75, 110.38. MALDI-TOF MS: calcd for C₃₇H₂₇N₃ 513.22 g/mol, found 513.26 g/mol. HRMS (FAB⁺) [M+H: C₃₇H₂₈N₃]: calcd for 514.2283, found 514.2283. Anal. Calcd. For C₃₇H₂₇N₃: C, 86.52; H, 5.30; N, 8.18. Found: C, 86.05; H, 5.18; N, 8.11.

4',4''-(1H-benzo[d]imidazole-1,2-diyl)bis(N,N-diphenylbiphenyl-4-amine)

(T2B). Using an approach similar to that used for the synthesis of T1B by the Suzuki

coupling reaction, a white powder was obtained (0.65 g, 74%). ^1H NMR (400 MHz, CDCl_3) δ 7.89 (d, $J = 8.4$ Hz, 1H), 7.70 (d, $J = 8.4$ Hz, 2H), 7.66 (d, $J = 8.4$ Hz, 2H), 7.52 (dd, $J = 8.4$, 2 Hz, 4H), 7.46 (d, $J = 8.4$ Hz, 2H), 7.38 (d, $J = 8.4$ Hz, 2H), 7.34~7.23 (m, 11H), 7.17~7.09 (m, 12H), 7.03 (q, $J = 8.4$ Hz, 4H). ^{13}C NMR (CDCl_3 , 100 MHz) δ 152.19, 147.85, 147.65, 147.51, 147.48, 143.09, 141.40, 140.81, 137.32, 135.59, 133.67, 133.17, 129.83, 129.34, 129.28, 128.20, 127.78, 127.72, 127.63, 126.28, 124.61, 124.52, 123.62, 123.28, 123.21, 123.08, 122.99, 119.78, 110.46. MALDI-TOF MS: calcd for $\text{C}_{55}\text{H}_{40}\text{N}_4$ 756.33 g/mol, found 756.77 g/mol. HRMS (FAB $^+$)[M+H: $\text{C}_{55}\text{H}_{41}\text{N}_4$]: calcd for 757.3331, found 757.3331. Anal. Calcd. For $\text{C}_{55}\text{H}_{40}\text{N}_4$: C, 87.27; H, 5.33; N, 7.40. Found: C, 86.72; H, 5.28; N, 7.30.

2.3. Measurements.

^1H and ^{13}C NMR spectra were recorded using an Agilent 400 MHz Varian spectrometer in CDCl_3 . ^1H NMR chemical shifts in CDCl_3 were referenced to CHCl_3 (7.27 ppm) and ^{13}C NMR chemical shifts in CDCl_3 were reported relative to CHCl_3 (77.23 ppm). UV-visible spectra were recorded on a Beckman DU650 spectrophotometer. Fluorescence spectra were recorded on a Jasco FP-6500 spectrophotometer. The fluorescent quantum yield in the solid film was recorded on an Otsuka electronics QE-2000 spectrophotometer. For time-resolved PL spectroscopy, we employed excitation light sources as a femtosecond pulsed Ti:sapphire laser for a prompt component and a nanosecond pulsed Nd:YAG laser for a delayed component, and a monochromator-attached photomultiplier tube was used as an optical detection system. Mass spectra were obtained using matrix-assisted laser desorption-ionization time-of-flight mass spectrometry (MALDI-TOF MS) from Bruker. High-resolution masses were measured by either

fast atom bombardment (FAB) or electron ionization (EI) using a JEOL HP 5890 series. Analytical thin-layer chromatography was performed using Kieselgel 60F-254 plates from Merck. Column chromatography was carried out on Merck silica gel 60 (70~230 mesh). All solvents and reagents were commercially available and used without further purification unless otherwise noted. Decomposition temperatures (T_d) and glass transition temperatures (T_g) were obtained using Q-5000-IR thermogravimetric analysis (TGA) and DSC-Q-1000 differential scanning calorimetry (DSC), respectively. The TGA and DSC analyses were performed at $10\text{ }^\circ\text{C min}^{-1}$ under a nitrogen atmosphere. T_g was determined from the third heating scan. The electrochemical properties of **T1B** and **T2B** were studied using cyclic voltammetry (CV) in CH_2Cl_2 solutions (1.00 mM) with 0.1 M tetra-n-butylammoniumhexafluorophosphate (TBAPF_6) as the supporting electrolyte. A glassy carbon electrode was employed as the working electrode and referenced to a Ag reference electrode. All potential values were calibrated against the ferrocene/ferrocenium (Fc/Fc^+) redox couple. The onset potential was determined from the intersection of two tangents drawn at the rising and background current of the cyclic voltammogram.

2.4. Computational calculation.

The optimized geometries and frontier molecular orbital energy levels for **T1B** and **T2B** were obtained using density functional theory (DFT) calculations with the Gaussian '09 program package. The geometries were optimized using the Becke 3-parameter Lee-Yang-Parr (B3LYP) functional with the 6-311G-level atomic basis set.

2.5. Deep-blue FLOLEDs fabrication and electro-optical characterization.

N,N'-di(1-naphthyl)-*N,N'*-diphenylbenzidine (NPB), 4,4',4''-tris(*N*-carbazolyl)triphenylamine (TCTA), and 1,3,5-tris(*N*-phenylbenzimidazol-2-yl)benzene (TPBI) were purchased from commercial sources and used without purification. Fabrication of organic light-emitting diodes (OLEDs) was conducted through high-vacuum (2×10^{-6} Torr) thermal evaporation of the organic materials onto indium tin oxide (ITO)-coated glass (sheet resistance: 15 Ω /square; Applied Film Corp.). Glass substrates with patterned ITO electrodes were washed with isopropyl alcohol and then cleaned through O₂ plasma treatment. OLED devices were fabricated with a configuration of ITO/NPB/TCTA/T1B or T2B/TPBI/LiF/Al. NPB and TCTA as hole transporting layers, TPBI as an electron transporting layer, LiF and Al electrodes were deposited on the substrate in the order of sequence. The emission properties were determined using a PR-650 SpectraScan SpectraColorimeter as a source meter. Current-voltage characteristics were measured using a programmable electrometer equipped with current and voltage sources (Keithley 2400).

3. Results and Discussion

3.1. Computational calculation.

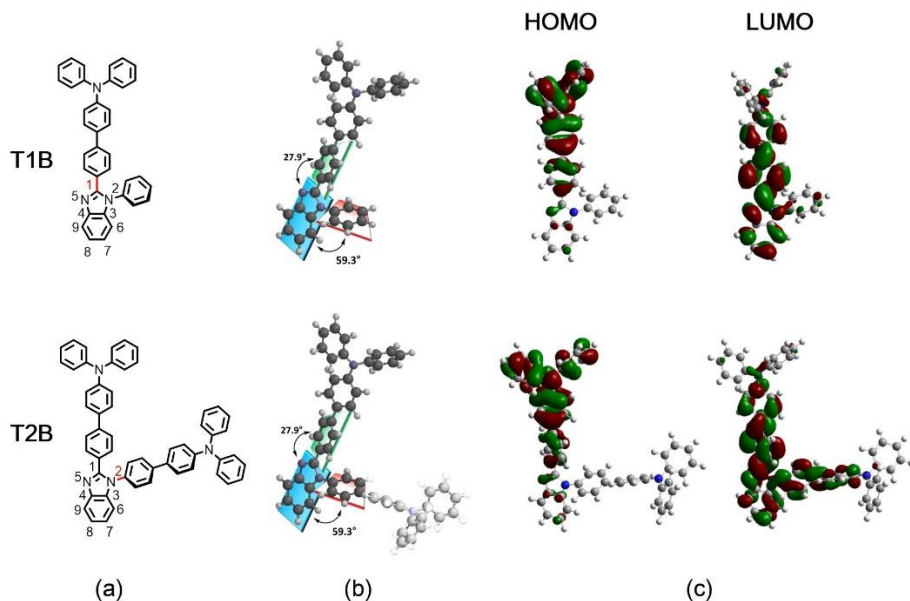


Figure 1. DFT calculations of **T1B** and **T2B** were performed at B3LYP/6-311G level: (a) chemical structures, (b) three-dimensional optimized geometries, and (c) HOMO and LUMO electron density map.

To predict the optimized geometries and frontier molecular orbital energy levels for **T1B** and **T2B**, DFT calculations were carried out with the B3LYP/6-311G level using Gaussian '09. The highest occupied molecular orbital (HOMO) and lowest unoccupied molecular orbital (LUMO) distributions of **T1B** and **T2B** are shown in Figure 1. The HOMO of **T1B** and **T2B** was localized on the triphenylamine (TPA) unit, whereas the LUMO of **T1B** and **T2B** was dispersed over the benzimidazole (BI) unit. DFT analysis indicates that the HOMO and LUMO energy levels of **T1B** and **T2B** are similar (5.23 eV and 1.60 eV, respectively, for T1B; 5.21 eV and 1.58 eV, respectively, for T2B).⁹⁵

DFT analysis of the molecular conformation revealed that the phenyl ring at the 1-position of BI was twisted with respect to the BI plane, with a dihedral angle of 27.9° , whereas the phenyl ring at the 2-position of BI was twisted with respect to the BI plane with a dihedral angle of 59.3° . Furthermore, the conjugation length of **T2B** was similar to that of **T1B** because the phenyl moiety at the 2-position of BI was almost perpendicular to the TPA moiety, thereby increasing the steric bulkiness in **T2B** as compared to **T1B**. In general, bulky, nonplanar structures suppress the molecular packing through steric hindrance, thus decreasing charge carrier transport and excimer formation. Therefore, relative bulky structure in **T2B** makes it possible to have higher efficiency than **T1B**.^{47, 82, 95-96}

3.2. Synthesis

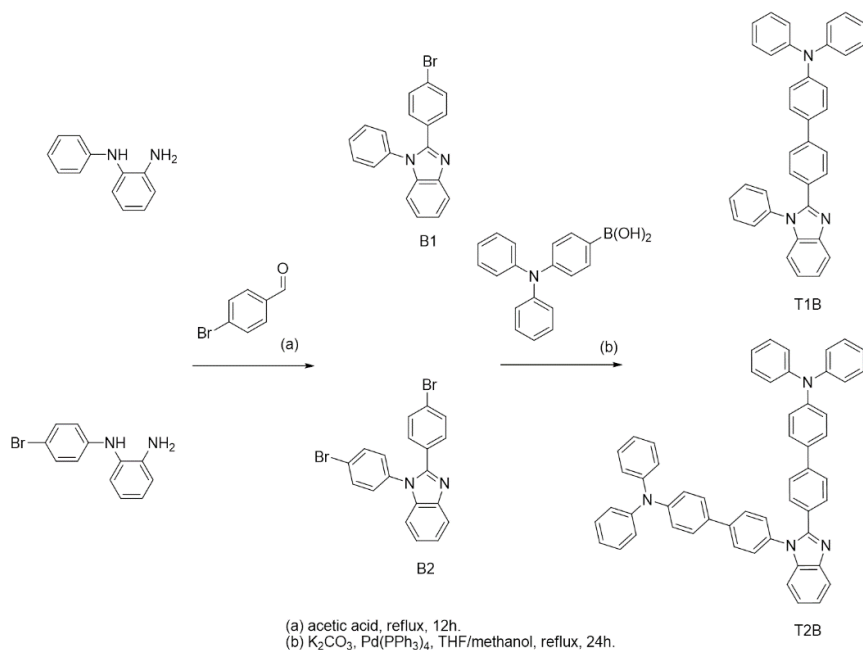


Figure 2. Synthetic routes of **T1B** and **T2B**.

The synthetic routes and molecular structures of **T1B** and **T2B** are illustrated in Figure 2. **T1B** and **T2B** comprise two main components: TPA as the donor moiety and BI as the acceptor moiety; these two components were connected through a phenyl linkage by the Suzuki coupling reaction.⁹⁷⁻⁹⁸ In **T1B**, the TPA unit was directly linked to the *para* position of the 2-phenyl moiety of 1,2-diphenylbenzimidazole. However, in **T2B**, the two TPA units were attached to the *para* positions of the two pendant phenyl moieties of 1,2-diphenylbenzimidazole, which would suppress exciton quenching by limited molecular packing owing to the more bulky three-dimensional structure. Synthetic yields of the Suzuki reactions leading to **T1B** and **T2B** were 76% and 74%, respectively, after purification by column chromatography and vacuum sublimation. **T1B** and **T2B** were characterized by ¹H NMR, ¹³C NMR, and low- and high-resolution mass spectrometry.

3.3. Thermal properties

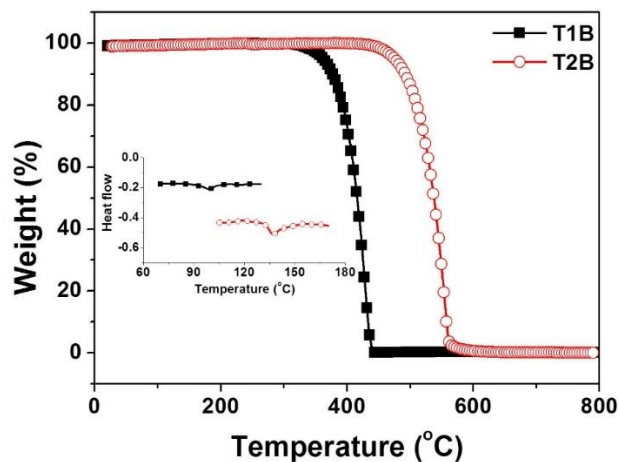


Figure 3. TGA thermograms of **T1B** and **T2B** (inset: DSC analysis of **T1B** and **T2B**).

The thermal properties of **T1B** and **T2B** were investigated with TGA and DSC (Figure 3). T_d , defined as the temperature at which 5% mass loss occurs, was measured by TGA. The T_d values of **T1B** and **T2B** were 362 and 475 °C, respectively, whereas their T_g values were 97 and 137 °C, respectively. T_g of **T2B** was increased by 40 °C by the additional TPA unit. This indicates that a **T2B** emitter would be much better than a **T1B** emitter in terms of thermal stability.⁹⁹

3.4. Photophysical properties

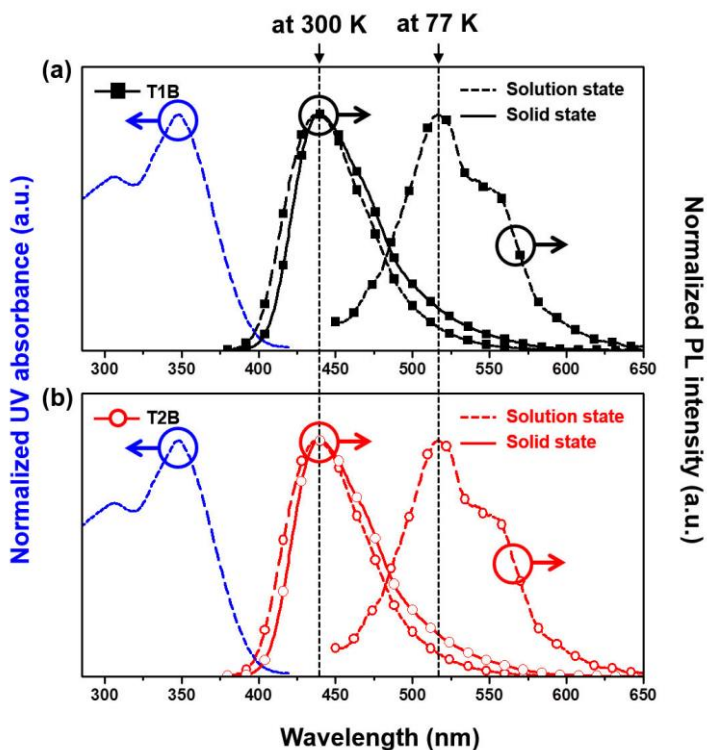


Figure 4. UV-vis absorption and photoluminescence (PL) spectra of (a) **T1B** and (b) **T2B**. (Dashed lines perpendicular to the x-axis correspond to λ_{\max} of PL spectra.)

Figure 4 depicts the normalized UV-vis absorbance (at 300 K) and photoluminescence (PL) spectra (at 300 K and 77 K) of **T1B** and **T2B**. The absorption bands around 300 nm for **T1B** and **T2B** originate from the TPA-centered $n-\pi^*$ transition.⁹⁵ The absorption bands around 350 nm are attributed to the intramolecular charge-transfer transition from the electron-donating TPA moiety to the electron-accepting BI moiety.^{95, 100-101} The absorption edges of the UV-vis spectra were found to be 420 nm, which corresponds to the optical bandgap of 2.95 eV. From the optical bandgap and the HOMO energy level of 5.33 eV estimated from CV, LUMO energy level was calculated to be 2.38 eV (Figure 5)

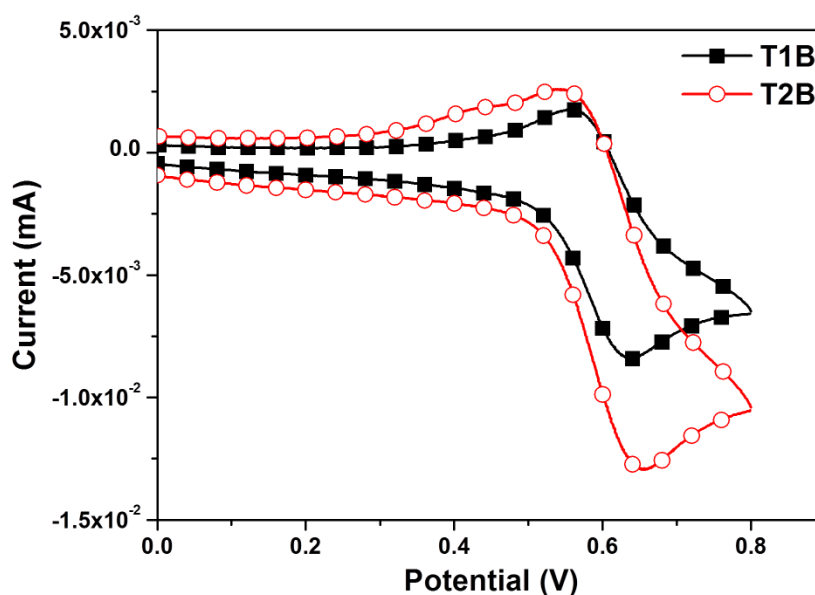


Figure 5. Cyclic voltammogram of T1B and T2B.

The PL λ_{max} peaks of **T1B** and **T2B** were observed around 440 nm without any vibration peaks. Although an extra TPA unit was introduced at the *para* position of the pendant 2-phenyl group in **T2B**, the emission spectra of **T1B** and **T2B** display the identical maxima in both the solution and the solid states. These results demonstrate that the additional TPA moiety connected to the *para* position of the pendant 2-phenyl group does not contribute to the extension of the conjugation length.⁴⁷ The nonplanar structures of **T1B** and **T2B** facilitate their use as emitters in non-doped deep-blue FLOLEDs owing to the efficient inhibition of π - π stacking in the film state by vapor deposition.

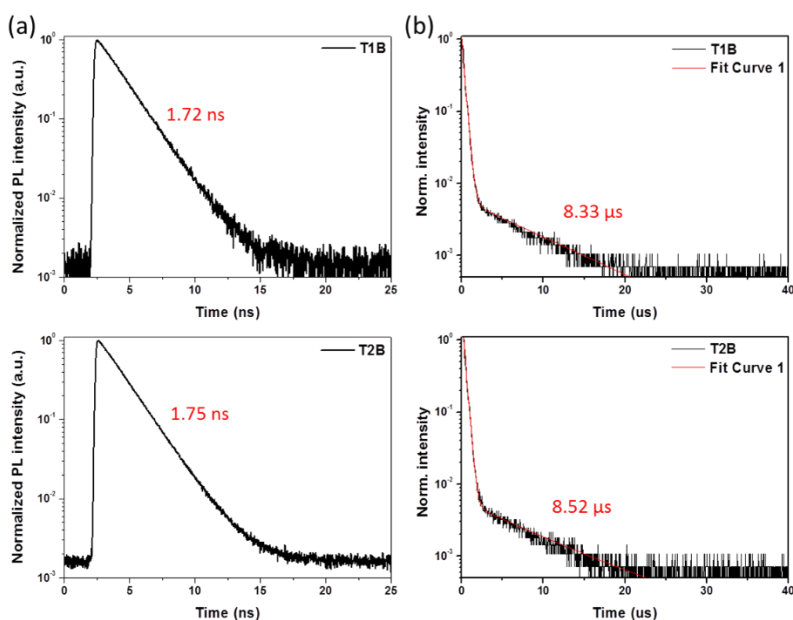


Figure 6. Transient PL decay lifetime of **T1B** and **T2B** (a) prompt and (b) delayed fluorescence.

On going from singlet (300 K) to triplet (77 K) states in PL spectra, a red-shift of 80 nm for **T1B** and 79 nm for **T2B** is observed, indicating the energy gap between the lowest excited singlet state and the lowest excited triplet state (ΔE_{ST}) of 0.44 and 0.43 eV, respectively. It has been known that a small ΔE_{ST} in aromatic organic compounds would facilitate the reverse intersystem crossing (RISC) even without heavy metals.^{2, 5, 102-103} These ΔE_{ST} values predict that the surrounding thermal energies may enable RISC in **T1B** and **T2B**, which could contribute to the increased device efficiency over the intrinsic limitations of fluorescent device performances. We investigated the emission lifetime of **T1B** and **T2B** by using transient PL decay measurement in order to evaluate the possibility of RISC in terms of delayed fluorescence (Figure 6). In general, PL decay lifetime is divided into prompt fluorescence (fast decay component) and delayed fluorescence (slow decay component). PL decay lifetime of **T1B** and **T2B** are 1.72 ns and 1.75 ns for prompt fluorescence, and 8.33 μ s and 8.52 μ s for delayed fluorescence, respectively. Therefore, it is clear from this data that the delayed fluorescence originates from the RISC process despite the relatively large of ΔE_{ST} in **T1B** and **T2B**.

The photoluminescence quantum yields (PLQY) of **T1B** and **T2B** in solution were measured to be 0.72 and 0.66, respectively, using 9,10-di(naphth-2-yl)anthracene (ADN, 0.57) as a reference at room temperature.¹⁰⁴ The PLQY of **T1B** and **T2B** are 0.50 and 0.60 in the solid state, respectively. The reduction value of **T1B** PLQY is 30.6 %, whereas only 9.1 % for **T2B**. These results indicated that **T2B** suppress exciton quenching by limited molecular packing owing to the structure hindrance compared to **T1B**.

3.5. Electroluminescence properties.

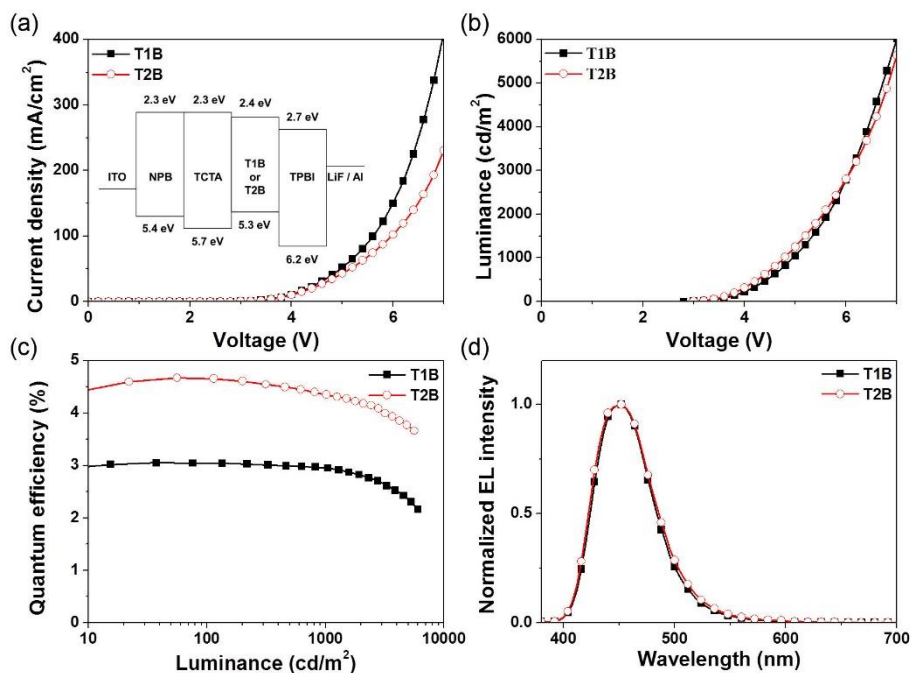


Figure 7. Device performance of deep-blue FLOLEDs with **T1B** and **T2B**. (a) current density–voltage characteristics (inset: energy level diagram of the FLOLEDs), (b) luminance–voltage characteristics, (c) quantum efficiency–luminance characteristics and (d) electroluminescence spectra.

Non-doped FLOLEDs were fabricated using **T1B** and **T2B** as deep-blue fluorescent emitters in the EML, with a device configuration of ITO/NPB (40 nm)/TCTA (20 nm)/EML (**T1B** or **T2B**, 40 nm)/TPBI (20 nm)/LiF (1 nm)/Al (100 nm). Two different blue FLOLEDs, one using **T1B** and the other using **T2B** as a deep-blue emitter, were fabricated and the performance of each device was evaluated (Table 1).

Table 1. Electroluminescence (EL) device performance of T1B and T2B.

At 100 cd/m ²	Current density (mA/cm ²)	Quantum efficiency (%)	CIE (x, y)	EL λ_{\max} (nm)
T1B	5.12	3.05	0.15, 0.08	452
T2B	3.13	4.67	0.15, 0.08	452

Figure 7(a) shows current density–voltage characteristics of deep-blue fluorescent devices with **T1B** and **T2B**. The current density of the device with **T1B** was higher than that of the device with **T2B**, whereas the luminance values of the two devices with **T1B** and **T2B** emitters are similar at the same driving voltage as shown in Figure 7(b). The current density mainly depends on the differences in the energy levels of the organic thin layers in OLEDs.^{23, 105-106} Despite little difference in the energy levels of both deep-blue emitters, there is a discrepancy in the current densities at the same voltage. It is known that efficient packing of semiconductor molecules usually facilitates better current flow through the devices.⁹⁵ Thus, the alternation of the packing densities in the solid films derived from the structurally different **T1B** and **T2B** would result in different current densities; the current density of the device with the structurally less bulky **T1B** was higher than that of the device with the structurally more bulky **T2B**. These results are consistent with our simulation using DFT calculations. Unlike the current density characteristics of **T1B**- and **T2B**-based devices, similar luminance values of the two devices indicate that exciton formation and light emission are more efficient in **T2B**-based devices (Figure 7(b)).

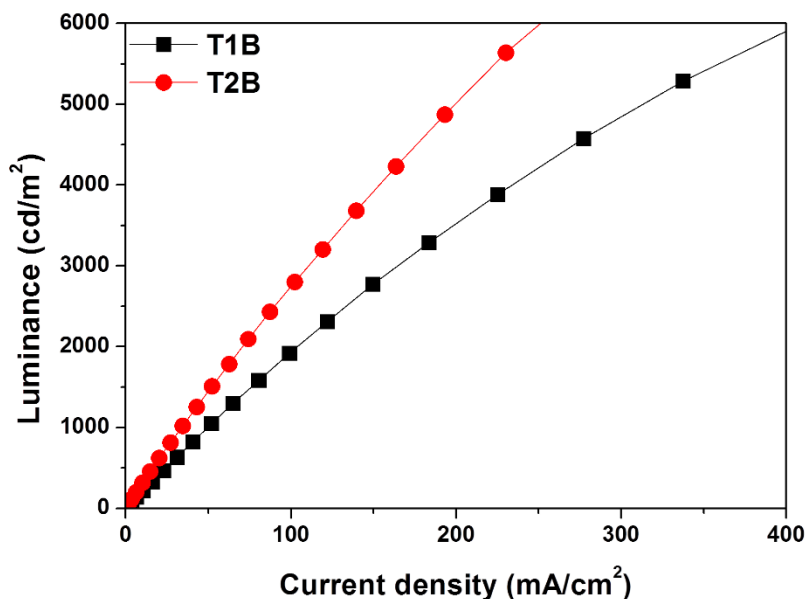


Figure 8. Luminance-current density characteristics of **T1B** and **T2B** as deep-blue fluorescent emitters in the EML with a device configuration of ITO/NPB (40 nm)/TCTA (20 nm)/EML (**T1B** or **T2B**, 40 nm)/TPBI (20 nm)/LiF (1 nm)/Al (100 nm).

Quantum efficiency–luminance of two devices was plotted in Figure 7(c) based on current density and luminance of devices. The **T2B**-based device shows a better maximum EQE of 4.67% compared with that of 3.05 % of the **T1B**-based device at 100 cd/m². In the case of **T2B**-based devices, EQE is about 1.4 times higher than the theoretical maximum EQE of about 3.3%, assuming that the EL quantum efficiency is the same as the PL quantum efficiency of 66%. Relatively high EQEs of the **T1B**- and **T2B**-based devices are attributed to thermally activated delayed fluorescence (TADF) by RISC that converts triplet excitons into singlet excited states.⁵⁻⁶ Recent researches proposed that two possible mechanisms for such an

unusual increase in EQE are the triplet–triplet annihilation (TTA) and the TADF.^{56, 107} For the TTA, the luminance is known to increase more than linearly along with the increase of current density¹⁰⁸, whereas in terms of TADF gradient slope appears a linear increase or less in luminance-current density curve (characteristics)¹⁰³ and/or a fluorescent molecule has sufficient spatially separated HOMO and LUMO.⁵ In this research, the gradient slope of the luminance showed linearly at very low current density, and then the change in the luminance appeared with the tendency of saturation at high current density in Figure 8. Consequently, enhanced efficiency by delayed fluorescence is not from TTA but from TADF. In addition, as expected from the molecular packing density of DFT simulations, the **T2B**-based device has relatively fewer sites for exciton recombination with respect to molecular concentrations, resulting in a smaller exciton density as compared to the **T1B**-based device. However, concentrated excitons caused by more efficient packing would be more easily quenched in **T1B**. Therefore, the device performance based on **T2B** is superior to that of **T1B**-based devices.

Figure 7(d) shows normalized EL spectra of the deep-blue fluorescent devices. A blue emission with a peak wavelength at 452 nm, which originated from the singlet excitons of blue emitters without any other emission from the adjacent layers, was observed in all devices. The EL spectra are essentially stable against changes in the molecular structure.

4. Conclusion

Two triphenylamine-attached benzimidazole derivatives (**T1B** and **T2B**) were designed and synthesized for use as deep-blue emitters in efficient non-doped

FLOLEDs. The fluorescent devices fabricated using T2B exhibited a high EQE of 4.67%, which is 1.4 times higher than the theoretical maximum EQE of 3.3%, along with the CIE coordinates of (0.15, 0.08). Considering the high color purity of the blue emission, **T2B** affords high EQE among the non-doped FLOLEDs. This study demonstrates a good example of the fact that the limited molecular packing density of the emitter suppresses the exciton quenching, thereby increasing the EQE in the non-doped FLOLEDs.

Section 3 Development of multifunctional materials for OLEDs using triphenylamine-quinoline, quinoxaline and quinazoline hybrid compounds for deep blue fluorescent emitters and host materials

Abstract

Three bipolar materials by triphenylamine donor attached quinoline, quinoxaline and quinazoline acceptor: N,N-diphenyl-4-(quinolin-2-yl)aniline (**QT**), N,N-diphenyl-4-(quinoxalin-2-yl)aniline (**XT**) and N,N-diphenyl-4-(quinazolin-4-yl)aniline (**ZT**) were synthesized for blue fluorescent emitting materials. Among them, **QT** based blue OLEDs show maximum EQE of 4.0% and 3.1%, with a CIE color coordinates of (0.146, 0.079) and (0.153, 0.054), in non-doped and doped in mCBP using as host material, respectively. Furthermore, **QT** exhibits excellent host performance with comparable to mCBP host in **XT** and **ZT** using as a dopant based devices.

Keywords: Multifunctional material, bipolar property, quinoline, quinoxaline, quinazoline.

1. Introduction

Since low-voltage, bright, and efficient organic light-emitting diodes (OLEDs) were realized by Tang's report on tris(8-hydroxyquinoline)aluminum (Alq₃)-based multilayer devices thirty years ago⁵⁴, OLEDs have been developed for many possibilities as future displays, from smart phones to large flat panel displays.¹⁵⁻¹⁶

The emitting materials were used only for an unipolar property like hole transporting (HT)³⁰⁻³⁴ or electron transporting (ET)³⁵⁻⁴⁰ in early OLEDs. These materials show the irreversible behaviors of electrochemical reactions and instability in cationic or anionic environments. For these reasons, unipolar emitting materials act not only as fluorescence quenchers, but also as charge traps, causing a significant decrease in the luminescence efficiency.^{97, 109} Therefore, emitting materials have evolved to possess bipolar property to permit for the formation of both stable cation and anion radicals that both HT and ET characteristics and matching the energy level for charge injection with adjacent layers.⁴³⁻⁴⁸ Since the charge-carrier transport in small molecules is a linkage of redox processes between the neutral molecules and the corresponding radical ions, electron-donating and electron-withdrawing moieties should have the potential ability to injection and transport both carriers. The most widely adopted strategy for obtaining bipolar properties is to incorporate donor-acceptor combinations in the same molecule, facilitating inject and transport of both holes and electrons. An improved performance and operational stability have been demonstrated in devices using bipolar materials as the light emitting layer.

Recently, bipolar non-doped blue-emitting materials (CIE_y < 0.10) based on organic molecules with balanced carrier-transport properties have drawn considerable attention due to their facile synthesis and low cost.^{49-50, 52} Aimed at developing efficient hosts for green and blue OLEDs as well as using them as non-

doped deep-blue fluorescent emitters, we designed and synthesized three bipolar materials by triphenylamine donor attached quinoline, quinoxaline, and quinazoline acceptor: N,N-diphenyl-4-(quinolin-2-yl)aniline (**QT**), N,N-diphenyl-4-(quinoxalin-2-yl)aniline (**XT**) and N,N-diphenyl-4-(quinazolin-4-yl)aniline (**ZT**). The three synthesized compounds show bipolar characteristic behavior because the N atom in the triphenylamine (TPA) unit acts as an electron-rich core while the N atom in the quinoline, quinoxaline, and quinoxaline unit acts as an electron withdrawing core. Their energy levels for the highest occupied molecular orbital (HOMO) and the lowest unoccupied molecular orbital (LUMO) are tuned by the number and orientations of nitrogen atoms, improving bipolarity and control emission color. **QT** based blue OLEDs show maximum EQEs of 4.0% and 3.1%, with CIE color coordinates of (0.146, 0.079) and (0.153, 0.054), in non-doped and doped in mCBP using as host material, respectively. Meanwhile, **QT** exhibits excellent host performance comparable to mCBP host in **XT** and **ZT** using dopant based devices.

2. Materials and general methods

2.1. Materials

All solvents and materials were used as received from commercial suppliers without further purification. Synthetic routes to **QT**, **XT**, and **ZT** are outlined in Scheme 1. The two final products (**QT**, **XT**, and **ZT**) were purified by temperature gradient vacuum sublimation.

2.2. Synthetic procedure

N,N-diphenyl-4-(quinolin-2-yl)aniline (QT). A mixture of A mixture of 2-chloroquinoline (0.70g, 4.28 mmol), 4-(diphenylamino)phenylboronic acid (1.36 g, 4.71 mmol), tetrakis(triphenylphosphine)palladium (0.25 g, 0.21 mmol), and aqueous sodium carbonate (2 M, 15 mL) in tetrahydrofuran (60 mL) and methanol (15 mL) was heated to reflux in a nitrogen atmosphere for 24 h. After the reaction mixture was concentrated in vacuo, the resulting mixture was extracted with dichloromethane. The organic layer was washed with water and brine and dried using anhydrous sodium sulfate. The filtrate was concentrated in vacuo to give a crude mixture, which was then subjected to column chromatography on silica gel using ethylacetate and hexane (v/v 1:9) as the eluent to afford analytically pure N,N-diphenyl-4-(quinolin-2-yl)aniline as a yellow solid (1.29 g, 81%). ¹H NMR (300 MHz, CDCl₃): δ (ppm) 8.19 (d, *J* = 8.6 Hz, 2H), 8.07 (d, *J* = 8.6 Hz, 2H), 7.83 (m, *J* = 7.2 Hz, 2H), 7.73 (t, *J* = 7.2 Hz, 1H), 7.52 (t, *J* = 7.5 Hz, 1H), 7.31 (t, *J* = 8.0 Hz, 5H), 7.20 (t, *J* = 9.0 Hz, 5H), 7.09 (t, *J* = 7.2 Hz, 2H). ¹³C NMR (CDCl₃, 75 Hz): δ (ppm) 160.98, 156.85, 147.34, 136.79, 129.68, 129.32, 128.50, 127.40, 127.11, 126.90, 125.99, 124.86, 123.38, 123.03, 118.65.

N,N-diphenyl-4-(quinoxalin-2-yl)aniline (XT). A mixture of A mixture of 2-chloroquinoxaline (0.60g, 3.65 mmol), 4-(diphenylamino)phenylboronic acid (1.16 g, 4.01 mmol), tetrakis(triphenylphosphine)palladium (0.21 g, 0.18 mmol), and aqueous sodium carbonate (2 M, 12 mL) in toluene (30 mL) and ethanol (12 mL) was heated to reflux in a nitrogen atmosphere for 24 h. After the reaction mixture was concentrated in vacuo, the resulting mixture was extracted with dichloromethane. The organic layer was washed with water and brine and dried using anhydrous sodium sulfate. The filtrate was concentrated in vacuo to give a crude mixture, which was then subjected to column chromatography on silica gel using dichloromethane

and hexane (v/v 1:2) as the eluent to afford analytically pure N,N-diphenyl-4-(quinoxalin-2-yl)aniline as a yellow solid (0.66 g, 48%). ¹H NMR (300 MHz, CDCl₃): δ (ppm) 9.30 (s, 1H), 8.12 (dd, *J* = 7.8, 6.3 Hz, 4H), 7.75 (m, 2H), 7.33 (t, *J* = 8.0 Hz, 4H), 7.21 (t, *J* = 8.0 Hz, 6H), 7.12 (t, *J* = 7.2 Hz, 2H). ¹³C NMR (CDCl₃, 75 Hz): δ (ppm) 151.37, 149.95, 147.02, 143.12, 141.09, 130.25, 129.45, 129.35, 129.27, 129.03, 129.00, 128.47, 125.25, 123.86, 122.44.

N,N-diphenyl-4-(quinazolin-2-yl)aniline (ZT). A mixture of A mixture of 4-chloroquinazoline (0.80g, 4.86 mmol), 4-(diphenylamino)phenylboronic acid (1.99 g, 5.35 mmol), tetrakis(triphenylphosphine)palladium (0.28 g, 0.24 mmol), and aqueous sodium carbonate (2 M, 16 mL) in toluene (40 mL) and ethanol (16 mL) was heated to reflux in a nitrogen atmosphere for 24 h. After the reaction mixture was concentrated in vacuo, the resulting mixture was extracted with dichloromethane. The organic layer was washed with water and brine and dried using anhydrous sodium sulfate. The filtrate was concentrated in vacuo to give a crude mixture, which was then subjected to column chromatography on silica gel using ethylacetate and hexane (v/v 1:9) as the eluent to afford analytically pure N,N-diphenyl-4-(quinoxalin-2-yl)aniline as a yellow solid (0.84 g, 46%). ¹H NMR (300 MHz, CDCl₃): δ (ppm) 9.35 (s, 1H), 8.29 (d, *J* = 8.3 Hz, 1H), 8.14 (d, *J* = 8.4 Hz, 1H), 7.93 (t, *J* = 7.1 Hz, 1H), 7.73 (d, *J* = 8.6 Hz, 2H), 7.65 (t, *J* = 8.1 Hz, 1H), 7.35 (t, *J* = 8 Hz, 5H), 7.23 (d, *J* = 8.5 Hz, 5H), 7.14 (t, *J* = 7.2 Hz, 2H). ¹³C NMR (CDCl₃, 75 Hz): δ (ppm) 167.82, 154.12, 150.15, 146.93, 133.80, 131.39, 129.51, 128.47, 127.66, 127.30, 126.24, 125.42, 125.31, 124.05, 122.93, 121.63.

2.3. General methods

^1H - and ^{13}C -NMR spectra were recorded using an Agilent 400 MHz Varian spectrometer in CDCl_3 . ^1H -NMR chemical shifts in CDCl_3 were referenced to CHCl_3 (7.27 ppm). ^{13}C -NMR chemical shifts in CDCl_3 were reported relative to CHCl_3 (77.23 ppm). UV-visible spectra were recorded on a Beckman DU650 spectrophotometer. Fluorescence spectra were recorded on a Jasco FP-6500 spectrophotometer. Fluorescent quantum yields in the solid films were recorded on an Otsuka electronics QE-2000 spectrophotometer. Analytical thin-layer chromatography was performed using Kieselgel 60F-254 plates from Merck. Column chromatography was carried out on Merck silica gel 60 (70~230 mesh). The electrochemical properties of **QT**, **XT**, and **ZT** were studied using cyclic voltammetry (CV) in CH_2Cl_2 solutions (1.00 mM) with 0.1 M tetra-*n*-butylammonium hexafluorophosphate (TBAPF_6) as the supporting electrolyte. A glassy carbon electrode was employed as the working electrode and referenced to a Ag reference electrode. All potential values were calibrated against the ferrocene/ferrocenium (Fc/Fc^+) redox couple. The onset potential was determined from the intersection of two tangents drawn at the rising and background current of the cyclic voltammogram.

2.4. Theoretical calculations

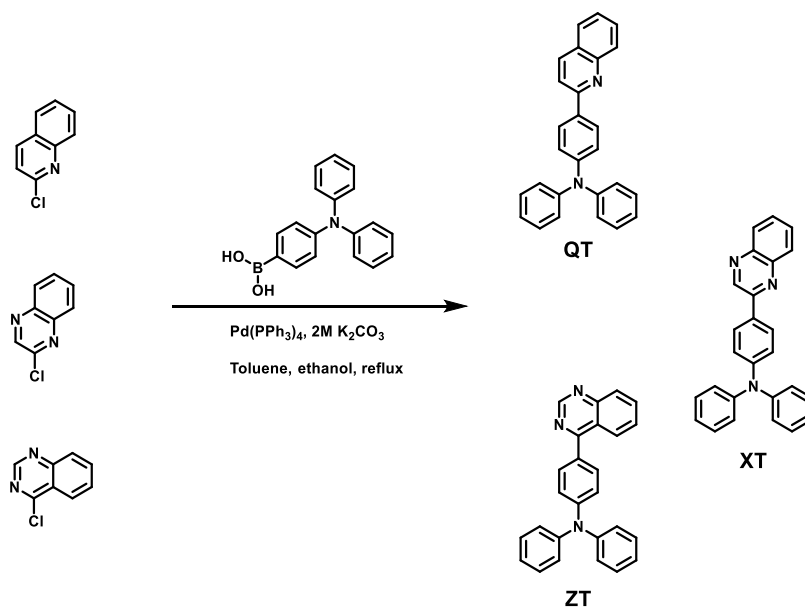
The optimized geometries and frontier molecular orbital energy levels for **QT**, **XT** and **ZT** were obtained using density functional theory (DFT) calculations with Gaussian '09. The geometries were optimized using the Becke 3-parameter Lee-Yang-Parr (B3LYP) functional with the 6-31G(d)-level atomic basis set.

2.5. Device fabrication & characterization

N,N'-Di(1-naphthyl)-N,N'-diphenyl-(1,1'-biphenyl)-4,4'-diamine (NPB), 4,4'-Cyclohexylidenebis[N,N-bis(4-methylphenyl)benzenamine] (TAPC), and 1,3,5-tris(N-phenylbenzimidazol-2-yl)benzene (TPBI) were purchased from commercial sources and used without purification. The fabrication of OLEDs was conducted by the high-vacuum (2×10^{-6} Torr) thermal evaporation of the organic materials onto indium tin oxide (ITO)-coated glass (sheet resistance: $15 \Omega/\text{square}$; Applied Film Corp.). Glass substrates with patterned ITO electrodes were washed with isopropyl alcohol and then cleaned by O_2 plasma treatment. The OLED devices were fabricated with a configuration of ITO/NPB/TAPC/EML/TPBI/LiF/Al. NPB and TAPC (hole transporting layers), TPBI (electron transporting layer), LiF (electron injection layer), and Al electrodes were deposited sequentially on the substrate. The emitting layer (EML) of non-doped devices are consist of 100% of **QT**, **XT** and **ZT**, whereas doped devices were consist of 20% of **QT**, **XT** and **ZT** as dopant materials, and mCBP or **QT** using as host materials. The emission properties were determined using a PR-650 SpectraScan SpectraColorimeter as a source meter. The current-voltage characteristics were measured using a programmable electrometer equipped with current and voltage sources (Keithley 2400).

3. Results and discussion

3.1. Synthesis



Scheme 1. Synthetic routes of **QT**, **XT**, and **ZT**.

The synthetic routes for **QT**, **XT**, and **ZT** are illustrated in Scheme 1. Each compound is comprised of two main components: TPA as the donor moiety and quinoline, quinoxaline, and quinazoline as the acceptor moiety. Synthetic yields of the Suzuki reactions leading to **QT**, **XT**, and **ZT** were 81%, 48% and 46%, respectively, after purification by column chromatography and vacuum sublimation. Finally, the synthesized compounds were characterized by ^1H NMR and ^{13}C NMR.

3.2. Theoretical calculations

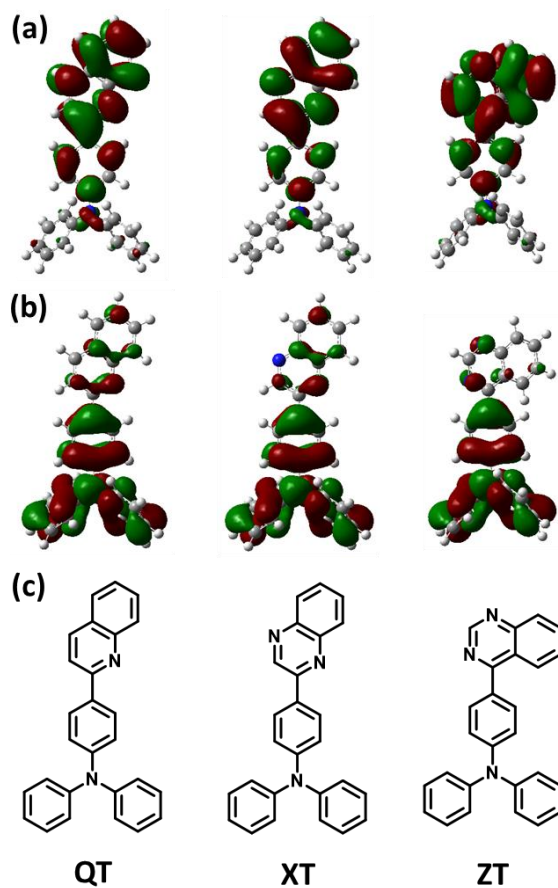


Figure 1. Optimized structures and calculated highest occupied molecular orbital and lowest occupied molecular orbital density maps obtained from DFT calculations of **QT**, **XT**, and **ZT**, performed at the B3LYP/6-31G(d) level. Electron densities of (a) LUMO and (b) HOMO with the (c) structure of each molecule.

To predict the optimized geometries and frontier molecular orbital energy levels for **QT**, **XT**, and **ZT**, DFT calculations were carried out at the B3LYP/6-31G(d) level using Gaussian '09. The highest occupied molecular orbital (HOMO)

and lowest unoccupied molecular orbital (LUMO) distributions of **QT**, **XT** and **ZT** are shown in Figure 1. The HOMOs of each compound were mainly localized on the TPA unit, whereas the LUMOs were mainly dispersed over each acceptor unit. DFT analysis indicates that **QT** has wider calculated band gap energy than those of **XT** and **ZT**. Stable LUMO of **XT** and **ZT** are predicted to be affected by strong withdrawing effect of an additional N atom in each acceptor moiety (1.76, 2.12 and 2.02 eV for **QT**, **XT**, and **ZT**, respectively). However, because additional N atom in acceptor moiety affect not only LUMO but also HOMO of **XT** and **ZT**, DFT calculation results show that electronic distribution of HOMOs are distributed from the donor moieties to some part of acceptor moieties.^{74, 110} Thus, HOMOs of **XT** and **ZT** are also more stable than that of **QT** (5.19, 5.32 and 5.39 eV for **QT**, **XT**, and **ZT**, respectively). On the basis of the combination site, two nitrogens of **XT** are located so that one is at the *ortho* position while the other is at the deactivated *meta* position, respectively. Meanwhile, both N atoms of **ZT** is located at the activated *ortho* and *para* positions.¹¹¹ Due to the π conjugation induced by lone-pair electrons of those nitrogen atoms, **ZT** predicts a smaller bandgap energy than **XT**. However, the opposite result was shown by theoretical calculation due to the acceptor part of **ZT** being more distorted than that of **XT**. The DFT analysis of the molecular conformation revealed that the dihedral angle between phenyl and 2-position of quinoxaline of **XT** is twisted about 15.6°, whereas the dihedral angle between phenyl and 4-position of quinazoline of **ZT** is twisted about 41.7°.

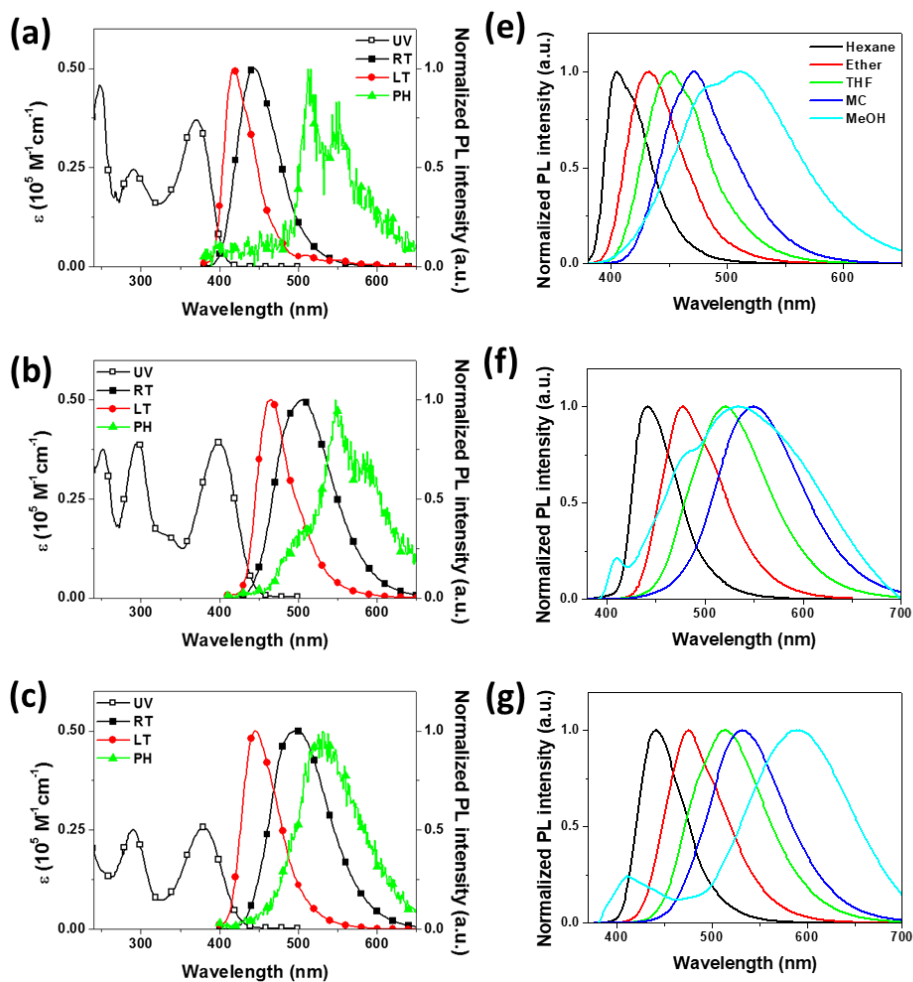


Figure 2. UV-Vis absorbance and photoluminescence of (a) **QT**, (b) **XT**, and (c) **ZT** in dichloromethane (10^{-5} M) (Black lines with open square symbols: absorption spectra, Black lines with closed square symbols: normalized photoluminescence at 300 K, green lines with closed triangle symbols: normalized photoluminescence at 77 K after 20 msec delay). Solvatochromic shift of (d) **QT**, (e) **XT** and **ZT** in various solvents (10^{-5} M).

Table 1. Physical properties of **QT**, **XT** and **ZT**.

	UV-Vis ^a (nm)	FL ^a (nm)	PH ^a (nm)	ΔE_{ST} (eV)	ϕ^a	E_g^b (nm)	HOMO _{CV} (nm)	LUMO _{cal} (nm)
QT	248, 291, 370	442	511	0.66	0.78	3.09	5.35	2.26
XT	251, 296, 399	504	547	0.59	0.85	2.86	5.39	2.53
ZT	290, 379	445	517	0.31	0.83	3.01	5.42	2.41

^a 10^{-5} M in dichloromethane solution, ^b calculated from absorption edge.

Figure 2 shows the UV-Vis absorbance and photoluminescence of each synthesized molecule and the photophysical data is summarized in Table 1. The absorption bands under 250 nm originate from the π - π^* transition of the acceptor unit and around 290 ~ 300 nm for each compound originate from the TPA-centered n- π^* transition. The absorption bands between 370 and 400 nm for each compound originate from the intramolecular charge-transfer transitions from the TPA donor to the N-contained acceptor.⁴² We also examined the PL solvatochromic shift of **QT**, **XT**, and **ZT** using various solvent at RT. Each material shows red shifted PL spectra increasing the dielectric constant. This indicates that their emissive S₁ states are dependent on the dielectric constant of solvent polarity where each molecule has bipolar characteristics.¹⁰⁹ The photoluminescence quantum yields (PLQYs) of **QT**, **XT**, and **ZT** in dichloromethane solution were measured to be 0.78, 0.85 and 0.83, respectively, using an integrating sphere.

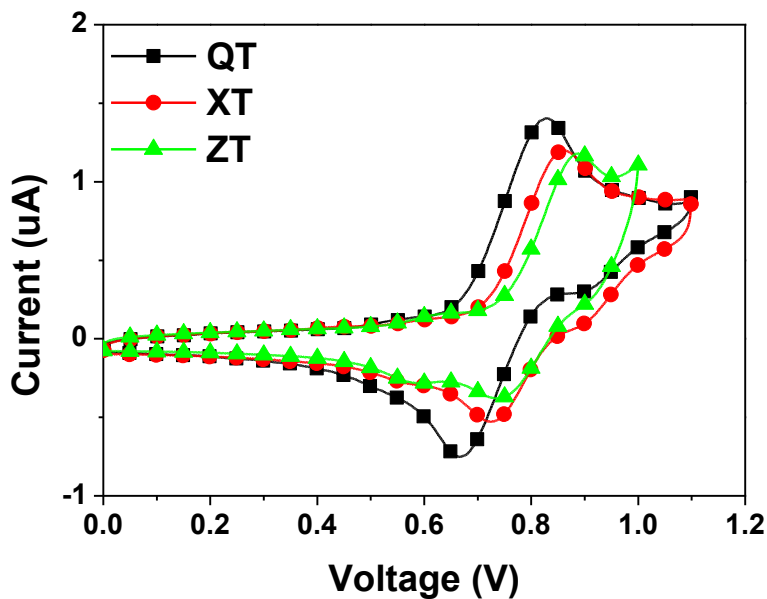


Figure 3. Cyclic voltammogram of **QT**, **XT**, and **ZT**.

The optical bandgaps of **QT**, **XT**, and **ZT** were determined by the absorption edges of the UV-Vis spectra which correspond to 3.09, 2.86, and 3.01 eV, respectively. From the optical bandgap and the HOMO energy levels 5.35, 5.39 and 5.42 eV for **QT**, **XT**, and **ZT**, respectively, estimated from CV in Figure 3, the LUMO energy levels were calculated to be 2.26, 2.53 and 2.41 eV for each compound, respectively. The PL λ_{\max} of **QT**, **XT**, and **ZT** were observed at 442, 504 and 445 nm in dichloromethane solution at 300 K (FL), respectively, which show the similar tendency as the theoretical results mentioned above. The PL λ_{\max} of each compound at a low temperature (77 K, PH) show 511, 547, and 517 nm, respectively. It is noted that **QT** and **XT** show structural emission dominated by the triplet of locally excited (LE) state characteristics, whereas **ZT** shows broad emission dominated by the triplet of a charge transfer (CT) state characteristic.¹⁰² As

mentioned above in the theoretical calculation part, **ZT** has more distortion between donor and acceptor than for **XT** and **QT**. These structural features determine the state that is mainly affected in the emissive state. Therefore, **ZT** show smaller singlet-triplet energy gap (ΔE_{ST}) than those of **QT** and **XT** due to the triplet CT state dominant excited state.

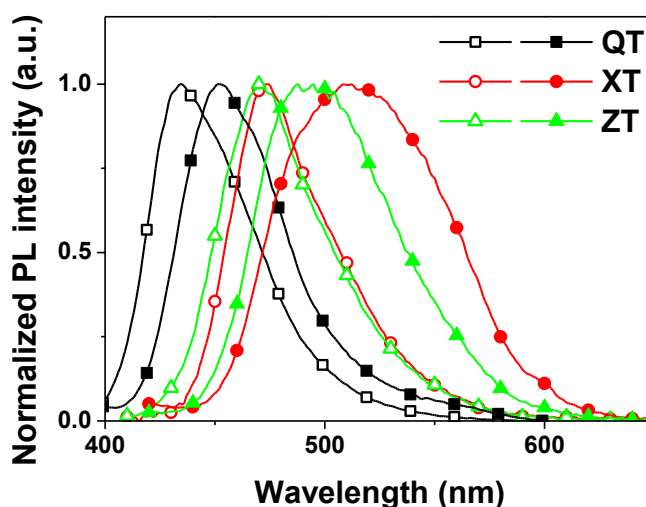


Figure 4. PL spectra of **QT**, **XT**, and **ZT** in neat and doped film (20 wt% in the mCBP). (Open symbols: 20 wt% doped in the mCBP, closed symbols: neat film)

PL spectra of **QT**, **XT**, and **ZT** in neat and doped film (20 wt% in the mCBP) also analyzed (Figure 4). **QT**, **XT**, and **ZT** exhibit PL λ_{max} at 434, 473 and 471 nm in the doped film, respectively, as well as 452, 509, and 491 nm in neat film, respectively, red-shifted to those of the doped condition state. These results are presumed to be π - π stacking or intermolecular aggregation in the neat condition.

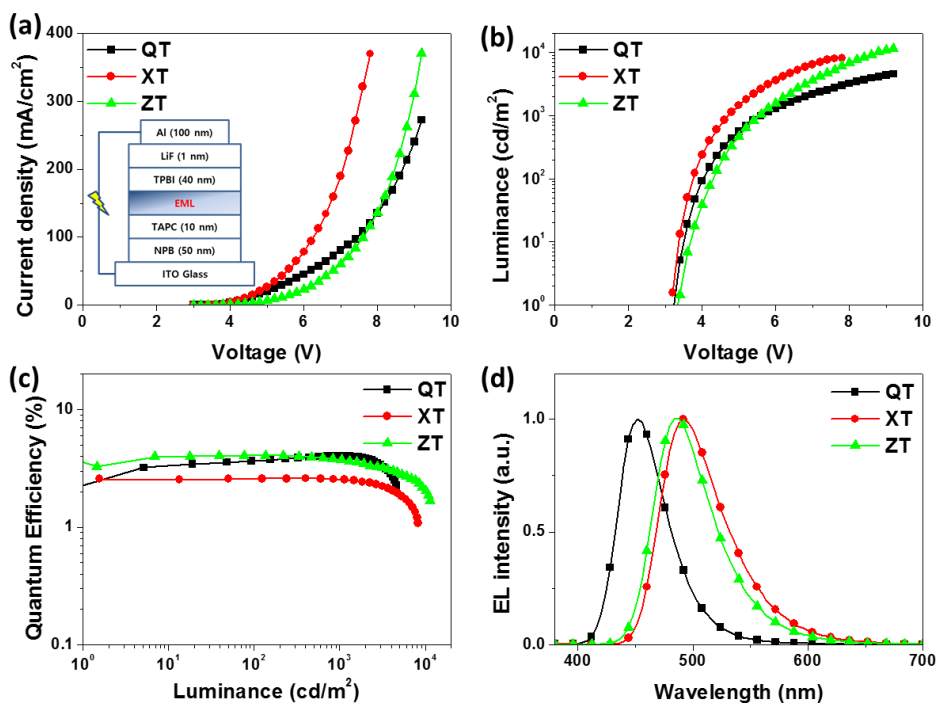


Figure 5. Device performance of non-doped FLOLEDs with **QT**, **XT**, and **ZT**. (a) Current density-voltage characteristics (inset: device structure of the FLOLEDs), (b) luminance-voltage characteristics, (c) quantum efficiency-luminance characteristics and (d) electroluminescence spectra.

Three different non-doped FLOLEDs were fabricated and performed using **QT**, **XT**, and **ZT** as an EML without a host, respectively, with a device configuration of ITO/NPB (50 nm)/TAPC (10 nm)/EML (**QT**, **XT**, and **ZT**, 30 nm)/TPBI (40 nm)/LiF (1 nm)/Al (100 nm) (Figure 5, Table 2). The current density and luminance of the device with **XT** is the highest value among the three devices at the same driving voltage, as shown in Figure 5(a) and (b). Meanwhile, the quantum efficiency of the device with **XT** is the lowest value than other conditions at the same luminance

(Figure 5(c)). It is known that efficient packing of semiconductor molecules usually facilitates better current flow through the devices.⁹⁵ Thus, an alternation of the packing densities in the solid films derived from the structurally different **QT**, **XT**, and **ZT** would result in different current densities. Because the structure of non-doped nature with relatively less distorted **XT** is better packed than that of **ZT**, it results in better current density and luminance at the same driving voltage. However, the maximum luminance and quantum efficiency of the **ZT**-based device is higher than those of **XT**-based device, which means that the higher packing density of the **XT**-based device causes more exciton quenching than for the **ZT**-based device at the same current density. These results are consistent with our simulation using DFT calculations and indicate that the electroluminescent (EL) performance of the **ZT**-based device is more efficient than that of the **XT**-based device. The **QT**-based device shows saturated blue EL emission of 452 nm with a CIE color coordinate of (0.146, 0.079) and exhibits a maximum EQE of 4.0%.

Table 2. EL Performance of **QT**, **XT**, and **ZT** based devices

EML	V _{on} ^a (V)	EQE _{max} (%)	Luminance _{max} (cd/m ²)	λ _{max} ^b (nm)	CIE ^b (x, y)
A	3.2	4.0	4559	452	0.146, 0.079
B	3.2	2.6	8188	492	0.177, 0.439
C	3.2	4.1	11440	484	0.154, 0.357
D	3.4	3.1	3019	444	0.151, 0.054
E	3.6	2.6	12300	488	0.159, 0.379
F	3.2	3.3	10350	476	0.145, 0.247
G	3.2	3.4	7285	484	0.157, 0.356
H	3.2	4.1	13090	480	0.147, 0.295

EL Device configuration of ITO/NPB (50 nm)/TAPC (10 nm)/EML (A~H, 30 nm)/TPBI (40 nm)/LiF (1 nm)/Al (100 nm), condition of EML A: QT, B:XT, C:ZT, D: mCBP:QT = 4:1, E: mCBP:XT = 4:1, F: mCBP:ZT = 4:1, G: QT:XT = 4:1, H: QT:ZT = 4:1, ^a at 1 cd/m², ^b at maximum EQE.

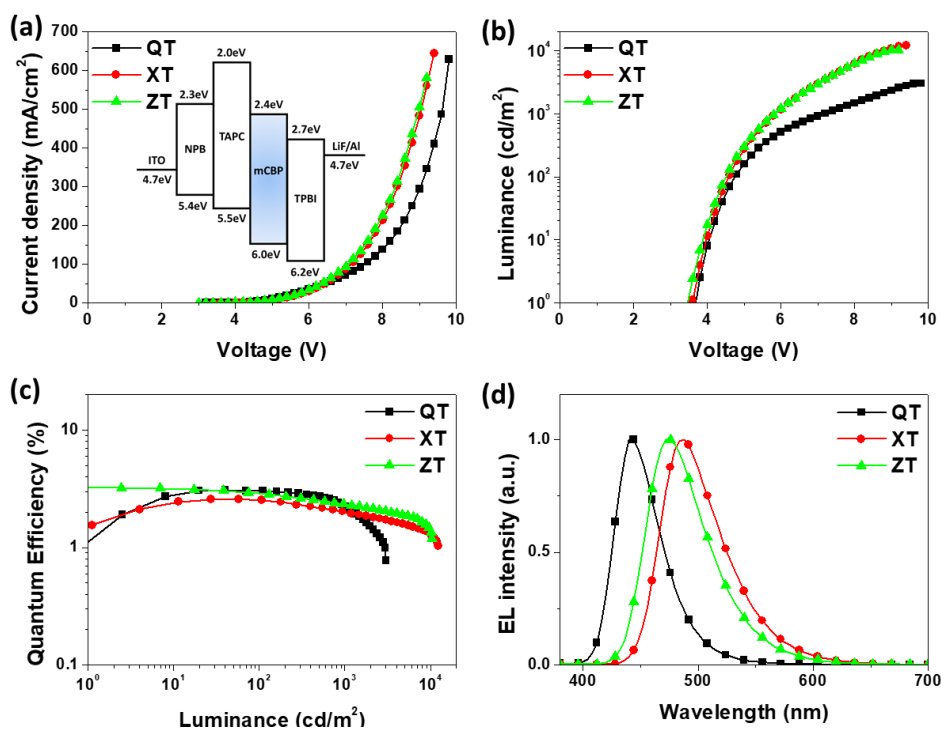


Figure 6. Device performance of mCBP doped FLOLEDs with **QT**, **XT**, and **ZT**. (a) Current density-voltage characteristics (inset: energy level diagram of FLOLEDs), (b) luminance-voltage characteristics, (c) quantum efficiency-luminance characteristics and (d) electroluminescence spectra.

To further investigate the potential application of these blue-emitting compounds, we fabricated doped OLED devices with the structure ITO/NPB (50 nm)/TAPC (10 nm)/EML (30 nm)/TPBI (40 nm)/LiF/Al (100 nm), where **QT** (device D), **XT** (device E), and **ZT** (device F) were used as the dopant materials in the mCBP host. The performance of devices D~F is also summarized in Table 2. As shown in Figure 6d, all the resulting EL spectra showed blue shifted emission peak around 444 to 488 nm compared to the A~C devices, which corresponded well with

the PL spectra in doped film (Figure 4). More specifically, EL spectra of **QT**-based doped device D exhibited saturated deep-blue emission with CIE coordinates of (0.151, 0.054). All of these dopant-based devices showed excellent EL efficiencies. It is noted that the current density-voltage characteristics and their corresponding luminance of **XT** and **ZT** were observed to be approximately similar. This means that the exciton quenching due to molecular packing is inhibited by mCBP host material in doped EML compared to non-doped environment.

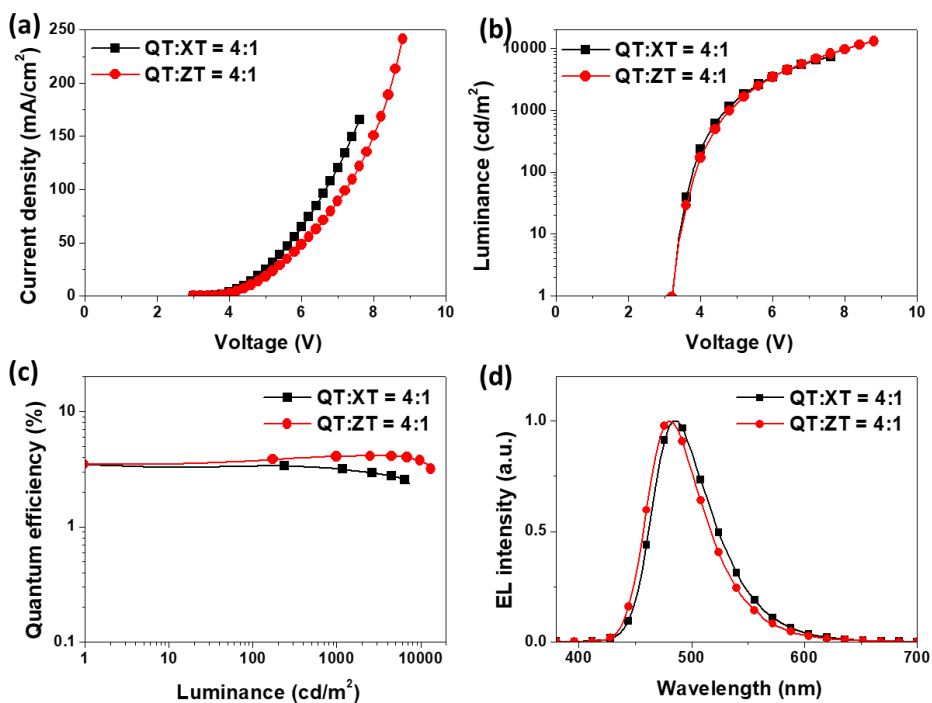


Figure 7. Device performance of **XT** and **ZT**-based FLOLEDs using **QT** as a host material. (a) Current density-voltage characteristics, (b) luminance-voltage characteristics, (c) quantum efficiency-luminance characteristics and (d) electroluminescence spectra.

Deep blue emitted **QT** was then employed as the host material for **XT** and **ZT** based fluorescent OLEDs. Device structures are ITO/NPB (50 nm)/TAPC (10 nm)/**QT**: 20% **XT** or **ZT** (30 nm)/TPBI (40 nm)/LiF/Al (100 nm). In the device using **QT** as the host, the **XT** and **ZT**-based devices showed similar emission wavelengths and CIE color coordinates, but showed higher efficiency than those of the device using mCBP as the host. This means that **QT** can act not only as a blue fluorescent emitter, but also as a host of materials for sky-blue to green dopant materials (Figure 7).

4. Conclusion

In summary, three bipolar materials were comprised by triphenylamine donor attached quinoline, quinoxaline and quiazoline acceptor where **QT**, **XT**, and **ZT** have been synthesized and investigated. Each material-based non-doped OLED performs saturated blue to sky-blue EL emissions with appropriate efficiency. In doped devices using mCBP as the host material, the **QT**-based device shows a deep-blue EL emission with a low CIE coordinate of $y = 0.054$ and EQE of 3.1%. Furthermore, **QT** is capable of acting as a host material in using **XT** and **ZT** as dopant materials. **QT** has been used not only as an emitter for non-doped blue OLEDs with high efficiency, but also as a host material for highly efficient sky-blue to green OLEDs. We successfully present multifunctional blue fluorophores that can exhibit high-efficiency blue emissions and be employed as high performance hosts.

Section 4 Extremely deep-blue fluorescent emitters with CIE_y ≤ 0.04 for non-doped organic light-emitting diodes based on an indenophenanthrene core

Abstract

The fluorescent molecules 7,7-dimethyl-*N,N*-diphenyl-7H-indeno[1,2-*a*]phenanthren-9-amine (**DIP**) and 4-(7,7-dimethyl-7H-indeno[1,2-*a*]phenanthren-9-yl)-*N,N*-diphenylaniline (**TIP**), with indenophenanthrene cores and attached arylamine structures, were synthesized for use as extremely deep blue fluorescent emitting materials. A non-doped device using **DIP** as an emitting material exhibited a maximum external quantum efficiency of 3.27% and had Commission Internationale de l'Éclairage (CIE) color coordinates of (0.158, 0.040).

Keywords: Deep-blue emitter, non-doped system, fluorescent organic light-emitting diodes, indenophenanthrene; charge balance.

1. Introduction

Full-color displays and white lighting require three primary color emissions (red, green, and blue (RGB)) of relatively equal stability, efficiency, and color purity.⁵⁵ In particular, extremely deep-blue-emitting materials play an important role in the development of efficient organic light-emitting diodes (OLEDs) because the deep blue emission is more energy efficient than a normal blue color when strong microcavity structures are chosen to enhance color purity.¹¹²

Current deep-blue emitters are based on chromophores consisting of flat aromatic compounds such as anthracene, fluorene, and pyrene, which show high electroluminescence efficiencies. The 9-alkylated fluorene moiety is expected to be a good electroluminescent backbone for blue-emitting materials because of its excellent fluorescence properties and excellent morphological, thermal, and electrochemical stabilities.^{25, 113} However, in most planar aromatic compounds utilized for emitting materials, excimers or exciplexes are usually formed by intramolecular or intermolecular interactions between the emitters, resulting in bathochromic shifts of the Commission Internationale de l'Eclairage (CIE) chromaticity coordinates and low quantum efficiencies; this occurs because the emitters tend to be closely packed and aggregated in the emitting layer.^{75, 85, 114} To overcome these problems, bulky side groups or spiro moieties were introduced to reduce packing between the molecules and limit the emission quenching, and this should enhance the purity and stability of the blue emissions, along with the photoluminescence (PL) quantum efficiency.^{25, 115-116} However, the introduction of bulky side groups or spiro moieties in flat blue emitters sometimes results in an unexpected bathochromic shift of the emitters in the solid state.¹¹⁷⁻¹¹⁸ Therefore, an alternative way of developing deep blue emitters is required.

Deep-blue fluorescence OLEDs based on spirocyclic aromatic hydrocarbon derivatives and purine derivatives exhibit CIE coordinates of (0.16, 0.08) with a maximum current efficiency of 1.1 cd/A and CIE coordinates of (0.15, 0.06) with an external quantum efficiency (EQE) of 3.1%, respectively.^{81, 93} In addition, deep-blue emitters based on twisted asymmetric anthracene derivatives with triphenyltriazine- or triphenylamine-substituted xylene units have been reported to exhibit EQEs of 4.62 and 6.6% with CIE coordinates of (0.154, 0.049) and (0.145, 0.068), respectively.^{113, 119} Nevertheless, there have been few reports concerning color-pure, deep-blue fluorescent materials with CIE *y*-values around 0.04 and EQEs greater than 3% in non-doped devices.¹²⁰

In this study, we designed and synthesized two extremely deep-blue emitting materials based on an indenophenanthrene core for non-doped blue OLEDs with excellent color purity: 7,7-dimethyl-*N,N*-diphenyl-7H-indeno[1,2-*a*]phenanthren-9-amine (**DIP**) and 4-(7,7-dimethyl-7H-indeno[1,2-*a*]phenanthren-9-yl)-*N,N*-diphenylaniline (**TIP**). Because phenanthrene is less conjugated than anthracene,¹²¹ we designed an indenophenanthrene core by hybridizing a phenanthrene moiety with fluorene to induce a deep blue emission.¹²² The non-doped OLED device using **DIP** as an emitting material had a maximum EQE of 3.27% with CIE color coordinates of (0.158, 0.040), and is therefore better than the device fabricated using the **TIP** emitter in terms of the EQE and CIE color coordinates because of the better charge balance.

2. Materials and general methods

2.1. Materials

All solvents and materials were used as received from commercial suppliers without further purification. Synthetic routes to **DIP** and **TIP** are outlined in Figure 2. The two final products (**DIP** and **TIP**) were purified by temperature gradient vacuum sublimation.

2.2. Synthetic procedure

1-((Z)-2-(2-Bromophenyl)-1-ethenyl)-2-iodobenzene (2). To a cooled (0 °C) suspension of (2-bromobenzyl)triphenylphosphonium bromide (**1**) (33.000 g, 64.425 mmol) in tetrahydrofuran (THF, 350 mL), potassium *tert*-butoxide (8.434 g, 75.163 mmol) in THF (50 mL) was added. After 30 min, 2-iodobenzaldehyde (12.457 g, 53.688 mmol) in THF (100 mL) was added over 1 h. The reaction was left to warm to room temperature (RT) and was stirred for 24 h. Then, water (100 mL) was added. The aqueous phase was separated and extracted with diethyl ether (3 × 300 mL). The combined organic extracts were dried (MgSO₄), concentrated in vacuo, and purified by column chromatography (SiO₂, hexane) to yield an inseparable 9:1 mixture of (*Z*)- and (*E*)-isomers (18.7 g, 48.566 mmol, 90.5%) as a pale-yellow oil. ¹H NMR of (*Z*)-isomer (300 MHz, CDCl₃): δ (ppm) 7.87 (dd, *J* = 7.9, 1.1 Hz, 1H), 7.57 (dd, *J* = 7.3, 1.8 Hz, 1H), 7.11~6.93 (m, 5H), 6.89 (td, *J* = 7.7, 1.9 Hz, 1H), 6.76 (d, *J* = 11.8 Hz, 1H), 6.68 (d, *J* = 11.8 Hz, 1H). ¹³C NMR of (*Z*)-isomer (75 MHz, CDCl₃): δ (ppm) 140.9, 139.2, 137.0, 135.4, 132.8, 131.1, 130.8, 130.6, 129.0, 128.9, 128.0, 127.1, 124.3, 100.0. HRMS (FAB+): [M + H: C₁₄H₁₀Br] 383.9011, found 383.9018.

1-Bromophenanthrene (3). A solution of stilbene **2** (9:1 mixture of (*Z*)- and (*E*)-isomers, 15.1 g, 39.217 mmol), tributyltin hydride (13.697 g, 47.060 mmol), and azobisisobutyronitrile (AIBN) (1.288 g, 7.843 mmol) in toluene (200 mL) was

heated at 90 °C for 16 h in nitrogen atmosphere and then cooled to RT. Additional tributyltin hydride (2.283 g, 7.843 mmol) and AIBN (0.258 g, 1.569 mmol) were added, and the reaction was heated for a further 8 h at 90 °C. After cooling to RT and concentration in vacuo, the resulting mixture was extracted with excess dichloromethane. The organic layer was washed successively with water and brine and dried using anhydrous sodium sulfate, which was filtered through celite and potassium fluoride. The product mixture was purified by column chromatography (10% KF/SiO₂, hexane) to afford 1-bromophenanthrene (8.4 g, 32.668 mmol, 83.3%) as a white solid. ¹H NMR (300 MHz, CDCl₃): δ (ppm) 8.68 (d, *J* = 8.2 Hz, 2H), 8.23 (d, *J* = 9.2 Hz, 1H), 7.95~6.89 (m, 2H), 7.86 (d, *J* = 9.2 Hz, 1H), 7.73~7.62 (m, 2H), 7.50 (dd, *J* = 8.2, 7.9 Hz, 1H). ¹³C NMR (75 MHz, CDCl₃): δ (ppm) 132.2, 132.1, 130.9, 130.8, 130.1, 128.9, 128.7, 127.4, 127.3, 127.0, 125.5, 123.9, 123.1, 122.5. HR-Mass (EI⁺): calcd for C₁₄H₉Br 255.9888, found 255.9886.

Phenanthren-1-ylboronic acid (4). 1-Bromophenanthrene (**3**) (3.0 g, 11.667 mmol) was dissolved in dry THF (100 mL) under an atmosphere of nitrogen. This solution was cooled to -78 °C, followed by the dropwise addition of *n*-butyllithium (2.5 M in hexane, 11.667 mL, 29.168 mmol). This mixture was stirred for 1 h and then treated with trimethylborate (6.539 mL, 58.336 mmol). After stirring at RT for 15 h, the reaction mixture was added to an aqueous solution of HCl (1 N) and stirred for 2 h. The aqueous phase was separated and extracted with dichloromethane (3 × 50 mL). The combined organic extracts were dried using sodium sulfate, concentrated in vacuo, and purified by column chromatography (SiO₂, dichloromethane:methanol = 9:1) to afford phenanthren-1-ylboronic acid (1.8 g, 8.105 mmol, 69.5%) as a white solid. ¹H NMR (300 MHz, acetone-*d*₆): δ (ppm) 8.88 (dd, *J* = 8.4, 5.4 Hz, 2H), 8.51 (d, *J* = 9.0 Hz, 1H), 7.97 (d, *J* = 7.2 Hz, 2H), 7.82 (d,

$J = 9.0$ Hz, 1H), 7.71~7.60 (m, 3H). ^{13}C NMR (75 MHz, acetone- d_6): δ (ppm) 135.0, 132.8, 131.8, 130.6, 128.3, 127.7, 126.5, 126.4, 126.3, 125.7, 124.0, 122.7. HR-Mass (EI+): calcd for $\text{C}_{14}\text{H}_{11}\text{BO}_2$ 222.0852, found 222.0848.

Methyl 5-bromo-2-(phenanthren-1-yl)benzoate (5). A mixture of methyl 5-bromo-2-iodobenzoate (3.849 g, 11.259 mmol), phenanthren-1-ylboronic acid (**4**) (3 g, 13.510 mmol), 2 M aqueous potassium carbonate (30 mL), and tetrakis(triphenylphosphine)palladium (0.651 g, 0.563 mmol) in THF (100 mL) and methanol (30 mL) was heated at reflux in a nitrogen atmosphere for 24 h. After the reaction mixture had been concentrated in vacuo, the resulting mixture was extracted with dichloromethane. The organic layer was washed with water and brine and dried using anhydrous sodium sulfate. The filtrate was concentrated in vacuo to give a crude mixture that was purified by column chromatography (SiO_2 , dichloromethane:hexane = 1:4) to afford methyl 5-bromo-2-(phenanthren-1-yl)benzoate (3.5 g, 8.945 mmol, 79%) as a white solid. ^1H NMR (300 MHz, CDCl_3): δ (ppm) 8.80 (d, $J = 12.6$ Hz, 2H), 8.22 (s, 1H), 7.88 (d, $J = 7.8$ Hz, 1H), 7.77 (dd, $J = 5.1, 1.8$ Hz, 1H), 7.73~7.60 (m, 4H), 7.40 (dd, $J = 7.8, 1.5$ Hz, 2H), 7.32 (d, $J = 8.1$ Hz, 1H), 3.41 (s, 3H). ^{13}C NMR (75 MHz, CDCl_3): δ (ppm) 166.4, 140.7, 139.0, 134.6, 133.5, 133.1, 131.7, 130.3, 130.2, 130.0, 128.5, 127.2, 126.8, 126.7, 125.7, 123.9, 122.9, 122.4, 121.5, 52.1. HR-Mass (EI+): calcd for $\text{C}_{22}\text{H}_{15}\text{BrO}_2$ 390.0255, found 392.0257.

2-(5-Bromo-2-(phenanthren-1-yl)phenyl)propan-2-ol (6). To a solution of methyl 5-bromo-2-(phenanthren-1-yl)benzoate (**5**) dissolved in dry THF (120 mL) under a nitrogen atmosphere, a solution of methylmagnesium bromide solution in diethyl ether (1.4 M, 14.85 mL, 21.162 mmol) was slowly added. The mixture was heated at reflux for 4 h. After the reaction mixture had been concentrated in vacuo,

the resulting mixture was extracted with dichloromethane. The organic layer was washed with water and brine and dried using anhydrous sodium sulfate. The filtrate was concentrated in vacuo to give a crude mixture that was purified by column chromatography (SiO₂, ethyl acetate:hexane = 1:20) to afford the 2-(5-bromo-2-(phenanthren-1-yl)phenyl)propan-2-ol (2.7 g, 6.900 mmol, 75%) as a white solid. ¹H NMR (300 MHz, CDCl₃): δ (ppm) 8.77 (d, *J* = 5.1 Hz, 2H), 8.03 (d, *J* = 1.8 Hz, 1H), 7.89 (d, *J* = 4.5 Hz, 1H), 7.88~7.62 (m, 4H), 7.52~7.47 (m, 2H), 7.33 (d, *J* = 9.3 Hz, 2H), 7.03 (d, *J* = 8.1 Hz, 1H), 1.39 (s, 3H), 1.22 (s, 3H). ¹³C NMR (75 MHz, CDCl₃): δ (ppm) 149.5, 140.4, 136.7, 134.2, 131.7, 131.0, 130.5, 130.2, 129.6, 129.4, 128.6, 128.0, 127.2, 126.9, 125.4, 125.0, 122.9, 122.5, 122.1, 73.7, 32.3, 31.7. found 392.0, HR-Mass (EI+): calcd for C₂₃H₁₉BrO 390.0619, found 390.0622.

9-Bromo-7,7-dimethyl-7H-indeno[1,2-*a*]phenanthrene (7).

Concentrated sulfuric acid (4.5 mL) was added to a stirred solution of 2-(5-bromo-2-(phenanthren-1-yl)phenyl)propan-2-ol (**6**) (2.7 g, 6.918 mmol) in acetic acid (139 mL) at 100 °C. After stirring for 3 h at 100 °C, the mixture was poured into water and extracted with dichloromethane. The organic layer was washed with water and brine and dried using anhydrous sodium sulfate. The filtrate was concentrated in vacuo to give a crude mixture that was purified by column chromatography (SiO₂, hexane) to afford 9-bromo-7,7-dimethyl-7H-indeno[1,2-*a*]phenanthrene (1.8 g, 4.830 mmol, 70.0%) as a white solid. ¹H NMR (300 MHz, CDCl₃): δ (ppm) 8.76 (t, *J* = 5.4 Hz, 2H), 8.63 (d, *J* = 9.3 Hz, 1H), 8.24 (d, *J* = 8.4 Hz, 1H), 7.74 (d, *J* = 8.7 Hz, 1H), 7.97~7.91 (m, 2H), 7.71~7.59 (m, 4H), 1.59 (s, 6H). ¹³C NMR (75 MHz, CDCl₃): δ (ppm) 157.0, 152.7, 130.2, 128.6, 127.9, 126.9, 126.7, 126.5, 126.2, 124.7, 123.0, 122.3, 120.9, 120.7, 46.6, 26.9. HR-Mass (EI+): calcd for C₂₃H₁₇Br 372.0514, found 372.0514.

7,7-Dimethyl-N,N-diphenyl-7H-indeno[1,2-*a*]phenanthren-9-amine

(DIP). To a mixture of 9-bromo-7,7-dimethyl-7H-indeno[1,2-*a*]phenanthrene (**7**) (2.65 g, 7.099 mmol), diphenylamine (1.561 g, 9.229 mmol), and palladium acetate (0.111 g, 0.497 mmol) in dry toluene (80 mL) under an N₂ atmosphere, a solution of tri-*tert*-butylphosphine (0.287 g, 1.420 mmol) and potassium *tert*-butoxide (3.187 g, 28.389 mmol) in toluene (20 mL) was added. The mixture was heated to reflux under nitrogen. After 12 h, the reaction mixture was concentrated in vacuo, and the resulting mixture was extracted with dichloromethane. The organic layer was washed successively with water and brine and dried using anhydrous sodium sulfate. The filtrate was concentrated in vacuo to give a crude mixture, which was purified by column chromatography (SiO₂, hexane) to afford 7,7-dimethyl-*N,N*-diphenyl-7H-indeno[1,2-*a*]phenanthren-9-amine (2.15 g, 4.658 mmol, 66%) as a bright yellow solid. ¹H NMR (400 MHz, CDCl₃): δ (ppm) 8.66 (d, *J* = 8.4 Hz, 1H), 8.61 (d, *J* = 8.4 Hz, 1H), 8.56 (d, *J* = 9.2 Hz, 1H), 8.14 (d, *J* = 8.0 Hz, 1H), 7.84 (d, *J* = 8.0 Hz, 1H), 7.79 (d, *J* = 9.6 Hz, 1H), 7.64 (d, *J* = 8.0 Hz, 1H), 7.59 (t, *J* = 7.2 Hz, 1H), 7.52 (t, *J* = 7.2 Hz, 1H), 7.26~7.18 (m, 6H), 7.12~7.05 (m, 4H), 6.98 (t, *J* = 7.2 Hz, 2H), 1.43 (s, 6H). ¹³C NMR (100 MHz, CDCl₃): δ (ppm) 157.0, 152.7, 130.2, 128.6, 127.9, 126.9, 126.7, 126.5, 126.2, 124.7, 123.0, 122.3, 120.9, 120.7, 46.6, 26.9. HR-Mass (EI+): calcd for C₃₅H₂₇N 461.2143, found 461.2147.

4-(7,7-Dimethyl-7H-indeno[1,2-*a*]phenanthren-9-yl)-N,N-

diphenylaniline (TIP). A mixture of 9-bromo-7,7-dimethyl-7H-indeno[1,2-*a*]phenanthrene (**7**) (1.5 g, 4.018 mmol), 4-(diphenylamino)-phenylboronic acid (1.4 g, 4.822 mmol), tetrakis(triphenylphosphine)palladium (0.232 g, 0.201 mmol), and aqueous sodium carbonate (2 M, 20 mL) in THF (100 mL) and methanol (20 mL) was heated to reflux in a nitrogen atmosphere for 24 h. After the reaction mixture

had been concentrated in vacuo and the resulting mixture extracted with dichloromethane, the organic layer was washed with water and brine and dried using anhydrous sodium sulfate. The filtrate was concentrated in vacuo to give a crude mixture, which was purified by column chromatography (SiO₂, dichloromethane:hexane = 1:9) to afford 4-(7,7-dimethyl-7H-indeno[1,2-*a*]phenanthren-9-yl)-*N,N*-diphenylaniline (1.4 g, 2.604 mmol, 64.8%) as a yellow solid. ¹H NMR (400 MHz, CDCl₃): δ (ppm) 8.73 (d, *J* = 8.4 Hz, 3H), 8.40 (d, *J* = 7.6 Hz, 1H), 7.94~7.87 (m, 3H), 7.76 (d, *J* = 8.4 Hz, 1H), 7.73 (s, 1H), 7.69~7.65 (m, 2H), 7.62~7.56 (m, 4H), 7.29 (t, *J* = 8.0 Hz, 4H), 7.16 (t, *J* = 8.8 Hz, 4H), 7.02 (t, *J* = 7.6 Hz, 3H) 1.52 (s, 6H). ¹³C NMR (100 MHz, CDCl₃): δ (ppm) 155.5, 152.7, 147.6, 147.2, 139.0, 138.9, 134.3, 133.3, 131.3, 130.0, 129.3, 128.5, 127.8, 127.6, 126.8, 126.3, 125.7, 124.4, 124.4, 124.0, 123.9, 123.6, 122.9, 122.7, 122.3, 121.0, 120.8, 46.5, 27.1. HR-Mass (FAB+): calcd for C₄₁H₃₁N 537.2457, found 537.2457.

2.3. General methods

¹H- and ¹³C-NMR spectra were recorded using an Agilent 400 MHz Varian spectrometer in CDCl₃. ¹H-NMR chemical shifts in CDCl₃ were referenced to CHCl₃ (7.27 ppm). ¹³C-NMR chemical shifts in CDCl₃ were reported relative to CHCl₃ (77.23 ppm). UV-visible spectra were recorded on a Beckman DU650 spectrophotometer. Fluorescence spectra were recorded on a Jasco FP-6500 spectrophotometer. Fluorescent quantum yields in the solid films were recorded on an Otsuka electronics QE-2000 spectrophotometer. Mass spectra were obtained using matrix-assisted laser desorption–ionization time-of-flight mass spectrometry (MALDI-TOF-MS) from Bruker. High-resolution masses were measured by either fast atom bombardment (FAB) or electron ionization (EI) using a JEOL HP 5890.

Analytical thin-layer chromatography was performed using Kieselgel 60F-254 plates from Merck. Column chromatography was carried out on Merck silica gel 60 (70–230 mesh). Decomposition temperatures (T_d) and glass transition temperatures (T_g) were obtained by thermogravimetric analysis (TGA, Q-5000-IR) and differential scanning calorimetry (DSC, DSC-Q-1000), respectively. The TGA and DSC analyses were performed at a heating rate of $10\text{ }^\circ\text{C min}^{-1}$ under a nitrogen atmosphere. The T_g was determined from the third heating scan. The electrochemical properties of **DIP** and **TIP** were studied using cyclic voltammetry (CV) in CH_2Cl_2 solutions (1.00 mM) with 0.1 M tetra-*n*-butylammonium hexafluorophosphate (TBAPF_6) as the supporting electrolyte. A glassy carbon electrode was employed as the working electrode and referenced to a Ag reference electrode. All potential values were calibrated against the ferrocene/ferrocenium (Fc/Fc^+) redox couple. The onset potential was determined from the intersection of two tangents drawn at the rising and background current of the cyclic voltammogram.

2.4. Theoretical calculations

The optimized geometries and frontier molecular orbital energy levels for DIP and TIP were obtained using density functional theory (DFT) calculations with Gaussian '09. The geometries were optimized using the Becke 3-parameter Lee-Yang-Parr (B3LYP) functional with the 6-311G-level atomic basis set.

2.5. Device fabrication & characterization

N,N'-Di(1-naphthyl)-*N,N'*-diphenyl-(1,1'-biphenyl)-4,4'-diamine (NPB),
4,4',4''-tris(*N*-carbazolyl)triphenylamine (TCTA), and 1,3,5-tris(*N*-

phenylbenzimidazol-2-yl)benzene (TPBI) were purchased from commercial sources and used without purification. The fabrication of OLEDs was conducted by the high-vacuum (2×10^{-6} Torr) thermal evaporation of the organic materials onto indium tin oxide (ITO)-coated glass (sheet resistance: $15 \Omega/\text{square}$; Applied Film Corp.). Glass substrates with patterned ITO electrodes were washed with isopropyl alcohol and then cleaned by O_2 plasma treatment. The OLED devices were fabricated with a configuration of ITO/NPB/TCTA/DIP or TIP/TPBI/LiF/Al. NPB and TCTA (hole transporting layers), TPBI (electron transporting layer), LiF (electron injection layer), and Al electrodes were deposited sequentially on the substrate. The emission properties were determined using a PR-650 SpectraScan SpectraColorimeter as a source meter. The current–voltage characteristics were measured using a programmable electrometer equipped with current and voltage sources (Keithley 2400).

3. Results and discussion

3.1. Theoretical calculation

Optimized geometries and frontier molecular orbital energy levels for **DIP** and **TIP** were obtained from DFT calculations at the B3LYP/6-311G level using Gaussian '09. As shown in Figure 1, the indenophenanthrene moiety is slightly distorted from the perfect planarity because of the *syn*-pentane-like interactions between the hydrogen at the C5 position and the hydrogen at the C14 position of **DIP** and the C13 position of **TIP**. The calculated results show that the dihedral angle connecting the C5-C4-C9-C14 of **DIP** is twisted about 1.7° , and the dihedral angle

connecting the C5-C4-C8-C14 of **TIP** is 2.4° , respectively. In **TIP**, the dihedral angle between additional phenyl ring and indenophenanthrene moiety is 37.1° . The introduction of the twisted structure of the diphenylamine and triphenylamine moieties inhibited the aggregation of **DIP** and **TIP** in the non-doped film.

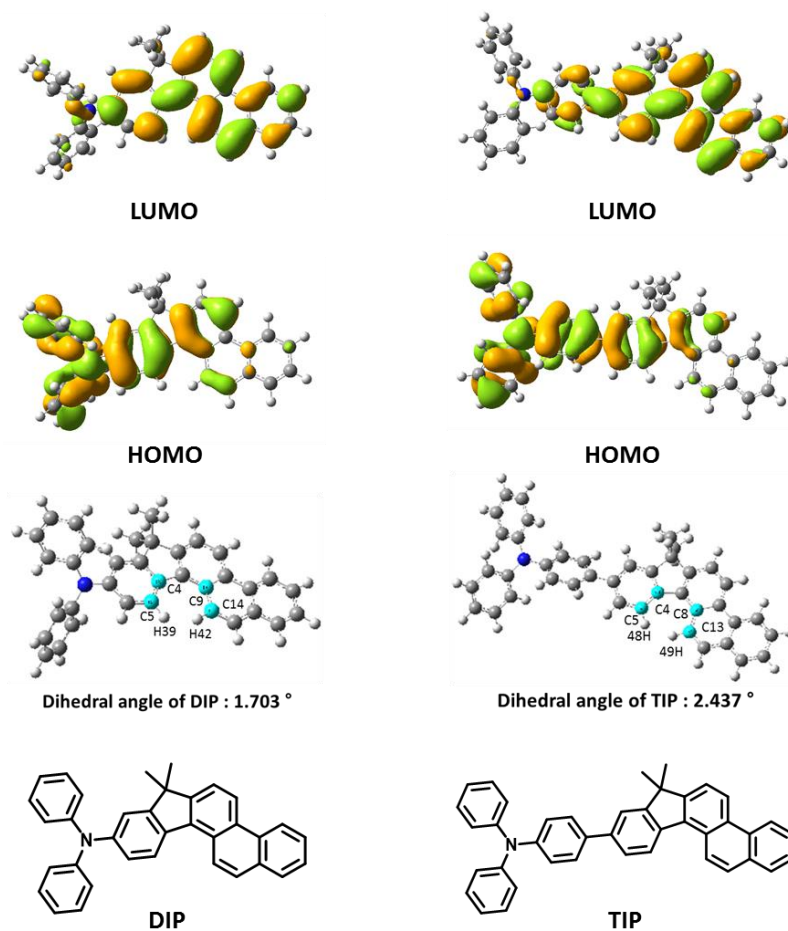


Figure 1. Optimized structures and calculated highest occupied molecular orbital and lowest occupied molecular orbital density maps obtained from DFT calculations of **DIP** and **TIP**, performed at the B3LYP/6-311G level of theory.

The highest occupied molecule orbitals (HOMOs) of **DIP** and **TIP** are localized on the diphenylamine and triphenylamine moieties along with the fluorene moiety of indenophenanthrene, while the lowest unoccupied molecular orbitals (LUMOs) of **DIP** and **TIP** are dispersed over the indenophenanthrene core.⁴⁷ The DFT-calculated HOMO and LUMO energies are similar, at 5.23 and 1.60 eV for **DIP** and 5.21 and 1.58 eV for **TIP**, respectively.¹²³

3.2. Synthesis

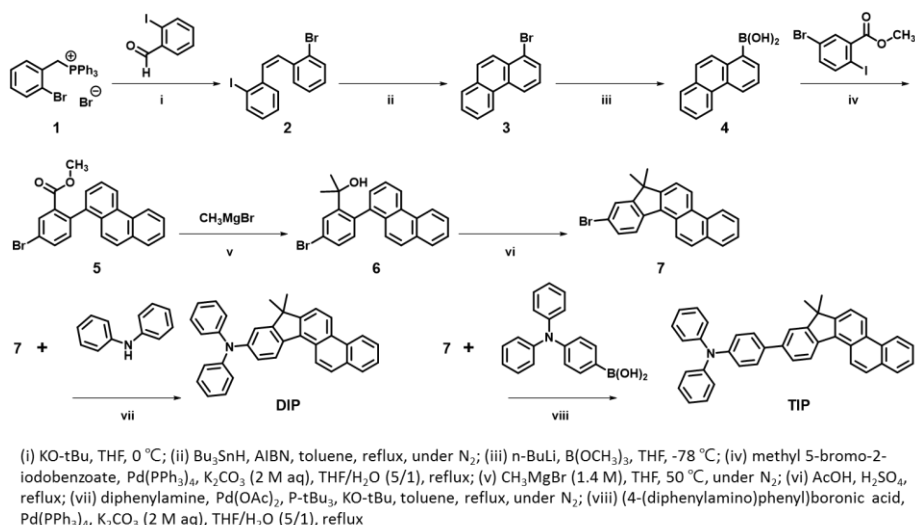


Figure 2. Synthetic routes to **DIP** and **TIP**.

The synthetic routes to **DIP** and **TIP** are illustrated in Figure 2. The synthesis of 9-bromo-7,7-dimethyl-7H-indeno[1,2-*a*]phenanthrene (**7**) was started from 1-bromophenanthrene (**3**).¹²⁴ Methyl 5-bromo-2-(phenanthren-1-yl)benzoate (**5**) was obtained using a Suzuki cross-coupling reaction between phenanthren-1-ylboronic

acid (**4**) and methyl 5-bromo-2-iodobenzoate. Next, Grignard methylation followed by Friedel-Craft cyclization under acidic conditions afforded compound **7**. **DIP** and **TIP** consist of two main components: either diphenylamine or triphenylamine as the hole-transporting moiety and indenophenanthrene as the emissive moiety; these two components were connected by the Buchwald cross-coupling and the Suzuki cross-coupling reactions, respectively.¹²⁵ **DIP** and **TIP** were characterized by ¹H-NMR, ¹³C-NMR, and low- and high-resolution mass spectrometry. These two blue emitting materials were purified further by train sublimation under reduced pressure (<10⁻⁴ Torr).

3.3. Thermal properties

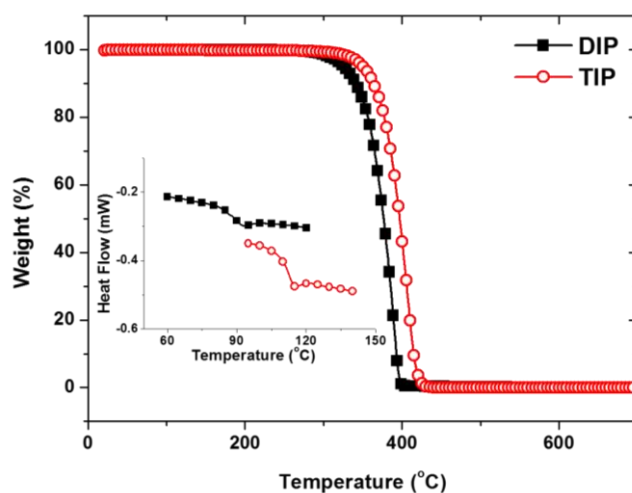


Figure 3. DSC and TGA graphs of **DIP** and **TIP**

The thermal properties of **DIP** and **TIP** were investigated using DSC and TGA (Figure 3). **DIP** and **TIP** exhibit high thermal stability with a decomposition

temperature (T_d , corresponding to 5% weight loss) of 326.9 and 354.4°C, respectively, and a T_g of 90.3 and 112.8°C, respectively. **TIP** is more thermally stable than **DIP** because of the additional phenyl linker moiety.⁶¹

3.4. Photophysical properties

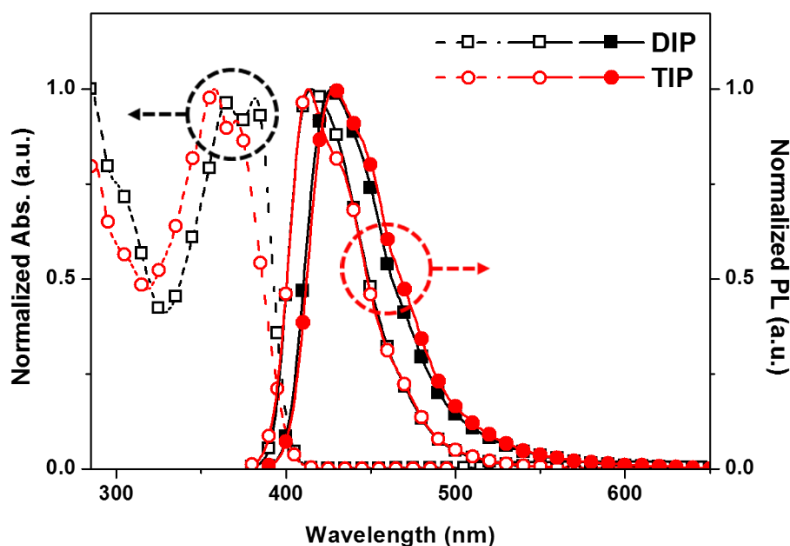


Figure 4. UV-vis absorption and PL spectra of **DIP** (black squares) and **TIP** (red circles). (Dashed lines and open symbols: UV-vis absorption; solid lines and open symbols: PL spectra in toluene; and solid lines and filled symbols: PL spectra in the film state.)

Figure 4 shows the normalized UV-vis absorbance and PL spectra of **DIP** and **TIP** (Table 1). All absorption bands between 330 and 400 nm for **DIP** and **TIP** originate from the intramolecular charge-transfer transitions from the arylamine to indenophenanthrene moiety. The absorption band shape of the brominated

indenophenanthrene (**7**), an intermediate synthetic compound, is similar compared to those of **DIP** and **TIP** (Figure 5). In toluene, the PL λ_{\max} peaks of **DIP** and **TIP** were observed around 420 nm. Compared to the solution state, the emission maxima of **DIP** and **TIP** in the solid state show a slight bathochromic shift of about 10 nm, indicating that the aggregation effect is rarely observed in the solid states of **DIP** and **TIP**. Despite the extra phenyl unit introduced in **TIP**, the PL emission spectra in solution and solid states of **DIP** and **TIP** are very similar.¹²³ These results demonstrate that the additional phenyl ring of **TIP** does not contribute to the extension of the conjugation length because of the distorted dihedral angle (37.1°) between the additional phenyl ring and the indenophenanthrene moiety.

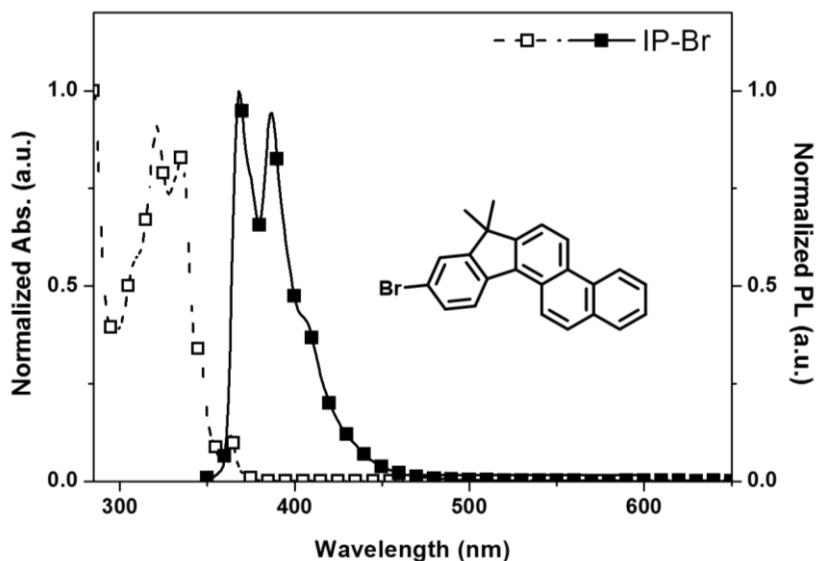


Figure 5. UV-vis absorption (open squares) and PL spectra (filled squares) of 9-bromo-7,7-dimethyl-7H-indeno[1,2-a]phenanthrene (**7**).

Table 1. Thermal and photophysical properties of **DIP** and **TIP**

	T_d/T_g (°C)	λ_{abs}^a (nm)	λ_{PL}^a (nm)	λ_{PL}^b (nm)	Φ_{fl}	E_g^c (eV)	HOMO ^d /LUMO ^e (eV)
DIP	326.9/90.3	364, 382	415	426	0.77 ^a , 0.44 ^b	3.1	5.3, 2.2
TIP	354.4/112.8	358, 370	413, 429	428	0.90 ^a , 0.52 ^b	3.1	5.4, 2.3

^a 10 μ M in toluene. ^b Neat film. ^c Onset absorption wavelength in toluene. ^d CV oxidation potential in dichloromethane (Fc/Fc⁺ as reference: 4.7 eV). ^e Deduced from HOMO and E_g .

The fluorescence quantum yields (Φ_{fl}) of **DIP** and **TIP** were measured to be 0.77 and 0.90, respectively, using 9,10-di(naphth-2-yl)anthracene (ADN, $\Phi_{fl} = 0.57$) as a reference at room temperature (Table 1).¹⁰⁴ And the fluorescence quantum yields (Φ_{fl}) of solid **DIP** and **DIP** are 0.44 and 0.52, respectively.

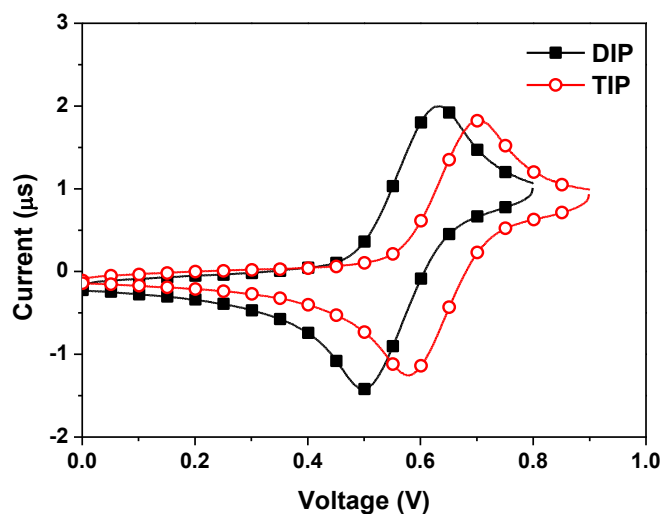


Figure 6. Cyclic voltammograms of **DIP** and **TIP**.

The absorption onsets of the UV-vis spectra of **DIP** and **TIP** were both found to be 400 nm, which corresponds to an optical bandgap of 3.1 eV. From the optical bandgap and the HOMO energy levels of 5.3 and 5.4 eV for **DIP** and **TIP**, respectively, estimated from the CV measurements, the LUMO energy levels were calculated to be 2.2 and 2.3 eV for **DIP** and **TIP**, respectively (Figure 6, Table 1).

3.5. Electroluminescence properties

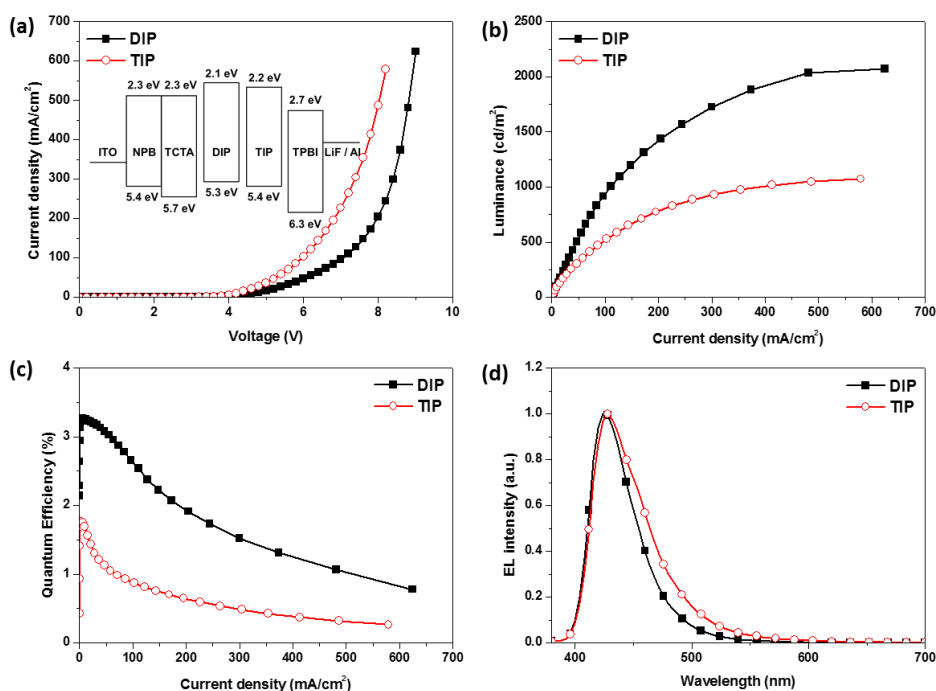


Figure 7. Device performance of the deep-blue OLEDs containing **DIP** and **TIP**. (a) The current density–voltage characteristics (inset: energy level diagram of the devices), (b) luminance–current density characteristics, (c) quantum efficiency–current density characteristics, and (d) electroluminescence spectra.

Table 2. The performance of the non-doped deep blue devices containing **DIP** and **TIP** as the emitting layers.

EML	V_{on}^a (V)	EQE_{max} (%)	EQE^b (%)	LE_{max}^c ($cd\ A^{-1}$)	PE_{max}^d ($lm\ W^{-1}$)	EL_{max}^b (nm)	CIE^b (x, y)	$FWHM^b$ (nm)
DIP	3.2	3.27	3.25	1.11	0.89	424	(0.158, 0.040)	44
TIP	3.2	1.77	1.70	1.00	0.83	428	(0.158, 0.069)	52

^a Turn-on voltage at 1 cd/m^2 , ^b At 10 mA/cm^2 .

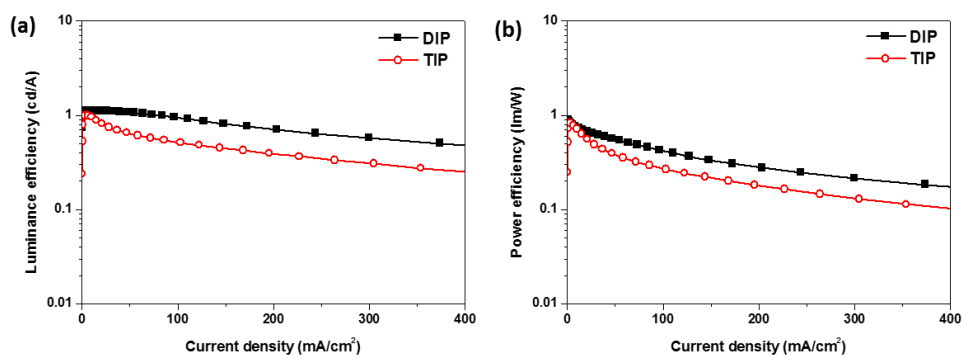


Figure 8. Device performance of the deep-blue OLEDs containing **DIP** and **TIP**. (a) luminance efficiency, (b) power efficiency.

OLED devices were fabricated using **DIP** or **TIP** as a non-doped deep-blue fluorescent emitter in the emitting layer (EML). The device configuration was ITO/NPB (40 nm)/TCTA (20 nm)/EML (**DIP** or **TIP**, 30 nm)/TPBI (15 nm)/LiF (1 nm)/Al (100 nm). Figure 7(a) shows the current density-voltage characteristics of the OLED devices containing **DIP** and **TIP** used as the EML, and the performances of the OLEDs are summarized in Table 2 and Figure 8. Both of the devices had low turn-on voltages (at a luminance of 1 cd/m^2) at 3.2 V, possibly originating from the small injection barriers in the devices. The current density of the **TIP**-based device

was higher than that of the **DIP**-based device at the same voltage, whereas the luminance values of the **DIP**-based devices was higher than that of the **TIP**-based device at the same current density, as shown in Figure 7(b). The current density mainly depends on the differences in the energy levels of the thin organic layers in OLEDs.¹²⁶ These results indicate that the electroluminescent (EL) performance of the **DIP**-based device is more efficient than that of the **TIP**-based device. The quantum efficiency-current density of two devices is plotted in Figure 7(c). The **DIP**-based device shows a better maximum EQE of 3.27% compared to that (1.77%) of the **TIP**-based device. Figure 7(d) shows the normalized EL spectra of the **DIP** and **TIP**-based devices with maximum peak wavelengths at 424 and 428 nm, respectively, which originates from the singlet exciton of each emitter without any other emission from the adjacent layers. The CIE coordinates of the **DIP** and **TIP**-based devices are (0.158, 0.040) and (0.158, 0.069), respectively. The much smaller y-coordinate value of the **DIP**-based device results from its narrower EL spectrum (the full width at half maximum (FWHM) of 44 nm) compared to the **TIP**-based device (the FWHM of 52 nm).¹²⁷

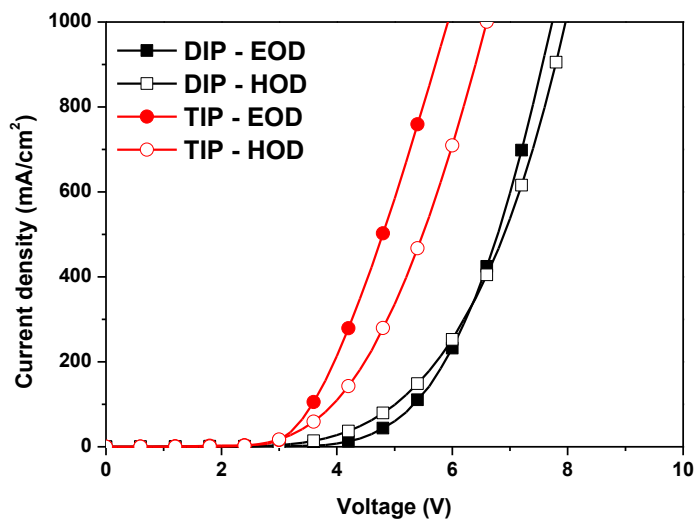


Figure 9. Current density versus driving voltage characteristics of the hole-only (open symbols) and electron-only devices (solid symbols) based on **DIP** (squares) and **TIP** (circles).

For the investigation of the carrier balance of the **DIP** and **TIP**-based devices, hole-only and electron-only devices were also fabricated. The configuration of the hole-only devices was ITO/NPB (40 nm)/TCTA (20 nm)/DIP or TIP (30 nm)/NPB (5 nm)/Al (100 nm), and the electron-only devices had an ITO/TPBI (5 nm)/DIP or TIP (30 nm)/TPBI (15 nm)/LiF (1 nm)/Al (100 nm) structure. NPB (LUMO: 2.3 eV) on the cathode side of the hole-only devices and TPBI (HOMO: 6.3 eV) on the anode side of the electron-only devices were utilized to block electron injection from Al (4.3 eV, corresponding to a large energy barrier of 2.0 eV) and hole injection from ITO (4.8 eV, corresponding to a large energy barrier of 1.5 eV), respectively. Figure 9 shows the current density-voltage curves of hole-only and electron-only devices of **DIP** and **TIP**, respectively. Both the hole and electron carrier densities of the **TIP**-

based device are higher than carrier density of the **DIP**-based device at the same voltage. However, in the case of the **TIP**-based device, the hole density is lower in comparison with electron density at the same voltage, whereas, in the case of the **DIP**-based device, the hole and electron densities are well matched at the same voltage. This phenomenon can be explained by the differences in the HOMO and LUMO energy levels between **DIP** and **TIP**. Because of the higher HOMO energy level of 5.3 eV of **DIP** and 5.4 eV of **TIP** than that (5.7 eV) of TCTA, neither have a hole injection barrier from the hole transport layer (HTL) to the EML. In contrast, the LUMO energy levels of **DIP** and **TIP** are 2.1 and 2.2 eV, respectively, indicating that electron injection from the electron transport layer (ETL) to the EML of **TIP** is easier than to that of **DIP**. Despite the small difference in the energy levels of both deep-blue emitters, there is a discrepancy in the current densities at the same voltage (Figure 7(a)).

Thus, the **DIP**-based device is more efficient than the **TIP**-based device because of the relatively better hole and electron charge balance. Although more excitons were generated from the **TIP**-based device than the **DIP**-based device, the excess electron injection caused exciton-polaron quenching, arising from the hole and electron imbalance. Therefore, the **DIP**-based device exhibited higher efficiency than the **TIP**-based device.^{123, 128} These results agree with the energy level diagrams of devices using **DIP** and **TIP** as EMLs (Figure 7(a) inset)

4. Conclusion

Novel luminescent molecules with indenophenanthrene cores attached to either triphenylamine or diphenylamine moieties were designed and synthesized for

use as extremely deep blue fluorescent emitting materials. Because the **DIP**-based OLED device has a well-matched hole and electron density at the same voltage, the **DIP**-based device exhibited a higher efficiency than the **TIP**-based device. A non-doped device using **DIP** as the emitting material exhibited a maximum EQE of 3.27% with CIE color coordinates of (0.158, 0.040). The introduction of the indenophenanthrene moiety reported in this study suggests a new strategy for the molecular design of highly efficient non-doped deep blue OLED materials.

**Part III. Development of Non-doped Thermally
Activated Delayed Fluorescent Materials for OLEDs**

Background

1. Delayed fluorescent from singlet exciton

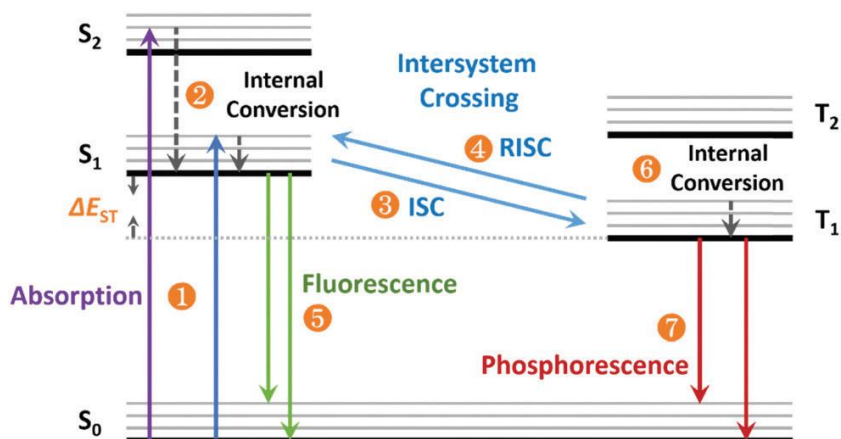


Figure 3.1. The transition process of photogenerated excitons for fluorescence (1 \rightarrow 2 \rightarrow 5), phosphorescence (1 \rightarrow 2 \rightarrow 3 \rightarrow 6 \rightarrow 7) and thermally activated delayed fluorescence (1 \rightarrow 2 \rightarrow 3 \rightarrow 4 \rightarrow 5) in organic molecules. 1: absorption, 2 and 6: internal conversion (IC), 3: intersystem crossing, 4: reverse intersystem crossing, 5: fluorescence, 7: phosphorescence. Copyright 2017, The Royal Society of Chemistry.¹²⁹

OLEDs have been utilized in next-generation flat-panel displays and solid-state lighting technologies due to the variable advantages which have been attracting the attention from both academic and industrial communities. The luminescent materials that are employed in OLED devices include small molecular materials and polymeric materials, which can be synthesized by using different synthetic strategies. Therefore, since Tang and VanSlyke reported the first OLED device in 1987, many

organic luminescent materials with advanced device performances have been reported, which has significantly promoted the progress of OLEDs.

In general, the electroluminescence (EL) quantum efficiency is the most essential parameter for an OLED device and in particular the EQE, which is defined as the ratio of the number of emitted photons outside the device to the apparent number of charges injected into the device. It is well known that exciton formation under electrical excitation typically results in 25% singlet and 75% triplet excitons. As mentioned above, only the radiative transition process of singlet excitons from the S_1 state to the S_0 state can be utilized for emitting light, i.e., fluorescence, which is quantum mechanically allowed. Therefore, in organic fluorescent materials, the electrically generated 75% triplet excitons are emitted as heat rather than light. Even if the photoluminescence quantum efficiency (PLQY) of conventional fluorescent molecules can reach nearly 100%, in theory, the EQE maximum value may only reach roughly 5% due to the light out-coupling efficiency of ~20% in the OLED device. Therefore, in order to increase the efficiency of OLED devices, it is necessary to break the theoretical upper limit of quantum efficiency and utilize the non-emissive triplet exciton as much as possible. The study of harvesting both singlet and triplet excitons for EL is attractive for the enhancement of OLED device efficiency. Several strategies based on emissive molecules with special photophysical characteristics have been introduced to “turn on” these non-emissive triplet excitons for emission in OLEDs.

The most successful type of materials for higher OLED efficiencies are phosphorescent emitters that are based on organic metal complexes, which emit from the T_1 state to the S_0 state. In phosphorescent molecules, both the intersystem crossing (ISC) of singlet excitons from the S_1 state to the T_1 state and the transition

of triplet excitons from the T_1 state to the S_0 state are dramatically enhanced by the spin-orbit coupling from heavy metal atoms. Thus, both triplet and singlet excitons can be finally harvested for phosphorescence, resulting in nearly 100% internal quantum efficiency of the device. With respect to green and red host-dopant PHOLED systems, high external quantum efficiency (EQE) values of over 20% can be attained, and even values of over 30% can also be reached in some systems. However, the metals that are used in these emissive organic metal complexes are confined to a few noble metals, such as Iridium and Platinum. In addition, due to the limited global resources of these noble metals they are rather expensive, leading to the currently higher cost of OLED products compared to their LCD counterparts. Development of phosphorescent blue emitting materials have become a bottleneck due to the low color purity, low efficiency and inefficient operation lifetimes for commercial applications.

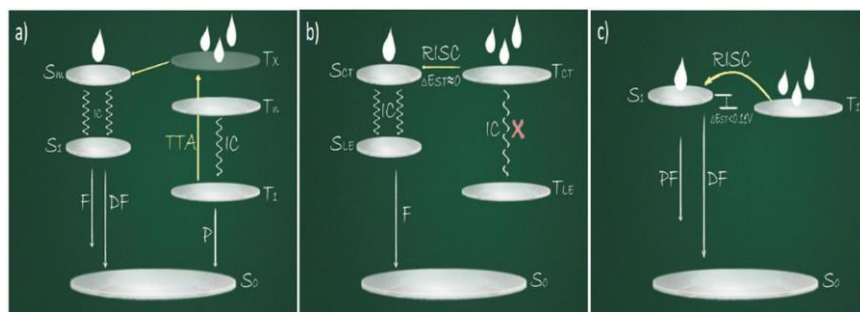


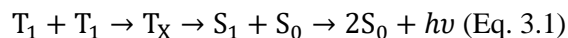
Figure 3.2. Triplet exciton harvesting process of a) TTA, b) HLCT and c) TADF.

Copyright 2017, The Royal Society of Chemistry.¹²⁹

In pursuit of cheaper luminescent materials and developing state-of-the-art emitter materials for OLED applications, several other strategies to harvest the 75% triplet excitons for luminescence, such as triplet-triplet annihilation (TTA), hybridized local and charge-transfer state (HLCT) and thermally activated delayed fluorescence (TADF), have also been utilized. Among them, TADF-based materials for OLEDs have attracted more attention and have experienced the most rapid progress in recent years.

1.1. TTA

The process to harvest triplet excitons by TTA utilizes a bimolecular process of two triplet excitons (Figure 3.2a). Because triplet excitons are lived longer than singlet excitons, bimolecular interactions can easily occur. In the TTA process, two excited molecules in the triplet states combine their energy to produce one excited molecule in a high-lying singlet state, whose energy is close to twice that of the original triplet one. Then, the generated additional singlet excitons emit delayed fluorescence (DF) with a long lifetime and contribute to the light output of the OLED device. In general, this P-type (first observed for pyrene) DF can be described by the following two-process reaction.¹³⁰



Where T_1 , S_1 and S_0 stand for the lowest triplet excited state, the lowest singlet excited state and the ground state, respectively. In this process, the two adjacent molecules in the triplet excited state recombine to generate a singlet excited molecule and another molecule in the ground state, in which a long-lived DF can be observed when the singlet exciton releases its energy radiatively. It differs from the prompt

fluorescence (PF) process, in which the lifetime of such DF is much longer and approximately half that of the triplet exciton in dilute solution.^{2, 131} However, the efficiency of generating singlet excitons by TTA is only 37.5% at maximum depending on the up-conversion ratio. Thus, it is worth noting that the theoretical maximum of exciton utilization for luminescence is 62.5% for TTA-based OLEDs. To obtain an efficient TTA process, concentrated triplet excitons in a device are essential, which results in inevitable device efficiency roll-off.

1.2. HLCT

Another successful utilization of non-emissive triplet excitons is in harvesting the hot triplet excitons in a HLCT state (Figure 3.2b). Located Excitons in the upper excited state called hot excitons are higher than the S_1 and T_1 .¹³² In some cases, the exchange between these singlet and triplet hot excitons may also occur through the reverse intersystem crossing (RISC) in the HLCT state. In this manner, all the non-emissive triplet excitons may be converted into emissive singlet excitons, which can enhance the internal quantum efficiency of OLED devices.

Some principles for designing HLCT materials have been proposed, in which the molecule should ideally contain electron donor (D) and electron acceptor (A) units. After excitation of such a molecule is accompanied with a large dipole moment which HOMO and LUMO are separated. In order to obtain a more stable state, the molecule should adjust and twist its geometry between the D and A moieties. In this situation, when the bond between D-A in the molecule is weakened, some materials show the HLCT state depending on the angle of twist in the ratio of local excited (LE) and charge transfer (CT) state.^{48, 133} The LE state provides high efficiency fluorescence emission, while the charge transfer CT state possesses a weak bonding

energy of the exciton, which promotes the RISC process of hot triplet excitons. In fact, the HLCT state is not a mixture of LE and CT states but a pure excited state and can be verified by a single exponential of the fluorescence lifetime of the material in different polar solvents. The molecular dipole moment exhibits a slow decrease in low polarity solvents and a rapid increase in high polarity solvents, which is a characteristic of the HLCT state.

Theoretically, a HLCT device can achieve 100% exciton utilization efficiency when all non-luminescent triplet excitons are transferred to singlet ones via RISC. However, it is difficult to directly observe both DF and breakthrough of the singlet exciton ratio of 25% in the HLCT apparatus. Also, the proposed RISC process involving hot excitons at higher energy excited levels only shown from indirect experimental evidence. On the other hand, according to Kasha's rule, the majority of the excited molecules tend to preferentially occupy the S_1 or T_1 states instead of the upper excited states. Thus, it is difficult that the internal conversion (IC) process to T_1 state of the hot triplet excitons is blocked in HLCT molecules. The construction and synthesis of a molecular system with a HLCT excited state structure is very challenging and also hard to verify.

1.3. TADF

The most promising and efficient approach to harvest triplet excitons involving the RISC process is the utilization of TADF emitters. This endothermic up-conversion of the RISC process from the T_1 to S_1 state can be thermally activated when the energy gap (ΔE_{ST}) between the participating S_1 and T_1 states is small and the lifetime of the T_1 excitons is long enough (Figure 3.2c).^{4, 134-135} The RISC up-conversion will result in emission with the almost same spectral distribution as PF

but with a much longer decay time. In a TADF emitter, such RISC up-conversion can be easily activated by the thermal motion of the molecule, at sufficient temperatures (>300 K). It allows all of the excitons that are generated upon electrical excitation in an OLED to eventually produce light through singlet decay, leading to a great breakthrough of the exciton statistical limit in fluorescent materials from 25% to 100%. (Despite the development of highly efficient TADF emitters involving metal-organic complexes, pure organic TADF-based materials are more promising for practical applications due to the relative ease in molecular structure modification.) Due to the continued efforts of researchers from around the world, OLEDs fabricated from pure organic TADF materials display colors covering the whole visible region and compete with PHOLEDs in terms of efficiency.

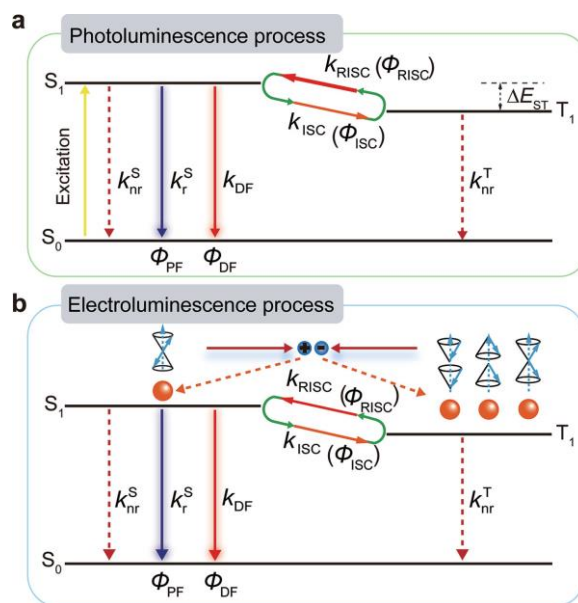


Figure 3.3. Photoluminescence (a) and electroluminescence (b) processes in TADF molecules. k_r^S and k_{DF} are the rate constants of PF and DF process, respectively; k_{ISC}

and k_{RISC} are the ISC and RISC rate constants, respectively; k_{nr}^{S} and k_{nr}^{T} are the non-radiative decay constants of S_1 and T_1 respectively; Φ_{PF} , Φ_{DF} , Φ_{RISC} , and Φ_{ISC} represent the prompt fluorescence efficiency, TADF efficiency, reverse intersystem crossing efficiency, and intersystem crossing efficiency, respectively. Copyright 2014, Wiley-VCH.¹

2. About TADF

2.1. Key process of TADF

Two distinct unimolecular mechanisms exist for thermally activated delayed fluorescence (Figure 3.3): PF and DF.¹³⁶⁻¹³⁷ In the PF mechanism of singlet excitons, the emission occurs almost immediately (within several nanoseconds) after the excitation with a fast decay from the S_1 to S_0 state. In the DF mechanism, triplet excitons have to be converted into luminescent singlet excitons for the PF process via a RISC mechanism; the additional process before fluorescence emission delays the luminescent process, leading to an increased fluorescent lifetime up to several microseconds.

When TADF materials are optically excited (Figure 3.3a), triplet excitons are formed after an efficient ISC process and both PF and DF can be observed with two different fluorescent lifetimes although they have the same spectral distribution as normal fluorescence. In devices, four important processes for TADF emission should be mentioned (Figure 3.3b): (1) singlet and triplet excitons are formed after electron/hole recombination in a singlet-to-triplet ratio of 1:3; (2) the high exciton states are transferred to the lowest exciton states (S_1 or T_1) via quick vibrational relaxation and IC; (3) the accumulated triplet excitons at T_1 are back transferred to S_1 via RISC process with the aid of thermal activation; (4) the singlet excitons at S_1 formed either initially after electronic excitation or back-transferred from T_1 are radiatively deactivated to S_0 following the PF mechanism for fluorescent emissions with different luminescence lifetimes of PF and DF. Some key parameters, such as rate constant of ISC (k_{ISC}) and RISC (k_{RISC}) as well as ΔE_{ST} , should be taken into strict consideration. Theoretically, the decay rate of S_1 and T_1 after removing the

excitation source can be written in Equation 3.2 and 3.3 under consideration of all of their decay channels as illustrated in Figure 3.3.

$$\frac{d[S_1]}{d[t]} = -(k_r^S + k_{nr}^S + k_{ISC})[S_1] + k_{RISC}[T_1] \quad (\text{Eq. 3.2})$$

$$\frac{d[T_1]}{d[t]} = -(k_{nr}^T + k_{RISC})[T_1] + k_{ISC}[S_1] \quad (\text{Eq. 3.3})$$

The solution of these differential equations can be expressed in a biexponential form as

$$[S_1] = C_1 \exp(k_{PF}t) + C_2 \exp(k_{DF}t) \quad (\text{Eq. 3.4})$$

where,

$$k_{PF}, k_{DF} = \frac{k_r^S + k_{nr}^S + k_{ISC} + k_{nr}^T + k_{RISC}}{2} \times \left(1 \pm \sqrt{1 - \frac{4(k_r^S + k_{nr}^S + k_{ISC})(k_{nr}^T + k_{RISC}) - 4k_{ISC}k_{RISC}}{(k_r^S + k_{nr}^S + k_{ISC} + k_{nr}^T + k_{RISC})}} \right) \quad (\text{Eq. 3.5})$$

when there are negligible deactivation channels from T_1 , the values of k_r^S , k_{nr}^S and k_{ISC} are significantly larger than those of k_{nr}^T and k_{RISC} . As a result, k_{PF} and k_{DF} can be approximated by the following formulas:

$$k_{PF} = k_r^S + k_{nr}^S + k_{ISC} \quad (\text{Eq. 3.6})$$

$$k_{DF} = k_{nr}^T + \left(1 - \frac{k_{ISC}}{k_r^S + k_{nr}^S + k_{ISC}} \right) k_{RISC} \quad (\text{Eq. 3.7})$$

Quantum efficiencies of Φ_{PF} , Φ_{DF} , Φ_{ISC} and Φ_{RISC} are written as:

$$\Phi_{PF} = \frac{k_r^S}{k_r^S + k_{nr}^S + k_{ISC}} = \frac{k_r^S}{k_{PF}} \quad (\text{Eq. 3.8})$$

$$\Phi_{DF} = \sum_{k=1}^{\infty} (\Phi_{ISC} \Phi_{RISC})^k \Phi_{PF} = \frac{\Phi_{ISC} \Phi_{RISC}}{1 - \Phi_{ISC} \Phi_{RISC}} \Phi_{PF} \quad (\text{Eq. 3.9})$$

$$\Phi_{\text{ISC}} = \frac{k_{\text{ISC}}}{k_{\text{r}}^{\text{S}} + k_{\text{nr}}^{\text{S}} + k_{\text{ISC}}} = \frac{k_{\text{ISC}}}{k_{\text{PF}}} \text{ (Eq. 3.10)}$$

$$\Phi_{\text{RISC}} = \frac{k_{\text{RISC}}}{k_{\text{RISC}} + k_{\text{nr}}^{\text{T}}} \text{ (Eq. 3.11)}$$

Experimentally, the fluorescence efficiency of PF (Φ_{PF}) and DF (Φ_{DF}) are distinguished from the total photoluminescence quantum yields (PLQY) by comparing the integrated intensity of their components in the transient photoluminescence spectra, according to their different luminescent lifetime.⁵ The two fluorescent lifetimes (τ_{PF} and τ_{DF}) can be revealed by fitting the decay curve of the time-resolved PL spectrum. Then their rate constants (k_{PF} and k_{DF}) can be obtained experimentally using Equation 3.12 and 3.13.

$$k_{\text{PF}} = \frac{\Phi_{\text{PF}}}{\tau_{\text{PF}}} \text{ (Eq. 3.12)}$$

$$k_{\text{DF}} = \frac{\Phi_{\text{DF}}}{\tau_{\text{DF}}} \text{ (Eq. 3.13)}$$

From Equation 3.6 to 3.10, both PF and DF processes are strongly related to the ISC, which is a non-radiative transition between two iso-energetic vibrational levels belonging to electronic states of different multiplicities.¹³⁷ Assuming that the non-radiative rate constants of the triplet state (k_{nr}^{T}) are significantly lower than k_{RISC} when T_1 is relatively stable, the quantum yield of the RISC is almost 100% ($\Phi_{\text{RISC}} \approx 1$), and thus, the k_{ISC} can be obtained from Equation 3.9 and 3.10.

$$k_{\text{ISC}} = \frac{\Phi_{\text{DF}}}{\Phi_{\text{PF}} + \Phi_{\text{DF}}} k_{\text{PF}} \text{ (Eq. 3.14)}$$

The rate of the intersystem crossing (k_{ISC}) was reported to be in the order of $10^6 \sim 10^{11} \text{ s}^{-1}$ in TADF molecules.^{4, 138-139}

The key process in the TADF phenomenon is the facilitated RISC ($T_1 \rightarrow S_1$) when the energy difference between S_1 and T_1 is small and T_1 is stable enough. Because RISC is a non-radiative transition from the lower vibrational level of T_1 to the higher one of S_1 in an excited molecule, the DF efficiency (Φ_{DF}) and its transient lifetime (τ_{DF}) are highly dependent on the RISC rate constant (k_{RISC}). According to Equation 3.7, 3.9, 3.10 and 3.11, k_{RISC} can be determined as follow:

$$k_{RISC} = \frac{k_{DF}\Phi_{RISC}}{1-\Phi_{ISC}\Phi_{RISC}} = \frac{k_{DF}k_{PF}\Phi_{DF}}{k_{ISC}\Phi_{PF}} \text{ (Eq. 3.15)}$$

From Equation 3.15, the rate of the reverse intersystem crossing (k_{RISC}) in TADF molecules is generally in the order of $10^3 \sim 10^6 \text{ s}^{-1}$ in TADF molecules, which is usually lower than k_{ISC} .^{4, 138-139}

RISC is temperature sensitive process. The dependence of the rate constant of RISC (k_{RISC}) on temperature can be expressed in a Boltzmann distribution relation. (Equation 3.16)

$$k_{RISC} \propto \exp \frac{\Delta E_{ST}}{k_B T} \text{ (Eq. 3.16)}$$

where k_B is the Boltzmann constant and T is the temperature. However, in most fluorescent materials TADF is negligible because of their large ΔE_{ST} , within the range of 0.5-1.0 eV, which is more than an order of magnitude greater than the thermal energy per particle at room temperature.¹⁴⁰ The ΔE_{ST} can be defined as follows the equation. (Equation 3.19).

$$E_S = E + K + J \text{ (Eq. 3.17)}$$

$$E_T = E + K - J \text{ (Eq. 3.18)}$$

$$\Delta E_{ST} = E_S - E_T = 2J \text{ (Eq. 3.19)}$$

where E is the orbital energy, K is the electron repulsion energy and J is the exchange energy.¹⁴¹ Hence, ΔE_{ST} which is the difference between E_S and E_T , is equal to the twice of J (equation 3.5). At S_1 or T_1 , the unpaired two electrons are mainly distributed on the frontier orbitals of the HOMO and LUMO, respectively, with the same J value regardless of the different spin states. Therefore, J of these two electrons at HOMO and LUMO can be calculated by equation 3.20.¹⁴²

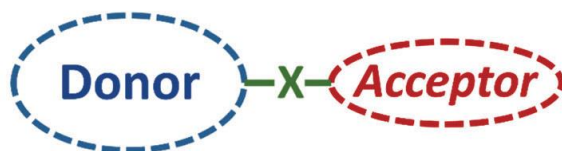
$$J = \iint \phi_L(1)\phi_H(2) \left(\frac{e^2}{r_{1-2}} \right) \phi_L(2)\phi_H(1) dr_1 dr_2 \text{ (Eq. 3.20)}$$

where Φ_H and Φ_L represent the HOMO and LUMO wave functions, respectively; e is the electron charge. From Equation 3.6, it is clear that a small ΔE_{ST} can be resulted via a small overlap integral of $\langle \Phi_H | \Phi_L \rangle$, i.e., via spatial wave function separation of HOMO and LUMO.¹⁴³⁻¹⁴⁴

Besides the ΔE_{ST} and k_{RISC} , a relatively large radiative rate constant (k_r) of the singlet exciton transition from the S_1 state to the S_0 state is also important to get efficient TADF emission. However, because of large k_r and small ΔE_{ST} are conflicted, molecular structures should be designed carefully to realize them simultaneously. For example, some ketone derivatives possess a relatively small ΔE_{ST} but only exhibit phosphorescence at low temperature instead of DF at room temperature because of the large k_r of their T_1 excitons.¹⁴⁵ On the other hand, due to their special conjugation break that results from the twisted central carbonyl group, several diphenyl ketones with different donor groups attached to the phenyl ring exhibit interesting dual emission and white light emission with TADF properties.¹⁴⁶

2.2. Design principles of organic TADF molecules

Key goal: Moderate radiative decay rate k_r with small ΔE_{ST}



Methods: Donor-Acceptor backbone

(1) X: Separation of HOMO and LUMO (small ΔE_{ST})

- (a) Introduction of steric hindrance;
- (b) Spiro linker, physical separation of donor and acceptor units;
- (c) X-shaped molecular structure;
- (d) Multiple resonance effect.

(2) Increase the radiative decay rate (k_r)

Increasing the overlap density distribution between the S_0 and S_1 states;
large delocalization of molecular orbitals.

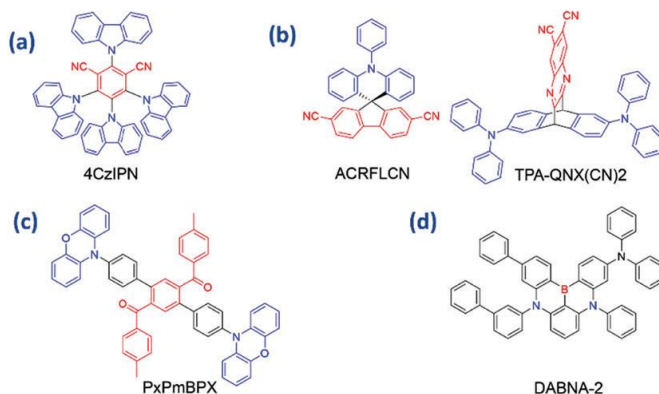


Figure 3.4. Design principles for D-A type TADF molecules. Copyright 2017, The Royal Society of Chemistry.¹²⁹

As mentioned above, TADF characteristics depend on a small ΔE_{ST} to aid the RISC from the triplet to the singlet excited state. A relatively large k_r of S_1 excitons is a requirement for obtaining a high EL efficiency. However, as large k_r and small ΔE_{ST} are conflicting, fine molecular design is required to realize them

simultaneously for efficient TADF OLEDs. It has been found that the electron-donating and electron-accepting interactions from intramolecular or intermolecular charge transfer can realize small ΔE_{ST} by reducing the overlap of the HOMO and LUMO of the molecules. To date, the reported organic TADF materials can be divided into two categories: (1) pure organic D-A molecular systems and (2) organic exciplex systems with two individual donor and acceptor materials.

The design principles of the pure D-A type TADF materials so far summarized are as follows (Figure 3.4). To achieve small ΔE_{ST} , D-A molecular structure with a twist between the donor and acceptor moieties, caused by bulky substituents or a spiro-junction is needed. And densely combining donors and acceptors as well as strengthening the rigidity of the molecular structure to enhance radiative luminescence efficiency is needed for high k_r . On the other hand, for increasing the radiative decay rate from the S_1 to S_0 states with small ΔE_{ST} , two approaches have been found. One is way to increase the overlap density (ρ_{10}) distribution between the electronic wave functions of the ground state, in which the S_1 state can promote $S_1 \rightarrow S_0$ radiative decay to improve the PLQY of the TADF emitter.¹⁴⁷ Another approach is to suppress a decrease in radiative decay rate for fluorescence (k_f) with lowering ΔE_{ST} through large delocalization of molecular orbitals with well-separated HOMO and LUMO levels.¹⁴⁸

Recently, several new design strategies for efficient TADF molecules have been presented in the literature. From a structural point of view, for separation of HOMO and LUMO for small ΔE_{ST} , several new molecular design methods have been presented, including physical separation of D and A units,¹⁴⁹ X-shaped molecular structures,¹⁵⁰ dual D/A units, and multiple resonance effect.¹⁵¹ Also, in view of the luminescence characteristics, some novel TADF materials have been

proposed, such as asymmetric structures with two different donors¹⁵² to construct TADF materials showing novel properties (including aggregation induced emission (AIE) or dual emission).

3. Development of TADF emitters

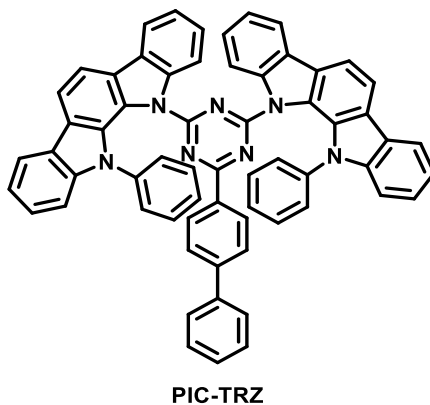


Figure 3.5. Chemical structure of **PIC-TRZ**.

The first purely organic TADF emitter **PIC-TRZ** (Figure 3.5) was reported in 2011 by Adachi et al.¹⁰³ Limited by its PLQY of 39% in doped thin film (6 wt% in mCP) and only 32% triplet utilization efficiency, the device using **PIC-TRZ** as an dopant shows an EQE of 5.3%. With the explosion of interest in the development of TADF emitters, there have been more than 100 new compounds reported. Numerous other TADF devices show an EQE of greater than 20%.

3.1. Blue TADF emitters

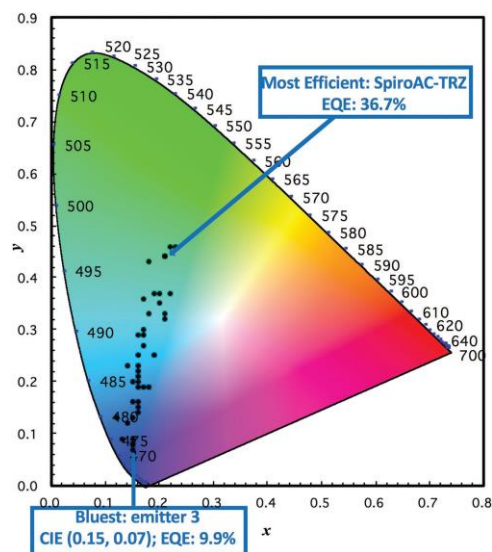


Figure 3.6. Summary of CIEs of blue TADF OLEDs. Copyright 2014, Wiley-VCH.¹

Blue emitters define under around 500 nm in electroluminescence peak wavelength (EL λ_{max}). The distribution of CIE coordinates for the OLEDs reported in this section is shown in Figure 8.6.

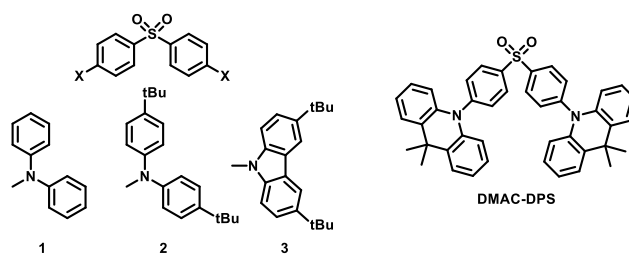


Figure 3.7. Chemical structures of sulfone-based blue TADF emitters.

In 2012, Adachi et al. reported the very first class of deep-blue TADF emitters (**1-3**) (Figure 3.7) based on diphenylsulfone as the acceptor.⁴ The best device within the study shows an EQE of 9.9% and CIE coordinates of (0.15, 0.07) with **3** used as the emitter. The authors suggested that in order to achieve a small ΔE_{ST} , the energy gap between the lower energy triplet donor-centered locally excited $\pi-\pi^*$ state (3LE) and the higher-energy triplet charge-transfer state (3CT) must be small. This hypothesis was verified by the appearance of delayed fluorescence when the medium of the emitter was changed from nonpolar hexane to polar methanol, where the 3CT is significantly stabilized, evidenced by the positive solvatochromic shift. Under these conditions reverse internal conversion (RIC) occurs from 3LE to 3CT , followed by efficient RISC to 1CT . Nevertheless, it is particularly challenging to design deep-blue TADF emitters that adhere to this ordering of excited states because of the high intrinsic energies of charge-transfer singlet and triplet states. Control of the conjugation length (e.g., through sterics¹⁵³ or substitution pattern¹⁵⁴⁻¹⁵⁵) and the choice of donor are important in this regard. However, Dias et al. proposed another plausible mechanism of RISC in this type of molecule.¹⁵⁶ They performed a detailed photophysical study on a series of emitters and found that, for emitters with ΔE_{ST} greater than 0.3 eV, RISC is still possible and may even be very efficient. The presence of heteroatom lone pairs form an important “hidden” $^3n-\pi^*$ state sandwiched between the higher 3CT and the lower 3LE state. Thus, up-conversion happens in an even more complex cascade manner: $^3LE \rightarrow ^3n\pi^* \rightarrow ^3CT \rightarrow ^1CT$.

In another publication by the same group, a structurally similar blue TADF emitter **DMAC-DPS** showed an EQE of 19.5%.¹⁰² The choice of the dimethylacridan donor results in a higher 3LE state than 3CT state, producing a small ΔE_{ST} of 0.08 eV. The methyl groups on the acridan moiety of **DMAC-DPS** prevent

intermolecular interactions in its neat film. Moreover, the Stokes shift of the emitter is sufficiently large to prevent self-quenching by Forster resonance energy transfer (FRET). As a result, both PLQYs and delayed component emission lifetimes of **DMAC-DPS** in neat (88%) and doped film (80%) are fairly similar. Among the original diphenylsulfone-based deep-blue TADF emitters, **DMAC-DPS** is the most promising due its smallest ΔE_{ST} and high solid state PLQY. This suggests the use of acridan donors is preferable to using carbazole or diphenylamine donors. This can be attributed to the electron richness of the acridan donor, which promotes greater HOMO and LUMO separation, along with its highly rigid structure, which contributes to reducing non-radiative decay paths from the excited state.

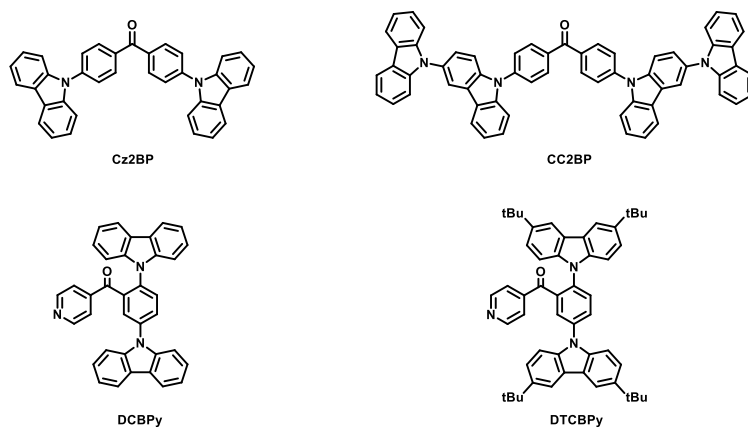


Figure 3.9. Chemical structures of benzophenone-based blue TADF emitters.

A benzophenone-type acceptor can also be used in the design of blue TADF emitters. Lee et al. fabricated two blue devices using **Cz2BP** and **CC2BP** as the blue emitters (Figure 3.9).¹³⁵ **CC2BP**, with an extended carbazole donor system, exhibits

a smaller ΔE_{ST} than **Cz2BP** by 0.07 eV. This also enhances the donor strength in **CC2BP** compared with **Cz2BP** and results in a significant redshifted emission (31 nm). Rajamalli et al. reported two novel TADF emitters based on a benzoylpyridine acceptor **DCBPy** and **DTCBPy** (Figure 3.9).¹⁵⁷ The only difference between these two emitters is the presence of *tert*-butyl groups in the **DTCBPy**. Given their modest electron-donating nature, **DTCBPy** shows a small redshift in emission wavelength by only 4 nm. Intramolecular through-space interaction between the *ortho*-carbazole donor and the benzoylpyridine acceptor is believed to induce efficient TADF. The interaction also suppresses intermolecular aggregation in the solid state, and thus the PLQY in the solid state is greatly enhanced in doped film (up to 90%) compared with solution. Compared with the **Cz2BP** and **CC2BP** series, **DCBPy** and **DTCBPy** have redshifted emission due to the enhanced acceptor strength conferred by the pyridine group in these molecules, which is evidenced by their deeper LUMO levels.

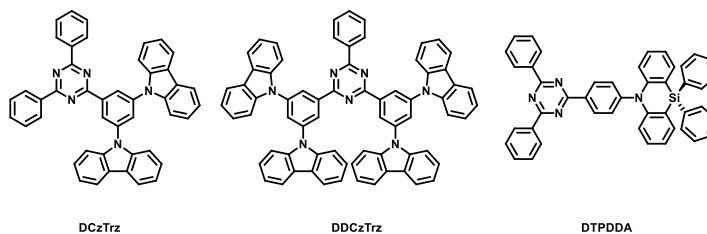


Figure 3.10. Chemical structures of 1,3,5-triazine-based blue TADF materials

1,3,5-triazine is one of the most common acceptors used for blue TADF emitters. In 2015, Kim et al. reported two blue TADF emitters **DCzTrz** and **DDCzTrz** with the only difference being two additional carbazole moieties attached to the phenyl ring in a *meta* fashion in **DDCzTrz**. (Figure 3.10) As “meta linkages”

limit conjugation length, the two emitters have similar emission energies and ΔE_{ST} . This approach effectively limits the conjugation length of the whole molecule as the number of π -conjugated systems keeps increasing in order to avoid redshifts in the emission and lowering of the triplet energy level.^{154-155, 158} In particular, this device shows an LT_{80} (the time required for the luminance to drop to 80% of its initial value) of 52 h, which is approximately three times longer than the common blue phosphorescent materials. The carbazole and triazine moieties are robust and the nearly planar structure of the molecule gives the peripheral carbazole moiety further stabilization through conjugation with the triazine, and the nature of charge transfer makes the excited state resemble a pair of positive carbazole and negative triazine polarons. These two reasons contribute positively to the device stability. Tsai et al. reported a sky-blue TADF emitter **DMAC-TRZ**. (Figure 3.10) Acridan, being a stronger donor than carbazole, redshifts the **DMAC-TRZ** compared with carbazole-based triazine TADF emitters. Interestingly, the emitter also demonstrates an excellent EQE of 20% in the absence of a host. Indeed, the PLQYs of the emitter in doped thin film (90%) and neat film (83%) are very similar, which is attributed to the methyl groups on the acridan unit that serve via sterics to suppress intermolecular interactions. Sun et al.¹⁵⁹ reported a potent deep-blue TADF emitter **DTPDDA** whose device performance reaches an outstanding EQE of 22.3% with CIE coordinates of (0.15, 0.20). (Figure 3.10) Silicon was chosen for its rigid tetrahedral configuration, which, due to its size, effectively suppresses nonradiative decay pathways and enhances the morphological stability of the molecule.

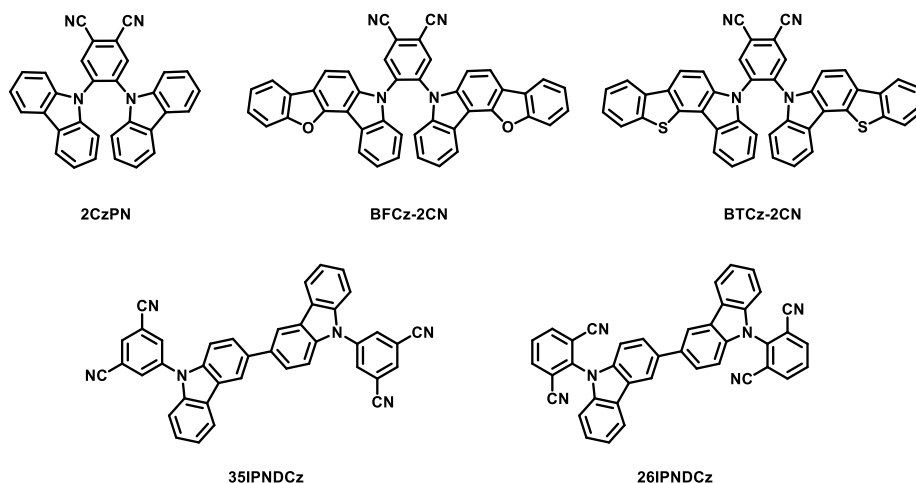


Figure 3.11. Chemical structures of cyano-based blue TADF materials

Cyano-based acceptors are some of the most common building blocks used for blue TADF emitters. The first of these reported by Adachi et al. is **2CzPN** (Figure 3.11), which generated a skyblue device with a decent EQE of 8.0% and EL λ_{\max} at ≈ 480 nm.¹³⁹ Lee et al. prepared two derivatives of **2CzPN** by replacing carbazole with benzofurocarbazole and benzothienocarbazole (Figure 3.11).¹⁶⁰ These derivatives have higher PLQYs but similar emission energies (94.6% and 94.0%, respectively compared with 47% for **2CzPN** probably due to the higher rigidity of benzofurocarbazole and benzothienocarbazole donors in addition to more efficient RISC processes. Li et al. compared two TADF emitters **26IPNDCz** and **35IPNDCz** to study the effect of the nitrile substituent position on the photophysical properties and device performance.¹⁶¹ With *ortho* substitution, the dihedral angle between the dicyanobenzene acceptor and the 3,3'-bicarbazolyl donor in **26IPNDCz** (69°) is larger than **35IPNDCz** (50°) due to the steric interactions between the nitriles and the donor moiety. Thus, a reduced exchange integral between the HOMO and the

LUMO is realized in **26IPNDCz**, resulting in a smaller ΔE_{ST} , evidenced by the markedly shorter delayed component lifetime (9.2 μs) than that of **35IPNDCz** (145 μs). The larger dihedral angle in **26IPNDCz** also limits the conjugation length, resulting in a slightly blue-shifted emission compared with **35IPNDCz**.

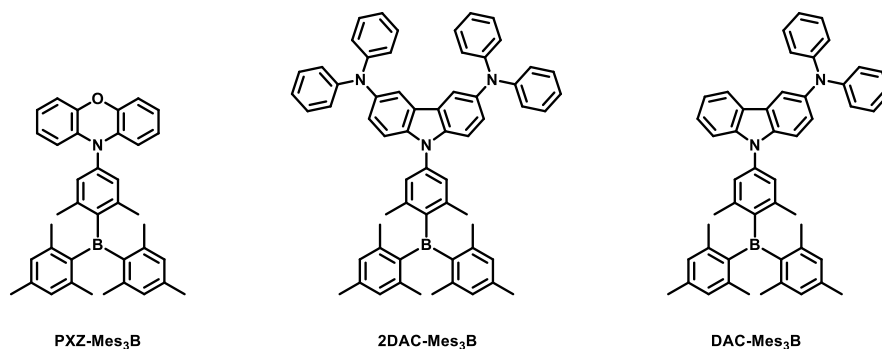


Figure 3.12. Chemical structures of boron-based blue TADF emitters.

Boronbased TADF emitters **PXZ-Mes₃B**, **2DAC-Mes₃B** and **DAC-Mes₃B** use triarylboron as the acceptor (Figure 3.12).¹⁶² **PXZ-Mes₃B** demonstrated the most red-shifted emission of the three emitters in the study due to its strong electron-donating power of phenoxazine moiety. In general, most of boron-based blue TADF emitters show small ΔE_{ST} (< 0.18 eV), probably because of the strong LUMO localization effect induced by the boron atom. Additionally, the majority of these emitters exhibit excellent PLQYs in the solid state (87~100%). These results suggest that boron-based TADF scaffold is a potent avenue for blue TADF emitters.

3.2. Green-Yellow TADF emitters

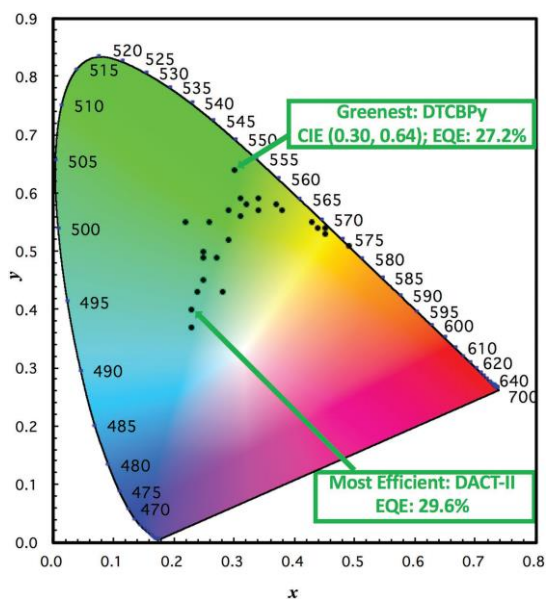


Figure 3.13. Summary of CIEs of green to yellow TADF OLEDs. Copyright 2014, Wiley-VCH.¹

Green to yellow emitters define between 500 to 580 nm in electroluminescence peak wavelength (EL λ_{\max}). The distribution of CIE coordinates for the OLEDs reported in this section is shown in Figure 3.13. A vast majority of green-to-yellow TADF emitters contain cyano-based acceptors. (Figure 3.14) Since initial report of Adachi group, **4CzIPN** has become the representative green TADF emitter and has been frequently used in photophysical,^{138, 163} mechanistic,¹⁶⁴⁻¹⁶⁷ host^{28, 168-173} and device-optimization studies.¹⁷⁴⁻¹⁷⁸ Lee et al. modified **4CzIPN** by adding solubilizing *tert*-butyl groups in **t4CzIPN** an emitter.¹⁷⁹ Taneda et al. prepared a highly efficient TADF material **3DPA3CN**, which demonstrates both 100% PLQY and 100% efficiency of triplet utilization via RISC.¹⁸⁰ Nakagawa et al. reported a yellow TADF emitter **spiro-CN** based on a spirobifluorene scaffold, which was

chosen for its excellent thermal and color stability.⁵ A very small ΔE_{ST} of 57 meV was achieved due to the well separated diphenylamine donor and cyano acceptor groups on the two different fragments of the spirobifluorene unit. The group reported another similarly structured green TADF emitter **ACRFLCN** in which the spiro acridine moiety is used to separate the donor amine and acceptor nitrile groups.¹⁴² Kawasumi et al. reported two TADF emitters **TPA-QNX(CN)₂** and **TPA-RPZ(CN)₂** based on an unusual triptycene scaffold in which a small ΔE_{ST} is realized by installing the diphenylamine donor and dicyanoquinoxaline or dicyanopyrazine acceptors on different arms of the propeller triptycene, which communicate with each other electronically by homoconjugation (i.e., a through-space interaction).¹⁴⁹

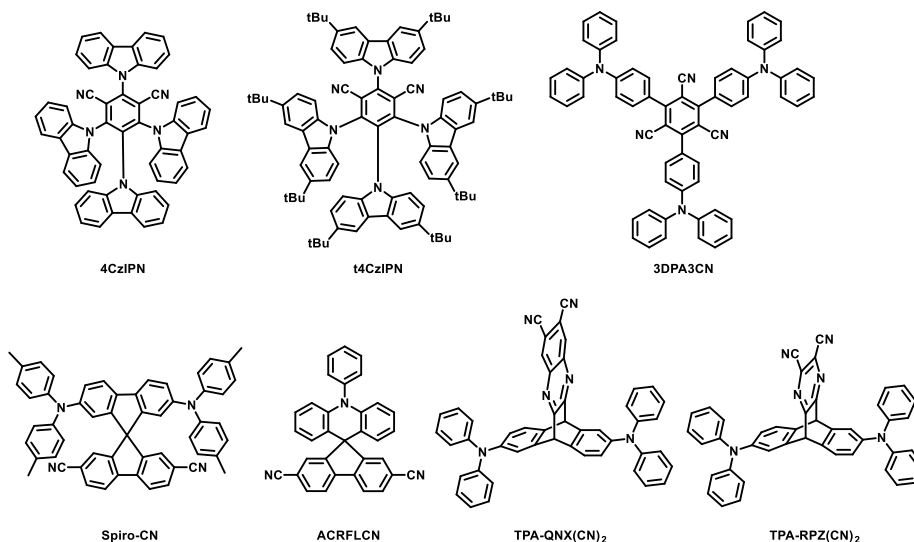


Figure 3.14. Chemical structures of cyano-based green TADF materials.

Cyano-based green TADF emitters can be divided into two classes: i). a monomeric series with *ortho* steric hindrance to realize HOMO and LUMO separation (**4CzIPN**, **t4CzIPN**, **3DPA3CN**, and **4CzCNPy**); ii) a homoconjugation series that relies on through-space interactions to realize HOMO and LUMO separation (**Spiro-CN**, **ACRFLCN**, **TPAPRZ(CN)₂**, and **TPA-QNX(CN)₂**). Monomeric emitters are already very potent green TADF emitters with small ΔE_{ST} (<0.1 eV) and high solid-state PLQYs (81.8~100%). On the other hand, HOMO and LUMO separation can be elegantly achieved by homoconjugation, but those emitters in general suffer from lower PLQYs compared with monomeric emitters. This reflects that homoconjugation limits orbital overlap too substantially, such that the transition dipole moment is significantly weakened, negatively impacting emission efficiency.

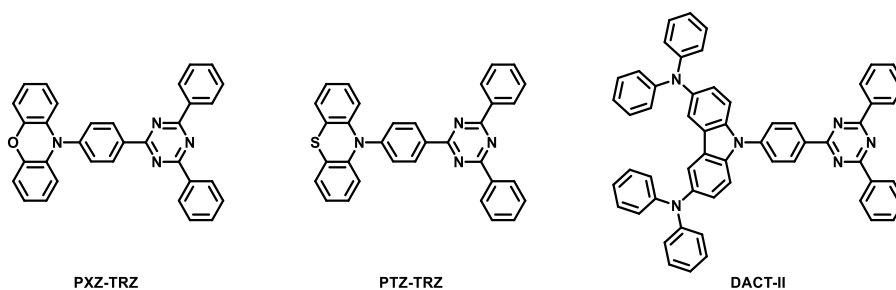


Figure 3.15. Chemical structures of 1,3,5-triazine-based green TADF materials.

Numerous green TADF emitters contain a 1,3,5-triazine acceptor. (Figure 3.15) **PXZ-TRZ** is a green TADF emitter built upon a phenoxazine donor.¹⁸¹ Although the molecule may seem largely planar at first sight, the dihedral angle between the donor and acceptor is indeed as high as 74.9°, based on the crystal

structure, which effectively localizes the HOMO and LUMO. Changing the phenoxazine (PXZ) to phenothiazine (PTZ) results in a dual intramolecular charge-transfer (ICT) emission due to two different conformations of the phenothiazine in the ground state.¹⁸² The former has a large ΔE_{ST} of 1.14 eV while the latter has a much smaller ΔE_{ST} of 0.18 eV, and, therefore, only the latter conformation produces TADF.

DACT-II realizes a simultaneous 100% emission and RISC efficiency, thus giving a state-of-art green device with an impressive EQE of 29.6%.¹⁸³ The excellent photophysical properties of **DACT-II** are a consequence of the fine tuning of the dihedral angle (α) between the central carbazole and the bridging phenyl ring so that the oscillator strength (f) and the ΔE_{ST} can be both optimized (f and ΔE_{ST} both increase with increasing conjugation). The former is responsible for the large radiative decay rate (k_r), and hence boosts the PLQY, while the latter is linked to the efficiency of the RISC process. Therefore, while **PXZ-TRZ**, with a large dihedral angle of 74.9° between the donor and the bridge, shows a PLQY of 66%, the PLQY of **DACT-II** reaches 100%. This result may seem that the torsional angle between the donor and the phenyl bridge plays a crucial role in the balance between PLQY and ΔE_{ST} .

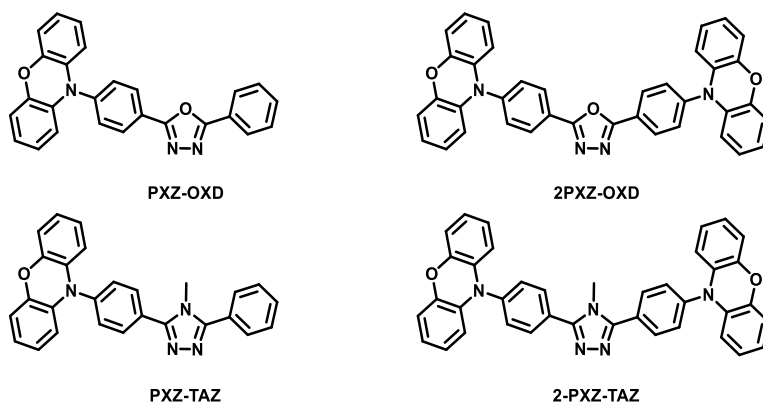


Figure 3.16. Chemical structures of 1,3,4-oxadiazole-, 1,2,4-triazole-based green TADF materials.

1,3,4-Oxadiazole and its derivatives are also commonly found in green TADF emitters. Lee et al. prepared a series of emitters (**PXZ-OXD**, **PXZ-TAZ**, **2PXZ-OXD**, and **2PXZ-TAZ**) based on phenoxazine as the donor and 1,3,4-oxadiazole and 1,2,4-triazole as the acceptor (Figure 3.16).¹⁸⁴ In their study, the D-A-D type molecules (**2PXZ-OXD** and **2PXZ-TAZ**) were found to show higher PLQYs along with a more efficient RISC process compared to D-A type analogs (**PXZ-OXD** and **PXZ-TAZ**).

3.3. Orange-Red TADF emitters

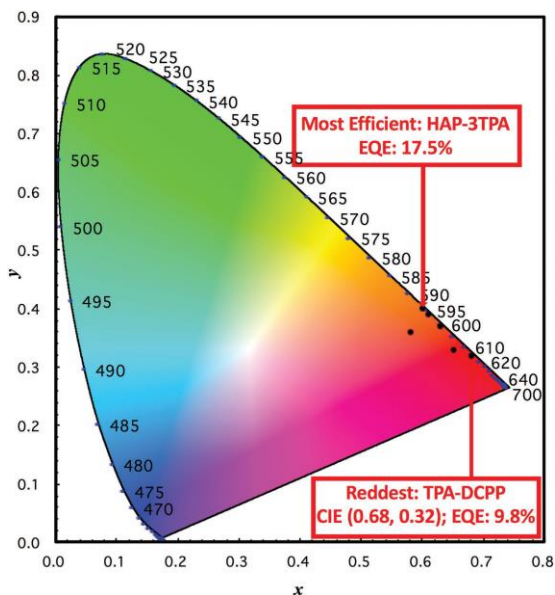


Figure 3.17. Summary of CIEs of orange to red TADF OLEDs. Copyright 2014, Wiley-VCH.¹

The distribution of CIE coordinates for the OLEDs reported in this section is shown in Figure 3.17. Compared with the number of reported blue and green counterparts, red TADF emitters are underexplored. An early orange TADF emitter, **4CzTPN-Ph**, reported by Adachi et al. achieved a remarkable EQE of 11.2% with EL_{\max} at ≈ 590 nm (Figure 3.18).⁴ The same research team then compared two series of anthraquinone-based orange-to-red TADF emitters based on D-A-D (**a1–a4**) and D-Ph-A-Ph-D (**b1–b4**) molecular scaffolds, with the key difference being the presence of an additional phenyl bridge separating the donor and the acceptor (Figure 3.18).¹⁸⁵ It was found that increased separation between the donor and the acceptor conferred by the phenyl bridge in the **b** series results in a higher transition dipole moment and thus an enhanced radiative rate constant, k_r . The phenyl bridge has a

negligible effect on ΔE_{ST} and it was verified by their higher PLQYs. On the other hand, the N-C stretching and twisting observed in D-A-D molecules helps to lower the ΔE_{ST} but at the same time reduces k_r and enhances k_{nr} due to increased vibronic coupling between the excited and ground states.

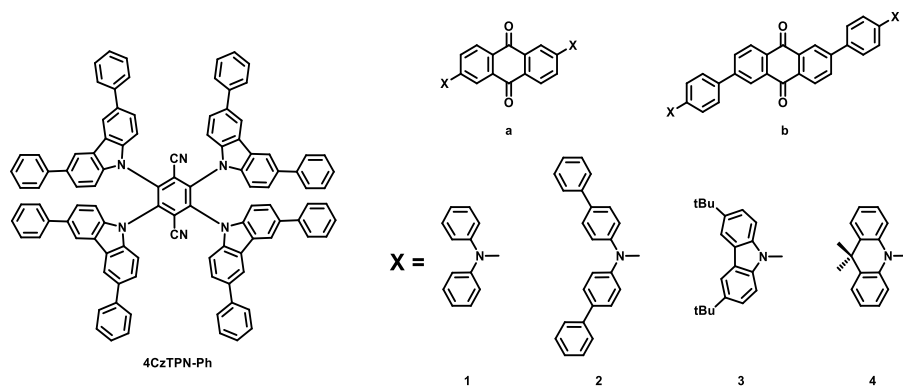


Figure 3.18. Chemical structure of **4CzTPN-Ph** and anthraquinone-based orange-to-red TADF materials.

3.4. Bimolecular TADF system

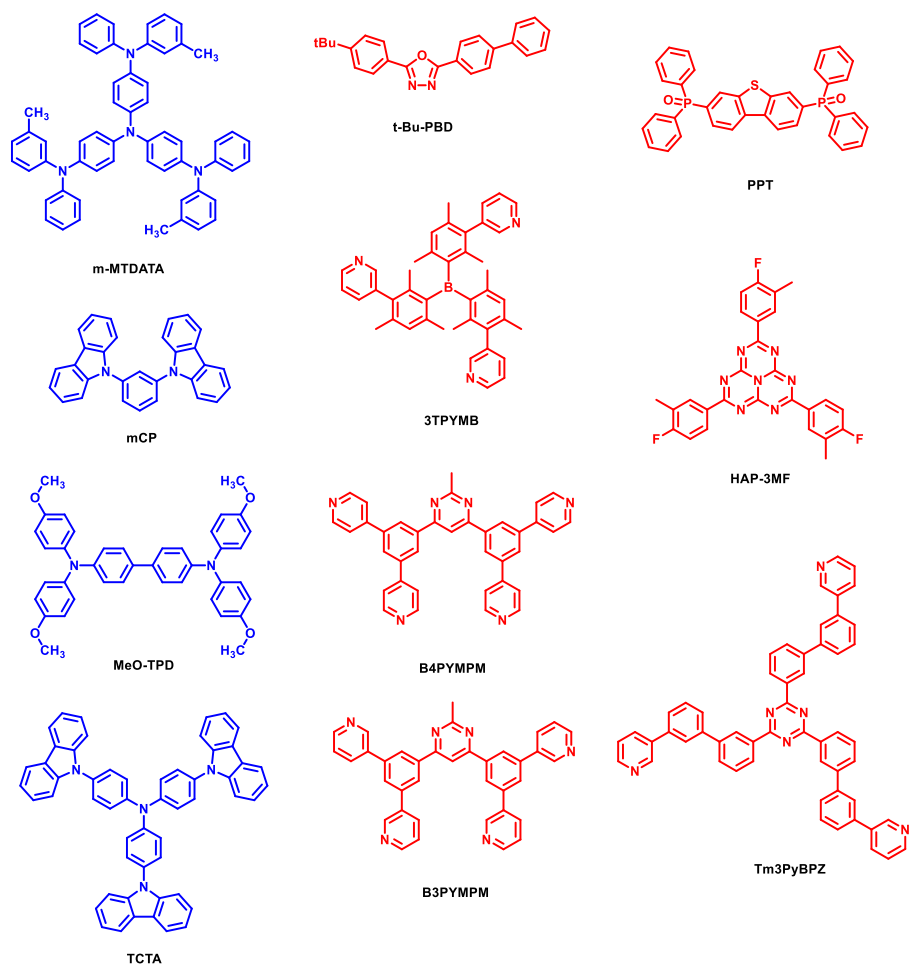


Figure 3.19. Chemical structures of donor (blue) and acceptor (red) materials used in TADF exciplexes.

Delayed fluorescence can also be realized from exciplex formation utilizing the intermolecular excited state between electron-donating and electron-accepting molecules. In principle, the exciplex is well known as a charge transfer state and its emission occurs as a result of electron transition from the LUMO of an acceptor to the HOMO of a donor. There are mainly located on the donor and acceptor molecules

in exciplexes, respectively, which are very close triplet and singlet levels as a result of spatially separated HOMO and LUMO levels. In comparison to intramolecular excited states in monomolecular TADF materials, the intermolecular excited state of an exciplex system can provide a smaller ΔE_{ST} . After the pioneering work regarding exciplex emitters for TADF by Adachi et al. many highly efficient delayed fluorescence exciplex systems have been reported in the last few years.¹⁸⁶⁻¹⁸⁷ High performance OLEDs utilizing exciplexes have also been demonstrated. Two representative ways to form TADF exciplex systems have been developed. The first common way is to mix hole-transport type donor materials with electron-transport type acceptor materials. The second way is to blend with D-A type bipolar materials to form an exciplex, including TADF materials, which generates an intermolecular CT excited state. (As for the TADF exciplex, a high k_{RISC} does not necessarily lead to efficient harvesting of the triplet exciplex if it occurs with a high nonradiative transition rate (k_{nr}) (Figure 3.19).)

Section 1. Highly Efficient Non-doped Thermally Activated Delayed Fluorescent Organic Light-emitting Diodes Using Intra- and Intermolecular Exciplex System by a meta-linked Acridine-Triazine Conjugate

Abstract

Exciton quenching or concentration quenching occurs due to intermolecular interactions between emitters when their intermolecular distance approaches. Alternative design is necessary to prevent intermolecular quenching in a solid environment of OLEDs. Herein, we designed emitters AmT and AmmT in which the donor and acceptor moieties are connected at the *meta* position so that intra- and intermolecular charge transfer (CT) states can be induced through exciplex-like interactions. With AmT or AmmT being closer to each other, intermolecular CT excitons are formed more favourably, which results in higher photoluminescence quantum yield (PLQY) of each emitter in the neat film than in the doped films. Photophysical analysis and single crystal x-ray structure revealed that AmmT is more uniformed and tightly packed in the solid state, leading to more efficient formation of induced intermolecular CT excitons than AmT. EL device using AmmT as an emitter without a host exhibits an EQE over 18%, which is better than the value of AmT, owing to higher intermolecular CT exciton formation via increased intermolecular interactions

Keywords: intramolecular charge transfer, intermolecular charge transfer, thermally activated delayed fluorescence, exciplex, non-doped OLEDs

1. Introduction

Since the report in 1987 by Tang and Vanslyke, organic light-emitting diodes (OLEDs)⁵⁴ have continued to draw attention because of their many possible applications in future displays, from smart phones to large flat panel displays.¹⁸⁸ Previously, the fluorescent emitting layer (EML) of OLED devices was constructed using a host-dopant system (doping system).^{19, 56, 189} Controlling intermolecular interactions through the doping system made it possible to achieve high-efficiency luminescence characteristics by preventing concentration quenching and controlling the color purity. However, the device performance of the doping system would seriously deteriorate during operation because of inherent phase separation.¹⁸⁹ In addition, a scrupulous design of the appropriate host is required based on the energy gap and charge-transporting characteristics of the dopant material. Therefore, developing non-doped (or host-free) emitters is desirable because the non-doped system has a simple device structure that employs only a single emitting material without using a complicated host-dopant co-deposition process.

Recently, there have been continuous efforts to overcome the limitations of fluorescence-based OLED devices by harvesting long-lived triplet excitons through thermally activated delayed fluorescence (TADF) utilizing additionally generated singlet excitons without using heavy atoms.^{4, 103} This approach can provide 100% internal quantum efficiency (IQE) because the triplet can be converted to a singlet because of the small energy difference between the singlet and triplet states (ΔE_{ST}), which leads to efficient reverse intersystem crossing (RISC). TADF molecules, which consist of isolated donor and acceptor moieties, have intramolecular charge transfer (ICT) characteristics and emit light by charge transfer (CT) processes with

a high IQE.¹⁹⁰⁻¹⁹¹ This makes it possible to overcome the efficiency problems of fluorescent materials.

However, TADF molecules can easily aggregate through π - π interactions that arise from their innate hydrophobicity and rigid planar structures and lead to aggregation-caused quenching (ACQ) and exciton concentration quenching in the solid state.^{102, 142, 191} These phenomena cause fatal weakness in OLEDs using solid state emission. To overcome these problems, the doping system was reintroduced into EML of TADF OLED devices, despite the aforementioned drawbacks.¹⁸³ An alternative method to avoid ACQ is to use aggregation-induced emission (AIE).¹⁹²⁻¹⁹³ An external quantum efficiency (EQE) of approximately 10% was obtained in an OLED device using non-doped EML materials that caused AIE and TADF.¹⁹⁴ However, there are a few reports of highly efficient OLED devices using AIE-TADF systems.

Since the report by Kim et al. in 2012, there have been many reports on TADF using intermolecular CT complexes based on two different materials (exciplex system).¹⁹⁵⁻¹⁹⁶ One can easily achieve appropriate charge balance and reduce the quenching process by lowering the charge carrier and exciton density in the EML using exciplex systems.¹⁹⁷⁻¹⁹⁸ Above all, exciplex systems should provide a small ΔE_{ST} . However, exciplex systems require careful consideration of the highest occupied molecular orbital (HOMO) and lowest unoccupied molecular orbital (LUMO) energies of the donor and acceptor, respectively, and it is difficult to match the ratio of the donor and acceptor materials when fabricating the device.^{186, 199} Therefore, we developed a non-doped TADF system based on a single molecule exciplex with the advantages of the exciplex system and the non-doped TADF.

In this study, we designed two emitting materials that have delayed fluorescence (DF) character by their intra- and intermolecular interactions; 10-(3-(4,6-diphenyl-1,3,5-triazin-2-yl)phenyl)-9,9-dimethyl-9,10-dihydroacridine (**AmT**) and 10-(3'-(4,6-diphenyl-1,3,5-triazin-2-yl)-[1,1'-biphenyl]-3-yl)-9,9-dimethyl-9,10-dihydroacridine (**AmmT**). **AmT** and **AmmT** consist of an acridine (Ac) donor and a triphenyltriazine (TRZ) acceptor, and have phenyl and biphenyl linkers that are connected to the donor and the diphenyltriazine moiety of the acceptor, respectively, through a meta linkage. Calculated structures of **AmT** and **AmmT** show that the electron distributions of the HOMO and LUMO are almost separated, providing small exchange energies and almost the same singlet and triplet energy levels. Because of the meta-positioned phenyl and biphenyl moieties, ICT-induced absorption bands of **AmT** and **AmmT** were not observed, and the resulting low oscillator strength should lead to poor luminescence. However, a strong emission with a large Stokes shift was observed in the neat film of **AmT** or **AmmT**; it originated from the intermolecular CT state (like exciplex) corresponding to the difference between the HOMO of the emitter donor moiety and the LUMO of the emitter acceptor moiety. This phenomenon results from the more favorable formation of an intermolecular exciplex in the neat film than in solution because of the reduced intermolecular distances in the neat film. In addition, **AmT** and **AmmT** show DF. Photophysical and single crystal X-ray structural analyses confirmed that intermolecular CT-induced DF can occur more effectively in **AmmT** because **AmmT** molecules are more uniformly and tightly packed in the neat film than **AmT**. OLEDs using **AmmT** as an emitter without a host showed an EQE above 18%, which is better than the EQE value of **AmT**-based OLEDs, because of the more efficient formation of intermolecular exciplexes of **AmmT**. This is the first example

of TADF molecules utilizing intermolecular CT excitons (exciplex) between donor-acceptor-type emitter molecules of a single species.

2. Materials and general methods

2.1. Materials

All solvents and materials were used as received from commercial suppliers without further purification.

2.2. Synthetic procedure

9,9-dimethyl-9,10-dihydroacridine (1, Ac). **1** was prepared according to the literature procedures.²⁰⁰ The compound **1** (3.80 g, 70%) was obtained as yellowish powder. ¹H NMR (400 MHz, CDCl₃, δ): 7.37 (dd, *J* = 7.7, 1.3 Hz, 2H), 7.09 (ddd, *J* = 7.7, 7.4, 1.3 Hz, 2H), 6.91 (ddd, *J* = 7.7, 7.4, 1.3 Hz, 2H), 6.67 (dd, *J* = 7.7, 1.3 Hz, 2H), 6.10 (s, 1H), 1.57 (s, 6H); ¹³C NMR (100 MHz, CDCl₃, δ): 138.6, 129.3, 16.9, 125.6, 120.7, 113.5, 36.3, 30.7.

10-(3-iodophenyl)-9,9-dimethyl-9,10-dihydro acridine (2). 9,9-dimethyl-10H-acridine (**1**) (3.80 g, 18.15 mmol), 1,3-diiodobenzene (17.97 g, 54.47 mmol), Cu powder (0.77 g, 12.11 mmol), potassium carbonate (10.03 g, 72.63 mmol) were introduced into nitrogen atmosphere. The mixture was heated to reflux under nitrogen in dry 1,2-dichlorobenzene (200 mL). After 2 days, the reaction mixture was concentrated in vacuo and extracted with dichloromethane. The organic layer

was washed with water and brine, and dried using anhydrous sodium sulfate. The filtrate was concentrated in vacuo to give a crude mixture, which was purified by column chromatography (SiO₂, DCM : hexane = 1 : 9) afford the compound **2** (3.6 g, 48.2%) as a white solid. ¹H NMR (400 MHz, CDCl₃, δ): 7.84 (dd, *J* = 7.2, 1.6 Hz, 1H), 7.70 (s, 1H), 7.44 (dd, *J* = 7.2, 1.6 Hz, 2H), 7.36~7.34 (m, 2H), 6.95 (m, 4H), 6.23 (dd, 8, 1.2 Hz, 2H), 1.67 (s, 6H); ¹³C NMR (100 MHz, CDCl₃, δ): 142.5, 140.5, 140.4, 137.4, 132.2, 131.0, 130.1, 126.4, 125.3, 120.9, 114.0, 95.3, 35.9, 31.3.

(3-(9,9-dimethylacridin-10(9H)-yl)phenyl)boronic acid (3). 10-(3-iodophenyl)-9,9-dimethyl-10H-acridine (**2**) was dissolved in dry THF (100 mL) under a nitrogen atmosphere. This solution was cooled to -78 °C followed by the dropwise addition of 2.5 M n-butyl lithium solution in hexane (4.38 mL, 10.94 mmol). This mixture was stirred for 1 hour at which time trimethylborate (1.57 mL, 16.41 mmol) was added. After stirring at room temperature for 15 hours, the reaction mixture was added to an aqueous solution of HCl (1 N) and stirred for 2 hours. The aqueous phase was separated and extracted with dichloromethane (3 × 50 mL). The combined organic extracts were dried using sodium sulfate, concentrated in vacuo and purified by column chromatography (SiO₂, dichloromethane : methanol = 20 : 1) afford the compound **3** (1.20 g, 66.8%) as a yellow sticky liquid. ¹H NMR (400 MHz, CDCl₃, δ): 8.10 (s, 1H), 7.91 (d, *J* = 7.2 Hz, 1H), 7.70 (s, 1H), 7.65 (t, *J* = 7.6 Hz, 1H), 7.35 (d, *J* = 8 Hz, 2H), 6.95~6.89 (m, 4H), 6.21 (d, *J* = 7.2 Hz, 2H), 5.19 (br s, 2H), 1.68 (s, 6H); ¹³C NMR (100 MHz, CDCl₃, δ): 140.9, 138.4, 134.2, 133.5, 130.5, 129.9, 126.4, 126.3, 125.3, 125.2, 120.5, 114.0, 35.9, 30.1.

2-(3-Bromo-Phenyl)-4,6-Diphenyl-1,3,5-Triazine (4). Aluminum trichloride (6.1 g, 45.57 mmol) was dissolved in 100 mL 1,2-dichlorobenzene. Thionylchloride (1.10 mL, 1.81 g, 13.67 mmol), 3-bromobenzoylchloride (6.01 mL, 10 g, 45.57 mmol), and benzonitrile (9.8 mL, 95.03 mmol) were added in the solution. The mixture was stirred for 20 hours at 100 °C. After cooling to room temperature, ammonium chloride (4.9 g, 91.61 mmol) was added to the reaction and stirred for 3 hours at 100 °C again. After cooling to room temperature, the reaction mixture was poured into 350 mL methanol and stirred for 1 hour. The solid product was filtered and washed with hot ethanol. After drying under reduced pressure at 60 °C, the compound **4** (7.1 g, 40%) was obtained as a white solid. ¹H NMR (500 MHz, CDCl₃, δ): 7.37 (t, *J* = 8.0 Hz, 1H), 7.51~7.59 (m, 6H), 7.67 (d, *J* = 8.0 Hz, 1H), 8.61 (d, *J* = 8.0 Hz, 1H), 8.68 (d, *J* = 7.1 Hz, 2H), 8.80 (s, 1H); ¹³C NMR (125 MHz, CDCl₃, δ): 122.8, 127.4, 128.6, 128.9, 130.0, 131.7, 32.6, 135.2, 135.8, 138.2, 170.2, 171.6.

9,9-dimethyl-10-phenyl-9,10-dihydroacridine (PhAc). To a solution of 9,9-dimethyl-10H-acridine (**1**) (0.30 g, 1.43 mmol) in dry toluene (5 mL) was added potassium carbonate (0.59 g, 4.30 mmol) and bromobenzene (0.25 g, 1.58 mmol). The reaction mixture was purged with nitrogen for 30 min, and then palladium (II) acetate (32 mg, 0.14 mmol) and tri-tert-butylphosphine tetrafluoroborate (50 mg, 0.172 mmol) was added. The reaction mixture was stirred at 110 °C for 12 hours under nitrogen. After the reaction mixture was concentrated in vacuo, was diluted with dichloromethane and water, extracted organic layer, washed with water and brine solution and dried using anhydrous sodium sulfate. The filtrate was

concentrated in vacuo to give a crude mixture, which was purified by column chromatography on silica gel eluted with hexane only to afford the **PhAc** (0.24 g, 80.0%) as a white solid. ¹H NMR (300 MHz, CDCl₃, δ): 7.66~7.61 (m, 2H), 7.53 (d, *J* = 6.9 Hz, 1H), 7.47 (d, *J* = 7.5 Hz, 2H), 7.35 (d, *J* = 7.5 Hz, 2H), 7.00~6.92 (m, 4H), 6.26 (d, *J* = 7.8 Hz, 2H), 1.70 (s, 6H); ¹³C NMR (75 MHz, CDCl₃, δ): 141.2, 141.0, 131.4, 130.9, 130.0, 128.2, 126.4, 125.2, 120.5, 114.0, 36.0, 31.3.

2,4,6-Triphenyl-1,3,5-triazine (TRZ). Benzonitrile (1.00 g, 9.72 mmol) was added to trifluoromethane sulfonic acid (4.95 g, 32.96 mmol) cooled to 0 °C in an ice-bath and stirred for 30 min. The mixture was further stirred at room temperature overnight. Water (50 mL) was added, and the resulting mixture was neutralized with sodium hydroxide. Then, a mixture of chloroform and acetone (1:1 (v/v), 50 mL) was added. The organic layer was separated and the aqueous layer was extracted with the same mixed solvents. The combined organic layers were washed with brine, dried over magnesium sulfate, and concentrated in vacuo. 2,4,6-triphenyl-1,3,5-triazine (0.80 g, 80.0%) was obtained as a white solid. ¹H NMR(300 MHz, CDCl₃, δ): 7.58 (m, 9H), 8.77 (d, 6H); ¹³C NMR(75 MHz, CDCl₃, δ): 128.6, 129.0, 132.5, 136.2, 171.6.

10-(3-(4,6-diphenyl-1,3,5-triazin-2-yl)phenyl)-9,9-dimethyl-9,10-dihydroacridine (AmT). 9,9-dimethyl-10H-acridine (**1**) (1.50 g, 7.42 mmol), 2-(3-Bromo-Phenyl)-4,6-Diphenyl-[1,3,5]-Triazine (**4**) (3.46 g, 8.90 mmol), palladium acetate (0.12 g, 0.52 mmol), Tri-tert-butylphosphine tetrafluoroborate (0.43 g, 1.48

mmol) and potassium tert-butoxide (1.66 g, 14.83 mmol) were introduced into a dried 250 mL two-neck round bottom flask under an atmosphere of nitrogen. Dry toluene (70 mL) was added and heated to reflux under nitrogen atmosphere for 12 hours. The reaction mixture was concentrated in vacuo and extracted with dichloromethane. The organic layer was washed with water and brine and dried using anhydrous sodium sulfate. The filtrate was concentrated in vacuo to give a crude mixture, which was purified by column chromatography (SiO₂, hexane) afford the **AmT** (2.23 g, 58.2%) as a yellow solid. ¹H NMR (400 MHz, CDCl₃, δ): 8.95 (ddd, *J* = 8, 1.4, 1.4 Hz, 1H), 8.79~8.74 (m, 5H), 7.85 (t, *J* = 8 Hz, 1H), 7.87~7.50 (m, 9H), 6.97 (qd, *J* = 5.6, 1.2 Hz, 4H), 6.36 (dd, *J* = 8, 1.6 Hz, 2H), 1.76 (s, 6H); ¹³C NMR (100 MHz, CDCl₃, δ): 171.8, 170.9, 141.7, 140.8, 139.4, 136.0, 135.6, 132.7, 132.1, 131.4, 130.0, 129.0, 129.0, 128.9, 128.7, 126.5, 125.4, 120.7, 114.1, 31.5; HRMS (ESI) *m/z* [EI +]: calcd for C₃₆H₂₈N₄, 516.2314; found, 516.2311.

10-(3'-(4,6-diphenyl-1,3,5-triazin-2-yl)-[1,1'-biphenyl]-3-yl)-9,9-dimethyl-9,10-dihydroacridine (AmmT). (3-(9,9-dimethylacridin-10(9H)-yl)phenyl)boronic acid (**3**) (1.60 g, 4.86 mmol), 2-(3-Bromo-Phenyl)-4,6-Diphenyl-[1,3,5]-Triazine (**4**) (1.89 g, 4.86 mmol), tetrakis(triphenylphosphine)palladium (0.28 g, 0.24 mmol) and aqueous sodium carbonate (2 M, 5 mL) in toluene (60 mL) and ethanol (5 mL) were heated to reflux in a nitrogen atmosphere for 24 h. After the reaction mixture was concentrated in vacuo, the resulting mixture was extracted with dichloromethane. The organic layer was washed with water and brine, and dried using anhydrous sodium sulfate. The filtrate was concentrated in vacuo to give a crude mixture, which was purified by column chromatography (SiO₂, ethyl acetate :

hexane = 1 : 25) afford the **AmmT** (1.6 g, 55.6%) as white solid. ^1H NMR (400 MHz, CDCl_3 , δ) δ (ppm) 9.03 (s, 1H), 8.78~8.76 (m, 5H), 7.88 (dd, $J = 22.4, 7.2$ Hz, 2H), 7.78 (t, $J = 8$ Hz, 1H), 7.73 (s, 1H), 7.66~7.54 (m, 7H), 7.48 (dd, $J = 7.6, 1.2$ Hz, 2H), 7.39 (d, $J = 8$ Hz, 1H), 6.98 (m, 4H), 6.43 (dd, $J = 7.6, 1.2$ Hz, 2H), 1.72 (s, 6H); ^{13}C NMR (100 MHz, CDCl_3 , δ): 171.7, 143.7, 141.8, 140.9, 140.6, 136.9, 136.1, 135.1, 132.6, 131.4, 131.1, 130.4, 130.1, 130.1, 129.3, 129.0, 128.7, 128.3, 127.5, 127.0, 126.4, 125.2, 120.6, 114.1, 31.1; HRMS (ESI) m/z [EI +]: calcd for $\text{C}_{42}\text{H}_{32}\text{N}_4$, 529.2627; found, 592.2628.

2.3. General methods

^1H - and ^{13}C -NMR spectra were recorded using an Agilent 400 MHz Varian spectrometer in CDCl_3 . ^1H -NMR chemical shifts in CDCl_3 were referenced to CHCl_3 (7.27 ppm). ^{13}C -NMR chemical shifts in CDCl_3 were reported relative to CHCl_3 (77.23 ppm). Mass spectra were obtained using matrix-assisted laser desorption–ionization time-of-flight mass spectrometry (MALDI-TOF-MS) from Bruker. High-resolution masses were measured by either fast atom bombardment (FAB) or electron ionization (EI) using a JEOL HP 5890. Analytical thin-layer chromatography was performed using Kieselgel 60F-254 plates from Merck. Column chromatography was carried out on Merck silica gel 60 (70–230 mesh). Decomposition temperatures (T_d) and glass transition temperatures (T_g) were obtained by thermogravimetric analysis (TGA, Q-5000-IR) and differential scanning calorimetry (DSC, DSC-Q-1000), respectively. The TGA and DSC analyses were performed at a heating rate of $10\text{ }^\circ\text{C min}^{-1}$ under a nitrogen atmosphere. The T_g was determined from the second heating scan.

2.4. Quantum Chemical Calculations

All quantum chemical calculations were performed using the Gaussian '09 program package. Gas-phase geometry optimizations for the lowest excited singlet and triplet states were carried out using time-dependent density functional theory calculations at the B3LYP/6-31G(d) level.

2.5. Photophysical measurements

UV-visible spectra were recorded on a Beckman DU650 spectrophotometer. Fluorescence spectra were recorded on a Jasco FP-6500 spectrophotometer. Fluorescent quantum yields in the solid films were recorded on an Otsuka electronics QE-2000 spectrophotometer. A photoluminescence decay kinetic profiles were obtained by monitoring emission from a sample excited at 266 nm pulses having a duration time of 6 ns from a Q-switched Quantel Brilliant Nd:YAG laser. Photoluminescence was wavelength-selected using a Kratos GM 200 double monochromator of 0.2 m, detected using a Hamamatsu R928 PMT, and digitized using a Lecroy Wavepro 950 oscilloscope of 1 GHz. Low-temperature measurements were conducted using a cryostat (Iwatani Industrial Gases, CRT-006-2000) with application of an InGa alloy as an adhesive to ensure good thermal conductivity between the silicon substrate and the sample holder.

2.6. Electrochemical measurements

Using cyclic voltammetry (CV) in CH_2Cl_2 solutions (1.00 mM) with 0.1 M tetra-n-butylammonium hexafluorophosphate (TBAPF_6) as the supporting electrolyte. A glassy carbon electrode was employed as the working electrode and

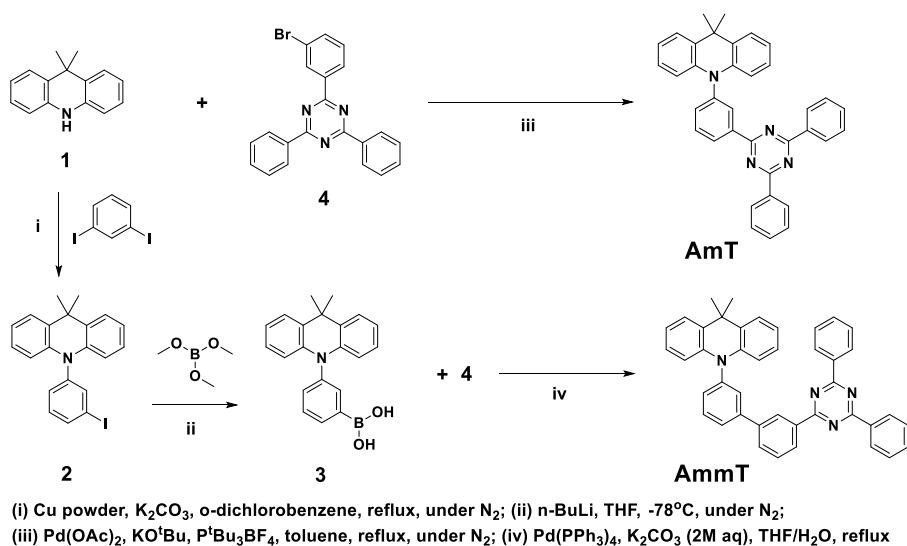
referenced to a Ag reference electrode. All potential values were calibrated against the ferrocene/ferrocenium (Fc/Fc⁺) redox couple. The onset potential was determined from the intersection of two tangents drawn at the rising and background current of the cyclic voltammogram.

2.7. Single crystal X-ray structure analysis

AmT (CCDC 1545856) and **AmmT** (CCDC 1546113) crystallographic data are summarized in the Supporting Information. These data can be obtained free of charge from The Cambridge Crystallographic Data Centre via www.ccdc.cam.ac.uk/data_request/cif.

3. Results and discussion

3.1. Synthesis



Scheme 1. Synthetic routes of **AmT** and **AmmT**

The synthetic routes of **AmT** and **AmmT** are illustrated in Scheme 1. 9,9-Dimethyl-9,10-dihydroacridine (Ac, **1**) and 2-(3-bromophenyl)-4,6-diphenyl-1,3,5-triazine (**4**) were synthesized according to previous methods.²⁰⁰⁻²⁰¹ 10-(3-Iodophenyl)-9,9-dimethyl-9,10-dihydroacridine (**2**) was obtained using the Ullmann cross coupling reaction between compound **1** and 1,3-diiodobenzene. (3-(9,9-dimethylacridin-10(*9H*)-yl)phenyl)boronic acid (**3**) was synthesized by reacting compound **2** with trimethyl borate at -78 °C. **AmT** and **AmmT** were prepared by Buchwald cross coupling between compounds **1** and **4** and by Suzuki cross coupling using compounds **3** and **4**, respectively. **AmT** and **AmmT** were characterized by ¹H NMR, ¹³C NMR, and low- and high-resolution mass spectrometry. These two compounds were purified further by train sublimation (twice) under a reduced pressure (<10⁻⁴ Torr).

3.2. DFT calculation and single crystal X-ray diffraction

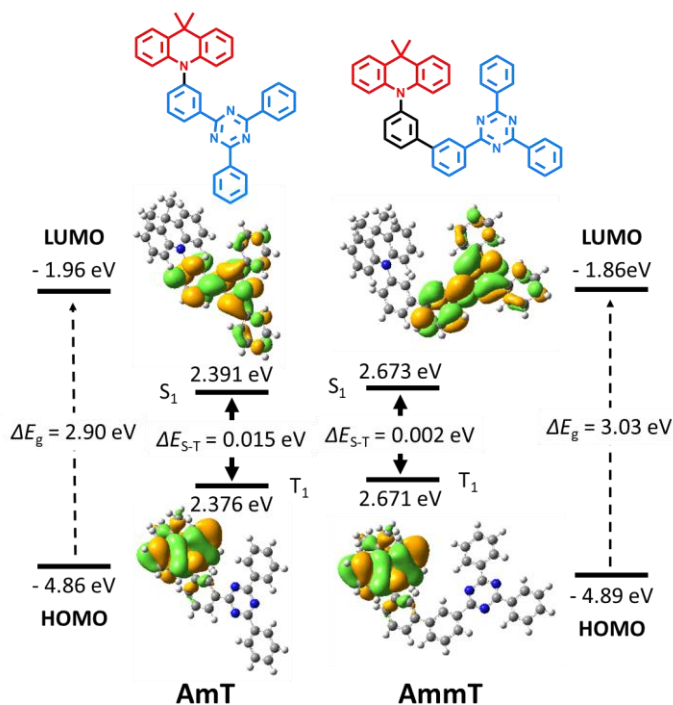


Figure 1. Molecular structures, HOMO and LUMO distribution and calculated singlet and triplet energy levels based on TD-DFT at the B3LYP/6-31G(d) level.

Figure 1 depicts the molecular structures and theoretical simulation of **AmT** and **AmmT**. The optimized geometries and electron density distributions of the frontier molecular orbitals were investigated using time-dependent density functional theory calculations at the B3LYP/6-31G(d) level using Gaussian '09. The HOMOs of **AmT** and **AmmT** are located on the Ac donors, whereas the LUMOs are distributed over the TRZ acceptors. The HOMO of **AmT** is extended slightly to the neighboring phenyl of the TRZ acceptor while its LUMO is extended over TRZ. There is a small orbital overlap between the HOMO and LUMO of **AmT** in the connecting phenyl moiety of TRZ, as shown in Figure 1. In contrast, the calculated

structure of **AmmT** shows totally separated electron distributions of the HOMO and LUMO because of an additional meta-linked phenylene moiety. Thus, **AmT** shows a small ΔE_{ST} value of 0.015 eV, whereas that of **AmmT** is even lower (0.002 eV).

Single crystal X-ray diffraction analysis of **AmT** and **AmmT** (grown from a dichloromethane-cyclopentane mixed solvent) reveals that the torsion angles between the Ac donor and the phenyl linker of **AmT** and **AmmT** are 79° and 81° , respectively. In addition, the dihedral angle between the two benzene rings of the biphenyl group in **AmmT** is 31° , providing additional twisting (Figure S1)²⁰² Details of the single-crystal structures of **AmT** and **AmmT** are given in Table S1.

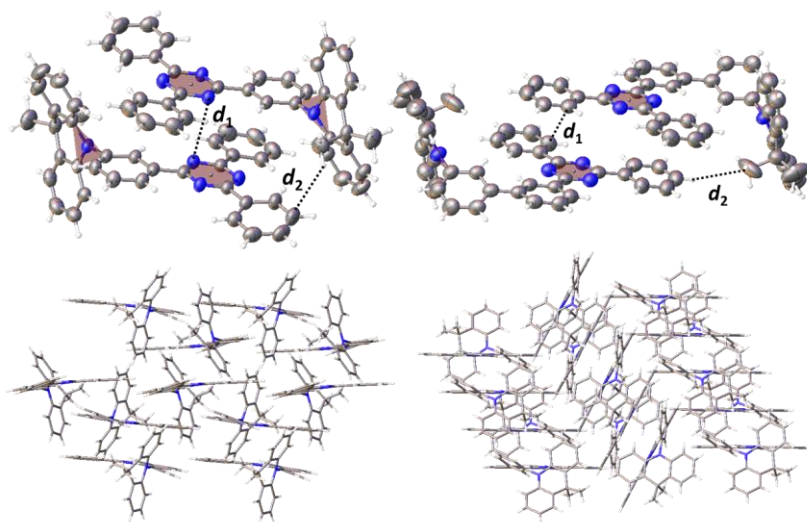


Figure 2. Packing patterns of **AmT** (left, $d_1 = 3.455 \text{ \AA}$, $d_2 = 3.137 \text{ \AA}$) and **AmmT** (right, $d_1 = 3.494 \text{ \AA}$, $d_2 = 3.122 \text{ \AA}$).

Figure 2 shows the packing patterns of **AmT** and **AmmT** in single crystals. For **AmT**, alternating pairs of adjacent TRZ moieties are partially stacked with distances of 3.455-3.512 Å. However, all pairs of adjacent planar TRZ moieties in **AmmT** are parallel, and their π -surfaces partially overlap with alternating distances of 3.452 and 3.494 Å; these properties would be beneficial for charge transport. Closely packed **AmmT** molecules in the crystal structure are expected to provide a more efficient environment for intermolecular interactions, thereby increasing the efficiency of exciplex (exciton) formation.

3.3. Photophysical properties

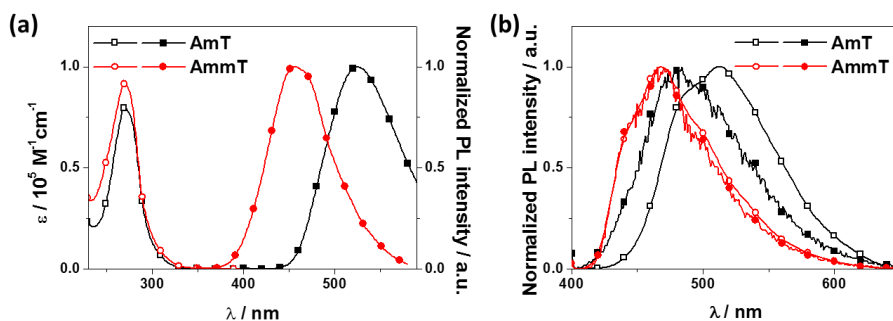


Figure 3. (a) UV (10 μM in dichloromethane) and PL spectra (10 μM in toluene) of **AmT** and **AmmT**, (b) PL spectra at low temperature (LT, 77 K, 10 μM in 2-methyltetrahydrofuran): open symbol with line - LT FL, closed symbol with line - PH.

The photophysical properties of **AmT** and **AmmT** were analyzed using ultraviolet-visible (UV-Vis) and photoluminescence (PL) spectroscopies, and transient PL decay measurements. At room temperature (300 K), each compound

shows almost the same UV-Vis absorbance around 270 nm, which is attributed to the π - π^* absorption band from the Ac donor and the TRZ acceptor in the dichloromethane solution (Figure 3(a)).^{182, 203} Both materials do not exhibit any absorption bands above 300 nm because of the ICT from the Ac to the TRZ. This is because the resonance effect was suppressed by the meta-positioned donor and acceptor moieties. However, the two compounds exhibit dim, broad emission with a large Stokes shift in toluene. The triplet energy levels of **AmT** and **AmmT** were identified in the PL spectra at low temperature (77 K) (Figure 3(b)). The low temperature fluorescence and phosphorescence (20 ms time delay) spectra of **AmT** show λ_{max} values at 514 and 484 nm, respectively. **AmmT** shows the same low temperature fluorescence and phosphorescence spectra at 468 nm. The structureless fluorescence and phosphorescence emission spectra of **AmT** and **AmmT** at low temperature indicate that their emissions are dominated by the CT state, which means that the T_1 states of **AmT** and **AmmT** originate from the ^3CT state. We examined the PL solvatochromic shift of **AmT** and **AmmT** using various solvents at room temperature (Figure S2). Both materials show that the PL spectra are red-shifted, and the PL intensities decrease as the dielectric constant of the solvents increases. This indicates that their emissive S_1 states are dependent on the dielectric constant of the solvent.

Because of the extremely low luminescence of the dilute CH_2Cl_2 solution (10 μM) of **AmT** and **AmmT** at room temperature, we wanted to investigate the luminescence characteristics according to the state of aggregation in tetrahydrofuran/water mixtures (Figure S3).²⁰⁴ The PL intensities are very weak when the water fraction (f_w) is low. When the f_w is larger than 70%, the PL intensities of each molecule increase rapidly, indicating AIE-like behavior.

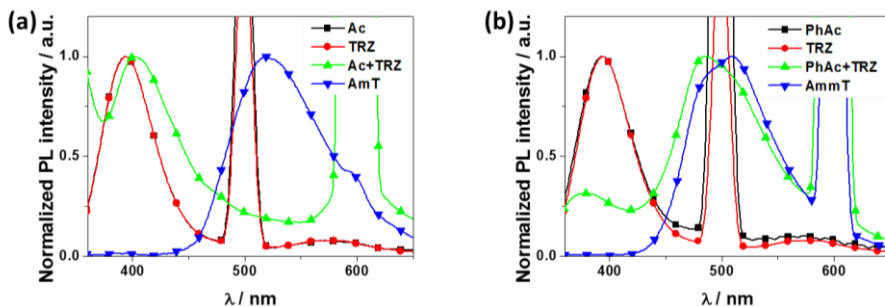


Figure 4. PL spectra of spin-coated films of Ac, PhAc, TRZ, and (a) a mixture of Ac and TRZ (1:1 mol ratio) compared to neat film of **AmT** and (b) a mixture of PhAc and TRZ (1:1 mol ratio) compared to neat film of **AmmT**. PL peaks at 500 nm are 2nd harmonic wavelength of excitation about Ac, PhAc and TRZ. PL peaks at 600 nm are 2nd harmonic wavelength of excitation about **AmT** and **AmmT**.

As shown in Figure 3(a), **AmT** and **AmmT** do not show ICT absorption bands. However, the large solvatochromic shift observed in **AmT** and **AmmT** is likely due to CT from the Ac donor to the TRZ acceptor. This was supported by additional photophysical experiments using Ac and 9,9-dimethyl-10-phenyl-9,10-dihydroacridine (PhAc) as the donors of **AmT** and **AmmT**, respectively, and TRZ as the acceptor. Figure 4 shows PL spectra of Ac:TRZ (1:1 molar ratio, film) and PhAc:TRZ (1:1 molar ratio, film) along with those of Ac, PhAc, and TRZ films. The PL spectra of Ac, PhAc, and TRZ are almost the same with a maximum wavelength of 400 nm. The PL spectrum of the 50 mol% Ac:TRZ film is similar to that of the Ac or TRZ film; however, that of the 50 mol% PhAc:TRZ film is significantly red-shifted compared to that of the PhAc or TRZ film. In particular, the PL spectrum of the 50 mol% PhAc:TRZ film is similar to that of the **AmmT** neat film. Cyclic

voltammetry (CV) measurements revealed that the HOMO energy levels of Ac and PhAc are 5.12 and 5.30 eV, respectively, and the LUMO energy level of TRZ is 2.48 eV (Figure S4). These results indicate that the emission of **AmT** results from the formation of an intramolecular exciplex-like formation between the HOMO of Ac and the LUMO of TRZ, and the emission of **AmmT** comes mostly from the intermolecular exciplex-like system between the HOMO of PhAc and the LUMO of TRZ.

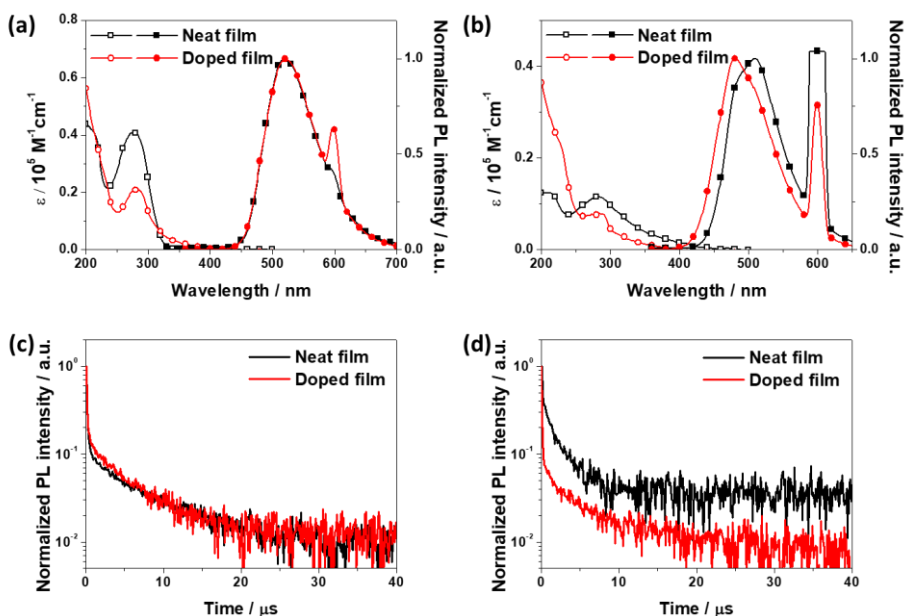


Figure 5. UV and PL spectra of neat and doped (20 wt% in DPEPO host) films of (a) **AmT** (b) **AmmT**. PL peaks at 600 nm are 2nd harmonic wavelength of excitation. Transient PL decay spectra in doped (20% in DPEPO) and neat films at 300 K of (c) **AmT** (d) **AmmT**.

The photophysical properties of **AmT** and **AmmT** in neat and doped films (20 wt% in Bis[2-(diphenylphosphino)phenyl] ether oxide (DPEPO) were also investigated at room temperature (Figure 5). The λ_{max} absorption peaks of **AmT** are 276 and 283 nm in the neat and doped films, respectively, and those of **AmmT** appear at 283 and 284 nm, respectively; the peaks are slightly red-shifted compared to those in the solution state because of aggregation in the solid state. The estimated emission onset of the PL spectra of **AmT** in both the neat and doped films was 456 nm, which corresponds to the optical bandgap of 2.72 eV. In contrast, the measured emission onset values of the PL spectra of **AmmT** in the neat and doped films were 443 and 427 nm, respectively, which correspond to optical bandgaps of 2.80 and 2.91 eV, respectively. The LUMO energy levels of **AmT** and **AmmT** in the neat film are 2.81 and 2.68 eV, respectively, which were calculated from the optical bandgap and the HOMO energy levels of 5.53 and 5.48 eV for **AmT** and **AmmT**, respectively, estimated from the CV in a dichloromethane solution (Figure S4(a)). The PL λ_{max} values of **AmT** in the neat and doped films are 519 and 522 nm, respectively. The PL λ_{max} values of **AmmT** in the neat and doped films are 509 and 480 nm, respectively. The PL quantum yields of the neat and doped films (measured using integrating spheres) are 0.52 and 0.27 (**AmT**), respectively, and 0.69 and 0.20 (**AmmT**), respectively. The higher PL quantum yields of **AmT** and **AmmT** in the neat film than those in the doped film indicate that the CT exciton that forms in the neat film is better than that of the doped film because of the decreased intermolecular distances in the neat film. This suggests that a crucial factor that affects the luminance of **AmT** and **AmmT** is the formation of CT excitons by intermolecular interactions, not the AIE phenomenon by restricting the intramolecular rotation.²⁰⁵ The higher PL quantum yield of **AmT** in the doped film than that of **AmmT** in the doped film indicates that the intramolecular exciplex formation of **AmT** is better

than that of **AmmT**. However, the PL quantum yield of **AmmT** in the neat film is much higher than that of **AmT** in the neat film because formation of an intermolecular exciplex is more favorable for **AmmT** than for **AmT**.

3.4. Transient PL decay measurements

Figures 5 (c) and (d) also depict the transient PL decay curves of the neat and doped films of **AmT** and **AmmT** at room temperature, and show double-exponential decay profiles, confirming the existence of the DF. The prompt component is assigned to an intra- and intermolecular exciplex, and the delayed component is attributed to (identical) DF occurring via the RISC process. The neat and doped films of **AmT** have prompt fluorescence decay times (τ_{PF}) of 93 and 79 ns, respectively, and the delayed fluorescence decay time (τ_{DF}) of 5.80 and 4.32 μ s, respectively. The neat and doped films of **AmmT** exhibit τ_{PF} values of 59 and 72 ns, respectively, and τ_{DF} values of 1.76 and 4.01 μ s, respectively. The τ_{PF} and τ_{DF} values of the neat film of **AmmT** are smaller than those of the doped film of **AmmT**, suggesting a more efficient radiative decay in the neat film than in the doped film. The PL quantum yields of **AmmT** contributed by a prompt component (Φ_{PF}) and delayed component (Φ_{DF}) were estimated from the decay lifetime and its amplitude (Table S2) as 0.16 and 0.53 in the neat film, respectively, while the values of Φ_{PF} and Φ_{DF} of **AmmT** are 0.04 and 0.16, respectively, in the doped film. However, the values of Φ_{PF} and Φ_{DF} of the **AmT** neat film are 0.16 and 0.36, respectively, and those of the **AmT** doped film are 0.08 and 0.19, respectively. Regardless of prompt or delayed fluorescence, the PL quantum yields of the **AmmT** neat film are 3 to 4 times higher than those of the **AmmT** doped film because of the decreased intermolecular

distances, whereas the **AmT** neat film showed PL quantum yields that were twice the value of those for the doped film of **AmT**.

We investigated the temperature dependence of the transient PL decay of **AmT** and **AmmT** measured from 78 to 300 K. The DF increases with temperature, indicating that **AmT** and **AmmT** exhibit strong TADF characters in both the neat and doped films (Figure S5). The RISC rate values (k_{RISC}) were estimated using the equations provided in the supplementary notes, and the calculated ΔE_{ST} values in the neat and doped films were 33.6 and 34.4 meV for **AmT**, and 56.5 and 31.7 meV for **AmmT**, respectively, from the Arrhenius plots of k_{RISC} between 125 and 250 K, as shown in Figure S6. The values of k_{RISC} for the doped films of **AmmT** did not show a clear temperature dependence. This is because formation of the intermolecular (exciplex) CT excitons for the doped film of **AmmT** is less efficient than that of the neat film (because of the relatively long distances between **AmmT** molecules in the doped film).

3.5. Electroluminescence properties

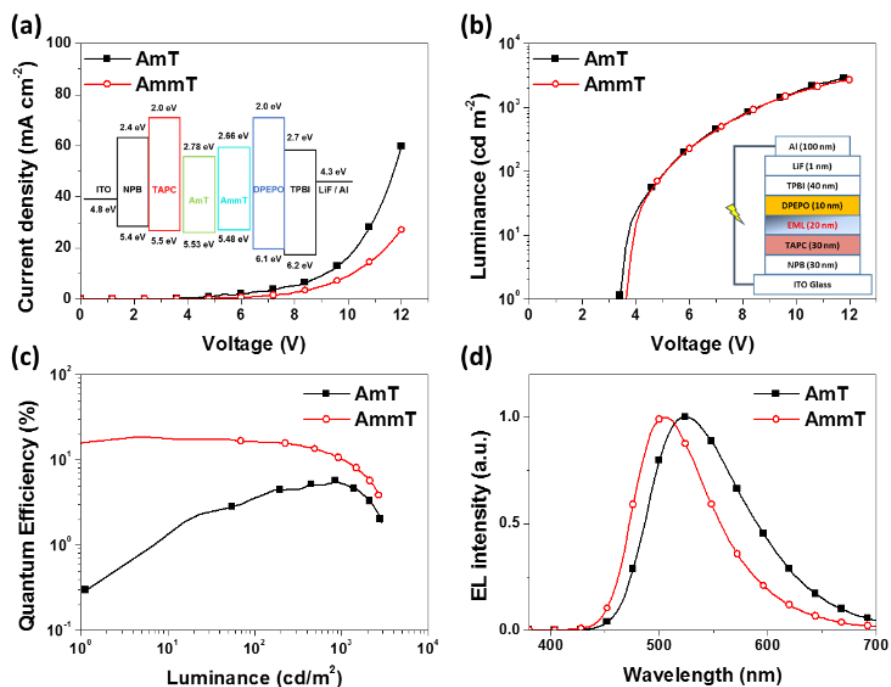


Figure 6. EL characteristics of **AmT**- and **AmmT**-based devices using non-doped system. (a) current density-voltage characteristics (inset: energy level diagram of the each device), (b) Luminance-voltage characteristics (inset: device structure), (c) quantum efficiency-luminance characteristics and (d) EL spectra.

Non-doped devices were fabricated using **AmT** and **AmmT** as emitters in the EML with the following device configuration: glass substrate/indium tin oxide/N,N'-di(1-naphthyl)-N,N'-diphenyl-(1,1-biphenyl)-4,4'-diamine (NPB) (30 nm)/4,4'-cyclohexylidenebis[N,N-bis(4-methylphenyl)benzenamine] (TAPC) (30 nm)/**AmT** or **AmmT** (20 nm)/DPEPO (10 nm)/2,2',2''-(1,3,5-benzinetriyl)-tris(1-phenyl-1-H-benzimidazole) (TPBI) (40 nm)/LiF (1 nm)/Al (100 nm). The following components were deposited on the substrate in sequential order: NPB and TAPC as hole

transporting layers, DPEPO with a deep HOMO energy level and high triplet energy (3.1 eV) as a hole blocking and an exciton confinement layer, TPBI as an electron transporting layer, an LiF as an electron injection layer, and Al cathode. Two different OLEDs were fabricated, and the performance of each device was evaluated (Table S3). Figure 6(a) shows the current density-voltage characteristics of each device with **AmT** and **AmmT**. The current density of the device with **AmT** is higher than that of the device with **AmmT**, whereas the luminance values and turn-on voltage of each device are similar at the same driving voltage as shown in Figure 6(b). Although **AmmT**-based devices show worse current density-voltage characteristics than **AmT**-based devices, the similar luminance values and turn-on voltages of the two devices indicate that **AmmT**-based devices generate intermolecular exciplexes more efficiently because of the high packing density of **AmmT** molecules in the non-doped environment; thus, **AmmT**-based devices produce light emission better than **AmT**-based devices. Quantum efficiency-luminance characteristics of two devices were plotted in Figure 6(c). **AmmT**-based devices show a maximum EQE of 18.66%, which is much higher than that of **AmT** based-devices (5.30%). Shorter τ_{PF} and τ_{DF} values of **AmmT** than those for **AmT** could explain the higher EQE of **AmmT**-based devices than **AmT**-based devices.

To understand the reasons for high efficiency of non-doped devices, we fabricated additional devices using 20 wt% **AmT** and **AmmT** doped into DPEPO in the EML (Figure S7). **AmT**- and **AmmT**-doped devices show maximum EQEs of 4.19% and 3.28%, respectively, supporting that the formation of an intermolecular CT exciton is a major contributor to the high efficiency of non-doped devices. The EQE of **AmmT**-based non-doped devices is about 3.5 times higher than that of **AmT**-based devices, and about 3.6-5.4 times higher than the theoretical maximum

EQE of approximately 3.45% to 5.18% (out-coupling efficiency = 0.2-0.3), assuming that the EL quantum efficiency is the same as the PL quantum efficiency of 0.69. Figure 6(d) shows normalized EL spectra obtained using non-doped devices. Inherent EL emission λ_{max} values of the **AmT**- and **AmmT**-based devices were observed at 524 and 504 nm, respectively, without any other emission from the adjacent layers.

Donor-acceptor-type TADF materials do not generally emit fluorescence by a Förster resonance energy transfer (FRET) mechanism because they have a small overlap between absorption and emission (large Stokes shift).²⁰⁶ Therefore, the effect of concentration quenching by FRET (of singlet excitons in the luminescence process) of **AmT** and **AmmT** is also negligible. In contrast, concentration quenching by electron-exchange interactions (for triplet excitons) is partially considered. Recently, Yasuda and co-workers reported that concentration quenching of TADF molecules was dominated by electron-exchange interactions for triplet excitons using the Dexter energy-transfer (DET) model.²⁰⁷ The maximum EQE of 18.66% in the **AmmT**-based device suggests that the exciton quenching in the neat film of **AmmT** is mainly caused by the DET process, but it is insignificant compared to the CT excitons generated by intermolecular interactions, as shown by the experimental results of the neat and doped films.

4. Conclusion

In conclusion, we developed TADF molecules (**AmT** and **AmmT**) for highly efficient non-doped OLEDs utilizing intra- and intermolecular CT excitons, which are composed of meta-linked Ac donor and TRZ acceptor molecules. Intermolecular

CT excitons of **AmT** and **AmmT** are generated more favorably under non-doped conditions than in solution or under doped conditions because of their spatial proximity. This means that efficient formation of CT excitons results from intermolecular interactions, rather than by AIE. **AmT** and **AmmT** are the first TADF molecules based on intermolecular CT exciplexes between donor-acceptor-type emitter molecules of a single species. While **AmT** shows more efficient intramolecular CT exciton formation than **AmmT**, the neat film of **AmmT** forms an intermolecular CT state-induced exciplex better than **AmT** because of the packing benefits and relatively shorter radiative lifetime of **AmmT**. As a result, EL devices that use **AmmT** as an emitter without a host exhibit an EQE over 18%. A single molecule exciplex-based TADF system using intra- and intermolecular CT excitons could be useful for developing high efficiency non-doped OLEDs.

5. Supplementary data

5.1. Supporting Tables and Figures

Table S1. Summary of crystal structure of AmT and AmmT.

	AmT (CCDC 1545856)	AmmT (CCDC 1546113)
Empirical formula	C ₃₆ H ₂₈ N ₄	C ₄₂ H ₃₂ N ₄
Formula weight	516.62	592.71
Temperature (K)	295.9(8)	295.9(2)
Wavelength (Å)		
Crystal system	Orthorhombic	Orthorhombic
Space group	Pbca	Pbca
a (Å)	13.7631(7)	17.1361(10)
b (Å)	11.4154(9)	8.1119(7)
c (Å)	34.944(4)	45.473(5)
α (°)	90	90
β (°)	90	90
γ (°)	90	90
Volume (Å ³)	5490.0(8)	6321.0(9)
Z	8	8
Density (calculated) (g/cm ³)	1.250	1.234
Absorption coefficient (mm ⁻¹)	0.575	0.568
F(000)	2176.0	2496.0
Reflections collected	15633	39350
Independent reflections	5703 [R(int) = 0.0285]	6598 [R(int) = 0.0946]
2θ range for data collection (°)	5.058 to 153.236	5.16 to 157.4
Goodness-of-fit on F ²	0.991	0.983
Final R indices [I > 2σ(I)]	R1 = 0.0438, wR2 = 0.1115	R1 = 0.0819, wR2 = 0.1981
R indices (all data)	R1 = 0.0693, wR2 = 0.1280	R1 = 0.1585, wR2 = 0.2641
Largest diff. peak and hole (e.Å ⁻³)	0.12 and -0.18	0.24 and -0.24

Table S2. Summary of transient PL decay data of neat and doped film of AmT and AmmT at 300 K under nitrogen.

Conditions/ Compounds	τ_1 (μ s)	τ_2 (μ s)	$A_1^{a)}$	$A_2^{a)}$	$R_{PF}^{b)}$	$R_{DF}^{c)}$
Neat film of AmT	0.093	5.804	2.606	0.092	0.312	0.688
Doped film of AmT ^{d)}	0.079	4.322	3.024	0.132	0.294	0.706
Neat film of AmmT	0.059	1.761	3.328	0.372	0.229	0.771
Doped film of AmmT ^{d)}	0.072	4.013	0.921	0.061	0.212	0.788

^{a)} A_i is the pre-exponential for lifetime; ^{b)} R_{PF} is component ratio for prompt fluorescence, $R_{PF} = \tau_1 A_1 / (\tau_1 A_1 + \tau_2 A_2)$; ^{c)} R_{DF} is component ratio for delayed fluorescence, $R_{DF} = \tau_2 A_2 / (\tau_1 A_1 + \tau_2 A_2)$; ^{d)} 20 wt% doped in DPEPO host.

Table S3. Device performance based on AmT and AmmT.

Device condition	$V_{on}^{a)}$ [V]	$EQE_{max}^{b)}$ [%]	C. E. $max^{c)}$ [cd A ⁻¹]	P. E. $max^{d)}$ [lm W ⁻¹]	λ_{max} [nm]	CIE (x, y)
Doped AmT ^{e)}	5.8	4.19	9.02	3.83	500	(0.24, 0.39)
Doped AmmT ^{e)}	4.1	3.28	5.67	2.97	476	(0.18, 0.27)
Non-doped AmT	3.4	5.68	15.04	5.76	524	(0.33, 0.54)
Non-doped AmmT	3.6	18.66	45.13	37.31	504	(0.24, 0.49)

^{a)} Turn-on voltage at 1 cd m⁻²; ^{b)} maximum external quantum efficiency; ^{c)} maximum current efficiency; ^{d)} maximum power efficiency; ^{e)} 20 wt% doped in DPEPO.

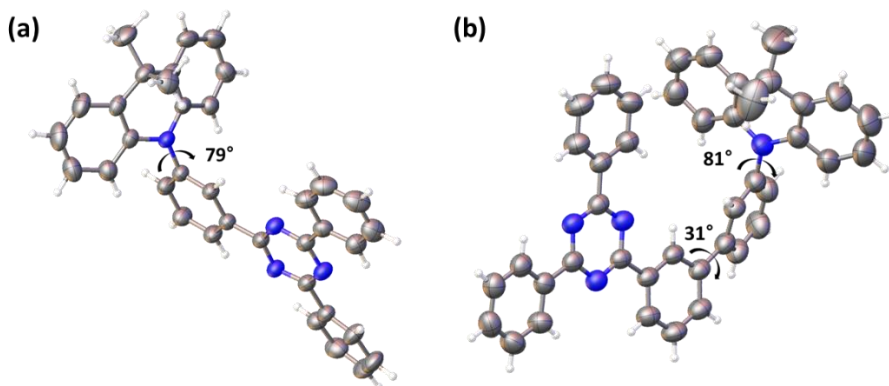


Figure S1. Single crystal structures of AmT (left, CCDC 1545856) and AmmT (right 1546113).

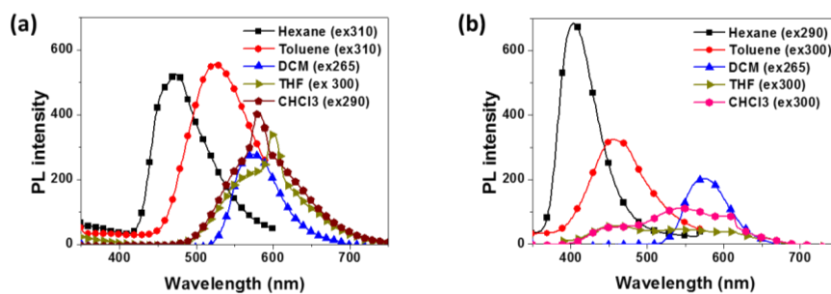


Figure S2. PL spectra of (a) AmT and (b) AmmT in various solvent (10^{-5} M).

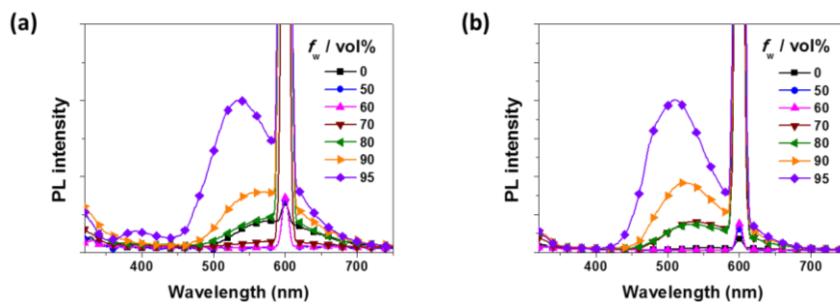


Figure S3. PL spectra in THF/water mixtures with different water fractions (f_w) of (a) AmT (b) AmmT. PL Peak at 600 nm is 2nd harmonic wavelength of excitation.

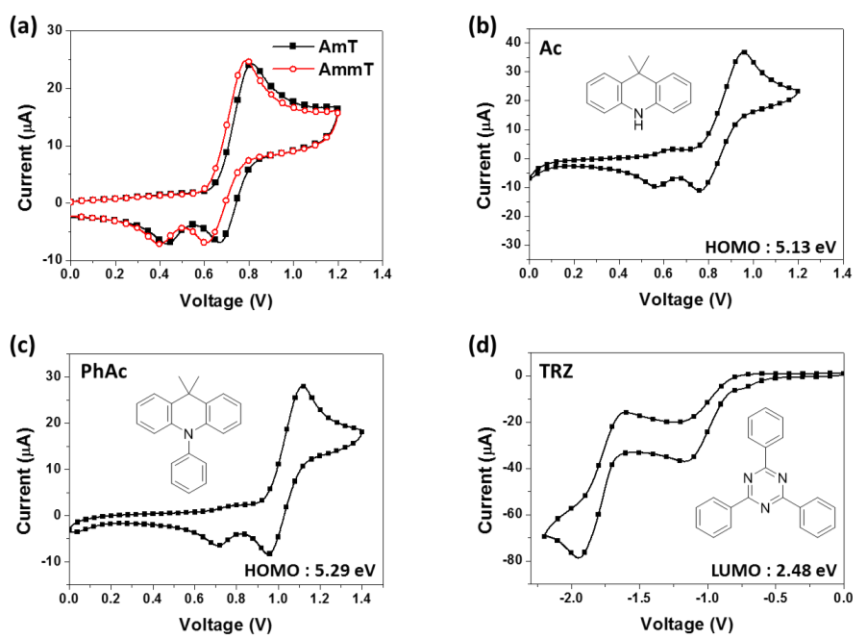


Figure S4. Cyclic voltammetry of (a) AmT and AmmT, (b) Ac, (c) PhAc and (d) TRZ in dichloromethane.

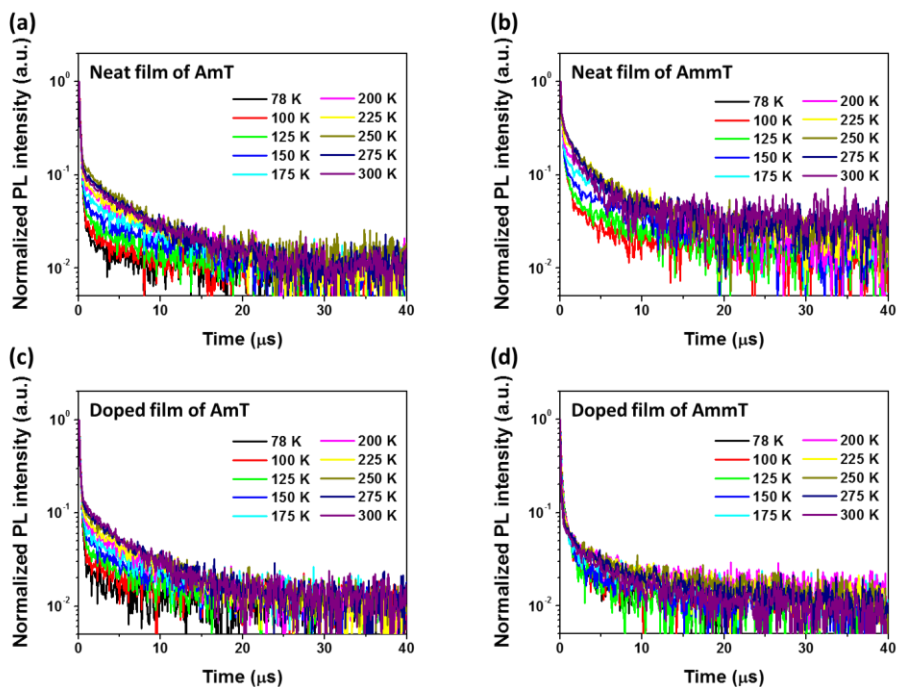


Figure S5. Temperature-dependent transient decay spectra of neat film and doped film (20 wt% in DPEPO) of AmT and AmmT.

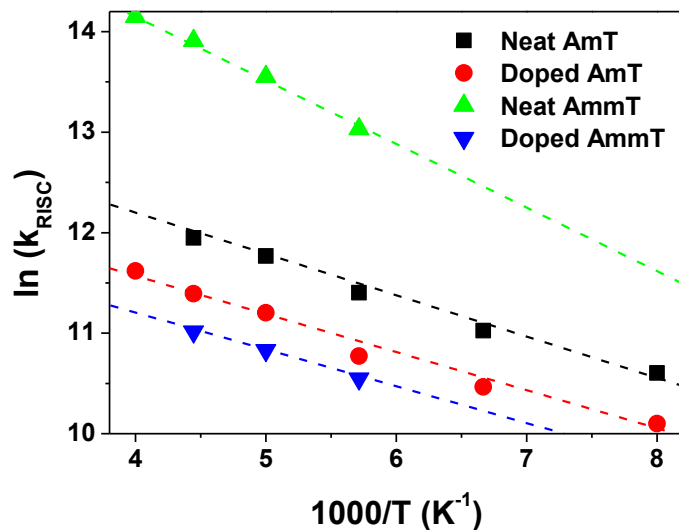


Figure S6. Arrhenius plot of the reverse ISC rate from the triplet to the singlet state of AmT and AmmT in neat and doped (20 wt% in the DPEPO) film.

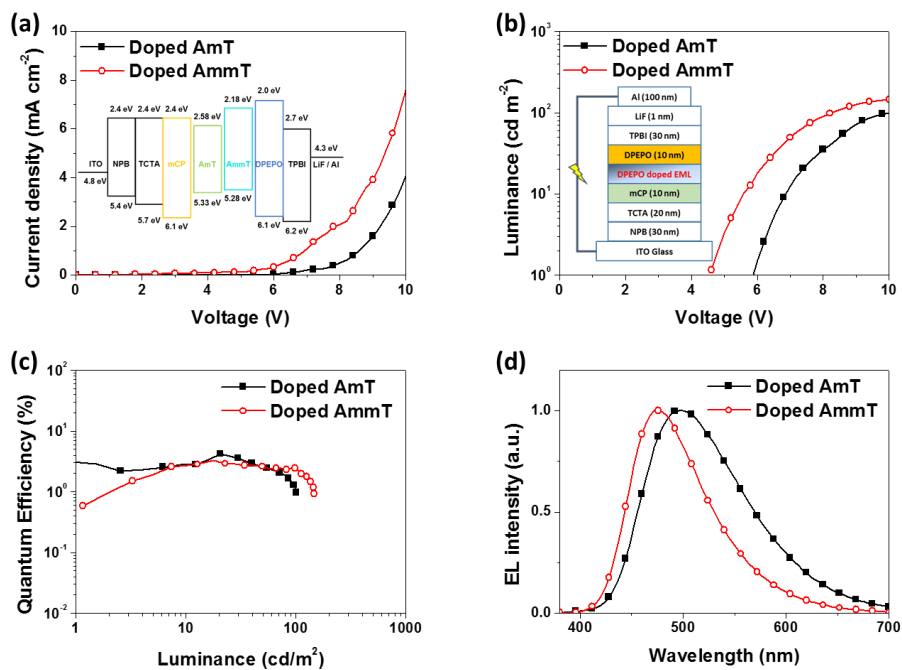


Figure S7. EL characteristics of DPEPO doped AmT and AmmT based devices (doping concentration: 20 wt%). (a) current density-voltage characteristics (inset: energy level diagram of the each device), (b) Luminance-voltage characteristics (inset: device structure), (c) quantum efficiency-luminance characteristics and (d) EL spectra.

5.2. Supplementary notes ^{187, 207}

The PL quantum efficiency of prompt fluorescence (Φ_{PF}) is expressed by

$$k_{\text{PF}} = k_{\text{r}}^{\text{S}} + k_{\text{nr}}^{\text{S}} + k_{\text{ISC}} \quad (1)$$

$$k_{\text{DF}} = k_{\text{nr}}^{\text{T}} + \left(1 - \frac{k_{\text{ISC}}}{k_{\text{r}}^{\text{S}} + k_{\text{nr}}^{\text{S}} + k_{\text{ISC}}}\right) k_{\text{RISC}} \quad (2)$$

$$\Phi_{\text{PF}} = \frac{k_{\text{r}}^{\text{S}}}{k_{\text{r}}^{\text{S}} + k_{\text{nr}}^{\text{S}} + k_{\text{ISC}}} = \frac{k_{\text{r}}^{\text{S}}}{k_{\text{PF}}} \quad (3)$$

$$\Phi_{\text{DF}} = \sum_{n=1}^{\infty} (\Phi_{\text{ISC}} \Phi_{\text{RISC}})^n \Phi_{\text{PF}} \quad (4)$$

$$\Phi_{\text{ISC}} = \frac{k_{\text{ISC}}}{k_{\text{r}}^{\text{S}} + k_{\text{nr}}^{\text{S}} + k_{\text{ISC}}} \quad (5)$$

By assuming (i) $k_{\text{RISC}} \gg k_{\text{r}}^{\text{T}}, k_{\text{nr}}^{\text{T}}$ and Φ_{RISC} is almost 1, solving supplementary equations (1) ~ (5)

$$k_{\text{ISC}} = \frac{\Phi_{\text{DF}} k_{\text{PF}}}{\Phi_{\text{PF}} + \Phi_{\text{DF}}} \quad (6)$$

$$k_{\text{RISC}} = \frac{k_{\text{PF}} k_{\text{DF}} \Phi_{\text{DF}}}{k_{\text{ISC}} \Phi_{\text{PF}}} \quad (7)$$

k_{ISC} and k_{RISC} were estimated from Supplementary equations (6) and (7)

**Part IV. Flexible and Stretchable Bio-Electronic
Devices Integrated with Color Tunable Organic
Light-emitting Diodes**

Background

1. Flexible and stretchable bio-electronic devices

1.1. Introduction

Rapid advances in the design of ultrathin electronic/optoelectronic devices, sensors²⁰⁸⁻²¹⁰ and actuators,²¹¹⁻²¹² and soft biocompatible/bioresorbable encapsulating layers²¹³⁻²¹⁴ have broadened the scope of flexible/stretchable electronics from foldable displays and curved solar panels to new classes of soft bioelectronics systems that interface with the complex geometries, curved surfaces, and time dynamic tissues of the human body.²¹⁵⁻²¹⁷

A wide range of biological signals, including electrophysiological (e.g., electroencephalogram (EEG), electrocardiogram (ECG)),²¹⁸⁻²¹⁹ physiological (e.g., pulse, temperature),²²⁰⁻²²¹ thermal (e.g., thermal conductivity, temperature distribution),²²¹⁻²²² mechanical (e.g., strain, pressure),^{220, 223} and biochemical (e.g., glucose, pH) information,²²⁴⁻²²⁵ continuously emanate from the human body. Each of these signals contains important clinical cues about normal bodily functions and the manifestation and progression of various diseases.²²⁶⁻²²⁸ There are significant challenges, however, in our ability to access target tissues/organs for high quality signal capture due to the rigid and bulky characteristics of conventional medical systems.

To achieve soft, stretchable bioelectronics requires novel approaches in material designs: i) strain minimization via nanoscale processing of established materials and ii) synthesis of new functional nanomaterials. Once bulk rigid materials are thinned and oriented into nano-structures, they become deformable. For example, the flexural rigidity of silicon nano-membranes (Si NMs) (≈ 2 nm) is

fifteen orders of magnitude smaller than that of silicon (Si) wafers ($\approx 200 \mu\text{m}$).²²⁹ A hybrid of top-down-processed nanomaterials and bottom-up-synthesized nanomaterials can create further multi-functionalities/high-performances without sacrificing the mechanical deformability. These chemically-synthesized nanomaterials exhibit unique electrical,²³⁰⁻²³¹ optical,²³²⁻²³³ and electrochemical²³⁴ properties that their bulk counterparts do not possess.

In the following, recent state of the art in soft, flexible and stretchable electronics/optoelectronics being employed in biomedicine for implantable, minimally invasive, and wearable applications are summarized. There is also present a brief introduction of nanostructured materials and related engineering technologies with emphasis on the nanometer-size designs for reliable performances under mechanical deformations. Finally, detailed description of flexible and stretchable sensors and actuators for skin-mounted and implanted systems are provided.

1.2. Bio-integrated flexible and stretchable systems

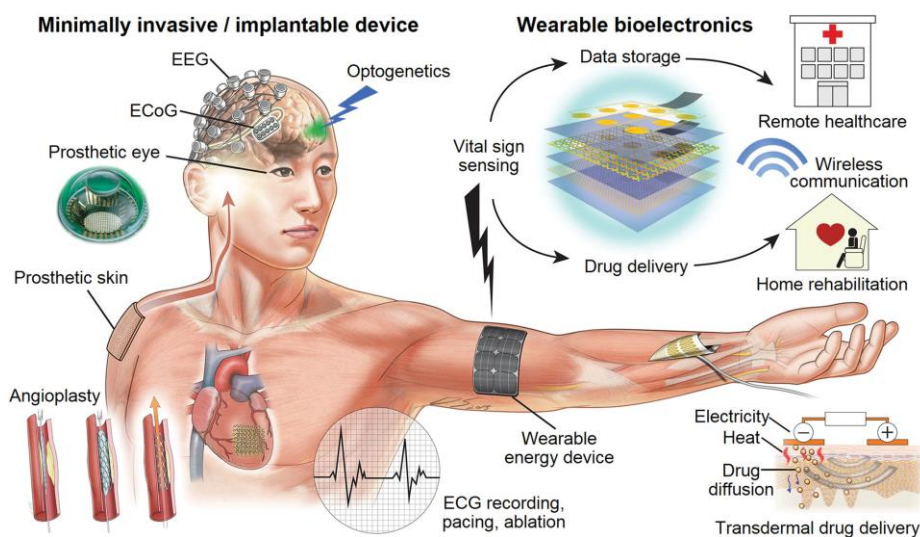


Figure 4.1. Bio-integrated flexible and stretchable systems. Schematic illustration of bio-integrated electronics in development today across a broad range of biomedical applications. Minimally invasive and implantable devices include electrophysiological sensors (ECoG, ECG), angioplasty tools, prosthetic eye/skin, and optoelectronic nerve stimulator, etc. Wearable bioelectronics include physiological sensors (pressure, strain, temperature sensors) integrated with transdermal drug delivery devices and data storage devices. Continuous monitoring and real time feedback therapy are performed in conjunction with the wireless communication. Energy supply module is an essential component to bioelectronics systems for mobile and personalized healthcare. Reproduced with permission.²³⁵⁻²³⁶ Copyright 2008, Copyright 2014, Nature Publishing Group.

Figure 4.1 shows examples of bio-integrated electronics/optoelectronics using flexible and stretchable devices. Electrophysiological signals from the brain (e.g., EEG, electrocorticography (ECoG)) consist of complex neural activity patterns,

which provide insight into normal brain function as well as neurological disorders, including epilepsy, dementia, Parkinson's disease, and restless leg syndrome (left top). Similarly, electrophysiological signals from the heart are coordinated by similar electrical signals, which provide critical insight into normal cardiac function as well as dysfunctions such as arrhythmias (center bottom). These biological signals emanate from soft and distributed cells and tissues, which are orders of magnitude smaller than the medical systems being applied to probe them. Novel microscale and nanoscale sensor designs, in arrayed formats, are thus required for measuring these fine signals. Sensor material properties, geometry (i.e., surface area), and conformal interfacial contact govern the sensing properties of these systems (e.g., signal to noise ratio). Furthermore, the mechanical properties of individual sensors must be closely matched with those of target organ tissues.

Additional circuits, sensors (e.g., strain gauges, thermal flux sensors), and actuators (LEDs, pacing/ablation electrodes) have been designed with these design considerations in order to enable conformal integration with soft and curvilinear organs. A few noteworthy examples include vision prosthesis systems consisting of stretchable photodiode arrays for image detection²³⁵ and injectable flexible LED arrays for optogenetic applications²³⁷ (left top). Minimally invasive systems have also exploited the soft, stretchable mechanical properties of bio-integrated electronics/opto-electronics. Instrumented balloon catheters integrated with stretchable electrodes and sensors have recently been demonstrated²³⁸ to provide sensing and feedback therapy during cardiac mapping and ablation²³⁹ procedures. Endovascular stents instrumented with flexible sensors and microelectronics for monitoring blood hemodynamics and the physical properties of arteries have also

been recently shown to provide sensing capability onboard an otherwise purely mechanical system.²⁴⁰

Wearable bio-integrated systems consist of a similar class of flexible/stretchable sensors and electronics as in minimally invasive and implantable applications; however, these skinbased sensors and electronics have a different set of electrical, mechanical, and optical constraints during monitoring, storing, analyzing, and transferring of data from the surface of human skin (right top).²⁴¹ Artificial skin instrumented with sensors and actuators, constitutes another important branch of skin electronics for advanced prosthetics applications (left middle).²³⁶ Transdermal drug delivery using nanoparticles loaded with pharmacological agents and activated with heat or electric field has been demonstrated in combination with these skin-based monitoring capabilities (right bottom),²⁴¹ thereby achieving both therapy and diagnostic capabilities onboard the same system. In the following sections, we review recent advances in these flexible and stretchable bioelectronic systems at the materials, device designs, and systems level.

1.3. Nanomaterials, assembly, and device designs for flexible and stretchable electronics

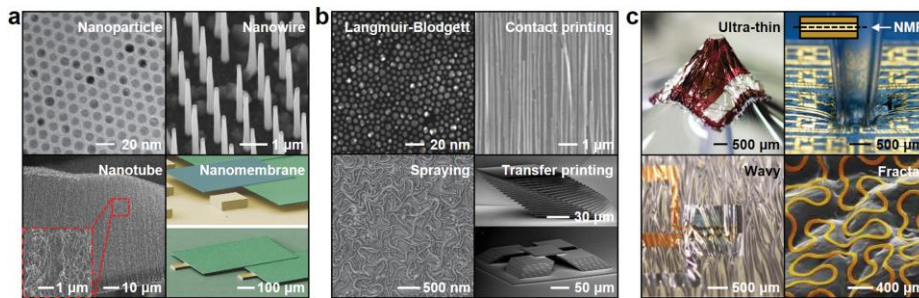


Figure 4.2. Nanomaterials, assembly, and device designs for flexible and stretchable electronics. a) Representative forms of nanomaterials: iron oxide nanoparticles (0D; left top), GaAs vertical NWs (1D; right top), vertical aligned carbon nanotube (CNT) (1D; left bottom), and Si NM (2D; right bottom). Reproduced with permission.²⁴²⁻²⁴⁵ Copyright 2004, Nature Publishing Group, Copyright 2014, American Chemical Society. Copyright 2014, Wiley-VCH, Copyright 2012, Wiley-VCH, respectively. b) Representative assembly method for nanomaterials. Langmuir-Blodgett assembly of nanoparticles (left top), contact printing of vertical growth Si NWs (right top), spraying coating of CNT (left bottom), and Si NMs stacked by transfer printing (right bottom). Reproduced with permission.^{223, 246-248} Copyright 2003, American Chemical Society, Copyright 2008, American Chemical Society, Copyright 2011, Nature Publishing Group, Copyright 2010, National Academy of Sciences USA, respectively. c) Device design strategies for flexible/stretchable electronics. Ultrathin (left top), neutral mechanical plane (NMP) (right top), wavy (left bottom), and fractal (right bottom) structures enhance the system-level deformability. Reproduced with permission.^{208, 249-251} Copyright 2012, Nature Publishing Group, Copyright 2008, AAAS, Copyright 2013, Nature Publishing Group, Copyright 2014, Nature Publishing Group, respectively.

Figure 4.2a shows representative forms of nanomaterials (0D, 1D, and 2D) for flexible and stretchable devices. The nanoscale dimensions of the materials dramatically decrease flexural rigidity of devices while acting as electrodes, transport channels, and light-emitting/photon-absorption materials. Zero dimensional nanoparticles (NPs; left top) have unique properties due to quantum confinement and large surface area.^{242, 252} One dimensional carrier transport is more efficient in nanowires (NWs; right top)²⁴³ and carbon nanotubes (CNTs; left bottom)²⁴⁴ compared to transport properties in NPs. The aligned configurations and/or percolated networks form electronic devices with robust interconnections in channels and electrodes. Two dimensional NMs (right bottom)²⁴⁵ show enhanced charge transport characteristics in planar device structures. The decreased rigidity owing to nanoscale dimensions helps mitigate the risks of mechanical failures under flexing/stretching cycles.

In the large area array of micro-/nanodevices, the uniformity of device performance is a key requirement. When nanoscale materials are uniformly fabricated/synthesized and assembled/integrated with the thickness range of less than a few micrometers, the ultrathin architecture of assembled layers decreases flexural rigidity²⁵³ and minimizes induced strain.²²⁹ Figure 2b shows examples for the assembly of 0D, 1D, and 2D materials. Langmuir-Blodgett (LB) technique utilizes an air-water interface to assemble a uniform, large area monolayer of nanomaterials (left top).²⁴⁶ Repeating the LB process can form double or triple monolayers. The dry contact printing is another effective method to align vertically grown NWs (right top).²⁴⁷ Contacting and sliding transfer NWs onto the receiver substrate. Dispersed 1D nanomaterials in a solution, such as CNTs, can be spray-

coated (left bottom),²²³ creating a uniform random network of CNTs over large areas. 2D NMs are transfer printed using elastomeric stamps (right bottom).²⁴⁸

In addition to the intrinsic flexibility of nanomaterials, advanced device design strategies have been used to enhance system-level deformations, as shown in Figure 4.2c. The induced strains are linearly and inversely proportional to thickness and bending radii, respectively. Reducing device thickness, therefore, decreases induced strains at the same bending radius (left top).²⁴⁹ Locating active regions between top and bottom layers of the same structures, i.e., in the neutral mechanical plane (NMP) region where compressive and tensile strains are compensated, mitigates risks of mechanical fractures (right top).²⁵⁰ Buckling enables not only bending but also stretching through elongation and contraction of wavy structures (left bottom).^{208, 254} Large scale stretchability is obtained via fractal/serpentine structures (right bottom).²⁵¹ These novel device structures enable new classes of wearable/implantable systems.

1.4. Flexible and Stretchable Bioelectronics Systems Using Established Materials

Soft bio-integrated electronic/optoelectronic systems require high quality materials, novel processes, and unconventional design strategies to achieve high performance as well as flexibility and stretchability. Several different classes of sensors, associated circuits, and power modules in ultrathin, deformable formats to achieve differentiated mechanical properties from existing conventional electronics were introduced in this section. These systems are applied in non-invasive,

minimally-invasive and implantable applications where diagnostic monitoring and therapeutic actuation are required.

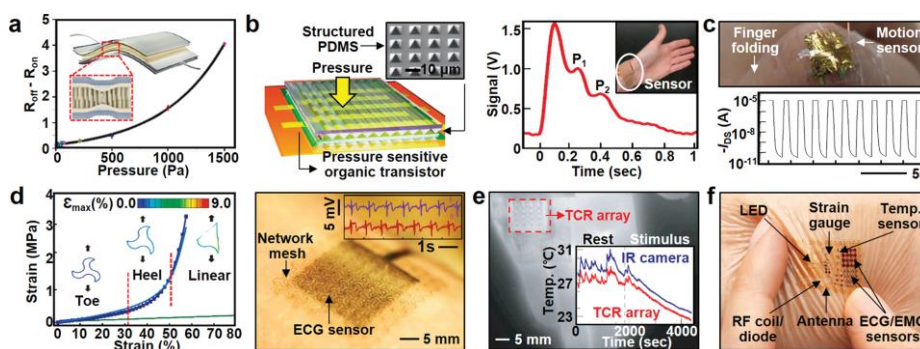


Figure 4.3. Epidermal electronics. a) Multiplexed, flexible strain-gauge array using an interlocked structure of Pt-coated polymer fibers. The difference of the electrical resistance between on and off contact ($R_{off} - R_{on}$) is measured as a function of applied pressures. Reproduced with permission.²⁵⁵ Copyright 2012, Nature Publishing Group. b) Flexible polymer transistor sensors using micro-structured PDMS as a gate dielectric layer (left). The highly sensitive pressure sensor attached on the wrist monitors pulse waves from the radial artery (right). Reproduced with permission.²²¹ Copyright 2013, Nature Publishing Group. c) Stretchable motion sensor based on the organic transistor array detects finger motions (bottom). The device is attached by the PVA adhesive gel (top). Reproduced with permission.²⁵⁶ Copyright 2014, Nature Publishing Group. d) The stress-strain response of the soft composite with a triangular lattice geometry: experimental (blue line) and computational (line with squares) data (left). Optical image of a skin-laminated ECG sensor on the forearm. The inset shows ECG signals measured by using the devices (right). Reproduced with permission.²⁵⁷ Copyright 2015, Nature Publishing Group. e) IR camera image

and corresponding temperature sensor measurement data (inset) of a palm under resting state and after stimulus. Reproduced with permission.²²¹ Copyright 2013, Nature Publishing Group. f) An integrated epidermal electronic system with multiple sensors (strain, temperature, ECG, EMG sensor) and other functional units (LED, RF coil/diode, antenna). Reproduced with permission.²¹⁰ Copyright 2011, AAAS.

[Epidermal electronics]

Strain and/or pressure sensors are widely employed in skinbased devices to detect motions (e.g., activity, tremor), cardiac signals (e.g., heartbeat, pulse shape), blood pressures, respiration conditions, and mechanical properties of skin. Figure 4.3a shows flexible strain gauges composed of vertical polymer rod structures coated with platinum.²⁵⁵ Resistance changes in the interlocked conducting arrays allow detection of changes in pressure, shear force, and torsion. The high sensitivity of the hair-like sensor arrays allows capture of faint signals, like pulse from the wrist.²⁵⁵ Figure 4.3b highlights another unique engineering approach for sensing pressure perturbations on human skin.²²⁰ The micro-structured, soft gate dielectric of an organic transistor (left) has a measurable channel conductance, which can be modulated with an applied external pressure,²⁵⁸ such as pulse wave signals measured from radial artery (right).

Further improvements in the signal to noise ratio can be achieved by reducing the bending stiffness and thickness of the system, or alternatively, by enhancing adhesion of the device to the skin. Ultrathin devices below tens of micrometers in thickness with gel-type adhesives, for example, have high sensitivity (Figure 4.3c).²⁵⁶ Another strategy to achieve reduced stiffness is to adopt serpentine pattern designs. Mechanically optimized serpentine geometries, such as the optimized arc

angle in the 2D serpentine filament,²⁵¹ can help soft network composites to match with the mechanical property of human epidermis (Figure 4.3d left).²⁵⁷ These design improvements provide better conformal contact, which gives rise to reduced effective impedance and noise for ECG measurements (right). Strategies that minimize stiffness are also applied for devices that spatially map (Figure 4.3e), hydration²²¹ and the elastic mechanical properties of skin.²⁵⁹

A representative example combines these multiple sensing modalities and device design strategies to yield a functional epidermal electronics system (Figure 4.3f).²¹⁰ Other functional units integrated in the system include a display component (LED) and wireless communication units (RF coil and high frequency diode). Although these skin-based devices are successfully applied for physiological and electrophysiological sensing, thermal mapping, and wound healing measurement,²⁶⁰ high capacity ultrathin batteries, wireless communication²¹⁸ via radio frequency connectivity, and other optoelectronic functionality are required to achieve practical utility in clinical applications. The multifunctional epidermal electronic system can be fabricated over large area by simply cutting and transferring electronic devices onto target substrates.²⁶¹

[Stretchable optoelectronic devices]

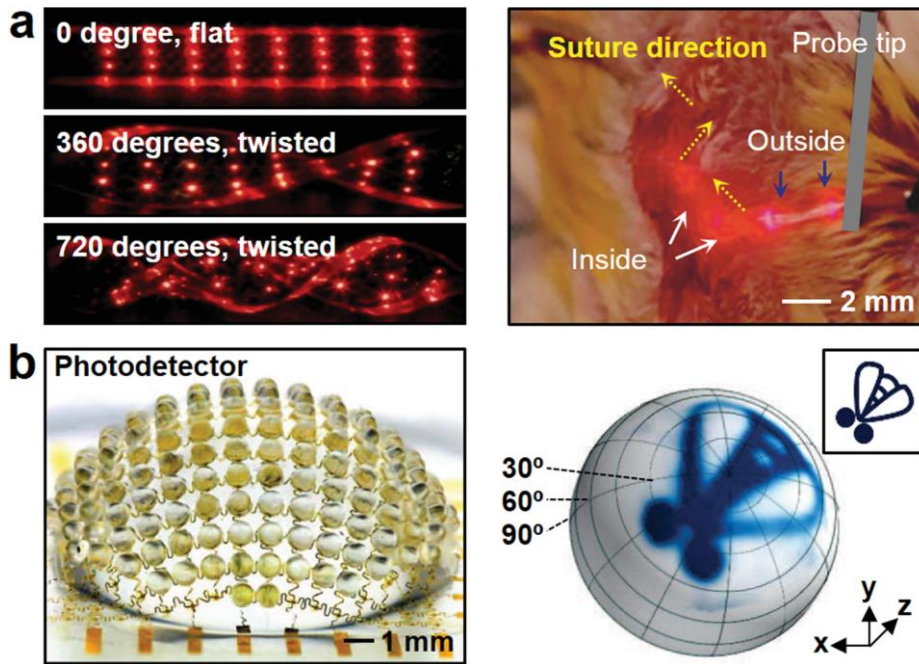


Figure 4.4. Stretchable optoelectronic devices. a) An optical camera images of a μ -ILED array in a flat (0°) and twisted (360° and 720°) state (left). An in vivo animal experiment demonstration of the light-emitting suture (right). Reproduced with permission.²⁶² Copyright 2010, Nature Publishing Group. b) An optical camera image of a photodetector array inspired by an arthropod eye (left). An illustration of a fly is captured by the photodetectors and rendered on a hemispherical surface (right). Reproduced with permission.²⁶³ Copyright 2013, Nature Publishing Group.

Although optoelectronic device research, including photodetector, phototransistor, and LED technologies are widely implemented in biomedical applications (e.g. light-based mechanical sensors,²⁶⁴ visual prosthesis,²⁶⁵ and optogenetics,²⁶⁶ conventional optoelectronic devices have limitations due to the mechanical mismatch between soft, curvilinear human body and rigid optoelectronic

devices. Soft, stretchable optoelectronics for stimulation and sensing provide new possibilities for phototherapy and optogenetics research, while solving these issues. Figure 4.4a left, for example, shows images of stretchable LED arrays, undergoing twisting (360° and 720°).²⁶² The stretchable micro-LED array can be mounted on various substrates including elastomeric ones for various medical-related functionalities. As a representative example, micro-LED arrays on an inflatable balloon catheter easily gain access to the target sites inside the human body, such as endovascular and endocardial surfaces, and enable light-based sensing and therapies in vivo. Moreover, light-based stimulation of skin wounds using micro-LED arrays mounted on sutures can help accelerate healing processes (right). The close proximity between the LEDs and target tissue maximizes photon absorption over a given surface area. Photodetector arrays are in a similar ultrathin and stretchable format and are now being applied for ocular prosthesis. A hemispherical photodetector array inspired by the arthropod's eye is shown in Figure 4.4.b left.²⁶³ The microlens and hemispherical design provide wide field of view and minimize image distortions, respectively (right).

2. Color-tunable devices

High efficiency and chromaticity tunable OLEDs are striking for numerous applications. However, it is difficult to achieve both chromaticity tunability and high efficiency simultaneously. In recent years, several efforts have been made to devise the chromaticity-tunable OLEDs. For example, employment of color temperature tunable emitters, variant dopant concentrations²⁶⁷, employment of appropriate host materials with suitable work function²⁶⁸, shifting the ultra-thin yellow emissive layer position in a blue matrix of complementary emitter-based white OLED devices²⁶⁹, and employment of nano CMLs.²⁷⁰⁻²⁷¹

2.1. Effect of CML on chromaticity tuning

Among these, the nano CML approach is considered to be the most favorable because of its numerous superlative characteristics, such as carrier regulation function, ability to confine the excitons within the specific emissive layer, and choice of materials for CML. For example, Forrest's group reported a chromaticity tunable OLED device by inserting a 5-nm BCP layer as an exciton-blocking layer. The CIE coordinates of chromaticity-tunable OLEDs varied from (0.35, 0.36) to (0.37, 0.40).²⁷² Xie's and Li's groups reported a chromaticity-tunable hybrid OLED device by varying the CML thickness from 0 to 8 nm, where CBP is used as a nano CML. The resultant devices exhibited color coordinates from (0.24, 0.24) to (0.36, 0.40).²⁷³ Liu et al. reported a color-tunable OLED device by using a 16-nm CML between the blue and yellow emissive layers. The resultant device exhibited a current efficiency of 77.4, 70.4, and 33.7 cd A⁻¹, respectively, for blue, white, and yellow emission. Furthermore, they also found that as the CML thickness varied from 8 to 24 nm, the

emissive zone shifted towards the blue emissive layer because of the maximum number of holes blocked at the CML/blue emissive layer interface. Resultant chromaticity coordinates ranged from (0.23, 0.32) to (0.38, 0.41) as luminance increased from 1000 to 5800 cd m^{-2} .²⁷⁴

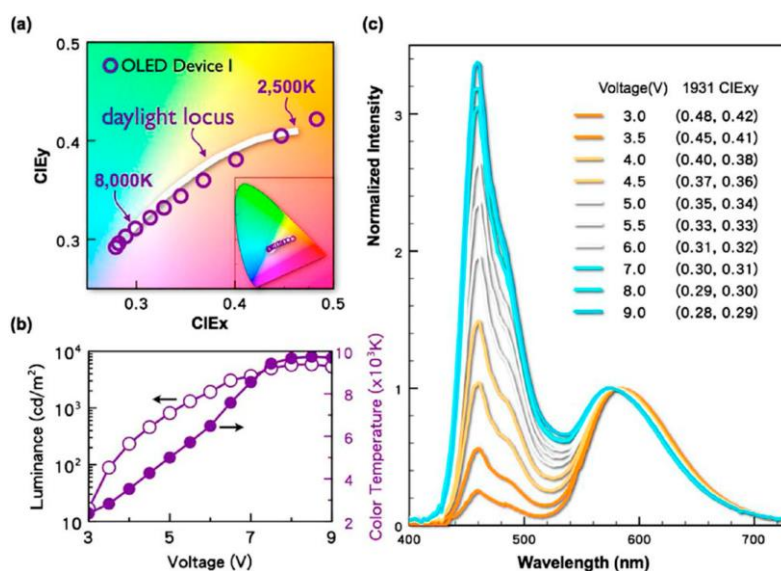


Figure 4.5. Chromaticity and color-temperature characteristics of the sunlight-style OLED (a) emission track on CIE 1931 chromaticity space matches closely to the daylight locus between 2500 and 8000 K; (b) color temperature changes from 2300 to 9700 K and brightness from 20 to 5900 cd m^{-2} as the voltage increased from 3 to 9 V; (c) EL-spectra at various applied.²⁷⁵

In 2009, Jou's group reported a sunlight-style chromaticity-tunable OLED device by employing a 3-nm CML of TPBi between green and red EMLs. This device exhibited an emission track that closely matches with the daylight locus on

CIE 1931 space (Figure 4.5a). As shown in Figure 4.5c, the EL-spectra of device initially shows a predominantly red-emission spectrum at 3 V with CIE coordinates of (0.48, 0.42), turns to pure white (0.33, 0.33) at 5.5 V, and becomes bluish white (0.28, 0.29) at 9 V.²⁷⁵

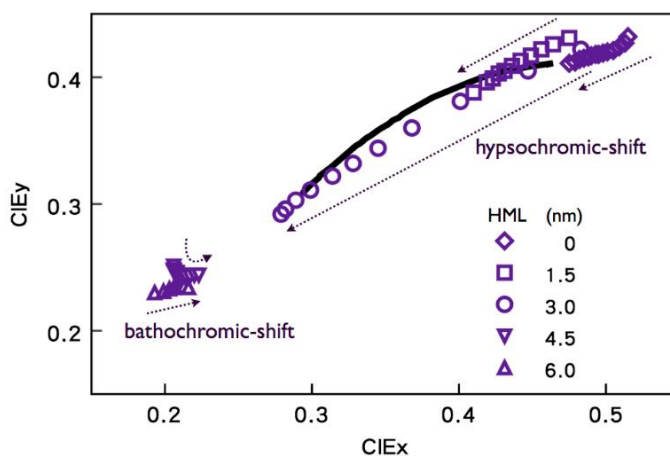


Figure 4.6. The effect of CML thickness on the device emission tracks, in terms of CIE coordinates.²⁷⁶

As shown in Figure 4.6, varying the thickness of CML from 0 to 6 nm, the emission gradually changes from the red-emission region to the blue-emission dominated region. Its corresponding chromaticity span gradually increases as the thickness increases, and achieves a maximum at 3 nm. Moreover, as much as the CML thickness increased from 3 to 4.5 or 6 nm, the color coordinates showed a strong blue shift. At 3 nm, the entire emission span is sufficiently wide enough to cover that of daylight, and its emission track matches most closely with the daylight locus. In addition, there exists a chromic-shift turning-point in the vicinity of 4.5 nm,

below which all the emissions show a hypsochromic shift, while there is a bathochromic shift above that level. At 4.5 nm, the device shows emission straying around hypsochromic and bathochromic shift at varying voltages.²⁷⁶

2.2. Effect of CML on CT tuning

The color temperature of light plays a crucial role in human physiology and psychology.²⁷⁷⁻²⁸³ Numerous medical studies reported that white light sources with an intense blue emission (5000~6000 K) may cause some serious health issues, such as irreversible retinal damage, physiological disorders, and increasing risk of various cancers resulting from the suppression of melatonin secretion.²⁸⁴ High color temperature white light stimulates the secretion of cortisol, a hormone that keeps people awake and active.²⁷⁹ In contrast, a low color temperature light mildly suppresses the nocturnal secretion of oncostatic melatonin, which would help people relax after dusk and sleep well at night.^{280-281, 283} Devising new lighting sources with a very low color temperature to minimize melatonin suppression is hence no less urgent or less significant than realizing an even higher lighting efficiency. Low color temperature OLEDs can be realized by maximizing the long wavelength (red) emission and minimizing the short wavelength (blue) emission counterpart. Lately, it has been confirmed that an engineered nano CML played a crucial role in regulating the charge carrier (holes and electrons) injection Lighting for the human circadian.²⁸⁵ Jou's group reported a candlelight-style OLED device with a color temperature of 1920 K by using a TPBi nano CML.²⁸⁶ Jou's group also reported an OLED device with a color temperature of 1880 K and a power efficiency of 36 lm W⁻¹ (current efficiency of 54 cd A⁻¹), at 100 cd m⁻², by employing a 3-nm BSB:Spiro-2CBP (2:1) blend CML between the blue and orange red emissive layers.²⁸⁵ Most

recently, our group also reported a candlelight emission with fluorescent tube efficacy and color temperature of 2279 K at 100 cd m⁻².²⁸⁷

Moreover, it has also been found that the nano CML played a crucial role in realizing the tunable color temperature.^{275, 288-289} Devising a light source with tunable color temperature hence becomes imperative in order to obtain high-quality lighting. In 2009, Jou's group invented the first sunlight-style color temperature-tunable OLED device by employing a 3 nm TPBi as CML. The resultant sunlight-style OLED device exhibited a power efficiency of 7.0 lm W⁻¹ (at 100 cd m⁻²) with a color temperature ranging from 2300 and 9700 K (Figure 4.5b).²⁷⁵ Subsequently, Jou's group further enhanced the performance of the sunlight-style OLED device by using electro-phosphorescent emitters and double nano CMLs. The resultant device showed a power efficiency of 30 lm W⁻¹ with color temperature ranges from 1900 to 3100 K.²⁷⁶

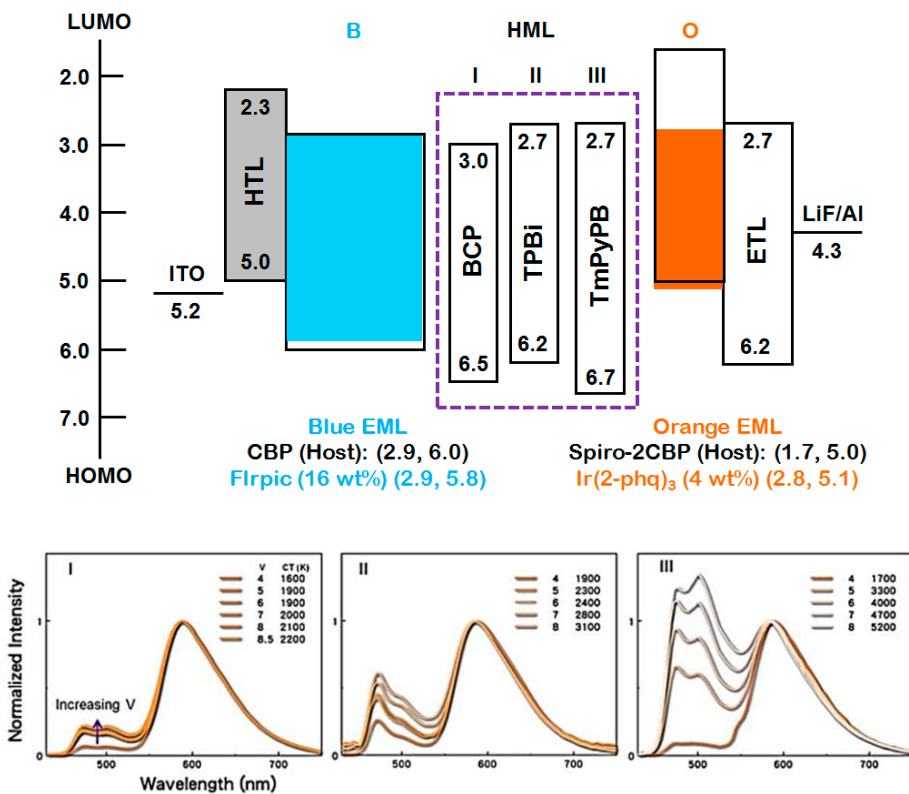


Figure 4.7. Energy level diagram of the studied devices with different CMLs and their EL spectra.²⁸⁹

As shown in Figure 4.7, three electron-transporting materials, BCP, TPBi, and TmPyPB, were investigated as CMLs in OLED devices to realize the large color temperature span. When **TmPyPB** is employed as a nano CML, the resultant OLED device exhibited the largest color temperature span of 3700 K. This may be attributed to the fact that **TmPyPB** possessed the highest hole-injection barrier (0.5 eV) and triplet energy (2.8 eV), effectively modulating the flux of holes and confining the triplet excitons within the blue emissive layer. In addition, **TmPyPB** also showed

relatively higher electron mobility than the BCP and TPBi counterparts, leading more excitons to be generated on the blue emissive layer as the operation voltage increased from 4 to 8 V (Figure 4.7).

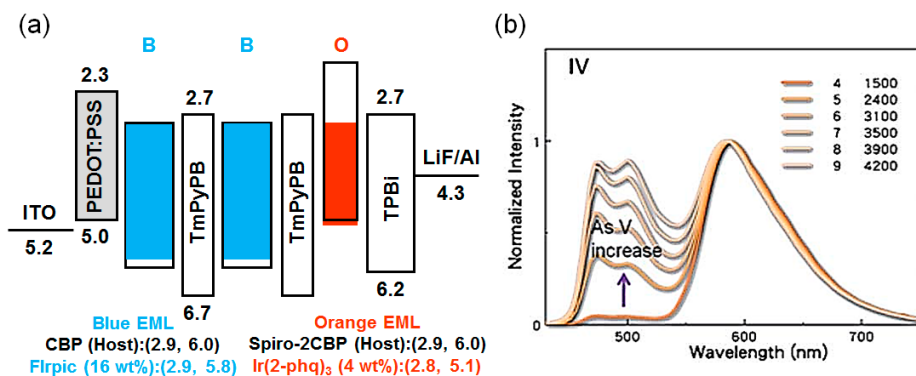


Figure 4.8. (a) Energy-level diagram of Device IV incorporating double CMLs; (b) the resulting EL-spectra of double CML device.²⁸⁹

As shown in Figure 4.8, the color temperature of device with **TmPyPB**-based nano CML can further reduce to 1500 K by introducing an additional TmPyPB between two sky-blue emissive layers. The resultant double nano CML-based device exhibited a power efficiency of 25 lm W⁻¹ with a color temperature ranging from 1500 to 4200 K as operation voltage increased from 4 to 9 V.²⁸⁹

Most recently, Jou's group also reported an OLED device with tunable color temperature from 1580 to 2600 K by using a TPBi CML. The resultant device exhibited the color temperature between dusk-hue (2500 K) and candlelight (1900 K). The color temperature of the OLED device is further tuned from 5200 to 2360

K, which covers daylight-like illumination, by simply adjusting the emissive layer thickness ratio.²⁸⁸

Unlike numerous favorable functions, a CML may also possess some limitations such as driving voltage enhancement and fabrication complexity in OLED devices. For example, the driving voltage of the sunlight-style OLED device increased from 4.3 to 4.5 as CML thickness increased from 3 to 5 nm.²⁷¹ Jou's group observed that the driving voltage increased from 4.1 to 4.7 V as the thickness of BSB:Spiro-2CBP blend CML increased from 3 to 6 nm.²⁸⁵ In contrast, host-free deep-blue and chromaticity-tunable OLED devices had not displayed any considerable enhancement in driving voltages when the hole-transporting TAPC and bipolar Spiro-2CBP materials are used as CML, respectively.^{288, 290} Hence, the driving voltage enhancement can be successfully controlled by using an optimized thickness of suitable carrier modulation material.

Section 1 Wearable Electrocardiogram Monitor Using Carbon Nanotube Electronics and Color-Tunable Organic Light-Emitting Diodes

Abstract

With the rapid advances in wearable electronics, the research on carbon-based and/or organic materials and devices has become increasingly important, owing to their advantages in terms of cost, weight, and mechanical deformability. Here, we report an effective material and device design for an integrative wearable cardiac monitor based on carbon nanotube (CNT) electronics and voltage-dependent color-tunable organic light-emitting diodes (CTOLEDs). A p-MOS inverter based on four CNT transistors allows high amplification and thereby successful acquisition of the electrocardiogram (ECG) signals. In the CTOLEDs, an ultrathin exciton block layer of bis[2-(diphenylphosphino)phenyl]ether oxide is used to manipulate the balance of charges between two adjacent emission layers, bis[2-(4,6-difluorophenyl)pyridinato-C₂,N](picolinato)iridium(III) and bis(2-phenylquinolyl-N,C(2'))-iridium(acetylacetonate), which thereby produces different colors with respect to applied voltages. The ultrathin nature of the fabricated devices supports extreme wearability and conformal integration of the sensor on human skin. The wearable CTOLEDs integrated with CNT electronics are used to display human ECG changes in real-time using tunable colors. These materials and device strategies provide opportunities for next generation wearable health indicators.

1. Introduction

The recent advances in flexible and stretchable electronics have triggered significant technological progress in wearable electronics and/or optoelectronics.^{210, 291-294} Noninvasive health monitoring and therapy devices have particularly benefitted from such technological evolution. Some examples include wearable biomedical electronic patches,^{241, 295} soft optogenetic devices,²⁹⁶⁻²⁹⁷ thermal therapy devices,²⁹⁸⁻²⁹⁹ and electronic skins.^{236, 300-301} These achievements were mainly accompanied by aggressive research on inorganicsbased ultrathin devices,^{262, 302-303} and they are expected to create huge synergies with the recent innovations in wearable electronics.³⁰⁴⁻³⁰⁶ However, the use of inorganic materials in wearable electronics poses several challenges in terms of sensing reliability and device stability, as their intrinsically brittle nature can result in mechanical breakdown after repetitive deformations occurring from the daily actions of the human body. Although the nanoscale assembly and integration of inorganic materials provides potential solutions,³⁰⁷⁻³⁰⁹ intrinsically soft materials are attracting attention owing to their mechanical stability.³¹⁰⁻³¹¹

Organic materials have thus been considered strong candidates for wearable electronics/optoelectronics.³¹²⁻³¹⁶ To utilize the well-established materials, facilities, and know-hows in the organic industry is another important advantage. For wearable electronic applications, networks of single-walled carbon nanotubes (CNTs) are promising semiconducting materials due to their excellent electrical properties, good uniformity, and robust performance under intense mechanical stresses/strains.³¹⁷⁻³²⁰ In particular, remarkable advances have been made in the field of high-performance CNT electronics based on solution-processed semiconducting CNTs, showing outstanding device-to-device uniformity in the medium scale, high on/off ratios and carrier conductance, and scalability down to a few micrometers.³²¹⁻³²³

Herein, we report a wearable electrocardiogram (ECG) monitor based on an ultrathin electrode and a p-MOS CNT signal amplifier. The integration of sensors and amplifiers enables continuous detection of the ECG signals, which are associated with diagnosis of clinical cardiac conditions such as arrhythmia and ischemia.³²⁴ In addition, the developed devices can be conformally attached to the skin, providing high reliability against severe mechanical deformations on skin, as proven through the cyclic mechanical deformation tests. We integrated our wearable electronics with an ultrathin voltage-dependent color-tunable organic light-emitting diode (CTOLED) for the colorimetric display of the retrieved ECG signals. An interlayer approach has been developed for color tuning the OLEDs, which involves the use of an ultrathin exciton-blocking layer (EBL) between two emitting layers (EMLs) for blue and red colors. By optimizing the material and thickness of the EBL, the wearable OLEDs exhibit ECG-dependent color changes from dark red, to pale red, to white, to sky blue, and finally to deep blue. The ultrathin design enables the CTOLEDs to conform to the curvilinear and dynamic surface of human skin and to exhibit excellent stability and reliability after repeated deformations.

2. Results and Discussion

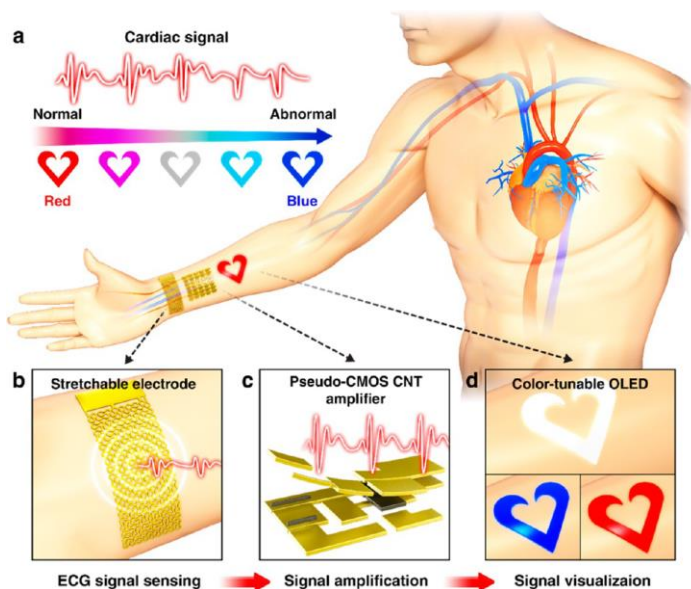


Figure 1. (a) Schematic illustration of the real-time wearable cardiac-monitoring system. The ECG signals are measured by (b) a stretchable Au electrode and then amplified by (c) a p-MOS CNT inverter for the high signal-to-noise ratio. The retrieved ECG signals are displayed via synchronized color changes of (d) the wearable CTOLED.

Significant efforts have been devoted toward developing more comfortable and softer wearable platforms for monitoring and displaying heart activities to help in the diagnosis and treatment of cardiac diseases.³²⁵⁻³²⁶ In this regard, we developed skin-mounted electrophysiology devices and signal amplifiers for real-time ECG monitoring. Figure 1a depicts a schematic illustration of our wearable cardiac-monitoring platform composed of an ultrathin ECG sensing electrode, a p-MOS CNT signal amplifier (hereinafter referred as p-MOS inverters or amplifiers), and a voltage-dependent CTOLED. For sensing ECG signals, a wearable electrode based

on a serpentine-shaped thin Au film (Figure 1b) is used. The retrieved signals are amplified by a p-MOS inverter, which comprises four transistors that employ dense networks of CNTs as their channel material (Figure 1c). After signal processing using a data acquisition unit (DAQ)/PC (not shown in the schematics), a voltage-dependent CTOLED displays the signals in real-time through color changes (Figure 1d). The ultrathin (less than approximately 3 μm) form factor of the system enables conformal integration on human skin. The detailed description of the fabrication processes for each unit is included in the Methods section.

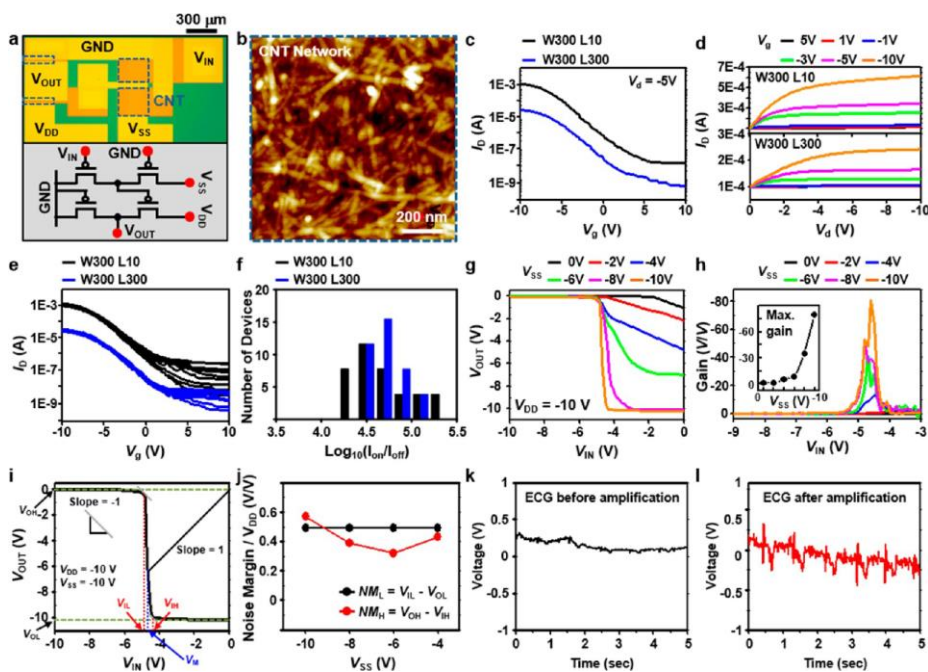


Figure 2. (a) Optical microscopic image of the p-MOS inverter (top) and corresponding schematic circuit diagram (bottom). (b) AFM image of the CNT channel showing a dense network of well-percolated CNTs. (c) Transfer curves of the CNT transistors with two different channel dimensions, at the applied drain

voltage of -5 V. (d) Output curves of the CNT transistors with two different channel dimensions, at various gate voltages. (e) Accumulated transfer characteristics of CNT transistors measured from 10 different p-MOS inverters (40 curves). (f) On-off ratio at $V_d = -5$ V. (g) Voltage transfer characteristics of the p-MOS inverter with various biasing conditions (V_{DD} fixed to -10 V). (h) Signal gain of the inverter with respect to V_{IN} under various biasing conditions (V_{DD} fixed to -10 V). (i) Characteristic curve of the p-MOS inverter. Several parameters (V_{OH} , V_{OL} , V_{IL} , V_{IH} , V_M) are indicated on the plot. (j) Noise margins of the p-MOS inverter as a function of V_{SS} . (k,l) ECG signals measured from the human wrist (k) before amplification and (l) after amplification using the p-MOS inverter.

The wearable signal amplifiers are built using p-MOS inverters based on four p-type CNT transistors; the actual device image and circuit design are shown in Figure 2a, top and bottom, respectively. The networked CNT channel is prepared from a solution of semiconducting CNTs (>99% purity; NanoIntegris Inc., USA), using the same method used in our previous report but with longer deposition time.³¹⁸ The atomic force microscopy (AFM) image in Figure 2b shows well-percolated networks of CNTs with high surface coverage, wherein the estimated unit density of a CNT network is approximately 50-60 tubes/ μm^2 . Given the physical dimensions of the channel (10 and 100 μm in length, 300 μm in width) and the densities of the CNTs, an electrically conductive path can be firmly established between the source and drain. Figure 2c,d shows the typical transfer and output curves, respectively, of the CNT transistors that constitute the p-MOS amplifier at an applied drain voltage of -5 V. The accumulated characteristic curves in Figure 2e are measured from 10

separate samples and show uniform electrical performances with average on/off ratios higher than 10^4 for both the 10 and 300 μm channel-length devices (Figure 2f).

Figure 2g plots the output voltages (V_{OUT}) of the amplifier with respect to the input voltages (V_{IN}) under various bias conditions (V_{SS} , V_{DD}). The gain of the amplifier increases with V_{SS} , and the maximum gain (V_{M}) is approximately 80 at a V_{IN} of approximately -4.6 V and V_{SS} of -10 V (Figure 2h). Further characteristics of the p-MOS inverter, including noise margins, are also calculated and presented in Figure 2i,j. The high- and low-state noise margins (NM_{H} and NM_{L} , respectively) with respect to different V_{SS} were calculated as $\text{NM}_{\text{H}} = V_{\text{OH}} - V_{\text{IH}}$ and $\text{NM}_{\text{L}} = V_{\text{IL}} - V_{\text{OL}}$, respectively, where V_{OH} , V_{IH} , V_{IL} , and V_{OL} denote the output high voltage, input high voltage, input low voltage, and output low voltage, respectively. The results demonstrate the reliable and robust operation of the ultrathin and soft p-MOS inverter.

The ECG signals are measured from human wrists by using wearable ECG sensors, with and without integration of the CNT amplifier for comparison (Figure 2k,l). Specifically, ECG sensors are worn on both wrists, and the potential differences between the two electrodes (ECG signals) are measured. The as-measured signals are amplified using the p-MOS inverter, and then, the noise is eliminated using high/low-pass filters (0.079/19.4 Hz). The ECG signals are measured from a healthy male subject (32 years old), First using a pure ECG sensor alone, and then using our p-MOS inverter as the signal amplifier.³²⁶ It can be estimated that the ECG signals are amplified by the p-MOS inverter with an effective gain of 60 or higher. It is observed that distinguishable ECG signals can be measured when the amplifier is used (Figure 2l), whereas a noise-like signal is acquired when the amplifier is not used (Figure 2k).

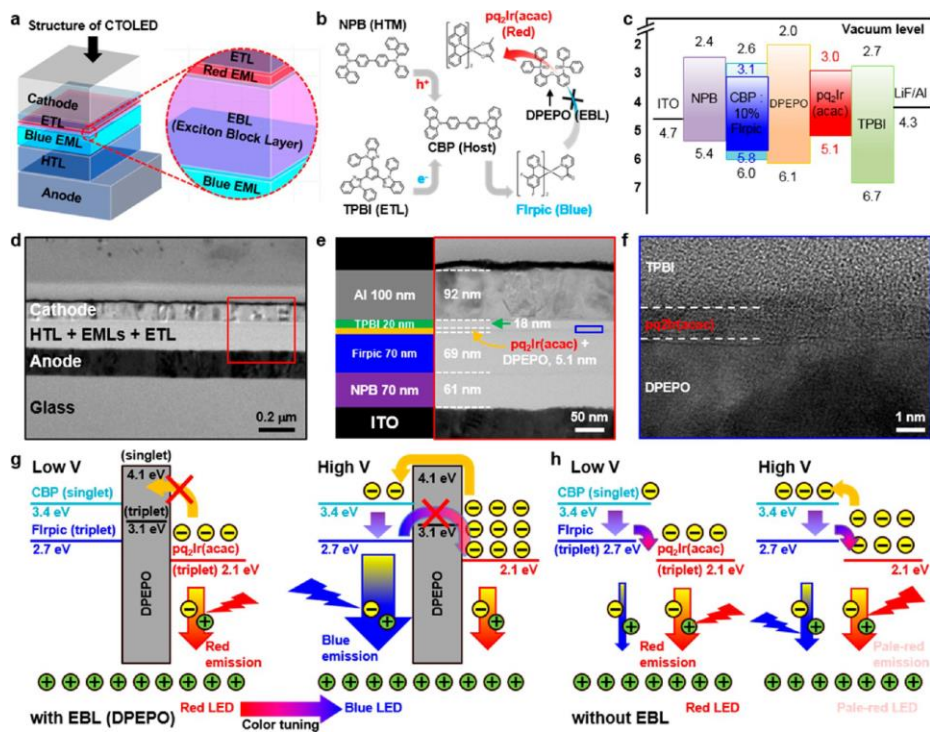


Figure 3. (a) Schematic illustration of the cross-sectional structure of a CTOLED. The magnified image shows the cross-sectional TEM image of an EBL sandwiched between two EMLs. (b) Chemical structures and brief roles of each layer of the CTOLED. (c) Energy band diagram of the CTOLED estimated using ultraviolet photoelectron spectrometry (thickness not drawn to scale). (d) Cross-sectional TEM image of the CTOLED. (e) Magnified TEM image showing the detailed cross-sectional structure of the CTOLED (red box in (d)). (f) High-resolution TEM image, magnified from the blue box in (e). (g,h) Schematic illustrations of the color-tuning mechanism (g) with and (h) without the EBL.

The measured ECG signals can be displayed in a colorimetric manner by using wearable CTOLEDs. The CTOLEDs are fabricated using an EBL (DPEPO) sandwiched between two emitting materials: a blue phosphorescent layer of bis[2-(4,6-difluorophenyl)pyridinato-C²,N](picolinato)iridium(III) (FIrpic) doped in a 4,4'-bis(N-carbazolyl)-1,1'-biphenyl (CBP) layer and an undoped red phosphorescent layer of bis(2-phenylquinolyl-N,C(2'))-iridium(acetylacetonate)(pq₂Ir(acac)). Figure 3a schematically illustrates the device structure of the CTOLED (total thickness of ~366 nm), which consists of ITO (100 nm), N,N'-di(1-naphthyl)-N,N'-diphenyl-(1,1'-biphenyl)-4,4'-diamine (NPB, 70 nm), CBP/10% FIrpic (70 nm), bis[2-(diphenylphosphino)-phenyl]ether oxide (DPEPO, 5 nm); pq₂Ir(acac) (1 nm), 2,2',2''-(1,3,5-benzinetriyl)-tris(1-phenyl-1H-benzimidazole) (TPBI, 20 nm), and LiF/Al (1 nm/100 nm). NPB is used as a hole-transporting layer (HTL), TPBI as an electron-transporting layer (ETL), LiF as an electroninjection layer, and Al as a cathode. The DPEPO between the EMLs acts as a selective charge- and exciton-blocking layer, which determines the color tunability (Figure 3b,c). The thickness of the red EML is elaborately controlled to be substantially lesser than that of the blue EML, allowing a sharp color contrast in the higher-voltage regime. Figure 3d shows the cross-sectional transmission electron microscopy (TEM) image of the CTOLED, confirming the stacked structures. The magnified TEM image (Figure 3e) that corresponds to the red box in Figure 3d provides the detailed layer information. The precise thickness control of the deposited layers can be confirmed through the high-resolution TEM image in Figure 3f (blue box in Figure 3e).

The detailed mechanism behind the color tunability is explained by the energy level and thickness of the layers. As can be seen from the energy band diagram in

Figure 3c, the holes injected from the ITO and HTL are easily transferred to the red EML throughout the entire working voltage regime, owing to the terraced highest occupied molecular orbitals (HOMOs) of the deposited layers. However, the electrons cannot overcome the barrier formed by the lowest unoccupied molecular orbitals (LUMOs) of DPEPO (2.0 eV) because of the electron blocking in the low-voltage regime (5~7 V), resulting in red emission by the recombination of triplet excitons in the red EML, as schematically described in Figure 3g. In the higher-voltage regime (11~13 V), the accumulated electrons in the LUMOs of the red EML gain sufficient energy to overcome the thin (5 nm) barrier of the DPEPO and generate the necessary excitons for recombination in the blue EML. At the same time, the DPEPO layer again acts as an energy barrier that blocks the energy transfer from the blue emission (2.7 eV) to the red emission (2.1 eV) owing to its high triplet energy ($T_{\text{DPEPO}} = 3.1 \text{ eV}$).³²⁷ Therefore, a clear blue emission results from the large amount of recombination in the blue EML, arising from the thickness difference between the two EMLs. Without the EBL, a red emission can be expected in both the low- and high-voltage regimes due to the favorable energy transfer from the blue EML to the red EML, as schematically depicted in Figure 3h. Although some recombination of excitons in the blue EML can be expected in all voltage ranges, the dominant region of emission would occur in the red EML, as the majority of the excitons in the blue EML would prefer a transfer to the lower triplet energy state of the red EML.

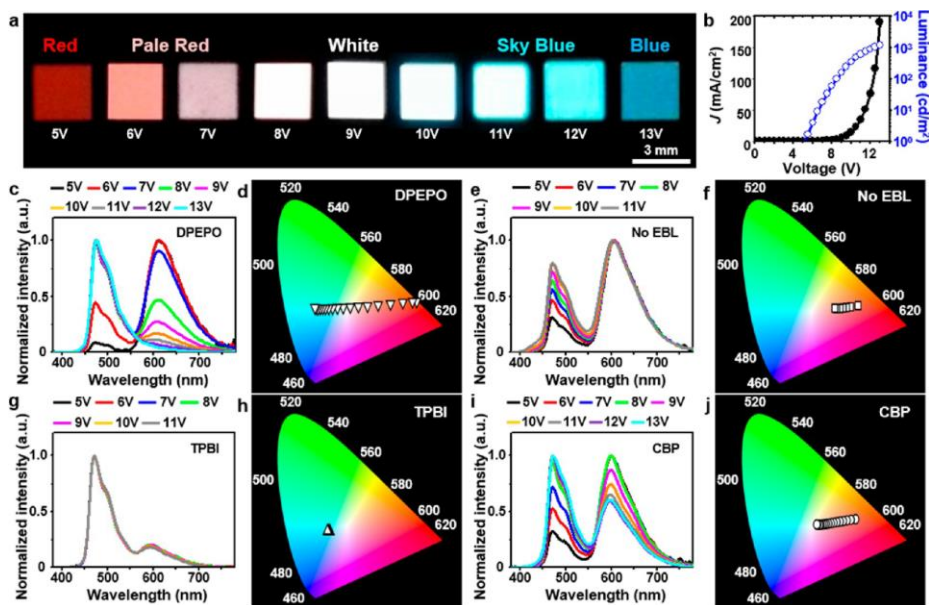


Figure 4. (a) Digital photographs of the CTOLED showing color changes from dark red, to pale red, to white, to sky blue, and to deep blue at different applied voltages. (b) J-V-L characteristics of the CTOLED. (c,e,g,i) EL spectra of the CTOLEDs using different EBLs of (c) DPEPO, (e) no EBL, (g) TPBI, and (i) CBP. The thicknesses of all EBLs are 5 nm, except for the no EBL case. (d,f,h,j) Corresponding CIE 1931 x-y chromaticity diagrams of the CTOLEDs using different EBLs of (d) DPEPO, (f) no EBL, (h) TPBI, and (j) CBP.

Figure 4a shows the optical camera images of the CTOLED at various operation voltages, illustrating a clear color change from dark red (5 V), to pale red (6~7 V), to white (8~10 V), to sky blue (11~12 V), and finally to deep blue (13 V). The current density (J)-voltage (V)-luminance (L) characteristics presented in Figure 4b show a turn-on voltage of 4.5 V and a maximum brightness of 1934 cd/m² at 13 V. The white emission can be explained by the balanced emission of blue and red.

The amount of triplet excitons generated in the blue EML is directly proportional to the applied voltage and so is the intensity of blue emission. Thus, it can be inferred that the color change from red to white and then to blue is the result of the color balance between the red and blue emissions. This behavior is in good accordance with the electroluminescence (EL) spectra and the corresponding Commission Internationale de L'Eclairage (CIE) coordinates characterized from the CTOLED using 5 nm thick DPEPO as the EBL (Figure 4c,d). According to the EL spectra, red-light emission is dominant at low operation voltages, whereas blue-light emission increases at higher operation voltages (Figure 4c). Due to the changes in the emission intensities in the two EMLs, the CIE coordinates shift from red (0.62, 0.36) to white (0.32, 0.34) and then to blue (0.17, 0.33) by increasing the operation voltage from 5 to 13 V (Figure 4d). The EL spectra and CIE coordinates of a CTOLED without the EBL indicate dominant emission of red light, which is also in good agreement with our hypothesis that the triplet excitons in the blue EML favor the energy transfer to the red EML, instead of relaxation as blue light in FIrpic (Figure 4e,f).

To further verify the role of EBL in the CTOLED devices, different materials have been tested as EBLs, and their EL spectra have been characterized along with their corresponding CIE coordinates. When a 5 nm thick TPBI is used as an EBL, the OLED emits only blue light (0.23, 0.31) in the same operation voltage ranges (Figure 4g,h). Unlike the case of DPEPO, electrons would be readily transferred to the blue EML even in the low-voltage regime because TPBI acts as an ETL, which explains the occurrence of blue emissions starting from the turn-on voltage. Meanwhile, the relatively high triplet energy of TPBI ($T_{\text{TPBI}} = 2.8$ eV) results in partial blockage of the energy transfer from the blue EML to the red EML in all

voltage ranges, allowing for some recombination of charges in the red EML. As a result, the emitted color from the OLED using TPBI as an EBL is light blue, and no color change is induced as the color balance between the red EML and the blue EML is maintained throughout the entire voltage regime. When a 5 nm thick CBP is used as an EBL, a slight color shift from red (0.52, 0.37) to white (0.34, 0.34) can be observed on increasing the operation voltage (Figure 4i,j). It can be attributed to the relatively low triplet energy of CBP ($T_{\text{CBP}} = 2.6$ eV), which allows a major energy transfer of triplet excitons from the blue EML to the red EML in the high-voltage regime. The effect of the EBL thickness on the color tunability has been verified and characterized in Supporting Information Figures S1~S3, by testing 1 nm thick and 10 nm thick DPEPOs.

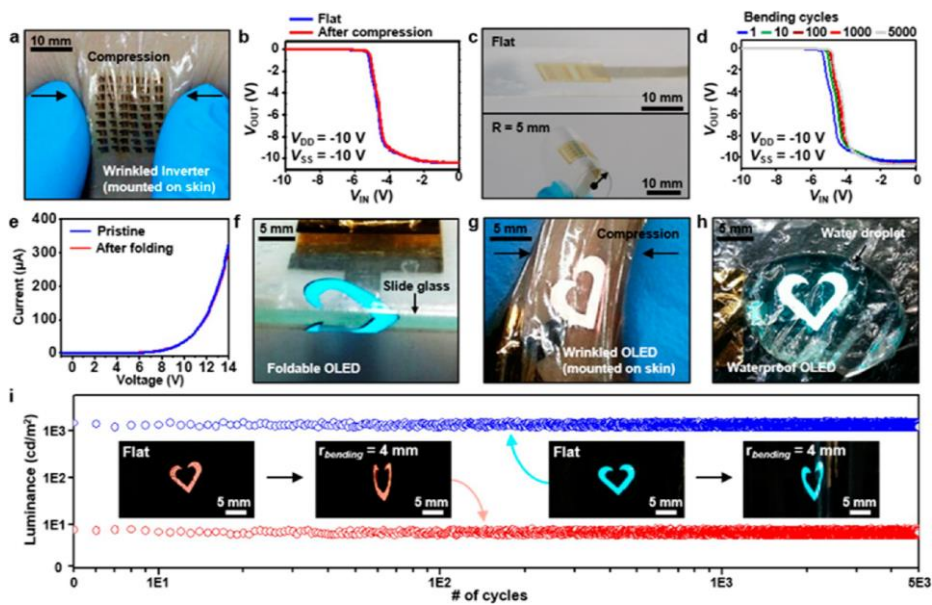


Figure 5. (a) Photograph of the CNT p-MOS inverter compressed after worn on human skin. (b) Voltage transfer characteristics of the inverter before and after compression, at V_{DD} and V_{SS} of -10 V. (c) Photographs of the inverter before bending (top) and after bending with a bending radius of 5 mm (bottom). (d) Voltage transfer characteristics of the inverter after the cyclic bending test up to 1000 times, at V_{DD} and V_{SS} of -10 V ($r_{\text{bending}} = 5$ mm). (e) J-V characteristics of the wearable CTOLED before and after bending. (f-h) Photographs of the CTOLEDs (f) after folding along a slide glass, (g) wrinkled after worn on human skin, and (h) under a water droplet. (i) Stable luminance of the blue and red emission during multiple bending experiments (with $r_{\text{bending}} = 4$ mm, 1000 times).

For wearable electronic/optoelectronic applications, it is crucial that the devices perform robustly even after repetitive deformations and that they withstand consequent fatigues. In this regard, the mechanical reliability of the p-MOS CNT

inverter and the ultrathin CTOLED is verified under various deformed conditions (Figure 5). The voltage transfer curves of the p-MOS inverter exhibit negligible changes after being worn on the skin and compressed inward (Figure 5a,b). For further validation of the stability, up to 5000 cycles of cyclic bending tests (to a bending radius of 5 mm) are performed, which show minimal shifts in the voltage transfer curves (Figure 5c,d). The deformability of the CTOLED is also tested. Although previous reports have already presented details of a substantial amount of effort toward developing flexible and/or stretchable LEDs based on inorganics,^{262, 302} quantum dots,³²⁸⁻³³¹ and polymers³³²⁻³³⁴ for wearable displays, the mechanical robustness of an ultrathin wearable OLED with color-changing features has not yet been reported. The strategy to develop a wearable CTOLED is schematically illustrated in Supporting Information Figure S4, and details are described in the Methods section. The deformable CTOLED shows no degradation in the diode characteristics after folding (Figure 5e). The photographs in Figure 5f-h further confirm the robust performance of the CTOLEDs after folding against a slide glass, wrinkling on skin, and underwater operations, respectively. The stability of the wearable CTOLED is verified through cyclic bending tests (Figure 5i), where both the red and blue emissions of the CTOLED remain stable after 5000 cycles of bending with a bending radius of 4 mm (Figure 5i, inset). In all, the excellent mechanical stability as well as wearability of our devices can be attributed to the ultrathin nature, use of intrinsically flexible materials, and effective passivation, and further improvements on the wearability can be expected by adopting stretchable designs (i.e., serpentine interconnections).²¹⁰

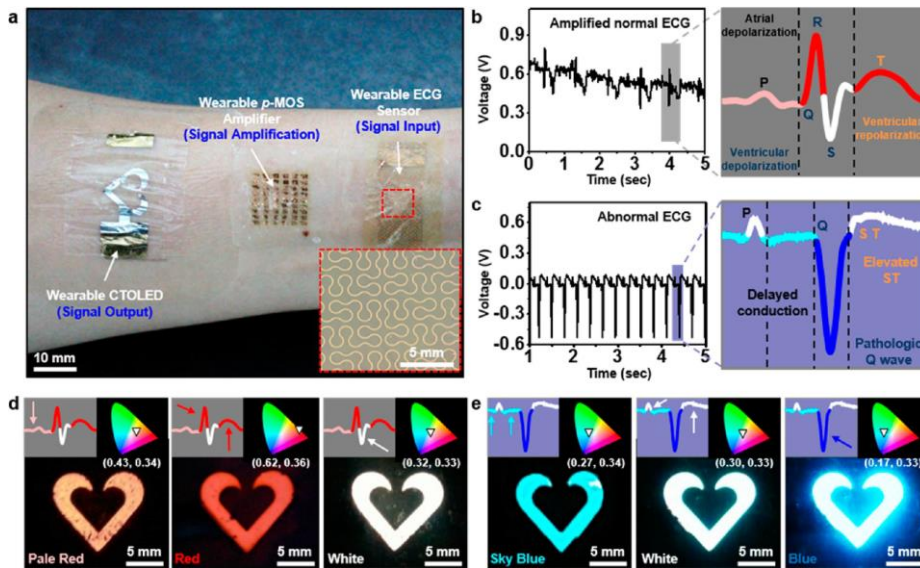


Figure 6. (a) Photograph of the wearable system for real-time visual monitoring of the ECG signals, composed of the wearable ECG electrode, CNT p-MOS inverters, and CTOLEDs. (b) Normal ECG signals measured from a human wrist by using a wearable ECG sensor (left) and the detailed view of a single ECG signal after amplification showing PQRST peaks (right). (c) Abnormal ECG signals measured from an 8-week post-MI rat (left) and the detailed view of a single abnormal ECG signal. (d) Real-time color changes of the CTOLED, synchronized with the shape of the measured normal ECG signal. The insets indicate (left) the region of ECG signal for respective color emission and (right) corresponding CIE coordinates. (e) Real-time color changes of the CTOLED, synchronized with the shape of the abnormal ECG signal. The insets indicate (left) the region of ECG signal for respective color emission and (right) corresponding CIE coordinates.

Finally, we demonstrate system-level integration of the wearable CTOLEDs with skin-mounted ECG electrodes and CNT signal amplifiers for the real-time display of cardiac signals through synchronized color changes of the CTOLED. Figure 6a depicts a photograph of wearable device components for the proposed monitoring system (inset shows a magnified view of the electrode). A DAQ and PC (not shown in picture) are used for analyzing the signals and delivering the adjusted voltage to the CTOLED. Specifically, the ECG signals are measured from human wrists using wearable ECG sensors and then amplified using our p-MOS CNT inverters. The noise is then eliminated using high/low-pass filters (0.079/19.4 Hz). A diagram of the ECG signal processing procedure and a photograph of actual components consisting our wearable ECG monitor are described in Figure S5. Customized software (LabVIEW, National Instruments, USA) analyzes the amplified ECG signals and delivers the adjusted voltage to the wearable CTOLED to indicate the cardiac health condition. Here, we deliberately program our software to distinguish a normal human ECG from an abnormal one (cf., abnormal cardiac signals were obtained from a postmyocardial infarction model³³⁵) through the color changes in the CTOLEDs (the detailed codes can be found in Supporting Information Figure S6). As illustrated in Figure 6b (right), a normal human ECG signal contains clear peaks of PQRST, which can be used to determine the activities of atrial depolarization, ventricular depolarization, and ventricular repolarization. When a wearable ECG sensor detects a normal human ECG signal, our software delivers voltages that correspond to pale red, red, and white emissions to the CTOLEDs (5~9 V), resulting in a synchronized display of the ECG signals with the respective colors (Figure 6d and Supplementary Video S1). On the other hand, when abnormal ECG signals (Figure 6c) exhibiting delayed electrocardial conduction, such as pathologic Q waves or elevated ST peaks, are measured, the program delivers voltages

corresponding to white, sky blue, and deep blue emissions to the wearable CTOLEDs (10~13 V). As a result, the CTOLEDs emit the respective colors that are synchronized with the amplitudes of the abnormal ECG signals (Figure 6e and Supplementary Video S2). The system-level demonstration verifies the feasibility of a wearable indicator to display normal and diseased ECG signals.

3. Conclusion

In summary, an approach for the fabrication of ultrathin CNT electronics and color-tunable OLEDs toward a wearable ECG monitor and display was proposed. p-MOS inverters based on CNT transistors were developed successfully for the amplification of ECG signals. A comparative analysis on the optical properties of CTOLEDs employing different EBLs confirmed their roles, accompanied by a proper mechanism for the respective color-tuning behaviors. The ultrathin CNT electronics and CTOLEDs demonstrated high resilience against extreme bending and folding conditions, verified through repetitive bending/fatigue tests. System-level integration was accomplished whereby real-time ECG signals were visually displayed using the wearable devices. These advances will offer many opportunities for the development of future wearable biomedical monitoring devices.

4. Supporting information

4.1. Method

Fabrication of p-MOS CNT Inverters. A polyimide (PI) layer (~1 μm) was spin-coated on a silicon oxide (SiO_2) wafer, followed by the formation of back-gate electrodes (Cr/Au, 7/70 nm) using thermal evaporation and photolithography. Two consecutive layers of ~30 nm thick aluminum oxide and ~3 nm thick SiO_2 were

deposited on top by plasma-enhanced atomic layer deposition and e-beam evaporation, respectively. Then, the top surface of SiO₂ was functionalized using poly-L-lysine (0.1 wt %, aqueous solution; Sigma-Aldrich) to form an amine-terminated surface, followed by consecutive immersions in semiconducting CNT solution (0.01 mg/ML, aqueous solution) for a few hours to form dense networks of CNTs on the top surface. After being rinsed with deionized water and isopropyl alcohol, the sample was annealed inside a glovebox at 200 °C for 1 h to remove the unwanted surfactants and carboxyl groups on the surface of the CNTs. Via connections were then formed, followed by the formation of source and drain electrodes (Cr/Au, 7/70 nm) through thermal evaporation and photolithography. The process was completed by spin-coating a top PI layer for passivation and mechanical stability.

Fabrication of CTOLEDs. NPB, CBP, FIrpic, TBPI, pq₂Ir(acac), and DPEPO were purchased from commercial sources and used without purification. The CTOLEDs were fabricated through highvacuum (2×10^{-6} Torr) thermal evaporation of the organic materials onto ITO-coated glass (sheet resistance: 15 Ω/square; Applied Film Corp.). The evaporation rates, monitored by a quartz crystal thickness monitor, were 1 Å/s for the organic materials and 3–4 Å/s for the metals. Glass substrates with patterned ITO electrodes were washed in isopropyl alcohol and then cleaned through O₂ plasma treatment. CTOLEDs were fabricated with a configuration of ITO/NPB (70 nm)/CBP/10% FIrpic (70 nm)/EBL (0, 1, 5, and 10 nm for various materials)/pq₂Ir(acac) (1 nm)/TPBI (20 nm)/LiF (1 nm)/Al (100 nm). NPB, CBP, FIrpic, different materials of EBL, pq₂Ir(acac), TPBI, LiF, and Al

electrodes were deposited on the substrate in a sequential order. DPEPO was used as an EBL. CBP and TPBI were also used as EBL materials for the color-tunable device.

Fabrication of Wearable CTOLEDs. A Parylene-C layer (500 nm) was evaporation-deposited on a Teflon-AF-coated glass, followed by spin-coating of epoxy (600 nm, SU-8 2000.5, MicroChem) at 3000 rpm for 30 s. After the photoresist was fully cured, Au (70 nm) was thermally evaporated and ITO was sputtered (50 W, 30 min, 5 mTorr, 200 °C), both using a shadow mask. The deposition of NPB, CBP, Flrpic, DPEPO, $\text{pq}_2\text{Ir}(\text{acac})$, TPBI, LiF, and Al followed the same procedures/thickness described above. Parylene-C was once again deposited, and Au electrodes were exposed by reactive ion etching (150 W, 100 sccm O_2 , 3 min) using a shadow mask. After flexible cables were connected for external wiring, the CTOLEDs were picked up using a commercial transparent water-proof tape (Tegaderm Film, 3M), resulting in a wearable CTOLED device.

Characterizations. The emission properties and external quantum efficiencies were determined using a PR-650 SpectraScan SpectraColorimeter as a source meter. The current-density-voltage characteristics and electrical performances of the CNT transistors were measured using a programmable electrometer equipped with current and voltage sources (Keithley 2400). The TEM images and highresolution TEM images were obtained using a JEOL 2100F electron microscope operated at 200 kV.

4.2. Supporting figures

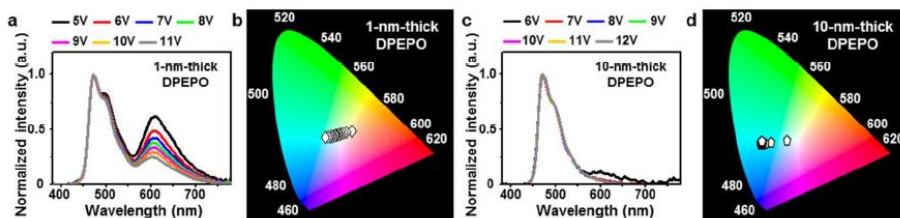


Figure S1. (a) EL spectra of the CTOLED using 1-nm-thick DPEPO as EBL and (b) its corresponding CIE diagram. (c) EL spectra of the CTOLED using 10-nm-thick DPEPO as EBL and (d) its corresponding CIE diagram.

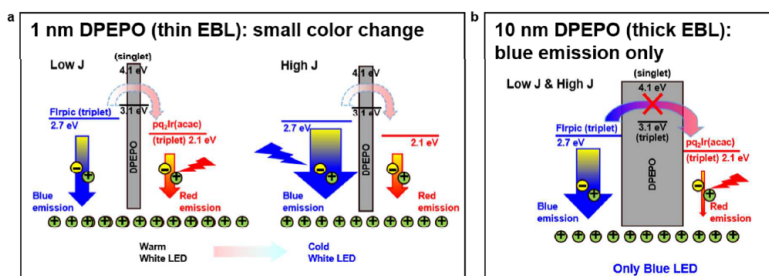


Figure S2. Schematic illustration of the mechanism explaining the color tuning behavior of the OLED with (a) 1-nm-thick EBL and (b) 10-nm-thick EBL.

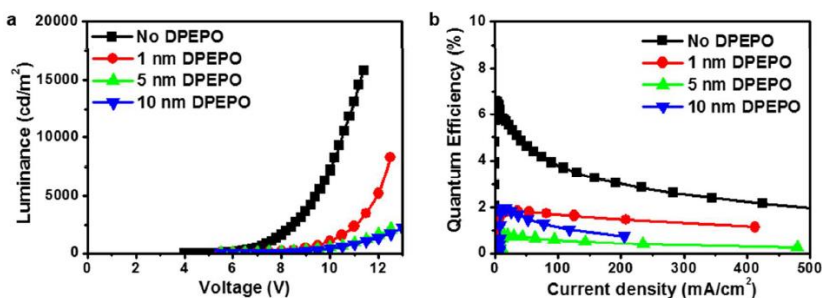


Figure S3. (a) Voltage-dependent luminance and (b) quantum efficiency characteristics of the fabricated CTOLED using EBLs with different thicknesses.

The effect of the EBL thickness on the color-tunability has been verified by testing 1-nm-thick and 10-nm-thick DPEPOs. A rather ambiguous color change from warm white (0.36, 0.37) to light blue (0.25, 0.34) is observed for the CTOLED with a 1-nm-thick DPEPO on increasing the operation voltages (Figure S1a and b), which can mainly be ascribed to the tunneling of both electrons and triplet excitons through the ultrathin DPEPO layer in low- and high-voltage regime, respectively (Figure S2a). However, when a 10-nm-thick DPEPO layer is deployed as the EBL, the OLED exhibited light blue emissions (0.27, 0.32) at a turn-on voltage of 5 V, followed by blue emissions at (0.19, 0.31) to (0.16, 0.32) at 13 V (Figure S1c and d). It may be ascribed to the ETL-like characteristics of DPEPO, whereby the increased thickness of 10 nm allows for substantially faster electron transfer to the blue EML than hole transfer to the red EML. The increased thickness of DPEPO further ensures the successful blocking of the exciton transfer from the blue EML to the red EML, which explains the blue emission on using 10-nm-thick DPEPO (Figure S2b). It should also be noted that the thickness of the EBL is in a reverse relationship with the luminance and quantum efficiency, since the charge balance between the two EMLs becomes uneven with the increased EBL thickness (Figure S3).

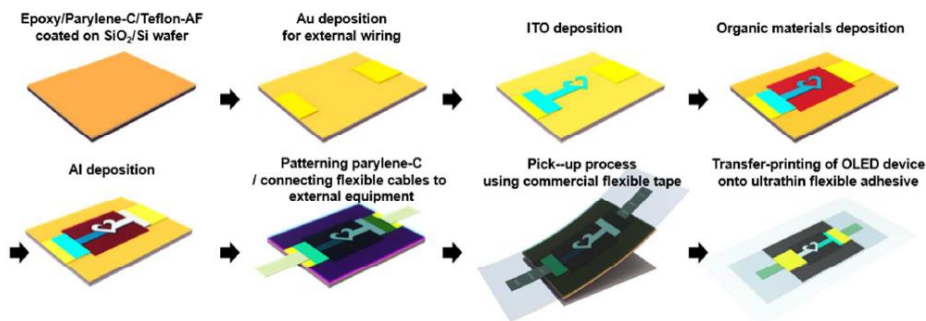


Figure S4. Schematic illustration of the fabrication process of wearable CTOLEDs.

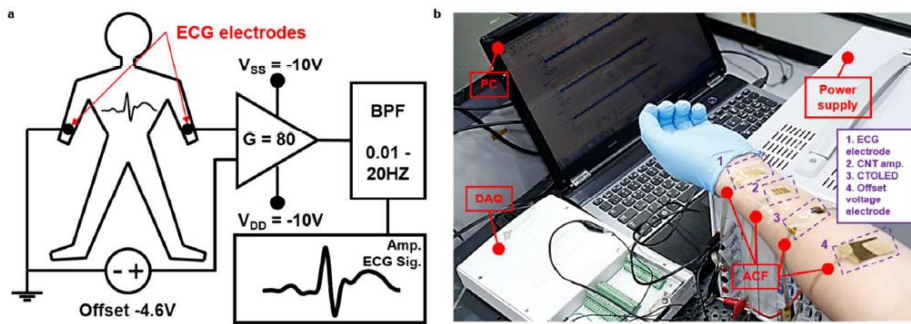


Figure S5. (a) Diagram of ECG signal processing procedure. (b) Photograph of the experimental setup including the DAQ unit, PC, and ACF wirings for the wearable ECG monitor system.

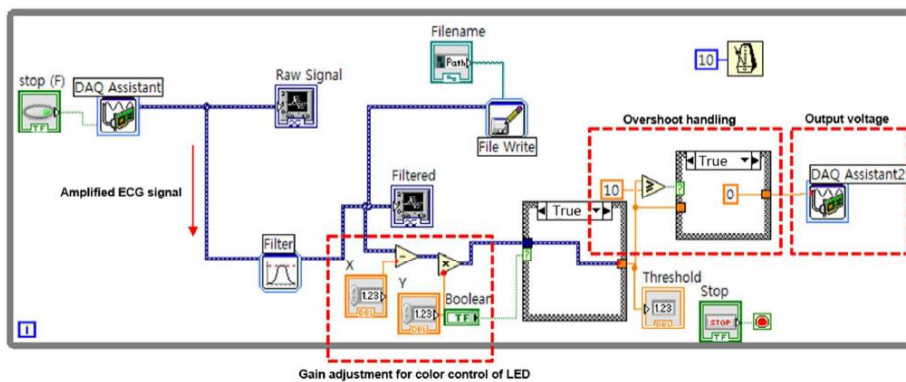


Figure S6. A block diagram of LabVIEW-based software for controlling the color of the OLED according to the ECG amplitude change.

References and Notes

1. Wong, M. Y.; Zysman-Colman, E., Purely Organic Thermally Activated Delayed Fluorescence Materials for Organic Light-Emitting Diodes. *Adv Mater* **2017**, *29* (22), 1605444.
2. Valeur, B., *Molecular Fluorescence and Applications*. Wiley-VCH: 2001.
3. Dias, F. B.; Penfold, T. J.; Monkman, A. P., Photophysics of thermally activated delayed fluorescence molecules. *Methods Appl Fluores* **2017**, *5* (1), 012001.
4. Uoyama, H.; Goushi, K.; Shizu, K.; Nomura, H.; Adachi, C., Highly efficient organic light-emitting diodes from delayed fluorescence. *Nature* **2012**, *492* (7428), 234-240.
5. Nakagawa, T.; Ku, S. Y.; Wong, K. T.; Adachi, C., Electroluminescence based on thermally activated delayed fluorescence generated by a spirobifluorene donor-acceptor structure. *Chem Commun* **2012**, *48* (77), 9580-9582.
6. Birks, J. B., *Photophysics of aromatic molecules*. Wiley-Interscience: 1970.
7. Luo, J. D.; Xie, Z. L.; Lam, J. W. Y.; Cheng, L.; Chen, H. Y.; Qiu, C. F.; Kwok, H. S.; Zhan, X. W.; Liu, Y. Q.; Zhu, D. B.; Tang, B. Z., Aggregation-induced emission of 1-methyl-1,2,3,4,5-pentaphenylsilole. *Chem Commun* **2001**, (18), 1740-1741.
8. Tang, B. Z.; Zhan, X. W.; Yu, G.; Lee, P. P. S.; Liu, Y. Q.; Zhu, D. B., Efficient blue emission from siloles. *J Mater Chem* **2001**, *11* (12), 2974-2978.
9. Hong, Y. N.; Lam, J. W. Y.; Tang, B. Z., Aggregation-induced emission: phenomenon, mechanism and applications. *Chem Commun* **2009**, (29), 4332-4353.
10. Chen, J. W.; Xu, B.; Ouyang, X. Y.; Tang, B. Z.; Cao, Y., Aggregation-induced emission of cis,cis-1,2,3,4-tetraphenylbutadiene from restricted intramolecular rotation. *J Phys Chem A* **2004**, *108* (37), 7522-7526.
11. Tong, H.; Hong, Y. N.; Dong, Y. Q.; Ren, Y.; Haussler, M.; Lam, J. W. Y.; Wong, K. S.; Tang, B. Z., Color-tunable, aggregation-induced emission of a butterfly-shaped molecule comprising a pyran skeleton and two cholesteryl wings. *J Phys Chem B* **2007**, *111* (8), 2000-2007.
12. Tong, H.; Zhu, Y. J.; Yang, L. X.; Li, L.; Zhang, L.; Chang, J.; An, L. Q.; Wang, S. W., Self-assembled ZnS nanostructured spheres: Controllable crystal phase and morphology. *J Phys Chem C* **2007**, *111* (10), 3893-3900.
13. Zeng, Q.; Li, Z.; Dong, Y. Q.; Di, C. A.; Qin, A. J.; Hong, Y. N.; Ji, L.; Zhu, Z. C.; Jim, C. K. W.; Yu, G.; Li, Q. Q.; Li, Z. A.; Liu, Y. Q.; Qin, J. G.; Tang, B. Z., Fluorescence enhancements of benzene-cored luminophors by restricted intramolecular rotations: AIE and AIEE effects. *Chem Commun* **2007**, (1), 70-72.
14. Dong, Y. Q.; Lam, J. W. Y.; Qin, A. J.; Liu, J. Z.; Li, Z.; Tang, B. Z., Aggregation-induced emissions of tetraphenylethene derivatives and their utilities as chemical vapor sensors and in organic light-emitting diodes. *Appl Phys Lett* **2007**, *91* (1), 011111.

15. Kamtekar, K. T.; Monkman, A. P.; Bryce, M. R., Recent Advances in White Organic Light-Emitting Materials and Devices (WOLEDs). *Adv Mater* **2010**, *22* (5), 572-582.
16. Farinola, G. M.; Ragni, R., Electroluminescent materials for white organic light emitting diodes. *Chem Soc Rev* **2011**, *40* (7), 3467-3482.
17. Chi, Y.; Chou, P. T., Transition-metal phosphors with cyclometalating ligands: fundamentals and applications. *Chem Soc Rev* **2010**, *39* (2), 638-655.
18. Schwartz, G.; Reineke, S.; Rosenow, T. C.; Walzer, K.; Leo, K., Triplet Harvesting in Hybrid White Organic Light-Emitting Diodes. *Adv Funct Mater* **2009**, *19* (9), 1319-1333.
19. Pu, Y. J.; Nakata, G.; Satoh, F.; Sasabe, H.; Yokoyama, D.; Kido, J., Optimizing the Charge Balance of Fluorescent Organic Light-Emitting Devices to Achieve High External Quantum Efficiency Beyond the Conventional Upper Limit. *Adv Mater* **2012**, *24* (13), 1765-1770.
20. Adachi, C.; Tsutsui, T.; Saito, S., Blue Light-Emitting Organic Electroluminescent Devices. *Appl Phys Lett* **1990**, *56* (9), 799-801.
21. Lee, M. T.; Chen, H. H.; Liao, C. H.; Tsai, C. H.; Chen, C. H., Stable styrylamine-doped blue organic electroluminescent device based on 2-methyl-9,10-di(2-naphthyl)anthracene. *Appl Phys Lett* **2004**, *85* (15), 3301-3303.
22. Shi, J. M.; Tang, C. W., Anthracene derivatives for stable blue-emitting organic electroluminescence devices. *Appl Phys Lett* **2002**, *80* (17), 3201-3203.
23. Kim, Y. H.; Jeong, H. C.; Kim, S. H.; Yang, K. Y.; Kwon, S. K., High-purity-blue and high-efficiency electroluminescent devices based on anthracene. *Adv Funct Mater* **2005**, *15* (11), 1799-1805.
24. Shih, P. I.; Chuang, C. Y.; Chien, C. H.; Diao, E. W. G.; Shu, C. F., Highly efficient non-doped blue-light-emitting diodes based on an anthracene derivative end-capped with tetraphenylethylene groups. *Adv Funct Mater* **2007**, *17* (16), 3141-3146.
25. Kim, S. K.; Yang, B.; Ma, Y.; Lee, J. H.; Park, J. W., Exceedingly efficient deep-blue electroluminescence from new anthracenes obtained using rational molecular design. *J Mater Chem* **2008**, *18* (28), 3376-3384.
26. Kim, Y. H.; Shin, D. C.; Kim, S. H.; Ko, C. H.; Yu, H. S.; Chae, Y. S.; Kwon, S. K., Novel blue emitting material with high color purity. *Adv Mater* **2001**, *13* (22), 1690-1693.
27. Wu, C. H.; Chien, C. H.; Hsu, F. M.; Shih, P. I.; Shu, C. F., Efficient non-doped blue-light-emitting diodes incorporating an anthracene derivative end-capped with fluorene groups. *J Mater Chem* **2009**, *19* (10), 1464-1470.
28. Chao, T. C.; Lin, Y. T.; Yang, C. Y.; Hung, T. S.; Chou, H. C.; Wu, C. C.; Wong, K. T., Highly efficient UV organic light-emitting devices based on bi(9,9-diarylfuorene)s. *Adv Mater* **2005**, *17* (8), 992-996.
29. Tao, Y. T.; Yang, C. L.; Qin, J. G., Organic host materials for phosphorescent organic light-emitting diodes. *Chem Soc Rev* **2011**, *40* (5), 2943-2970.

30. Tao, S.; Zhou, Y. C.; Lee, C. S.; Lee, S. T.; Huang, D.; Zhang, X. H., Highly efficient nondoped blue organic light-emitting diodes based on anthracene-triphenylamine derivatives. *J Phys Chem C* **2008**, *112* (37), 14603-14606.
31. Kim, S. K.; Yang, B.; Park, Y. I.; Ma, Y. G.; Lee, J. Y.; Kim, H. J.; Park, J., Synthesis and electroluminescent properties of highly efficient anthracene derivatives with bulky side groups. *Org Electron* **2009**, *10* (5), 822-833.
32. Moorthy, J. N.; Venkatakrishnan, P.; Huang, D. F.; Chow, T. J., Blue light-emitting and hole-transporting amorphous molecular materials based on diarylamino-biphenyl-functionalized bimesitylenes. *Chem Commun* **2008**, (18), 2146-2148.
33. Tao, S. L.; Zhou, Y. C.; Lee, C. S.; Zhang, X. H.; Lee, S. T., High-Efficiency Nondoped Deep-Blue-Emitting Organic Electroluminescent Device. *Chem Mater* **2010**, *22* (6), 2138-2141.
34. Jiang, Z. Q.; Yao, H. Q.; Liu, Z. Y.; Yang, C. L.; Zhong, C.; Qin, J.; Yu, G.; Liu, Y. Q., Bent Ladder-Type Hexaphenylene with Carbazole Core and Spiro Linkage as Stable and Efficient Blue Emitter. *Org Lett* **2009**, *11* (18), 4132-4135.
35. Park, Y. I.; Son, J. H.; Kang, J. S.; Kim, S. K.; Lee, J. H.; Park, J. W., Synthesis and electroluminescence properties of novel deep blue emitting 6,12-dihydro-diindeno[1,2-b : 1',2'-e] pyrazine derivatives. *Chem Commun* **2008**, (18), 2143-2145.
36. Tonzola, C. J.; Kulkarni, A. P.; Gifford, A. P.; Kaminsky, W.; Jenekhe, S. A., Blue-light-emitting oligoquinolines: Synthesis, properties, and high-efficiency blue-light-emitting diodes. *Adv Funct Mater* **2007**, *17* (6), 863-874.
37. Kuo, C. J.; Li, T. Y.; Lien, C. C.; Liu, C. H.; Wu, F. I.; Huang, M. J., Bis(phenanthroimidazolyl)biphenyl derivatives as saturated blue emitters for electroluminescent devices. *J Mater Chem* **2009**, *19* (13), 1865-1871.
38. Wang, Z. M.; Lu, P.; Chen, S. M.; Gao, Z.; Shen, F. Z.; Zhang, W. S.; Xu, Y. X.; Kwok, H. S.; Ma, Y. G., Phenanthro[9,10-d]imidazole as a new building block for blue light emitting materials. *J Mater Chem* **2011**, *21* (14), 5451-5456.
39. Wan, J.; Zheng, C. J.; Fung, M. K.; Liu, X. K.; Lee, C. S.; Zhang, X. H., Multifunctional electron-transporting indolizine derivatives for highly efficient blue fluorescence, orange phosphorescence host and two-color based white OLEDs. *J Mater Chem* **2012**, *22* (10), 4502-4510.
40. Chien, C. H.; Chen, C. K.; Hsu, F. M.; Shu, C. F.; Chou, P. T.; Lai, C. H., Multifunctional Deep-Blue Emitter Comprising an Anthracene Core and Terminal Triphenylphosphine Oxide Groups. *Adv Funct Mater* **2009**, *19* (4), 560-566.
41. Yeh, H. C.; Lee, R. H.; Chan, L. H.; Lin, T. Y. J.; Chen, C. T.; Balasubramaniam, E.; Tao, Y. T., Synthesis, properties, and applications of tetraphenylmethane-based molecular materials for light-emitting devices. *Chem Mater* **2001**, *13* (9), 2788-2796.
42. Zhu, M. R.; Wang, Q. A.; Gu, Y.; Cao, X. S.; Zhong, C.; Ma, D. G.; Qin, J. G.; Yang, C. L., Efficient deep-blue emitters comprised of an anthracene core and

- terminal bifunctional groups for nondoped electroluminescence. *J Mater Chem* **2011**, *21* (17), 6409-6415.
43. Huang, J. H.; Su, J. H.; Li, X.; Lam, M. K.; Fung, K. M.; Fan, H. H.; Cheah, K. W.; Chen, C. H.; Tian, H., Bipolar anthracene derivatives containing hole- and electron-transporting moieties for highly efficient blue electroluminescence devices. *J Mater Chem* **2011**, *21* (9), 2957-2964.
44. Shirota, Y.; Kinoshita, M.; Noda, T.; Okumoto, K.; Ohara, T., A novel class of emitting amorphous molecular materials as bipolar radical formants: 2-[4-[bis(4-methylphenyl)amino]phenyl]-5-(dimesitylboryl)thiophene and 2-(4-[bis(9,9-dimethylfluorenyl)amino]phenyl)-5-(dimesitylboryl) thiophene. *J Am Chem Soc* **2000**, *122* (44), 11021-11022.
45. Lin, S. L.; Chan, L. H.; Lee, R. H.; Yen, M. Y.; Kuo, W. J.; Chen, C. T.; Jeng, R. J., Highly Efficient Carbazole-pi-Dimesitylborane Bipolar Fluorophores for Nondoped Blue Organic Light-Emitting Diodes. *Adv Mater* **2008**, *20* (20), 3947-3952.
46. Lee, S. J.; Park, J. S.; Yoon, K. J.; Kim, Y. I.; Jin, S. H.; Kang, S. K.; Gal, Y. S.; Kang, S.; Lee, J. Y.; Kang, J. W.; Lee, S. H.; Park, H. D.; Kim, J. J., High-Efficiency Deep-Blue Light-Emitting Diodes Based on Phenylquinoline/Carbazole-Based Compounds. *Adv Funct Mater* **2008**, *18* (24), 3922-3930.
47. Zhang, Y.; Lai, S. L.; Tong, Q. X.; Lo, M. F.; Ng, T. W.; Chan, M. Y.; Wen, Z. C.; He, J.; Jeff, K. S.; Tang, X. L.; Liu, W. M.; Ko, C. C.; Wang, P. F.; Lee, C. S., High Efficiency Nondoped Deep-Blue Organic Light Emitting Devices Based on Imidazole-pi-triphenylamine Derivatives. *Chem Mater* **2012**, *24* (1), 61-70.
48. Li, W. J.; Liu, D. D.; Shen, F. Z.; Ma, D. G.; Wang, Z. M.; Feng, T.; Xu, Y. X.; Yang, B.; Ma, Y. G., A Twisting Donor-Acceptor Molecule with an Intercrossed Excited State for Highly Efficient, Deep-Blue Electroluminescence. *Adv Funct Mater* **2012**, *22* (13), 2797-2803.
49. Tsai, T. C.; Hung, W. Y.; Chi, L. C.; Wong, K. T.; Hsieh, C. C.; Chou, P. T., A new ambipolar blue emitter for NTSC standard blue organic light-emitting device. *Org Electron* **2009**, *10* (1), 158-162.
50. Lai, M. Y.; Chen, C. H.; Huang, W. S.; Lin, J. T.; Ke, T. H.; Chen, L. Y.; Tsai, M. H.; Wu, C. C., Benzimidazole/amine-based compounds capable of ambipolar transport for application in single-layer blue-emitting OLEDs and as hosts for phosphorescent emitters. *Angew Chem Int Edit* **2008**, *47* (3), 581-585.
51. Tao, Y. T.; Wang, Q.; Shang, Y.; Yang, C. L.; Ao, L.; Qin, J. G.; Ma, D. G.; Shuai, Z. G., Multifunctional bipolar triphenylamine/oxadiazole derivatives: highly efficient blue fluorescence, red phosphorescence host and two-color based white OLEDs. *Chem Commun* **2009**, (1), 77-79.
52. Hung, W. Y.; Chi, L. C.; Chen, W. J.; Chen, Y. M.; Chou, S. H.; Wong, K. T., A new benzimidazole/carbazole hybrid bipolar material for highly efficient deep-blue electrofluorescence, yellow-green electrophosphorescence, and two-color-based white OLEDs. *J Mater Chem* **2010**, *20* (45), 10113-10119.

53. Lyu, Y. Y.; Kwak, J.; Kwon, O.; Lee, S. H.; Kim, D.; Lee, C.; Char, K., Silicon-cored anthracene derivatives as host materials for highly efficient blue organic light-emitting devices. *Adv Mater* **2008**, *20* (14), 2720-2729.
54. Tang, C. W.; Vanslyke, S. A., Organic Electroluminescent Diodes. *Appl Phys Lett* **1987**, *51* (12), 913-915.
55. Zhu, M. R.; Yang, C. L., Blue fluorescent emitters: design tactics and applications in organic light-emitting diodes. *Chem Soc Rev* **2013**, *42* (12), 4963-4976.
56. Kondakov, D. Y., Role of triplet-triplet annihilation in highly efficient fluorescent devices. *J Soc Inf Display* **2009**, *17* (2), 137-144.
57. Li, N.; Lai, S. L.; Liu, W. M.; Wang, P. F.; You, J. J.; Lee, C. S.; Liu, Z. T., Synthesis and properties of n-type triphenylpyridine derivatives and applications in deep-blue organic light-emitting devices as electron-transporting layer. *J Mater Chem* **2011**, *21* (34), 12977-12985.
58. Tong, Q. X.; Lai, S. L.; Chan, M. Y.; Zhou, Y. C.; Kwong, H. L.; Lee, C. S.; Lee, S. T., Highly Efficient Blue Organic Light-Emitting Device Based on a Nondoped Electroluminescent Material. *Chem Mater* **2008**, *20* (20), 6310-6312.
59. Wu, K. C.; Ku, P. J.; Lin, C. S.; Shih, H. T.; Wu, F. I.; Huang, M. J.; Lin, J. J.; Chen, I. C.; Cheng, C. H., The photophysical properties of dipyrrenylbenzenes and their application as exceedingly efficient blue emitters for electroluminescent devices. *Adv Funct Mater* **2008**, *18* (1), 67-75.
60. You, J. J.; Lai, S. L.; Liu, W. M.; Ng, T. W.; Wang, P. F.; Lee, C. S., Bipolar cyano-substituted pyridine derivatives for applications in organic light-emitting devices. *J Mater Chem* **2012**, *22* (18), 8922-8929.
61. Chen, C. H.; Huang, W. S.; Lai, M. Y.; Tsao, W. C.; Lin, J. T.; Wu, Y. H.; Ke, T. H.; Chen, L. Y.; Wu, C. C., Versatile, Benzimidazole/Amine-Based Ambipolar Compounds for Electroluminescent Applications: Single-Layer, Blue, Fluorescent OLEDs, Hosts for Single-Layer, Phosphorescent OLEDs. *Adv Funct Mater* **2009**, *19* (16), 2661-2670.
62. Park, H.; Lee, J.; Kang, I.; Chu, H. Y.; Lee, J. I.; Kwon, S. K.; Kim, Y. H., Highly rigid and twisted anthracene derivatives: a strategy for deep blue OLED materials with theoretical limit efficiency. *J Mater Chem* **2012**, *22* (6), 2695-2700.
63. Kim, R.; Yoo, S. J.; Kim, E. K.; Yu, H. S.; Shin, S. C.; Lee, S. K.; Kwon, S. K.; Kim, Y. H., New limb structured blue light emitting materials for OLEDs. *Dyes Pigments* **2012**, *95* (2), 384-391.
64. Raghunath, P.; Reddy, M. A.; Gouri, C.; Bhanuprakash, K.; Rao, V. J., Electronic properties of anthracene derivatives for blue light emitting electroluminescent layers in organic light emitting diodes: A density functional theory study. *J Phys Chem A* **2006**, *110* (3), 1152-1162.
65. Shen, W. J.; Dodda, R.; Wu, C. C.; Wu, F. I.; Liu, T. H.; Chen, H. H.; Chen, C. H.; Shu, C. F., Spirobifluorene-linked bisanthracene: An efficient blue emitter with pronounced thermal stability. *Chem Mater* **2004**, *16* (5), 930-934.

66. Adachi, C.; Tokito, S.; Tsutsui, T.; Saito, S., Electroluminescence in Organic Films with 3-Layer Structure. *Jpn J Appl Phys* **2** **1988**, *27* (2), L269-L271.
67. Garay, R. O.; Naarmann, H.; Mullen, K., Synthesis and Characterization of Poly(1,4-Anthrylenevinylene). *Macromolecules* **1994**, *27* (7), 1922-1927.
68. Bezman, R.; Faulkner, L. R., Mechanisms of Chemiluminescent Electron-Transfer Reactions .4. Absolute Measurements of 9,10-Diphenylanthracene Luminescence in N,N-Dimethylformamide. *J Am Chem Soc* **1972**, *94* (18), 6317-6323.
69. Aleshin, A. N.; Lee, J. Y.; Chu, S. W.; Kim, J. S.; Park, Y. W., Mobility studies of field-effect transistor structures based on anthracene single crystals. *Appl Phys Lett* **2004**, *84* (26), 5383-5385.
70. Ando, S.; Nishida, J.; Fujiwara, E.; Tada, H.; Inoue, Y.; Tokito, S.; Yamashita, Y., Novel p- and n-type organic semiconductors with an anthracene unit. *Chem Mater* **2005**, *17* (6), 1261-1264.
71. Takahashi, M.; Morimoto, H.; Suzuki, Y.; Yamashita, M.; Kawai, H.; Sei, Y.; Yamaguchi, K., Construction of divergent anthracene arrays within dendritic frameworks. *Tetrahedron* **2006**, *62* (13), 3065-3074.
72. Wild, A.; Egbe, D. A. M.; Birckner, E.; Cimrova, V.; Baumann, R.; Grummt, U. W.; Schubert, U. S., Anthracene- and Thiophene-Containing MEH-PPE-PPVs: Synthesis and Study of the Effect of the Aromatic Ring Position on the Photophysical and Electrochemical Properties. *J Polym Sci Pol Chem* **2009**, *47* (9), 2243-2261.
73. Zheng, C. J.; Zhao, W. M.; Wang, Z. Q.; Huang, D.; Ye, J.; Ou, X. M.; Zhang, X. H.; Lee, C. S.; Lee, S. T., Highly efficient non-doped deep-blue organic light-emitting diodes based on anthracene derivatives. *J Mater Chem* **2010**, *20* (8), 1560-1566.
74. Cias, P.; Slugovc, C.; Gescheidt, G., Hole Transport in Triphenylamine Based OLED Devices: From Theoretical Modeling to Properties Prediction. *J Phys Chem A* **2011**, *115* (50), 14519-14525.
75. Yu, M. X.; Duan, J. P.; Lin, C. H.; Cheng, C. H.; Tao, Y. T., Diaminoanthracene derivatives as high-performance green host electroluminescent materials. *Chem Mater* **2002**, *14* (9), 3958-3963.
76. Okumoto, K.; Kanno, H.; Hamada, Y.; Takahashi, H.; Shibata, K., Green fluorescent organic light-emitting device with external quantum efficiency of nearly 10% (vol 89, art no 063504 2006). *Appl Phys Lett* **2006**, *89* (16), 063504.
77. Oh, J. J.; Pu, Y. J.; Sasabe, H.; Nakayama, K.; Kido, J., 9,10-Bis(bipyridyl, pyridylphenyl, phenylpyridyl, and biphenyl)anthracenes Combining High Electron Transport and Injection, Efficiency and Stability in Fluorescent Organic Light-emitting Devices. *Chem Lett* **2011**, *40* (10), 1092-1094.
78. Chiang, C. J.; Kimyonok, A.; Etherington, M. K.; Griffiths, G. C.; Jankus, V.; Tursoy, F.; Monkman, A. P., Ultrahigh Efficiency Fluorescent Single and Bi-Layer Organic Light Emitting Diodes: The Key Role of Triplet Fusion. *Adv Funct Mater* **2013**, *23* (6), 739-746.

79. Fisher, A. L.; Linton, K. E.; Kamtekar, K. T.; Pearson, C.; Bryce, M. R.; Petty, M. C., Efficient Deep-Blue Electroluminescence from an Ambipolar Fluorescent Emitter in a Single-Active-Layer Device. *Chem Mater* **2011**, *23* (7), 1640-1642.
80. Linton, K. E.; Fisher, A. L.; Pearson, C.; Fox, M. A.; Palsson, L. O.; Bryce, M. R.; Petty, M. C., Colour tuning of blue electroluminescence using bipolar carbazole-oxadiazole molecules in single-active-layer organic light emitting devices (OLEDs). *J Mater Chem* **2012**, *22* (23), 11816-11825.
81. Yang, Y. X.; Cohn, P.; Dyer, A. L.; Eom, S. H.; Reynolds, J. R.; Castellano, R. K.; Xue, J. G., Blue-Violet Electroluminescence from a Highly Fluorescent Purine. *Chem Mater* **2010**, *22* (12), 3580-3582.
82. Chen, Y. H.; Lin, S. L.; Chang, Y. C.; Chen, Y. C.; Lin, J. T.; Lee, R. H.; Kuo, W. J.; Jeng, R. J., Efficient non-doped blue light emitting diodes based on novel carbazole-substituted anthracene derivatives. *Org Electron* **2012**, *13* (1), 43-52.
83. Wu, C. L.; Chang, C. H.; Chang, Y. T.; Chen, C. T.; Chen, C. T.; Su, C. J., High efficiency non-dopant blue organic light-emitting diodes based on anthracene-based fluorophores with molecular design of charge transport and red-shifted emission proof. *J Mater Chem C* **2014**, *2* (35), 7188-7200.
84. Yoon, J. A.; Kim, Y. H.; Kim, N. H.; Yoo, S. I.; Lee, S. Y.; Zhu, F. R.; Kim, W. Y., Highly efficient blue organic light-emitting diodes using quantum well-like multiple emissive layer structure. *Nanoscale Res Lett* **2014**, *9*, 191.
85. Zhang, T.; Liu, D.; Wang, Q.; Wang, R. J.; Ren, H. C.; Li, J. Y., Deep-blue and white organic light-emitting diodes based on novel fluorene-cored derivatives with naphthylanthracene endcaps. *J Mater Chem* **2011**, *21* (34), 12969-12976.
86. Kim, M. K.; Kwon, J.; Kwon, T. H.; Hong, J. I., A bipolar host containing 1,2,3-triazole for realizing highly efficient phosphorescent organic light-emitting diodes. *New J Chem* **2010**, *34* (7), 1317-1322.
87. Lee, K. H.; Park, J. K.; Seo, J. H.; Park, S. W.; Kim, Y. S.; Kim, Y. K.; Yoon, S. S., Efficient deep-blue and white organic light-emitting diodes based on triphenylsilane-substituted anthracene derivatives. *J Mater Chem* **2011**, *21* (35), 13640-13648.
88. Wen, S. W.; Lee, M. T.; Chen, C. H., Recent Development of Blue Fluorescent OLED Materials and Devices. *J Disp Technol* **2005**, *1* (1), 90-99.
89. Gao, Z. Q.; Mi, B. X.; Chen, C. H.; Cheah, K. W.; Cheng, Y. K.; Wen, W. S., High-efficiency deep blue host for organic light-emitting devices. *Appl Phys Lett* **2007**, *90* (12), 123560.
90. Kamino, B. A.; Chang, Y. L.; Lu, Z. H.; Bender, T. P., Phthalonitrile based fluorophores as fluorescent dopant emitters in deep-blue OLEDs: Approaching the NTSC standard for blue. *Org Electron* **2012**, *13* (8), 1479-1485.
91. Lee, M. T.; Liao, C. H.; Tsai, C. H.; Chen, C. H., Highly efficient, deep-blue doped organic light-emitting devices. *Adv Mater* **2005**, *17* (20), 2493-2497.

92. Gong, M. S.; Lee, H. S.; Jeon, Y. M., Highly efficient blue OLED based on 9-anthracene-spirobenzofluorene derivatives as host materials. *J Mater Chem* **2010**, *20* (47), 10735-10746.
93. Liu, F.; Xie, L. H.; Tang, C.; Liang, J.; Chen, Q. Q.; Peng, B.; Wei, W.; Cao, Y.; Huang, W., Facile Synthesis of Spirocyclic Aromatic Hydrocarbon Derivatives Based on o-Halobiaryl Route and Domino Reaction for Deep-Blue Organic Semiconductors. *Org Lett* **2009**, *11* (17), 3850-3853.
94. Liu, Y.; Nishiura, M.; Wang, Y.; Hou, Z. M., pi-Conjugated aromatic enynes as a single-emitting component for white electroluminescence. *J Am Chem Soc* **2006**, *128* (17), 5592-5593.
95. Ge, Z. Y.; Hayakawa, T.; Ando, S.; Ueda, M.; Akiike, T.; Miyamoto, H.; Kajita, T.; Kakimoto, M. A., Spin-coated highly efficient phosphorescent organic light-emitting diodes based on bipolar triphenylamine-benzimidazole derivatives. *Adv Funct Mater* **2008**, *18* (4), 584-590.
96. Gu, J. F.; Xie, G. H.; Zhang, L.; Chen, S. F.; Lin, Z. Q.; Zhang, Z. S.; Zhao, J. F.; Xie, L. H.; Tang, C.; Zhao, Y.; Liu, S. Y.; Huang, W., Dumbbell-Shaped Spirocyclic Aromatic Hydrocarbon to Control Intermolecular pi-pi Stacking Interaction for High-Performance Nondoped Deep-Blue Organic Light-Emitting Devices. *J Phys Chem Lett* **2010**, *1* (19), 2849-2853.
97. Takizawa, S. Y.; Montes, V. A.; Anzenbacher, P., Phenylbenzimidazole-Based New Bipolar Host Materials for Efficient Phosphorescent Organic Light-Emitting Diodes. *Chem Mater* **2009**, *21* (12), 2452-2458.
98. Ding, J. Q.; Wang, B.; Yue, Z. Y.; Yao, B.; Xie, Z. Y.; Cheng, Y. X.; Wang, L. X.; Jing, X. B.; Wang, F. S., Bifunctional Green Iridium Dendrimers with a "Self-Host" Feature for Highly Efficient Nondoped Electrophosphorescent Devices. *Angew Chem Int Edit* **2009**, *48* (36), 6664-6666.
99. Liu, J.; Teng, M. Y.; Zhang, X. P.; Wang, K.; Li, C. H.; Zheng, Y. X.; You, X. Z., Efficient blue emitters based on 1,3,5-triazine for nondoped organic light emitting diode applications. *Org Electron* **2012**, *13* (10), 2177-2184.
100. Grabowski, Z. R.; Rotkiewicz, K.; Rettig, W., Structural changes accompanying intramolecular electron transfer: Focus on twisted intramolecular charge-transfer states and structures. *Chem Rev* **2003**, *103* (10), 3899-4031.
101. Herbich, J.; Kapturkiewicz, A., Electronic structure and molecular conformation in the excited charge transfer singlet-states of 9-acridyl and other aryl derivatives of aromatic amines. *J Am Chem Soc* **1998**, *120* (5), 1014-1029.
102. Zhang, Q. S.; Li, J.; Shizu, K.; Huang, S. P.; Hirata, S.; Miyazaki, H.; Adachi, C., Design of Efficient Thermally Activated Delayed Fluorescence Materials for Pure Blue Organic Light Emitting Diodes. *J Am Chem Soc* **2012**, *134* (36), 14706-14709.
103. Endo, A.; Sato, K.; Yoshimura, K.; Kai, T.; Kawada, A.; Miyazaki, H.; Adachi, C., Efficient up-conversion of triplet excitons into a singlet state and its application for organic light emitting diodes. *Appl Phys Lett* **2011**, *98* (8), 083302.

104. Ding, B. D.; Zhu, W. Q.; Jiang, X. Y.; Zhang, Z. L., Pure blue emission from undoped organic light emitting diode based on anthracene derivative. *Curr Appl Phys* **2008**, *8* (5), 523-526.
105. Kim, S. H.; Jang, J.; Lee, J. Y., Effect of doping concentration on device performances of triplet mixed host devices. *Synthetic Met* **2009**, *159* (13), 1295-1297.
106. Kim, S. H.; Jang, J. S.; Lee, J. Y., High efficiency phosphorescent organic light-emitting diodes using carbazole-type triplet exciton blocking layer. *Appl Phys Lett* **2007**, *90* (22), 223505.
107. Endo, A.; Ogasawara, M.; Takahashi, A.; Yokoyama, D.; Kato, Y.; Adachi, C., Thermally Activated Delayed Fluorescence from Sn⁴⁺-Porphyrin Complexes and Their Application to Organic Light-Emitting Diodes - A Novel Mechanism for Electroluminescence. *Adv Mater* **2009**, *21* (47), 4802-4806.
108. Ganzorig, C.; Fujihira, M., A possible mechanism for enhanced electrofluorescence emission through triplet-triplet annihilation in organic electroluminescent devices. *Appl Phys Lett* **2002**, *81* (17), 3137-3139.
109. Hsu, F. M.; Chien, C. H.; Shu, C. F.; Lai, C. H.; Hsieh, C. C.; Wang, K. W.; Chou, P. T., A Bipolar Host Material Containing Triphenylamine and Diphenylphosphoryl-Substituted Fluorene Units for Highly Efficient Blue Electrophosphorescence. *Adv Funct Mater* **2009**, *19* (17), 2834-2843.
110. Eakins, G. L.; Alford, J. S.; Tiegs, B. J.; Breyfogle, B. E.; Stearman, C. J., Tuning HOMO-LUMO levels: trends leading to the design of 9-fluorenone scaffolds with predictable electronic and optoelectronic properties. *J Phys Org Chem* **2011**, *24* (11), 1119-1128.
111. Su, S. J.; Sasabe, H.; Pu, Y. J.; Nakayama, K.; Kido, J., Tuning Energy Levels of Electron-Transport Materials by Nitrogen Orientation for Electrophosphorescent Devices with an 'Ideal' Operating Voltage. *Adv Mater* **2010**, *22* (30), 3311-3316.
112. Chen, S. F.; Deng, L. L.; Xie, J.; Peng, L.; Xie, L. H.; Fan, Q. L.; Huang, W., Recent Developments in Top-Emitting Organic Light-Emitting Diodes. *Adv Mater* **2010**, *22* (46), 5227-5239.
113. Kim, R.; Lee, S.; Kim, K. H.; Lee, Y. J.; Kwon, S. K.; Kim, J. J.; Kim, Y. H., Extremely deep blue and highly efficient non-doped organic light emitting diodes using an asymmetric anthracene derivative with a xylene unit. *Chem Commun* **2013**, *49* (41), 4664-4666.
114. Liu, F.; Lai, W. Y.; Tang, C.; Wu, H. B.; Chen, Q. Q.; Peng, B.; Wei, W.; Huang, W.; Cao, Y., Synthesis and characterization of pyrene-centered Starburst oligofluorenes. *Macromol Rapid Comm* **2008**, *29* (8), 659-664.
115. Park, Y.; Lee, J. H.; Jung, D. H.; Liu, S. H.; Lin, Y. H.; Chen, L. Y.; Wu, C. C.; Park, J., An aromatic imine group enhances the EL efficiency and carrier transport properties of highly efficient blue emitter for OLEDs. *J Mater Chem* **2010**, *20* (28), 5930-5936.
116. Wang, Z. X.; Shao, H. X.; Ye, J. C.; Zhang, L.; Lu, P., Substituent effects on crosslike packing of 2',7'-diaryl-spiro(cyclopropane-1,9'-fluorene) derivatives:

Synthesis and crystallographic, optical, and thermal properties. *Adv Funct Mater* **2007**, *17* (2), 253-263.

117. Tao, S. L.; Peng, Z. K.; Zhang, X. H.; Wang, P. F.; Lee, C. S.; Lee, S. T., Highly efficient non-doped blue organic light-emitting diodes based on fluorene derivatives with high thermal stability. *Adv Funct Mater* **2005**, *15* (10), 1716-1721.

118. Lee, H. W.; Kim, H. J.; Kim, Y. S.; Kim, J.; Lee, S. E.; Lee, H. W.; Kim, Y. K.; Yoon, S. S., Blue electroluminescent materials based on phenylanthracene-substituted fluorene derivatives for organic light-emitting diodes. *Displays* **2015**, *39*, 1-5.

119. Kim, K. H.; Baek, J. Y.; Cheon, C. W.; Moon, C. K.; Sim, B.; Choi, M. Y.; Kim, J. J.; Kim, Y. H., Highly efficient non-doped deep blue fluorescent emitters with horizontal emitting dipoles using interconnecting units between chromophores. *Chem Commun* **2016**, *52* (73), 10956-10959.

120. Shin, H.; Jung, H.; Kim, B.; Lee, J.; Moon, J.; Kim, J.; Park, J., Highly efficient emitters of ultra-deep-blue light made from chrysene chromophores. *J Mater Chem C* **2016**, *4* (17), 3833-3842.

121. Tang, S.; Li, W. J.; Shen, F. Z.; Liu, D. D.; Yang, B.; Ma, Y. G., Highly efficient deep-blue electroluminescence based on the triphenylamine-cored and peripheral blue emitters with segregative HOMO-LUMO characteristics. *J Mater Chem* **2012**, *22* (10), 4401-4408.

122. Xing, X.; Xiao, L. X.; Zheng, L. L.; Hu, S. Y.; Chen, Z. J.; Qu, B.; Gong, Q. H., Spirobifluorene derivative: a pure blue emitter (CIEy approximate to 0.08) with high efficiency and thermal stability. *J Mater Chem* **2012**, *22* (30), 15136-15140.

123. Pudzich, R.; Salbeck, J., Synthesis and characterization of new oxadiazoleamine based spiro-linked fluorescence dyes. *Synthetic Met* **2003**, *138* (1-2), 21-31.

124. Harrowven, D. C.; Guy, I. L.; Nanson, L., Efficient phenanthrene, helicene, and azahelicene syntheses. *Angew Chem Int Edit* **2006**, *45* (14), 2242-2245.

125. Lee, I. H.; Seo, J. A.; Gong, M. S., Deep Blue Fluorescent Host Materials Based on a Novel Spiro[benzo[c]fluorene-7,9'-fluorene] Core Structure with Side Aromatic Wings. *B Korean Chem Soc* **2012**, *33* (7), 2287-2294.

126. Jeong, S.; Kim, M. K.; Kim, S. H.; Hong, J. I., Efficient deep-blue emitters based on triphenylamine-linked benzimidazole derivatives for nondoped fluorescent organic light-emitting diodes. *Org Electron* **2013**, *14* (10), 2497-2504.

127. Li, W. J.; Yao, L.; Liu, H. C.; Wang, Z. M.; Zhang, S. T.; Xiao, R.; Zhang, H. H.; Lu, P.; Yang, B.; Ma, Y. G., Highly efficient deep-blue OLED with an extraordinarily narrow FWHM of 35 nm and a y coordinate < 0.05 based on a fully twisting donor-acceptor molecule. *J Mater Chem C* **2014**, *2* (24), 4733-4736.

128. Lee, C. W.; Lee, J. Y., Benzo[4,5]thieno[2,3-b]pyridine derivatives as host materials for high efficiency green and blue phosphorescent organic light-emitting diodes. *Chem Commun* **2013**, *49* (14), 1446-1448.

129. Yang, Z. Y.; Mao, Z.; Xie, Z. L.; Zhang, Y.; Liu, S. W.; Zhao, J.; Xu, J. R.; Chi, Z. G.; Aldred, M. P., Recent advances in organic thermally activated delayed fluorescence materials. *Chem Soc Rev* **2017**, *46* (3), 915-1016.
130. Kondakov, D. Y., Triplet-triplet annihilation in highly efficient fluorescent organic light-emitting diodes: current state and future outlook. *Philos TR Soc A* **2015**, *373* (2044).
131. Luo, Y. C.; Aziz, H., Correlation Between Triplet Triplet Annihilation and Electroluminescence Efficiency in Doped Fluorescent Organic Light-Emitting Devices. *Adv Funct Mater* **2010**, *20* (8), 1285-1293.
132. Hu, D. H.; Yao, L.; Yang, B.; Ma, Y. G., m Reverse intersystem crossing from upper triplet levels to excited singlet: a 'hot excitation' path for organic light-emitting diodes. *Philos TR Soc A* **2015**, *373* (2044).
133. Li, W. J.; Pan, Y. Y.; Xiao, R.; Peng, Q. M.; Zhang, S. T.; Ma, D. G.; Li, F.; Shen, F. Z.; Wang, Y. H.; Yang, B.; Ma, Y. G., Employing similar to 100% Excitons in OLEDs by Utilizing a Fluorescent Molecule with Hybridized Local and Charge Transfer Excited State. *Adv Funct Mater* **2014**, *24* (11), 1609-1614.
134. Zhang, Q. S.; Li, B.; Huang, S. P.; Nomura, H.; Tanaka, H.; Adachi, C., Efficient blue organic light-emitting diodes employing thermally activated delayed fluorescence. *Nat Photonics* **2014**, *8* (4), 326-332.
135. Lee, S. Y.; Yasuda, T.; Yang, Y. S.; Zhang, Q. S.; Adachi, C., Luminous Butterflies: Efficient Exciton Harvesting by Benzophenone Derivatives for Full-Color Delayed Fluorescence OLEDs. *Angew Chem Int Edit* **2014**, *53* (25), 6402-6406.
136. Parker, C. A., *Photoluminescence of Solutions*. Elsevier Publishing Company, USA: 1968.
137. B. Valeur, M. N. B.-S., *Molecular Fluorescence: Principles and Applications*. John Wiley & Sons, Germany: 2013.
138. Ishimatsu, R.; Matsunami, S.; Shizu, K.; Adachi, C.; Nakano, K.; Imato, T., Solvent Effect on Thermally Activated Delayed Fluorescence by 1,2,3,5-Tetrakis(carbazol-9-yl)-4,6-dicyanobenzene. *J Phys Chem A* **2013**, *117* (27), 5607-5612.
139. Masui, K.; Nakanotani, H.; Adachi, C., Analysis of exciton annihilation in high-efficiency sky-blue organic light-emitting diodes with thermally activated delayed fluorescence. *Org Electron* **2013**, *14* (11), 2721-2726.
140. Miller, J., Fluorescent molecules offer another route to efficient organic LEDs. *Phys Today* **2013**, *66* (2), 10-11.
141. Tao, Y.; Yuan, K.; Chen, T.; Xu, P.; Li, H. H.; Chen, R. F.; Zheng, C.; Zhang, L.; Huang, W., Thermally Activated Delayed Fluorescence Materials Towards the Breakthrough of Organoelectronics. *Adv Mater* **2014**, *26* (47), 7931-7958.
142. Mehes, G.; Nomura, H.; Zhang, Q. S.; Nakagawa, T.; Adachi, C., Enhanced Electroluminescence Efficiency in a Spiro-Acridine Derivative through Thermally Activated Delayed Fluorescence. *Angew Chem Int Edit* **2012**, *51* (45), 11311-11315.

143. Klessinger, M., Conical Intersections and the Mechanism of Singlet Photoreactions. *Angewandte Chemie-International Edition in English* **1995**, *34* (5), 549-551.
144. Bittl, R.; Schulten, K., A Static Ensemble Approximation for Stochastically Modulated Quantum-Systems. *J Chem Phys* **1989**, *90* (3), 1794-1803.
145. Sun, J. W.; Lee, J. H.; Moon, C. K.; Kim, K. H.; Shin, H.; Kim, J. J., A Fluorescent Organic Light-Emitting Diode with 30% External Quantum Efficiency. *Adv Mater* **2014**, *26* (32), 5684-5688.
146. Lee, D. R.; Kim, B. S.; Lee, C. W.; Im, Y.; Yook, K. S.; Hwang, S. H.; Lee, J. Y., Above 30% External Quantum Efficiency in Green Delayed Fluorescent Organic Light-Emitting Diodes. *Acs Appl Mater Inter* **2015**, *7* (18), 9625-9629.
147. Shizu, K.; Noda, H.; Tanaka, H.; Taneda, M.; Uejima, M.; Sato, T.; Tanaka, K.; Kaji, H.; Adachi, C., Highly Efficient Blue Electroluminescence Using Delayed-Fluorescence Emitters with Large Overlap Density between Luminescent and Ground States. *J Phys Chem C* **2015**, *119* (47), 26283-26289.
148. Hirata, S.; Sakai, Y.; Masui, K.; Tanaka, H.; Lee, S. Y.; Nomura, H.; Nakamura, N.; Yasumatsu, M.; Nakanotani, H.; Zhang, Q. S.; Shizu, K.; Miyazaki, H.; Adachi, C., Highly efficient blue electroluminescence based on thermally activated delayed fluorescence. *Nat Mater* **2015**, *14* (3), 330-336.
149. Kawasumi, K.; Wu, T.; Zhu, T. Y.; Chae, H. S.; Van Voorhis, T.; Baldo, M. A.; Swager, T. M., Thermally Activated Delayed Fluorescence Materials Based on Homoconjugation Effect of Donor-Acceptor Triptycenes. *J Am Chem Soc* **2015**, *137* (37), 11908-11911.
150. Lee, S. Y.; Yasuda, T.; Park, I. S.; Adachi, C., X-shaped benzoylbenzophenone derivatives with crossed donors and acceptors for highly efficient thermally activated delayed fluorescence. *Dalton T* **2015**, *44* (18), 8356-8359.
151. Cho, Y. J.; Jeon, S. K.; Chin, B. D.; Yu, E.; Lee, J. Y., The Design of Dual Emitting Cores for Green Thermally Activated Delayed Fluorescent Materials. *Angew Chem Int Edit* **2015**, *54* (17), 5201-5204.
152. Xie, Z. L.; Chen, C. J.; Xu, S. D.; Li, J.; Zhang, Y.; Liu, S. W.; Xu, J. R.; Chi, Z. G., White-Light Emission Strategy of a Single Organic Compound with Aggregation-Induced Emission and Delayed Fluorescence Properties. *Angew Chem Int Edit* **2015**, *54* (24), 7181-7184.
153. Bagnich, S. A.; Athanasopoulos, S.; Rudnick, A.; Schroegel, P.; Bauer, I.; Greenham, N. C.; Stroehriegl, P.; Kohler, A., Excimer Formation by Steric Twisting in Carbazole and Triphenylamine-Based Host Materials. *J Phys Chem C* **2015**, *119* (5), 2380-2387.
154. Ritchie, J.; Crayston, J. A.; Markham, J. P. J.; Samuel, I. D. W., Effect of meta-linkages on the photoluminescence and electroluminescence properties of light-emitting polyfluorene alternating copolymers. *J Mater Chem* **2006**, *16* (17), 1651-1656.

155. Hong, S. Y.; Kim, D. Y.; Kim, C. Y.; Hoffmann, R., Origin of the broken conjugation in m-phenylene linked conjugated polymers. *Macromolecules* **2001**, *34* (18), 6474-6481.
156. Dias, F. B.; Bourdakos, K. N.; Jankus, V.; Moss, K. C.; Kamtekar, K. T.; Bhalla, V.; Santos, J.; Bryce, M. R.; Monkman, A. P., Triplet Harvesting with 100% Efficiency by Way of Thermally Activated Delayed Fluorescence in Charge Transfer OLED Emitters. *Adv Mater* **2013**, *25* (27), 3707-3714.
157. Rajamalli, P.; Senthilkumar, N.; Gandeepan, P.; Huang, P. Y.; Huang, M. J.; Ren-Wu, C. Z.; Yang, C. Y.; Chiu, M. J.; Chu, L. K.; Lin, H. W.; Cheng, C. H., A New Molecular Design Based on Thermally Activated Delayed Fluorescence for Highly Efficient Organic Light Emitting Diodes. *J Am Chem Soc* **2016**, *138* (2), 628-634.
158. Ahn, T.; Jang, M. S.; Shim, H. K.; Hwang, D. H.; Zyung, T., Blue electroluminescent polymers: Control of conjugation length by kink linkages and substituents in the poly(p-phenylenevinylene)-related copolymers. *Macromolecules* **1999**, *32* (10), 3279-3285.
159. Sun, J. W.; Baek, J. Y.; Kim, K. H.; Moon, C. K.; Lee, J. H.; Kwon, S. K.; Kim, Y. H.; Kim, J. J., Thermally Activated Delayed Fluorescence from Azasilene Based Intramolecular Charge-Transfer Emitter (DTPDDA) and a Highly Efficient Blue Light Emitting Diode. *Chem Mater* **2015**, *27* (19), 6675-6681.
160. Lee, D. R.; Hwang, S. H.; Jeon, S. K.; Lee, C. W.; Lee, J. Y., Benzofurocarbazole and benzothienocarbazole as donors for improved quantum efficiency in blue thermally activated delayed fluorescent devices. *Chem Commun* **2015**, *51* (38), 8105-8107.
161. Li, B.; Nomura, H.; Miyazaki, H.; Zhang, Q. S.; Yoshida, K.; Suzuma, Y.; Orita, A.; Otera, J.; Adachi, C., Dicarbazolyldicyanobenzenes as Thermally Activated Delayed Fluorescence Emitters: Effect of Substitution Position on Photo luminescent and Electroluminescent Properties. *Chem Lett* **2014**, *43* (3), 319-321.
162. Suzuki, K.; Kubo, S.; Shizu, K.; Fukushima, T.; Wakamiya, A.; Murata, Y.; Adachi, C.; Kaji, H., Triarylboron-Based Fluorescent Organic Light-Emitting Diodes with External Quantum Efficiencies Exceeding 20 %. *Angew Chem Int Edit* **2015**, *54* (50), 15231-15235.
163. Niwa, A.; Kobayashi, T.; Nagase, T.; Goushi, K.; Adachi, C.; Naito, H., Temperature dependence of photoluminescence properties in a thermally activated delayed fluorescence emitter. *Appl Phys Lett* **2014**, *104* (21), 213303.
164. Deaton, J. C.; Switalski, S. C.; Kondakov, D. Y.; Young, R. H.; Pawlik, T. D.; Giesen, D. J.; Harkins, S. B.; Miller, A. J. M.; Mickenberg, S. F.; Peters, J. C., E-Type Delayed Fluorescence of a Phosphine-Supported Cu-2(μ -NAr₂)(2) Diamond Core: Harvesting Singlet and Triplet Excitons in OLEDs. *J Am Chem Soc* **2010**, *132* (27), 9499-9508.
165. Noguchi, Y.; Kim, H. J.; Ishino, R.; Goushi, K.; Adachi, C.; Nakayama, Y.; Ishii, H., Charge carrier dynamics and degradation phenomena in organic light-

- emitting diodes doped by a thermally activated delayed fluorescence emitter. *Org Electron* **2015**, *17*, 184-191.
166. Sandanayaka, A. S. D.; Matsushima, T.; Adachi, C., Degradation Mechanisms of Organic Light-Emitting Diodes Based on Thermally Activated Delayed Fluorescence Molecules. *J Phys Chem C* **2015**, *119* (42), 23845-23851.
167. Sandanayaka, A. S. D.; Yoshida, K.; Matsushima, T.; Adachi, C., Exciton Quenching Behavior of Thermally Activated Delayed Fluorescence Molecules by Charge Carriers. *J Phys Chem C* **2015**, *119* (14), 7631-7636.
168. Cui, L. S.; Xie, Y. M.; Wang, Y. K.; Zhong, C.; Deng, Y. L.; Liu, X. Y.; Jiang, Z. Q.; Liao, L. S., Pure Hydrocarbon Hosts for approximate to 100% Exciton Harvesting in Both Phosphorescent and Fluorescent Light-Emitting Devices. *Adv Mater* **2015**, *27* (28), 4213-4217.
169. Lee, C. W.; Lee, J. Y., Systematic Control of Photophysical Properties of Host Materials for High Quantum Efficiency above 25% in Green Thermally Activated Delayed Fluorescent Devices. *Acs Appl Mater Inter* **2015**, *7* (4), 2899-2904.
170. Kim, B. S.; Lee, J. Y., Phosphine Oxide Type Bipolar Host Material for High Quantum Efficiency in Thermally Activated Delayed Fluorescent Device. *Acs Appl Mater Inter* **2014**, *6* (11), 8396-8400.
171. Im, Y.; Lee, J. Y., Above 20% External Quantum Efficiency in Thermally Activated Delayed Fluorescence Device Using Furodipyridine-Type Host Materials. *Chem Mater* **2014**, *26* (3), 1413-1419.
172. Gaj, M. P.; Fuentes-Hernandez, C.; Zhang, Y. D.; Marder, S. R.; Kippelen, B., Highly efficient Organic Light-Emitting Diodes from thermally activated delayed fluorescence using a sulfone-carbazole host material. *Org Electron* **2015**, *16*, 109-112.
173. Zhao, Y. L.; Wu, C.; Qiu, P. L.; Li, X. P.; Wang, Q.; Chen, J. S.; Ma, D. G., New Benzimidazole-Based Bipolar Hosts: Highly Efficient Phosphorescent and Thermally Activated Delayed Fluorescent Organic Light-Emitting Diodes Employing the Same Device Structure. *Acs Appl Mater Inter* **2016**, *8* (4), 2635-2643.
174. Kim, Y. H.; Wolf, C.; Cho, H.; Jeong, S. H.; Lee, T. W., Highly Efficient, Simplified, Solution-Processed Thermally Activated Delayed-Fluorescence Organic Light-Emitting Diodes. *Adv Mater* **2016**, *28* (4), 734-741.
175. Komatsu, R.; Sasabe, H.; Inomata, S.; Pu, Y. J.; Kido, J., High efficiency solution processed OLEDs using a thermally activated delayed fluorescence emitter. *Synthetic Met* **2015**, *202*, 165-168.
176. Nakanotani, H.; Masui, K.; Nishide, J.; Shibata, T.; Adachi, C., Promising operational stability of high-efficiency organic light-emitting diodes based on thermally activated delayed fluorescence. *Sci Rep-Uk* **2013**, *3*, 2127.
177. Seino, Y.; Inomata, S.; Sasabe, H.; Pu, Y. J.; Kido, J., High-Performance Green OLEDs Using Thermally Activated Delayed Fluorescence with a Power Efficiency of over 100 lm W⁻¹. *Adv Mater* **2016**, *28* (13), 2638-2643.

178. Tsang, D. P. K.; Adachi, C., Operational stability enhancement in organic light-emitting diodes with ultrathin Liq interlayers. *Sci Rep-Uk* **2016**, *6*, 22463.
179. Cho, Y. J.; Yook, K. S.; Lee, J. Y., High Efficiency in a Solution-Processed Thermally Activated Delayed-Fluorescence Device Using a Delayed-Fluorescence Emitting Material with Improved Solubility. *Adv Mater* **2014**, *26* (38), 6642-6646.
180. Taneda, M.; Shizu, K.; Tanaka, H.; Adachi, C., High efficiency thermally activated delayed fluorescence based on 1,3,5-tris(4-(diphenylamino) phenyl)-2,4,6-tricyanobenzene. *Chem Commun* **2015**, *51* (24), 5028-5031.
181. Tanaka, H.; Shizu, K.; Miyazaki, H.; Adachi, C., Efficient green thermally activated delayed fluorescence (TADF) from a phenoxazine-triphenyltriazine (PXZ-TRZ) derivative. *Chem Commun* **2012**, *48* (93), 11392-11394.
182. Tanaka, H.; Shizu, K.; Nakanotani, H.; Adachi, C., Dual Intramolecular Charge-Transfer Fluorescence Derived from a Phenothiazine-Triphenyltriazine Derivative. *J Phys Chem C* **2014**, *118* (29), 15985-15994.
183. Kaji, H.; Suzuki, H.; Fukushima, T.; Shizu, K.; Suzuki, K.; Kubo, S.; Komino, T.; Oiwa, H.; Suzuki, F.; Wakamiya, A.; Murata, Y.; Adachi, C., Purely organic electroluminescent material realizing 100% conversion from electricity to light. *Nat Commun* **2015**, *6*, 8476.
184. Lee, J.; Shizu, K.; Tanaka, H.; Nomura, H.; Yasuda, T.; Adachi, C., Oxadiazole- and triazole-based highly-efficient thermally activated delayed fluorescence emitters for organic light-emitting diodes. *J Mater Chem C* **2013**, *1* (30), 4599-4604.
185. Zhang, Q. S.; Kuwabara, H.; Potscavage, W. J.; Huang, S. P.; Hatae, Y.; Shibata, T.; Adachi, C., Anthraquinone-Based Intramolecular Charge-Transfer Compounds: Computational Molecular Design, Thermally Activated Delayed Fluorescence, and Highly Efficient Red Electroluminescence. *J Am Chem Soc* **2014**, *136* (52), 18070-18081.
186. Goushi, K.; Adachi, C., Efficient organic light-emitting diodes through up-conversion from triplet to singlet excited states of exciplexes. *Appl Phys Lett* **2012**, *101* (2), 023306.
187. Goushi, K.; Yoshida, K.; Sato, K.; Adachi, C., Organic light-emitting diodes employing efficient reverse intersystem crossing for triplet-to-singlet state conversion. *Nat Photonics* **2012**, *6* (4), 253-258.
188. Müllen, K.; Scherf, U., *Organic Light Emitting Devices: Synthesis, Properties and Applications*. Wiley-VCH, Weinheim, Germany, 2006.
189. Zhu, M.; Yang, C., Blue fluorescent emitters: design tactics and applications in organic light-emitting diodes. *Chem Soc Rev* **2013**, *42* (12), 4963-76.
190. Kim, M.; Jeon, S. K.; Hwang, S. H.; Lee, J. Y., Stable Blue Thermally Activated Delayed Fluorescent Organic Light-Emitting Diodes with Three Times Longer Lifetime than Phosphorescent Organic Light-Emitting Diodes. *Adv Mater* **2015**, *27* (15), 2515-2520.
191. Lin, T. A.; Chatterjee, T.; Tsai, W. L.; Lee, W. K.; Wu, M. J.; Jiao, M.; Pan, K. C.; Yi, C. L.; Chung, C. L.; Wong, K. T.; Wu, C. C., Sky-Blue Organic Light

Emitting Diode with 37% External Quantum Efficiency Using Thermally Activated Delayed Fluorescence from Spiroacridine-Triazine Hybrid. *Adv Mater* **2016**, *28* (32), 6976-6983.

192. Xu, S. D.; Liu, T. T.; Mu, Y. X.; Wang, Y. F.; Chi, Z. G.; Lo, C. C.; Liu, S. W.; Zhang, Y.; Lien, A.; Xu, J. R., An Organic Molecule with Asymmetric Structure Exhibiting Aggregation-Induced Emission, Delayed Fluorescence, and Mechanoluminescence. *Angew Chem Int Edit* **2015**, *54* (3), 874-878.

193. Sun, K. Y.; Jiang, W.; Ban, X. X.; Huang, B.; Zhang, Z. H.; Ye, M. Y.; Sun, Y. M., Novel aggregation-induced emission and thermally activated delayed fluorescence materials based on thianthrene-9,9',10,10'-tetraoxide derivatives. *Rsc Advances* **2016**, *6* (26), 22137-22143.

194. Furue, R.; Nishimoto, T.; Park, I. S.; Lee, J.; Yasuda, T., Aggregation-Induced Delayed Fluorescence Based on Donor/Acceptor-Tethered Janus Carborane Triads: Unique Photophysical Properties of Nondoped OLEDs. *Angew Chem Int Edit* **2016**, *55* (25), 7171-7175.

195. Goushi, K.; Yoshida, K.; Sato, K.; Adachi, C., Organic light-emitting diodes employing efficient reverse intersystem crossing for triplet-to-singlet state conversion. *Nature Photonics* **2012**, *6* (4), 234-248.

196. Park, Y. S.; Kim, K. H.; Kim, J. J., Efficient triplet harvesting by fluorescent molecules through exciplexes for high efficiency organic light-emitting diodes. *Appl Phys Lett* **2013**, *102* (15), 153306.

197. Chen, Z.; Liu, X. K.; Zheng, C. J.; Ye, J.; Liu, C. L.; Li, F.; Ou, X. M.; Lee, C. S.; Zhang, X. H., High Performance Exciplex-Based Fluorescence-Phosphorescence White Organic Light-Emitting Device with Highly Simplified Structure. *Chem Mater* **2015**, *27* (15), 5206-5211.

198. Wang, D.; Li, W. L.; Chu, B.; Su, Z. S.; Bi, D. F.; Zhang, D. Y.; Zhu, J. Z.; Yan, F.; Chen, Y. R.; Tsuboi, T., Highly efficient green organic light-emitting diodes from single exciplex emission. *Appl Phys Lett* **2008**, *92* (5), 053304.

199. Song, L.; Hu, Y. S.; Liu, Z. Q.; Lv, Y.; Guo, X. Y.; Liu, X. Y., Harvesting Triplet Excitons with Exciplex Thermally Activated Delayed Fluorescence Emitters toward High Performance Heterostructured Organic Light-Emitting Field Effect Transistors. *Acs Appl Mater Inter* **2017**, *9* (3), 2711-2719.

200. Bagriantsev, S. N.; Ang, K. H.; Gallardo-Godoy, A.; Clark, K. A.; Arkin, M. R.; Renslo, A. R.; Minor, D. L., A High-Throughput Functional Screen Identifies Small Molecule Regulators of Temperature- and Mechano-Sensitive K-2P Channels. *Acs Chemical Biology* **2013**, *8* (8), 1841-1851.

201. Suh, M. C.; Park, S. R.; Cho, Y. R.; Shin, D. H.; Kang, P. G.; Ahn, D. A.; Kim, H. S.; Kim, C. B., Synthesis of Soluble Host Materials for Highly Efficient Red Phosphorescent Organic Light-Emitting Diodes. *Acs Appl Mater Inter* **2016**, *8* (28), 18256-18265.

202. Spingler, B.; Schnidrig, S.; Todorova, T.; Wild, F., Some thoughts about the single crystal growth of small molecules. *Crystengcomm* **2012**, *14* (3), 751-757.

203. Tsai, W. L.; Huang, M. H.; Lee, W. K.; Hsu, Y. J.; Pan, K. C.; Huang, Y. H.; Ting, H. C.; Sarma, M.; Ho, Y. Y.; Hu, H. C.; Chen, C. C.; Lee, M. T.; Wong, K. T.; Wu, C. C., A versatile thermally activated delayed fluorescence emitter for both highly efficient doped and non-doped organic light emitting devices. *Chem Commun* **2015**, 51 (71), 13662-13665.
204. Hong, Y. N.; Lam, J. W. Y.; Tang, B. Z., Aggregation-induced emission. *Chem Soc Rev* **2011**, 40 (11), 5361-5388.
205. Guo, J. J.; Li, X. L.; Nie, H.; Luo, W. W.; Gan, S. F.; Hu, S. M.; Hu, R. R.; Qin, A. J.; Zhao, Z. J.; Su, S. J.; Tang, B., Achieving High-Performance Nondoped OLEDs with Extremely Small Efficiency Roll-Off by Combining Aggregation-Induced Emission and Thermally Activated Delayed Fluorescence. *Adv Funct Mater* **2017**, 27 (13), 1606458.
206. Kuhn, H., Classical Aspects of Energy Transfer in Molecular Systems. *J Chem Phys* **1970**, 53 (1), 101.
207. Lee, J.; Aizawa, N.; Numata, M.; Adachi, C.; Yasuda, T., Versatile Molecular Functionalization for Inhibiting Concentration Quenching of Thermally Activated Delayed Fluorescence. *Adv Mater* **2017**, 29 (4), 1604856.
208. Kaltenbrunner, M.; Sekitani, T.; Reeder, J.; Yokota, T.; Kuribara, K.; Tokuhara, T.; Drack, M.; Schwodiauer, R.; Graz, I.; Bauer-Gogonea, S.; Bauer, S.; Someya, T., An ultra-lightweight design for imperceptible plastic electronics. *Nature* **2013**, 499 (7459), 458-463.
209. Drack, M.; Graz, I.; Sekitani, T.; Someya, T.; Kaltenbrunner, M.; Bauer, S., An Imperceptible Plastic Electronic Wrap. *Adv Mater* **2015**, 27 (1), 34-40.
210. Kim, D. H.; Lu, N. S.; Ma, R.; Kim, Y. S.; Kim, R. H.; Wang, S. D.; Wu, J.; Won, S. M.; Tao, H.; Islam, A.; Yu, K. J.; Kim, T. I.; Chowdhury, R.; Ying, M.; Xu, L. Z.; Li, M.; Chung, H. J.; Keum, H.; McCormick, M.; Liu, P.; Zhang, Y. W.; Omenetto, F. G.; Huang, Y. G.; Coleman, T.; Rogers, J. A., Epidermal Electronics. *Science* **2011**, 333 (6044), 838-843.
211. Tao, H.; Hwang, S. W.; Marelli, B.; An, B.; Moreau, J. E.; Yang, M. M.; Brenckle, M. A.; Kim, S.; Kaplan, D. L.; Rogers, J. A.; Omenetto, F. G., Silk-based resorbable electronic devices for remotely controlled therapy and in vivo infection abatement. *P Natl Acad Sci USA* **2014**, 111 (49), 17385-17389.
212. Farra, R.; Sheppard, N. F.; McCabe, L.; Neer, R. M.; Anderson, J. M.; Santini, J. T.; Cima, M. J.; Langer, R., First-in-Human Testing of a Wirelessly Controlled Drug Delivery Microchip. *Sci Transl Med* **2012**, 4 (122).
213. Hwang, S. W.; Tao, H.; Kim, D. H.; Cheng, H. Y.; Song, J. K.; Rill, E.; Brenckle, M. A.; Panilaitis, B.; Won, S. M.; Kim, Y. S.; Song, Y. M.; Yu, K. J.; Ameen, A.; Li, R.; Su, Y. W.; Yang, M. M.; Kaplan, D. L.; Zakin, M. R.; Slepian, M. J.; Huang, Y. G.; Omenetto, F. G.; Rogers, J. A., A Physically Transient Form of Silicon Electronics. *Science* **2012**, 337 (6102), 1640-1644.
214. Kim, D. H.; Viventi, J.; Amsden, J. J.; Xiao, J. L.; Vigeland, L.; Kim, Y. S.; Blanco, J. A.; Panilaitis, B.; Frechette, E. S.; Contreras, D.; Kaplan, D. L.; Omenetto, F. G.; Huang, Y. G.; Hwang, K. C.; Zakin, M. R.; Litt, B.; Rogers, J. A., Dissolvable

films of silk fibroin for ultrathin conformal bio-integrated electronics. *Nat Mater* **2010**, *9* (6), 511-517.

215. Yamada, T.; Hayamizu, Y.; Yamamoto, Y.; Yomogida, Y.; Izadi-Najafabadi, A.; Futaba, D. N.; Hata, K., A stretchable carbon nanotube strain sensor for human-motion detection. *Nat Nanotechnol* **2011**, *6* (5), 296-301.

216. Norton, J. J. S.; Lee, D. S.; Lee, J. W.; Lee, W.; Kwon, O.; Won, P.; Jung, S. Y.; Cheng, H. Y.; Jeong, J. W.; Akce, A.; Umunna, S.; Na, I.; Kwon, Y. H.; Wang, X. Q.; Liu, Z. J.; Paik, U.; Huang, Y. G.; Bretl, T.; Yeo, W. H.; Rogers, J. A., Soft, curved electrode systems capable of integration on the auricle as a persistent brain-computer interface. *P Natl Acad Sci USA* **2015**, *112* (13), 3920-3925.

217. Yeo, W. H.; Kim, Y. S.; Lee, J.; Ameen, A.; Shi, L. K.; Li, M.; Wang, S. D.; Ma, R.; Jin, S. H.; Kang, Z.; Huang, Y. G.; Rogers, J. A., Multifunctional Epidermal Electronics Printed Directly Onto the Skin. *Adv Mater* **2013**, *25* (20), 2773-2778.

218. Xu, S.; Zhang, Y. H.; Jia, L.; Mathewson, K. E.; Jang, K. I.; Kim, J.; Fu, H. R.; Huang, X.; Chava, P.; Wang, R. H.; Bhole, S.; Wang, L. Z.; Na, Y. J.; Guan, Y.; Flavin, M.; Han, Z. S.; Huang, Y. G.; Rogers, J. A., Soft Microfluidic Assemblies of Sensors, Circuits, and Radios for the Skin. *Science* **2014**, *344* (6179), 70-74.

219. Jeong, J. W.; Yeo, W. H.; Akhtar, A.; Norton, J. J. S.; Kwack, Y. J.; Li, S.; Jung, S. Y.; Su, Y. W.; Lee, W.; Xia, J.; Cheng, H. Y.; Huang, Y. G.; Choi, W. S.; Bretl, T.; Rogers, J. A., Materials and Optimized Designs for Human-Machine Interfaces Via Epidermal Electronics. *Adv Mater* **2013**, *25* (47), 6839-6846.

220. Schwartz, G.; Tee, B. C. K.; Mei, J. G.; Appleton, A. L.; Kim, D. H.; Wang, H. L.; Bao, Z. N., Flexible polymer transistors with high pressure sensitivity for application in electronic skin and health monitoring. *Nat Commun* **2013**, *4*, 1859.

221. Webb, R. C.; Bonifas, A. P.; Behnaz, A.; Zhang, Y. H.; Yu, K. J.; Cheng, H. Y.; Shi, M. X.; Bian, Z. G.; Liu, Z. J.; Kim, Y. S.; Yeo, W. H.; Park, J. S.; Song, J. Z.; Li, Y. H.; Huang, Y. G.; Gorbach, A. M.; Rogers, J. A., Ultrathin conformal devices for precise and continuous thermal characterization of human skin. *Nat Mater* **2013**, *12* (10), 938-944.

222. Park, M.; Do, K.; Kim, J.; Son, D.; Koo, J. H.; Park, J.; Song, J. K.; Kim, J. H.; Lee, M.; Hyeon, T.; Kim, D. H., Oxide Nanomembrane Hybrids with Enhanced Mechano- and Thermo-Sensitivity for Semitransparent Epidermal Electronics. *Adv Healthc Mater* **2015**, *4* (7), 992-997.

223. Lipomi, D. J.; Vosgueritchian, M.; Tee, B. C. K.; Hellstrom, S. L.; Lee, J. A.; Fox, C. H.; Bao, Z. N., Skin-like pressure and strain sensors based on transparent elastic films of carbon nanotubes. *Nat Nanotechnol* **2011**, *6* (12), 788-792.

224. Bandodkar, A. J.; Jia, W. Z.; Yardimci, C.; Wang, X.; Ramirez, J.; Wang, J., Tattoo-Based Noninvasive Glucose Monitoring: A Proof-of-Concept Study. *Anal Chem* **2015**, *87* (1), 394-398.

225. Bandodkar, A. J.; Hung, V. W. S.; Jia, W. Z.; Valdes-Ramirez, G.; Windmiller, J. R.; Martinez, A. G.; Ramirez, J.; Chan, G.; Kerman, K.; Wang, J., Tattoo-based potentiometric ion-selective sensors for epidermal pH monitoring. *Analyst* **2013**, *138* (1), 123-128.

226. Nattel, S., New ideas about atrial fibrillation 50 years on. *Nature* **2002**, *415* (6868), 219-226.
227. Sanguinetti, M. C.; Tristani-Firouzi, M., hERG potassium channels and cardiac arrhythmia. *Nature* **2006**, *440* (7083), 463-469.
228. Massey, C. A.; Sowers, L. P.; Dlouhy, B. J.; Richerson, G. B., Mechanisms of sudden unexpected death in epilepsy: the pathway to prevention. *Nat Rev Neurol* **2014**, *10* (5), 271-282.
229. Rogers, J. A.; Lagally, M. G.; Nuzzo, R. G., Synthesis, assembly and applications of semiconductor nanomembranes. *Nature* **2011**, *477* (7362), 45-53.
230. Lee, P.; Lee, J.; Lee, H.; Yeo, J.; Hong, S.; Nam, K. H.; Lee, D.; Lee, S. S.; Ko, S. H., Highly Stretchable and Highly Conductive Metal Electrode by Very Long Metal Nanowire Percolation Network. *Adv Mater* **2012**, *24* (25), 3326-3332.
231. Schwierz, F., Graphene transistors. *Nat Nanotechnol* **2010**, *5* (7), 487-496.
232. Shirasaki, Y.; Supran, G. J.; Bawendi, M. G.; Bulovic, V., Emergence of colloidal quantum-dot light-emitting technologies. *Nat Photonics* **2013**, *7* (1), 13-23.
233. Bonaccorso, F.; Sun, Z.; Hasan, T.; Ferrari, A. C., Graphene photonics and optoelectronics. *Nat Photonics* **2010**, *4* (9), 611-622.
234. Reddy, A. L. M.; Gowda, S. R.; Shaijumon, M. M.; Ajayan, P. M., Hybrid Nanostructures for Energy Storage Applications. *Adv Mater* **2012**, *24* (37), 5045-5064.
235. Ko, H. C.; Stoykovich, M. P.; Song, J. Z.; Malyarchuk, V.; Choi, W. M.; Yu, C. J.; Geddes, J. B.; Xiao, J. L.; Wang, S. D.; Huang, Y. G.; Rogers, J. A., A hemispherical electronic eye camera based on compressible silicon optoelectronics. *Nature* **2008**, *454* (7205), 748-753.
236. Kim, J.; Lee, M.; Shim, H. J.; Ghaffari, R.; Cho, H. R.; Son, D.; Jung, Y. H.; Soh, M.; Choi, C.; Jung, S.; Chu, K.; Jeon, D.; Lee, S. T.; Kim, J. H.; Choi, S. H.; Hyeon, T.; Kim, D. H., Stretchable silicon nanoribbon electronics for skin prosthesis. *Nat Commun* **2014**, *5*, 5747.
237. Kim, T. I.; McCall, J. G.; Jung, Y. H.; Huang, X.; Siuda, E. R.; Li, Y. H.; Song, J. Z.; Song, Y. M.; Pao, H. A.; Kim, R. H.; Lu, C. F.; Lee, S. D.; Song, I. S.; Shin, G.; Al-Hasani, R.; Kim, S.; Tan, M. P.; Huang, Y. G.; Omenetto, F. G.; Rogers, J. A.; Bruchas, M. R., Injectable, Cellular-Scale Optoelectronics with Applications for Wireless Optogenetics. *Science* **2013**, *340* (6129), 211-216.
238. Kim, D. H.; Lu, N. S.; Ghaffari, R.; Kim, Y. S.; Lee, S. P.; Xu, L. Z.; Wu, J. A.; Kim, R. H.; Song, J. Z.; Liu, Z. J.; Viventi, J.; de Graff, B.; Elolampi, B.; Mansour, M.; Slepian, M. J.; Hwang, S.; Moss, J. D.; Won, S. M.; Huang, Y. G.; Litt, B.; Rogers, J. A., Materials for multifunctional balloon catheters with capabilities in cardiac electrophysiological mapping and ablation therapy. *Nat Mater* **2011**, *10* (4), 316-323.
239. Kim, D. H.; Ghaffari, R.; Lu, N. S.; Wang, S. D.; Lee, S. P.; Keum, H.; D'Angelo, R.; Klinker, L.; Su, Y. W.; Lu, C. F.; Kim, Y. S.; Ameen, A.; Li, Y. H.; Zhang, Y. H.; de Graff, B.; Hsu, Y. Y.; Liu, Z. J.; Ruskin, J.; Xu, L. Z.; Lu, C.; Omenetto, F. G.; Huang, Y. G.; Mansour, M.; Slepian, M. J.; Rogers, J. A.,

Electronic sensor and actuator webs for large-area complex geometry cardiac mapping and therapy. *P Natl Acad Sci USA* **2012**, *109* (49), 19910-19915.

240. Son, D.; Lee, J.; Lee, D. J.; Ghaffari, R.; Yun, S.; Kim, S. J.; Lee, J. E.; Cho, H. R.; Yoon, S.; Yang, S. X.; Lee, S.; Qiao, S. T.; Ling, D. S.; Shin, S.; Song, J. K.; Kim, J.; Kim, T.; Lee, H.; Kim, J.; Soh, M.; Lee, N.; Hwang, C. S.; Nam, S.; Lu, N. S.; Hyeon, T.; Choi, S. H.; Kim, D. H., Bioresorbable Electronic Stent Integrated with Therapeutic Nanoparticles for Endovascular Diseases. *Acs Nano* **2015**, *9* (6), 5937-5946.

241. Son, D.; Lee, J.; Qiao, S.; Ghaffari, R.; Kim, J.; Lee, J. E.; Song, C.; Kim, S. J.; Lee, D. J.; Jun, S. W.; Yang, S.; Park, M.; Shin, J.; Do, K.; Lee, M.; Kang, K.; Hwang, C. S.; Lu, N. S.; Hyeon, T.; Kim, D. H., Multifunctional wearable devices for diagnosis and therapy of movement disorders. *Nat Nanotechnol* **2014**, *9* (5), 397-404.

242. Park, J.; An, K. J.; Hwang, Y. S.; Park, J. G.; Noh, H. J.; Kim, J. Y.; Park, J. H.; Hwang, N. M.; Hyeon, T., Ultra-large-scale syntheses of monodisperse nanocrystals. *Nat Mater* **2004**, *3* (12), 891-895.

243. Munshi, A. M.; Dheeraj, D. L.; Fauske, V. T.; Kim, D. C.; Huh, J.; Reinertsen, J. F.; Ahtapodov, L.; Lee, K. D.; Heidari, B.; van Helvoort, A. T. J.; Fimland, B. O.; Weman, H., Position-Controlled Uniform GaAs Nanowires on Silicon using Nanoimprint Lithography. *Nano Lett* **2014**, *14* (2), 960-966.

244. Jung, S.; Lee, J.; Hyeon, T.; Lee, M.; Kim, D. H., Fabric-Based Integrated Energy Devices for Wearable Activity Monitors. *Adv Mater* **2014**, *26* (36), 6329-6334.

245. Kim, S.; Su, Y.; Mihi, A.; Lee, S.; Liu, Z.; Bhandakkar, T. K.; Wu, J.; Geddes, J. B.; Johnson, H. T.; Zhang, Y. W.; Park, J. K.; Braun, P. V.; Huang, Y. G.; Rogers, J. A., Imbricate Scales as a Design Construct for Microsystem Technologies. *Small* **2012**, *8* (6), 901-906.

246. Paul, S.; Pearson, C.; Molloy, A.; Cousins, M. A.; Green, M.; Kolliopoulou, S.; Dimitrakis, P.; Normand, P.; Tsoukalas, D.; Petty, M. C., Langmuir-Blodgett film deposition of metallic nanoparticles and their application to electronic memory structures. *Nano Lett* **2003**, *3* (4), 533-536.

247. Fan, Z. Y.; Ho, J. C.; Jacobson, Z. A.; Yerushalmi, R.; Alley, R. L.; Razavi, H.; Javey, A., Wafer-scale assembly of highly ordered semiconductor nanowire arrays by contact printing. *Nano Lett* **2008**, *8* (1), 20-25.

248. Kim, S.; Wu, J. A.; Carlson, A.; Jin, S. H.; Kovalsky, A.; Glass, P.; Liu, Z. J.; Ahmed, N.; Elgan, S. L.; Chen, W. Q.; Ferreira, P. M.; Sitti, M.; Huang, Y. G.; Rogers, J. A., Microstructured elastomeric surfaces with reversible adhesion and examples of their use in deterministic assembly by transfer printing. *P Natl Acad Sci USA* **2010**, *107* (40), 17095-17100.

249. Kaltenbrunner, M.; White, M. S.; Glowacki, E. D.; Sekitani, T.; Someya, T.; Sariciftci, N. S.; Bauer, S., Ultrathin and lightweight organic solar cells with high flexibility. *Nat Commun* **2012**, *3*, 770.

250. Kim, D. H.; Ahn, J. H.; Choi, W. M.; Kim, H. S.; Kim, T. H.; Song, J. Z.; Huang, Y. G. Y.; Liu, Z. J.; Lu, C.; Rogers, J. A., Stretchable and foldable silicon integrated circuits. *Science* **2008**, *320* (5875), 507-511.
251. Fan, J. A.; Yeo, W. H.; Su, Y. W.; Hattori, Y.; Lee, W.; Jung, S. Y.; Zhang, Y. H.; Liu, Z. J.; Cheng, H. Y.; Falgout, L.; Bajema, M.; Coleman, T.; Gregoire, D.; Larsen, R. J.; Huang, Y. G.; Rogers, J. A., Fractal design concepts for stretchable electronics. *Nat Commun* **2014**, *5*, 3266.
252. Roduner, E., Size matters: why nanomaterials are different. *Chem Soc Rev* **2006**, *35* (7), 583-592.
253. L. D. Landau, E. M. L., *Theory of Elasticity*. Butter-worth-Heinemann: Oxford, UK, 1986; Vol. 7.
254. Kim, D. H.; Choi, W. M.; Ahn, J. H.; Kim, H. S.; Song, J. Z.; Huang, Y. G.; Liu, Z. J.; Lu, C.; Koh, C. G.; Rogers, J. A., Complementary metal oxide silicon integrated circuits incorporating monolithically integrated stretchable wavy interconnects. *Appl Phys Lett* **2008**, *93* (4), 044102.
255. Pang, C.; Koo, J. H.; Nguyen, A.; Caves, J. M.; Kim, M. G.; Chortos, A.; Kim, K.; Wang, P. J.; Tok, J. B. H.; Bao, Z. A., Highly Skin-Conformal Microhairly Sensor for Pulse Signal Amplification. *Adv Mater* **2015**, *27* (4), 634-640.
256. Lee, S.; Inoue, Y.; Kim, D.; Reuveny, A.; Kuribara, K.; Yokota, T.; Reeder, J.; Sekino, M.; Sekitani, T.; Abe, Y.; Someya, T., A strain-absorbing design for tissue-machine interfaces using a tunable adhesive gel. *Nat Commun* **2014**, *5*, 5898.
257. Jang, K. I.; Chung, H. U.; Xu, S.; Lee, C. H.; Luan, H. W.; Jeong, J.; Cheng, H. Y.; Kim, G. T.; Han, S. Y.; Lee, J. W.; Kim, J.; Cho, M.; Miao, F. X.; Yang, Y. Y.; Jung, H. N.; Flavin, M.; Liu, H.; Kong, G. W.; Yu, K. J.; Rhee, S. I.; Chung, J.; Kim, B.; Kwak, J. W.; Yun, M. H.; Kim, J. Y.; Song, Y. M.; Paik, U.; Zhang, Y. H.; Huang, Y.; Rogers, J. A., Soft network composite materials with deterministic and bio-inspired designs. *Nat Commun* **2015**, *6*, 6566.
258. Mannsfeld, S. C. B.; Tee, B. C. K.; Stoltenberg, R. M.; Chen, C. V. H. H.; Barman, S.; Muir, B. V. O.; Sokolov, A. N.; Reese, C.; Bao, Z. N., Highly sensitive flexible pressure sensors with microstructured rubber dielectric layers. *Nat Mater* **2010**, *9* (10), 859-864.
259. Dagdeviren, C.; Shi, Y.; Joe, P.; Ghaffari, R.; Balooch, G.; Usgaonkar, K.; Gur, O.; Tran, P. L.; Crosby, J. R.; Meyer, M.; Su, Y. W.; Webb, R. C.; Tedesco, A. S.; Slepian, M. J.; Huang, Y. G.; Rogers, J. A., Conformal piezoelectric systems for clinical and experimental characterization of soft tissue biomechanics. *Nat Mater* **2015**, *14* (7), 728-736.
260. Hattori, Y.; Falgout, L.; Lee, W.; Jung, S. Y.; Poon, E.; Lee, J. W.; Na, I.; Geisler, A.; Sathwani, D.; Zhang, Y. H.; Su, Y. W.; Wang, X. Q.; Liu, Z. J.; Xia, J.; Cheng, H. Y.; Webb, R. C.; Bonifas, A. P.; Won, P.; Jeong, J. W.; Jang, K. I.; Song, Y. M.; Nardone, B.; Nodzenski, M.; Fan, J. A.; Huang, Y. G.; West, D. P.; Paller, A. S.; Alam, M.; Yeo, W. H.; Rogers, J. A., Multifunctional Skin-Like Electronics for Quantitative, Clinical Monitoring of Cutaneous Wound Healing. *Adv Healthc Mater* **2014**, *3* (10), 1597-1607.

261. Yang, S. X.; Chen, Y. C.; Nicolini, L.; Pasupathy, P.; Sacks, J.; Su, B.; Yang, R.; Sanchez, D.; Chang, Y. F.; Wang, P. L.; Schnyer, D.; Neikirk, D.; Lu, N. S., "Cut-and-Paste" Manufacture of Multiparametric Epidermal Sensor Systems. *Adv Mater* **2015**, *27* (41), 6423-6430.
262. Kim, R. H.; Kim, D. H.; Xiao, J. L.; Kim, B. H.; Park, S. I.; Panilaitis, B.; Ghaffari, R.; Yao, J. M.; Li, M.; Liu, Z. J.; Malyarchuk, V.; Kim, D. G.; Le, A. P.; Nuzzo, R. G.; Kaplan, D. L.; Omenetto, F. G.; Huang, Y. G.; Kang, Z.; Rogers, J. A., Waterproof AlInGaP optoelectronics on stretchable substrates with applications in biomedicine and robotics. *Nat Mater* **2010**, *9* (11), 929-937.
263. Song, Y. M.; Xie, Y. Z.; Malyarchuk, V.; Xiao, J. L.; Jung, I.; Choi, K. J.; Liu, Z. J.; Park, H.; Lu, C. F.; Kim, R. H.; Li, R.; Crozier, K. B.; Huang, Y. G.; Rogers, J. A., Digital cameras with designs inspired by the arthropod eye. *Nature* **2013**, *497* (7447), 95-99.
264. Ramuz, M.; Tee, B. C. K.; Tok, J. B. H.; Bao, Z. N., Transparent, Optical, Pressure-Sensitive Artificial Skin for Large-Area Stretchable Electronics. *Adv Mater* **2012**, *24* (24), 3223-3227.
265. Chader, G. J.; Weiland, J.; Humayun, M. S., Artificial vision: needs, functioning, and testing of a retinal electronic prosthesis. *Prog Brain Res* **2009**, *175*, 317-332.
266. Deisseroth, K., Optogenetics. *Nat Methods* **2011**, *8* (1), 26-29.
267. Cocchi, M.; Kalinowski, J.; Virgili, D.; Fattori, V.; Develay, S.; Williams, J. A. G., Single-dopant organic white electrophosphorescent diodes with very high efficiency and its reduced current density roll-off. *Appl Phys Lett* **2007**, *90* (16), 163508.
268. Huang, M. H.; Lin, W. C.; Fan, C. C.; Wang, Y. S.; Lin, H. W.; Liao, J. L.; Lin, C. H.; Chi, Y., Tunable chromaticity stability in solution-processed organic light emitting devices. *Org Electron* **2015**, *20*, 36-42.
269. Choukri, H.; Fischer, A.; Forget, S.; Chenais, S.; Castex, M. C.; Ades, D.; Siove, A.; Geffroy, B., White organic light-emitting diodes with fine chromaticity tuning via ultrathin layer position shifting. *Appl Phys Lett* **2006**, *89* (18), 183513.
270. Jou, J. H.; Chou, K. Y.; Yang, F. C.; Agrawal, A.; Chen, S. Z.; Tseng, J. R.; Lin, C. C.; Chen, P. W.; Wong, K. T.; Chi, Y., A universal, easy-to-apply light-quality index based on natural light spectrum resemblance. *Appl Phys Lett* **2014**, *104* (20), 203304.
271. Liao, S. Y.; Kumar, S.; Yu, H. H.; An, C. C.; Wang, Y. C.; Lin, J. W.; Wang, Y. L.; Liu, Y. C.; Wu, C. L.; Jou, J. H., Organic Light-Emitting Diode with Color Tunable between Bluish-White Daylight and Orange-White Dusk Hue. *Int J Photoenergy* **2014**, 480829.
272. D'Andrade, B. W.; Thompson, M. E.; Forrest, S. R., Controlling exciton diffusion in multilayer white phosphorescent organic light emitting devices. *Adv Mater* **2002**, *14* (2), 147-151.
273. Chen, P.; Xie, W. F.; Li, J.; Guan, T.; Duan, Y.; Zhao, Y.; Liu, S. Y.; Ma, C. S.; Zhang, L. Y.; Li, B., White organic light-emitting devices with a bipolar transport

layer between blue fluorescent and orange phosphorescent emitting layers. *Appl Phys Lett* **2007**, *91* (2), 023505.

274. Liu, S. Q.; Wu, R. F.; Huang, J.; Yu, J. S., Color-tunable and high-efficiency organic light-emitting diode by adjusting exciton bilateral migration zone. *Appl Phys Lett* **2013**, *103* (13), 133307.

275. Jou, J. H.; Wu, M. H.; Shen, S. M.; Wang, H. C.; Chen, S. Z.; Chen, S. H.; Lin, C. R.; Hsieh, Y. L., Sunlight-style color-temperature tunable organic light-emitting diode. *Appl Phys Lett* **2009**, *95* (1), 013307.

276. Jou, J. H.; Shen, S. M.; Wu, M. H.; Peng, S. H.; Wang, H. C., Sunlight-style organic light-emitting diodes. *J Photon Energy* **2011**, *1*, 011021.

277. van Bommel, W. J. M., Non-visual biological effect of lighting and the practical meaning for lighting for work. *Appl Ergon* **2006**, *37* (4), 461-466.

278. Mills, P. R.; Tomkins, S. C.; Schlangen, L. J., The effect of high correlated colour temperature office lighting on employee wellbeing and work performance. *J Circadian Rhythms* **2007**, *5*, 2.

279. Pauley, S. M., Lighting for the human circadian clock: recent research indicates that lighting has become a public health issue. *Med Hypotheses* **2004**, *63* (4), 588-596.

280. Lockley, S. W.; Brainard, G. C.; Czeisler, C. A., High sensitivity of the human circadian melatonin rhythm to resetting by short wavelength light. *J Clin Endocr Metab* **2003**, *88* (9), 4502-4505.

281. Brainard, G. C.; Richardson, B. A.; King, T. S.; Reiter, R. J., The Influence of Different Light Spectra on the Suppression of Pineal Melatonin Content in the Syrian-Hamster. *Brain Res* **1984**, *294* (2), 333-339.

282. Scheer, F. A. J. L.; Buijs, R. M., Light affects morning salivary cortisol in humans. *J Clin Endocr Metab* **1999**, *84* (9), 3395-3398.

283. Sato, M.; Sakaguchi, T.; Morita, T., The effects of exposure in the morning to light of different color temperatures on the behavior of core temperature and melatonin secretion in humans. *Biol Rhythm Res* **2005**, *36* (4), 287-292.

284. Behar-Cohen, F.; Martinsons, C.; Vienot, F.; Zissis, G.; Barlier-Salsi, A.; Cesarini, J. P.; Enouf, O.; Garcia, M.; Picaud, S.; Attia, D., Light-emitting diodes (LED) for domestic lighting: Any risks for the eye? *Prog Retin Eye Res* **2011**, *30* (4), 239-257.

285. Jou, J. H.; Chen, S. H.; Shen, S. M.; Jou, Y. C.; Lin, C. H.; Peng, S. H.; Hsia, S. P.; Wang, C. W.; Chen, C. C.; Wang, C. C., High efficiency low color-temperature organic light-emitting diodes with a blend interlayer. *J Mater Chem* **2011**, *21* (44), 17850-17854.

286. Jou, J. H.; Hsieh, C. Y.; Tseng, J. R.; Peng, S. H.; Jou, Y. C.; Hong, J. H.; Shen, S. M.; Tang, M. C.; Chen, P. C.; Lin, C. H., Candle Light-Style Organic Light-Emitting Diodes. *Adv Funct Mater* **2013**, *23* (21), 2750-2757.

287. Jou, J. H.; Kumar, S.; An, C. C.; Singh, M.; Yu, H. H.; Hsieh, C. Y.; Lin, Y. X.; Sung, C. F.; Wang, C. W., Enabling a blue-hazard free general lighting based on candle light-style OLED. *Opt Express* **2015**, *23* (11), A576-A581.

288. Jou, J. H.; Chen, P. W.; Chen, Y. L.; Jou, Y. C.; Tseng, J. R.; Wu, R. Z.; Hsieh, C. Y.; Hsieh, Y. C.; Joers, P.; Chen, S. H.; Wang, Y. S.; Tung, F. C.; Chen, C. C.; Wang, C. C., OLEDs with chromaticity tunable between dusk-hue and candle-light. *Org Electron* **2013**, *14* (1), 47-54.
289. Jou, J. H.; Wang, H. C.; Shen, S. M.; Peng, S. H.; Wu, M. H.; Chen, S. H.; Wu, P. H., Highly efficient color-temperature tunable organic light-emitting diodes. *J Mater Chem* **2012**, *22* (16), 8117-8120.
290. Jou, J. H.; Tseng, J. R.; Tseng, K. Y.; Wang, W. B.; Jou, Y. C.; Shen, S. M.; Chen, Y. L.; Hung, W. Y.; Chen, S. Z.; Ding, T. Y.; Wang, H. C., High-efficiency host free deep-blue organic light-emitting diode with double carrier regulating layers. *Org Electron* **2012**, *13* (12), 2893-2897.
291. Han, T. H.; Lee, Y.; Choi, M. R.; Woo, S. H.; Bae, S. H.; Hong, B. H.; Ahn, J. H.; Lee, T. W., Extremely efficient flexible organic light-emitting diodes with modified graphene anode. *Nat Photonics* **2012**, *6* (2), 105-110.
292. Sekitani, T.; Nakajima, H.; Maeda, H.; Fukushima, T.; Aida, T.; Hata, K.; Someya, T., Stretchable active-matrix organic light-emitting diode display using printable elastic conductors. *Nat Mater* **2009**, *8* (6), 494-499.
293. Yin, D.; Feng, J.; Ma, R.; Liu, Y. F.; Zhang, Y. L.; Zhang, X. L.; Bi, Y. G.; Chen, Q. D.; Sun, H. B., Efficient and mechanically robust stretchable organic light-emitting devices by a laser-programmable buckling process. *Nat Commun* **2016**, *7*, 11573.
294. Choi, S.; Lee, H.; Ghaffari, R.; Hyeon, T.; Kim, D. H., Recent Advances in Flexible and Stretchable Bio-Electronic Devices Integrated with Nanomaterials. *Adv Mater* **2016**, *28* (22), 4203-4218.
295. Lee, H.; Choi, T. K.; Lee, Y. B.; Cho, H. R.; Ghaffari, R.; Wang, L.; Choi, H. J.; Chung, T. D.; Lu, N. S.; Hyeon, T.; Choi, S. H.; Kim, D. H., A graphene-based electrochemical device with thermoresponsive microneedles for diabetes monitoring and therapy. *Nat Nanotechnol* **2016**, *11* (6), 566-572.
296. Steude, A.; Witts, E. C.; Miles, G. B.; Gather, M. C., Arrays of microscopic organic LEDs for high-resolution optogenetics. *Sci Adv* **2016**, *2* (5), e1600061.
297. Steude, A.; Jähnel, M.; Thomschke, M.; Schober, M.; Gather, M. C., Controlling the Behavior of Single Live Cells with High Density Arrays of Microscopic OLEDs. *Adv Mater* **2015**, *27* (46), 7657-7661.
298. Choi, S.; Park, J.; Hyun, W.; Kim, J.; Kim, J.; Lee, Y. B.; Song, C.; Hwang, H. J.; Kim, J. H.; Hyeon, T.; Kim, D. H., Stretchable Heater Using Ligand-Exchanged Silver Nanowire Nanocomposite for Wearable Articular Thermotherapy. *ACS Nano* **2015**, *9* (6), 6626-6633.
299. Jang, N. S.; Kim, K. H.; Ha, S. H.; Jung, S. H.; Lee, H. M.; Kim, J. M., Simple Approach to High-Performance Stretchable Heaters Based on Kirigami Patterning of Conductive Paper for Wearable Thermotherapy Applications. *ACS Appl Mater Inter* **2017**, *9* (23), 19612-19621.

300. Sokolov, A. N.; Tee, B. C. K.; Bettinger, C. J.; Tok, J. B. H.; Bao, Z. N., Chemical and Engineering Approaches To Enable Organic Field-Effect Transistors for Electronic Skin Applications. *Accounts Chem Res* **2012**, *45* (3), 361-371.
301. Hwang, B. U.; Lee, J. H.; Trung, T. Q.; Roh, E.; Kim, D. I.; Kim, S. W.; Lee, N. E., Transparent Stretchable Self-Powered Patchable Sensor Platform with Ultrasensitive Recognition of Human Activities. *Acs Nano* **2015**, *9* (9), 8801-8810.
302. Park, S. I.; Xiong, Y. J.; Kim, R. H.; Elvikis, P.; Meitl, M.; Kim, D. H.; Wu, J.; Yoon, J.; Yu, C. J.; Liu, Z. J.; Huang, Y. G.; Hwang, K.; Ferreira, P.; Li, X. L.; Choquette, K.; Rogers, J. A., Printed Assemblies of Inorganic Light-Emitting Diodes for Deformable and Semitransparent Displays. *Science* **2009**, *325* (5943), 977-981.
303. Dai, X.; Messanvi, A.; Zhang, H. Z.; Durand, C.; Eymery, J.; Bougerol, C.; Julien, F. H.; Tchernycheva, M., Flexible Light-Emitting Diodes Based on Vertical Nitride Nanowires. *Nano Lett* **2015**, *15* (10), 6958-6964.
304. Gao, W.; Emaminejad, S.; Nyein, H. Y. Y.; Challa, S.; Chen, K. V.; Peck, A.; Fahad, H. M.; Ota, H.; Shiraki, H.; Kiriya, D.; Lien, D. H.; Brooks, G. A.; Davis, R. W.; Javey, A., Fully integrated wearable sensor arrays for multiplexed in situ perspiration analysis. *Nature* **2016**, *529* (7587), 509-514.
305. Lee, H.; Song, C.; Hong, Y. S.; Kim, M. S.; Cho, H. R.; Kang, T.; Shin, K.; Choi, S. H.; Hyeon, T.; Kim, D. H., Wearable/disposable sweat-based glucose monitoring device with multistage transdermal drug delivery module. *Sci Adv* **2017**, *3* (3), e1601314.
306. Lee, S.; Reuveny, A.; Reeder, J.; Lee, S.; Jin, H.; Liu, Q. H.; Yokota, T.; Sekitani, T.; Isoyama, T.; Abe, Y.; Suo, Z. G.; Someya, T., A transparent bending-insensitive pressure sensor. *Nat Nanotechnol* **2016**, *11* (5), 472-478.
307. Yang, J.; Choi, M. K.; Kim, D. H.; Hyeon, T., Designed Assembly and Integration of Colloidal Nanocrystals for Device Applications. *Adv Mater* **2016**, *28* (6), 1176-1207.
308. Kovalenko, M. V.; Manna, L.; Cabot, A.; Hens, Z.; Talapin, D. V.; Kagan, C. R.; Klimov, V. I.; Rogach, A. L.; Reiss, P.; Milliron, D. J.; Guyot-Sionnest, P.; Konstantatos, G.; Parak, W. J.; Hyeon, T.; Korgel, B. A.; Murray, C. B.; Heiss, W., Prospects of Nanoscience with Nanocrystals. *Acs Nano* **2015**, *9* (2), 1012-1057.
309. Choi, J. H.; Wang, H.; Oh, S. J.; Paik, T.; Jo, P. S.; Sung, J.; Ye, X. C.; Zhao, T. S.; Diroll, B. T.; Murray, C. B.; Kagan, C. R., Exploiting the colloidal nanocrystal library to construct electronic devices. *Science* **2016**, *352* (6282), 205-208.
310. Tee, B. C. K.; Chortos, A.; Berndt, A.; Nguyen, A. K.; Tom, A.; McGuire, A.; Lin, Z. L. C.; Tien, K.; Bae, W. G.; Wang, H. L.; Mei, P.; Chou, H. H.; Cui, B. X.; Deisseroth, K.; Ng, T. N.; Bao, Z. N., A skin-inspired organic digital mechanoreceptor. *Science* **2015**, *350* (6258), 313-316.
311. Oh, J. Y.; Rondeau-Gagne, S.; Chiu, Y. C.; Chortos, A.; Lissel, F.; Wang, G. J. N.; Schroeder, B. C.; Kurosawa, T.; Lopez, J.; Katsumata, T.; Xu, J.; Zhu, C. X.; Gu, X. D.; Bae, W. G.; Kim, Y.; Jin, L. H.; Chung, J. W.; Tok, J. B. H.; Bao, Z. N., Intrinsically stretchable and healable semiconducting polymer for organic transistors. *Nature* **2016**, *539* (7629), 411-415.

312. Kelley, T. W.; Baude, P. F.; Gerlach, C.; Ender, D. E.; Muyres, D.; Haase, M. A.; Vogel, D. E.; Theiss, S. D., Recent progress in organic electronics: Materials, devices, and processes. *Chem Mater* **2004**, *16* (23), 4413-4422.
313. Forrest, S. R.; Thompson, M. E., Introduction: Organic electronics and optoelectronics. *Chem Rev* **2007**, *107* (4), 923-925.
314. Dimitrakopoulos, C. D.; Malenfant, P. R. L., Organic thin film transistors for large area electronics. *Adv Mater* **2002**, *14* (2), 99-117.
315. Kim, B. J.; Lee, S. K.; Kang, M. S.; Ahn, J. H.; Cho, J. H., Coplanar-Gate Transparent Graphene Transistors and Inverters on Plastic. *Acs Nano* **2012**, *6* (10), 8646-8651.
316. Park, Y. J.; Lee, S. K.; Kim, M. S.; Kim, H.; Ahn, J. H., Graphene-Based Conformal Devices. *Acs Nano* **2014**, *8* (8), 7655-7662.
317. Wang, C.; Hwang, D.; Yu, Z. B.; Takei, K.; Park, J.; Chen, T.; Ma, B. W.; Javey, A., User-interactive electronic skin for instantaneous pressure visualization. *Nat Mater* **2013**, *12* (10), 899-904.
318. Son, D.; Koo, J. H.; Song, J. K.; Kim, J.; Lee, M.; Shim, H. J.; Park, M.; Lee, M.; Kim, J. H.; Kim, D. H., Stretchable Carbon Nanotube Charge-Trap Floating-Gate Memory and Logic Devices for Wearable Electronics. *Acs Nano* **2015**, *9* (5), 5585-5593.
319. Chen, K.; Gao, W.; Emaminejad, S.; Kiriya, D.; Ota, H.; Nyein, H. Y. Y.; Takei, K.; Javey, A., Printed Carbon Nanotube Electronics and Sensor Systems. *Adv Mater* **2016**, *28* (22), 4397-4414.
320. Roh, E.; Hwang, B. U.; Kim, D.; Kim, B. Y.; Lee, N. E., Stretchable, Transparent, Ultrasensitive, and Patchable Strain Sensor for Human-Machine Interfaces Comprising a Nanohybrid of Carbon Nanotubes and Conductive Elastomers. *Acs Nano* **2015**, *9* (6), 6252-6261.
321. Yang, Y. J.; Ding, L.; Han, J.; Zhang, Z. Y.; Peng, L. M., High-Performance Complementary Transistors and Medium-Scale Integrated Circuits Based on Carbon Nanotube Thin Films. *Acs Nano* **2017**, *11* (4), 4124-4132.
322. Chen, B. Y.; Zhang, P. P.; Ding, L.; Han, J.; Qiu, S.; Li, Q. W.; Zhang, Z. Y.; Peng, L. M., Highly Uniform Carbon Nanotube Field-Effect Transistors and Medium Scale Integrated Circuits. *Nano Lett* **2016**, *16* (8), 5120-5128.
323. Qiu, C. G.; Zhang, Z. Y.; Xiao, M. M.; Yang, Y. J.; Zhong, D. L.; Peng, L. M., Scaling carbon nanotube complementary transistors to 5-nm gate lengths. *Science* **2017**, *355* (6322), 271-276.
324. Fang, H.; Yu, K. J.; Gloschat, C.; Yang, Z.; Chiang, C. H.; Zhao, J.; Won, S. M.; Xu, S.; Trumpis, M.; Zhong, Y.; Song, E.; Han, S. W.; Xue, Y.; Xu, D.; Cauwenberghs, G.; Kay, M.; Huang, Y.; Viventi, J.; Efimov, I. R.; Rogers, J. A., Capacitively Coupled Arrays of Multiplexed Flexible Silicon Transistors for Long-Term Cardiac Electrophysiology. *Nat Biomed Eng* **2017**, *1*, 0038.
325. Led, S.; Fernandez, J.; Serrano, L., Design of a wearable device for ECG continuous monitoring using wireless technology. *Conf Proc IEEE Eng Med Biol Soc* **2004**, *5*, 3318-21.

326. Kim, J.; Son, D.; Lee, M.; Song, C.; Song, J. K.; Koo, J. H.; Lee, D. J.; Shim, H. J.; Kim, J. H.; Lee, M.; Hyeon, T.; Kim, D. H., A wearable multiplexed silicon nonvolatile memory array using nanocrystal charge confinement. *Sci Adv* **2016**, *2* (1), e1501101.
327. Zhang, D. D.; Cai, M. H.; Bin, Z. Y.; Zhang, Y. G.; Zhang, D. Q.; Duan, L., Highly efficient blue thermally activated delayed fluorescent OLEDs with record-low driving voltages utilizing high triplet energy hosts with small singlet-triplet splittings. *Chemical Science* **2016**, *7* (5), 3355-3363.
328. Choi, M. K.; Yang, J.; Kang, K.; Kim, D. C.; Choi, C.; Park, C.; Kim, S. J.; Chae, S. I.; Kim, T. H.; Kim, J. H.; Hyeon, T.; Kim, D. H., Wearable red-green-blue quantum dot light-emitting diode array using high-resolution intaglio transfer printing. *Nat Commun* **2015**, *6*, 7149.
329. Choi, M. K.; Park, I.; Kim, D. C.; Joh, E.; Park, O. K.; Kim, J.; Kim, M.; Choi, C.; Yang, J.; Cho, K. W.; Hwang, J. H.; Nam, J. M.; Hyeon, T.; Kim, J. H.; Kim, D. H., Thermally Controlled, Patterned Graphene Transfer Printing for Transparent and Wearable Electronic/Optoelectronic System. *Adv Funct Mater* **2015**, *25* (46), 7109-7118.
330. Song, J. K.; Son, D.; Kim, J.; Yoo, Y. J.; Lee, G. J.; Wang, L.; Choi, M. K.; Yang, J.; Lee, M.; Do, K.; Koo, J. H.; Lu, N. S.; Kim, J. H.; Hyeon, T.; Song, Y. M.; Kim, D. H., Wearable Force Touch Sensor Array Using a Flexible and Transparent Electrode. *Adv Funct Mater* **2017**, *27* (6), 1605286.
331. Kim, J.; Shim, H. J.; Yang, J.; Choi, M. K.; Kim, D. C.; Kim, J.; Hyeon, T.; Kim, D. H., Ultrathin Quantum Dot Display Integrated with Wearable Electronics. *Adv Mater* **2017**, *29* (38).
332. White, M. S.; Kaltenbrunner, M.; Glowacki, E. D.; Gutnichenko, K.; Kettlgruber, G.; Graz, I.; Aazou, S.; Ulbricht, C.; Egbe, D. A. M.; Miron, M. C.; Major, Z.; Scharber, M. C.; Sekitani, T.; Someya, T.; Bauer, S.; Sariciftci, N. S., Ultrathin, highly flexible and stretchable PLEDs. *Nat Photonics* **2013**, *7* (10), 811-816.
333. Liang, J. J.; Li, L.; Niu, X. F.; Yu, Z. B.; Pei, Q. B., Elastomeric polymer light-emitting devices and displays. *Nat Photonics* **2013**, *7* (10), 817-824.
334. Yu, Z. B.; Niu, X. F.; Liu, Z. T.; Pei, Q. B., Intrinsically Stretchable Polymer Light-Emitting Devices Using Carbon Nanotube-Polymer Composite Electrodes. *Adv Mater* **2011**, *23* (34), 3989-3994.
335. Park, J.; Choi, S.; Janardhan, A. H.; Lee, S. Y.; Raut, S.; Soares, J.; Shin, K.; Yang, S. X.; Lee, C.; Kang, K. W.; Cho, H. R.; Kim, S. J.; Seo, P.; Hyun, W.; Jung, S.; Lee, H. J.; Lee, N.; Choi, S. H.; Sacks, M.; Lu, N. S.; Josephson, M. E.; Hyeon, T.; Kim, D. H.; Hwang, H. J., Electromechanical cardioplasty using a wrapped elasto-conductive epicardial mesh. *Sci Transl Med* **2016**, *8* (344), 344ra86.

국문초록

유기 발광 소자(organic light-emitting diodes, OLEDs)는 자발광, 고휘도 및 높은 명암비, 빠른 응답속도, 그리고 초박막 두께 등의 이점을 갖기에 휴대폰이나 대형 TV 등에 이용되는 등 차세대 디스플레이로서 많은 각광을 받고 있다. 유기 발광 소자에 사용되는 물질은 각 층을 구성하는 물질 자체의 제작 편의성 및 긴 구동 수명을 필요로 하며 그 중에서도 발광층(Emitting layer, EML)에 사용되는 발광 물질은 높은 색 순도 및 양자 효율(quantum efficiency), 그리고 발광층 구성의 재현성을 필요로 하기에, 유기 발광 소자에서의 핵심 부분이라 할 수 있다. 빛의 삼원색을 내는 물질 중, 청색 발광 물질은 청색 색좌표에 해당하는 색 순도를 구현하기 어렵고, 적색 및 녹색 대비 높은 효율을 얻기 어렵기 때문에 많은 연구가 필요하다. 따라서 본 연구에서는 발광층에서 호스트(host) 물질 없이 논도핑(non-doped) 조건으로 높은 색 순도를 갖는 청색 발광 물질 및 고효율의 지연 형광 물질의 개발에 관하여 논의하였다. 또한 엑시톤 차단층(exciton blocking layer, EBL)을 이용한 색 가변 유기 발광 소자(color-tunable OLEDs, CTOLEDs)를 제작하여 초박형 탄소 나노튜브(CNT) 기반의 심전도(electrocardiogram, ECG) 모니터의 개발에 적용하였다.

Part I 은 현재까지 개발된, 그리고 미래 OLEDs 에 관한 간략한 청사진과 전반적인 광물리적 현상의 이해에 관련된 기초 이론을 정리하였다. 흡수 및 방출 과정의 메커니즘과 관련된 이론을 이해함으로써 실제 소자에서의 양자 효율, 구동 수명(operating lifetime) 및 전자 발광(electroluminescence)의 원리를 분석할 수 있다. 이러한 이해는

OLEDs 에 사용되는 새로운 청색 발광체 및 지연 형광 물질을 고안하는 데 바탕이 된다.

Part II 는 호스트 물질없이 발광층을 구성하여 고효율의 청색 형광을 내는 물질의 개발에 관한 연구이다. 청색 물질은 높은 밴드갭(Band-gap) 에너지를 갖는 태생적 특성과 균일하지 않은 전하 수송 특성으로 인해, 표준 청색에 해당하는 색좌표인 CIE (0.15, 0.07) 을 구현하기 어렵고, 동시에 높은 효율을 얻기 힘들다는 단점을 갖는다. 또한 분자간 상호작용으로 인한 색순도와 효율의 저하를 막기 위해 발광 물질을 보조하는 호스트 물질이 필요하다. 이를 극복하기 위해 청색 발광 물질에 정공이나 전자 이동도가 높은 작용기를 발광체에 뒤틀린 형태로 결합하여 양극성(bipolar)의 특성을 지니면서 동시에 청색발광을 내는 물질을 고안하여 소자에 적용시켰다. 첫번째 섹션에서는 안트라센(anthracene) 발광체를 중심으로 정공 이동도가 좋은 아니솔(anisole)을 결합하고, 반대쪽에 전자 이동도가 좋은 피리딘(pyridine), 이소퀴놀린(isoquinoline), 퀴놀린(quinoline), 페난쓰롤린(phenanthroline)을 결합하여 양극성 특성을 가지면서 동시에 청색 발광을 내는 4 가지 물질(3PAA, IQAA, 3QAA, PTAA)을 고안 및 합성하였다. 퀴놀린을 결합한 3QAA 를 기준으로 3PAA 와 IQAA 는 더 단파장 영역에서 발광을 나타냈고, 반면에 페난쓰롤린을 결합한 PTAA 는 상대적으로 장파장 영역의 발광을 나타냈다. 이는 전자 이동도가 좋은 물질들의 공액 길이(conjugation length)의 차이로 인한 결과이다. 두번째 섹션에서는 정공 이동도가 좋은 트리페닐아민(triphenylamine)과 전자 이동도가 좋은 벤즈이미다졸(benzimidazole)을 직접적으로 결합하여

두가지 청색 형광 물질을 합성하고 물질들의 결합 위치의 변화에 따른 발광 파장의 변화를 알아보았다. 또한 합성된 물질의 농도평 소자에서, 분자구조에 기인한 분자간 밀도의 차이로 인하여 엑시톤 소광(quenching)을 막고 더 높은 효율을 얻을 수 있음을 확인하였다. 세번째 섹션에서는 정공 이동도가 좋은 트리페닐아민과 전자 이동도가 좋은 퀴놀린, 퀴옥살린(quinoxalin), 퀴나졸린(quinazoline)을 각각 결합하여 QT, XT, ZT 의 세가지 청색 물질을 개발하였다. 각각의 물질을 기반으로 한 농도평 및 mCBP 를 호스트로 사용한 OLEDs 소자에서 적절한 효율의 청색 전자 발광을 확인할 수 있었다. 또한 퀴놀린과 트리페닐아민을 결합한 QT 는 XT 와 ZT 의 호스트물질로서도 사용할 수 있음을 확인하였다. 네번째 섹션에서는 페난쓰렌(phenanthrene)과 플루오렌(flourene)을 하이브리드(hybrid)하여 새로운 인데노페난쓰렌(indenophenanthrene) 물질을 개발하고 정공 이동도가 좋은 트리페닐아민 및 디페닐아민(diphenylamine)과 각각 결합하여 TIP 와 DIP 를 합성하였다. DIP 를 기반으로 하는 농도평 소자는 TIP 기반의 소자보다 좋은 전하 균형을 보이기 때문에 우수한 청색 색순도와 그에 준하는 높은 외부 양자 효율(external quantum efficiency, EQE)을 얻을 수 있었다.

Part III 는 호스트 물질없이 지연 형광(Delayed fluorescence)을 내는 고효율의 물질 개발에 관련된 연구이다. 열 활성화 지연 형광(Thermally activated delayed fluorescence, TADF) 물질은 고유의 소수성 특징 평면 구조로 인한 파이-파이 상호작용에 의해 쉽게 응집하는 경향이 있다. 이로 인해 응집 유발 소광(aggregation-caused quenching, ACQ)이나 엑시톤

농도 소광(exciton concentration quenching)이 쉽게 유발되고 그 결과 양자 효율이 감소하게 된다. 이를 극복하기 위해 정공 이동도가 좋은 아크리딘(acridine)과 전자 이동도가 좋은 트리페닐트리아진(triphenyltriazine)을 페닐 링커를 사용하여 *meta* 위치로 결합한 AmT 와 AmmT 를 각각 고안 및 합성하였다. 고안된 분자는 단일 분자임에도 불구하고 분자내 상호작용에 의한 엑시톤 형성에 의한 발광 뿐만 아니라, 분자간 상호작용에 의한 엑시톤 형성에 의한 발광으로 인해 농도핑 OLEDs 소자에서 호스트 물질을 사용한 도핑소자보다 더 높은 외부 양자 효율을 보인다.

Part IV 는 탄소 나노튜브(CNT) 기반 초박형 전자소자와 색 가변 유기 발광 소자(CTOLEDs) 기반 디스플레이를 결합하여 착용 가능한(wearable) 심전도(electrocardiogram, ECG) 모니터 제조 방법을 개발하였다. CTOLEDs 는 bis[2-(4,6-difluorophenyl)pyridinato-C2, N](picolinato)iridium(III)(FIrpic) 청색 발광층과 bis(2-phenylquinolyl-N,C(2'))-iridium(acetylacetonate)(pq2Ir(acac)) 적색 발광층을 이용하고, 초박막 bis[2-(diphenylphosphino)phenyl]ether oxide (DPEPO) 엑시톤 차단층(exciton block layer, EBL)을 청색 발광층과 적색 발광층 사이에 삽입하여 구동 전압에 따라 청색 및 적색층에서의 엑시톤 생성 비율에 의하여 청색에서 적색으로의 변화가 가능하게 고안되었다. 정공형 금속 산화물 반도체(p-MOS) 인버터는 피부에서의 밀착감과 효율적인 ECG 신호 증폭을 위하여 4 개의 CNT 트랜지스터를 기반으로 제작되었다. 각각의 소자를 결합하여 제작된 센서는 초박형 특성을 지니기 때문에 피부 착용감과

일체감이 아주 좋은 것으로 판명되었을 뿐 아니라 극단적인 굽힘 및 접힘 조건에서도 높은 탄력성을 나타내는 것이 검증되었다. CNT 전자 소자와 결합된 착용 가능한 CTOLED 는 심전도 변화를 색변화에 의하여 실시간으로 표시하는 데 사용되었다.

주요어: 형광 유기 발광 소자, 양극성, 청색 형광 물질, 지연 형광 물질, 분자간 상호작용, 탄소 나노튜브, 색 가변 유기 발광 소자, 착용가능한 센서

학번: 2011-30103